Exploitation of pulse shape analysis for correlated background rejection and ortho-positronium identification in the Double Chooz experiment

Alessandro Minotti

To cite this version:

Alessandro Minotti. Exploitation of pulse shape analysis for correlated background rejection and ortho-positronium identification in the Double Chooz experiment. High Energy Physics - Experiment [hep-ex]. Université de Strasbourg, 2015. English. NNT : 2015STRAE046 . tel-01398615v1

HAL Id: tel-01398615
https://theses.hal.science/tel-01398615v1

Submitted on 17 Nov 2016 (v1), last revised 17 Nov 2016 (v2)

UNIVERSITÉ DE STRASBOURG

ÉCOLE DOCTORALE DE PHYSIQUE ET CHIMIE-PHYSIQUE

Institut Pluridisciplinaire Hubert Curien (IPHC) – UMR 7178

THÈSE présentée par :

Alessandro MINOTTI

soutenue le : **29 Octobre 2015**

pour obtenir le grade de : **Docteur de l'université de Strasbourg**

Discipline/ Spécialité : Physique des particules

Exploitation of pulse shape analysis for correlated background rejection and ortho-positronium identification in the Double Chooz experiment

THÈSE dirigée par :	
Mme. JOLLET Cécile	Université de Strasbourg - IPHC
RAPPORTEURS :	
M. PIQUEMAL Fabrice	CENBG, Bordeaux
M. ZITO Marco	CEA, Saclay
AUTRES MEMBRES DU JURY :	
M. BAUDOT Jérôme	Université de Strasbourg - IPHC
M. DUCHESNEAU Dominique	LAPP, Annecy
Mme. TONAZZO Alessandra	APC, Paris

Alessandro MINOTTI

Exploitation of pulse shape analysis for correlated background rejection and ortho-positronium identification in the Double Chooz experiment

Résumé

La mesure récente de l'angle de mélange theta-13, à laquelle l'expérience Double Chooz contribue, a ouvert la voie aux futures expériences de la physique des neutrinos. Dans ce manuscrit, la caractérisation des certains bruits de l'expérience sont décrits. Les muons cosmiques qui s'arrêtent and se désintégrent dans le détecteur sont mal reconstruits, résultant en distorsion de la distribution temporelle des signaux laquelle peut être utilisée pour identifier ce type de fond. Les neutrons rapides créés par spallation par les muons cosmiques produisent de nombreux protons de recul qui peuvent entraîner un décalage dans la distribution temporelle des signaux et ainsi être identifiés. Ces distributions temporelles ont aussi été utilisées pour identifier la formation de l'état d'ortho-positronium en observant et en mesurant un délai entre l'ionisation du positron et l'annihilation de celui-ci, pouvant permettre une séparation positron-électron.

Mots-clés: physique des neutrinos, oscillation des neutrinos, Double Chooz, pulse shape discrimination, ortho-positronium, vieillissement du scintillateur.

Abstract

The measurement of the theta-13 mixing angle, to which the Double Chooz experiment contributed, paves the way to future findings in neutrino physics. In this manuscript, we describe the characterization of some Double Chooz backgrounds. Cosmic muons that stop and decay in the detector are characterized by anisotropic emission of the scintillation light, causing the vertex to be poorly reconstructed. The resulting pulse shape distortion can be used to tag and remove such background. Fast spallation neutrons producing multiple recoil protons may produce a similar distortion in the pulse shape and can also be tagged. Pulse shapes are also used to identify the formation of ortho-positronium. The tagging of such electron-positron bound state is made possible by the induced distortion in the pulse shape due to the delay in the positron annihilation, and can be used for an electron-positron separation.

Key-words: neutrino physics, neutrino oscillation, Double Chooz, pulse shape discrimination, ortho-positronium, scintillator ageing.

EXPLOITATION OF PULSE SHAPE ANALYSIS FOR CORRELATED BACKGROUND REJECTION AND ORTHO-POSITRONIUM IDENTIFICATION IN THE DOUBLE CHOOZ EXPERIMENT

Alessandro Minotti

Acknowledgments

A PhD certainly isn't the most relaxing experience a person can have in his life. Yet as I look back at these past three years I can't avoid feeling a sense of nostalgia and peaceful fulfilment. It is a well known bias the one that makes our memories getting sweeter with time. But it is above all the knowledge that I've reached this milestone at the end of a difficult but formative path, that gives the right flavor to this experience. A path that I had the luck of sharing with some amazing people, that made lonely days full, sad days happy, frustrating tasks easy, and ultimately all this possible.

As I mention and thank these people, I cannot start elsewhere than from Cécile. She's been for me more than a mere supervisor, but a source of inspiration, guiding me through most of the difficulties, doubts, tough decisions that I encountered with a natural ease. Together with Anselmo she forms a perfect couple, in life and in physics. I'm glad to have met such wonderful persons, and honoured to have closely collaborated with such good physicists. I also want to thank Elian, who not only endured my noisy habits as my officemate, but actually enjoyed giving advices and support. Many thanks to my other group colleagues Eric, Marcos, and Nikos, to whom I wish good luck for his future in the far east, and also to my fellow Double Chooz collaborators.

Among my former labmates, a special thought goes to Xitzel, Alejandro, and Robert, for sharing such tremendous amount of interesting thoughts and stupid jokes, nice moments and complains, and most of all for being such good friends of mine. I'm grateful to have met them and the nice people around them. I also want to mention my friends Marco and Mattia, and my longtime friend Laurence, that I found again in Strasbourg for a beautiful twist of fate. I had a great time with all you guys. With you I got to know all the bars in Strasbourg, a task that is matched in difficulty maybe only by the PhD itself.

I also and undoubtedly owe my family for their inestimable support. This work is for you, as partial consideration for the unlimited faith you have always placed in me.

Finally, I'd like to thank the members of the commission, for enduring the task of reading and commenting this manuscript.

Note de l'auteur

Avant de parler des neutrinos, de Double Chooz, et de ma thèse, permettez-moi de faire une brève introduction sur moi-même et sur mon travail actuel. Je vais parler brièvement de moi, de ce que cette expérience de trois ans m'a apportée, et de l'avenir qui m'attend après la thèse.

Mon doctorat a débuté il y a 3 ans, en octobre 2012. J'ai alors travaillé pour ce fait avec l'équipe Neutrino au sein de la Direction de la Recherche Subatomique de l'Institut Pluridisciplinaire Hubert Curien au campus de Cronenbourg. Le sujet de ma thèse est relié à celui du mémoire de mon master obtenu à l'Université de Sapienza de Rome en Avril 2012 ; le sujet étant toujours la physique du neutrino. La thèse a pour objet l'étude des formes d'impulsion (pulse shapes en anglais) dans l'expérience sur l'oscillation des neutrinos Double Chooz. Le mémoire du master était aussi un travail d'analyse de données, cette fois là sur OPERA, une autre expérience sur l'oscillation des neutrinos.

La physique des neutrinos est un domaine prometteur de la recherche actuelle, en effet le prix nobel de la physique 2015 a été décerné à Takaaki Kajita et Arthur McDonald pour les oscillations de neutrinos prouvant que le neutrino est une particule massive. L'aspect de la phénoménologie des neutrinos qui intéresse le plus les physiciens depuis quelques décennies est sans conteste l'oscillation des neutrinos, cette propriété quantique grâce à laquelle les neutrinos au cours de leur propagation peuvent changer de saveur avec une probabilité non nulle fonction de l'énergie du neutrino émis et de la distance parcourue. Peu à peu, les pièces du puzzle de la compréhension de la physique des neutrinos se réunissent grâce aux paramètres dits d'oscillation. Ceci par l'entremise des expériences OPERA et Double Chooz, responsables respectivement de la découverte de l'oscillation des neutrinos muoniques par l'apparition des neutrinos tau et de la mesure de l'angle de mélange θ_{13} pour lequel longtemps une limite supérieure était donnée.

Par ailleurs, plusieurs autres découvertes sont attendues dans la physique des neutrinos. En particulier, beaucoup d'efforts sont engagés tour à tour dans la recherche sur la violation de la symétrie CP dans le secteur des neutrinos, la mesure de leurs masses absolues et le problème dit de la hiérarchie des masses c'est-à-dire l'ordre dans lequel les masses sont ordonnées, la distinction entre les neutrinos de Majorana et de Dirac ainsi que la détermination de leur échelle de masse absolue. Toutes ces découvertes auront des implications pertinentes dans la compréhension de la nature. Pour illustration, la violation CP pour les neutrinos pourrait être la clé pour comprendre l'asymétrie matière-antimatière dans l'univers via le scénario désigné comme la leptogenèse.

Actuellement, un grand nombre d'expériences de nouvelle génération sur les neutrinos sont soit en cours soit en préparation. Elles ont toutes pour objectif l'un des aspects cités ci-dessus mais également celui d'améliorer la précision sur les mesures des paramètres d'oscillation. L'ensemble de ces attentes au sujet des nouvelles découvertes sont rendues possibles grâce aux expériences telles que Double Chooz, qui au cours de ces dernières années ont contribué efficacement à une meilleure compréhension de la nature des neutrinos. En particulier, la mesure de l'angle de mélange θ_{13} permettra d'aller mesurer la phase de la violation de CP dans le secteur des neutrinos avec les implications mentionnées plus tôt.

Double Chooz est une collaboration internationale basée en France, précisément dans les Ardennes sur le site de la centrale nucléaire de Chooz. Elle étudie l'oscillation des antineutrinos électroniques produits en grande quantité dans les réactions de fission nucléaire qui ont lieu au cœur des réacteurs. L'expérience consiste en deux détecteurs désignés comme proche et lointain, aux caractéristiques quasi identiques et situés à des distances différentes des deux réacteurs du site de Chooz. Les détecteurs eux sont composés de deux cylindres concentriques remplis d'un liquide scintillant et entouré par des photomultiplicateurs.

La signature d'un antineutrino issu du réacteur et qui interagirait avec le liquide scintillant est obtenue grâce à la désintégration beta inverse (Inverse Beta Decay, IBD en anglais) dans laquelle l'antineutrino entre en interaction avec un proton pour donner en voie de sortie un neutron et un positron. La lumière de scintillation prompte et l'annihilation du positron qui s'en suit ainsi que la lumière émise dans la capture du neutron plus tard sont captées par les photomultiplicateurs, permettant alors la détection de ces particules. Une coïncidence temporelle entre le premier et le second signal signe une désintégration beta inverse.

Les détecteurs de Double Chooz mesurent le nombre des ces interactions des neutrinos et aussi leur énergie. De cette manière, il est possible d'étudier non seulement l'oscillation des antineutrinos électroniques mais en plus de donner la caractérisation d'un tel phénomène en fonction de l'énergie. L'oscillation des antineutrinos décelés par le détecteur lointain est intrinsèquement liée à la valeur de θ_{13}, ce qui permet la mesure directe de cet angle. Le détecteur proche, lui, mesure le flux et le spectre des neutrinos non oscillant, ce qui permet de minimiser l'erreur systématique.

Puisque la mesure de θ_{13} dépend de la connaissance précise du nombre des antineutrinos interagissant dans les deux détecteurs, l'élimination du bruit de fond est d'une importance capitale dans une expérience telle que Double Chooz.

Ma contribution à l'analyse de données dans l'expérience consistait principalement à l'étude de certaines composantes du bruit de fond, à savoir les événements corrélés qui imitent la coincidence en temps et en espace d'une IBD. En particulier, j'ai étudié les neutrons rapides qui entrent dans le détecteur, libérant les protons de recul avant d'être capturés, et des muons cosmiques qui s'arrêtent et se désintègrent dans la partie haute du détecteur générant ainsi un électron Michel. Pour caractériser ces particules, j'ai utilisé une discrimination de forme d'impulsion (Pulse shape discrimination, PSD en anglais) , une technique utilisée dans les détecteurs à scintillateur liquide pour extraire le signal du bruit de fond.

Les Pulse Shapes (formes d'impulsions) sont les profils en temps de la lumière émise par le scintillateur liquide en réponse au passage de particules chargées en son sein. Ce profil dépend de la nature des particules concernées, ainsi que de la position de l'interaction reconstruite. Ces caractéristiques peuvent être exploitées pour une identification des particules, et donc une réduction du bruit de fond. Les formes du courant de tous les photomultiplicateurs sont enregistrées dans Double Chooz pour chaque événement. Néanmoins, quand je suis arrivé en thèse, personne n'avait encore exploité l'idée d'utiliser les formes d'impulsion pour une identification des particules. La première partie de mon travail consistait donc en la reconstruction des pulse shapes, en tenant compte du fait que la contribution de tous les photomultiplicateurs doit être combinée pour construire une forme d'impulsion globale.

Les muons qui s'arrêtent dans le détecteur (stopping muons) émettent plus de lumière de scintillation dans la région du détecteur appelée cheminée, un passage étroit reliant l'intérieur et l'extérieur du détecteur et qui sert au déploiement de sources radioactives à des fins d'étalonnage. La lumière de scintillation émise par l'arrêt de muons n'est pas isotrope et ne permet donc pas une reconstruction précise du vertex de l'événement comparable à celle d'événements de neutrinos. En conséquence, les formes d'impulsion de stopping muons sont déformées, ce qui permet d'effectuer une PSD sur ce bruit de fond.

Les résultats de ces études, rapporté sà la collaboration, ont conduit à l'élaboration d'une coupure basée sur l'algorithme de reconstruction des positions de vertex de l'événement. Cette coupure, qui supprime le bruit de fond, principalement les stopping muons, a été incluse dans la dernière publication de Double Chooz qui exploite la capture de neutrons sur le gadolinium pour identifier les IBD. Le gadolinium est ajouté au liquide du scintillateur à hauteur de 1 g/l afin d'améliorer la détection des neutrons. En outre, une coupure plus précise basée sur les formes d'impulsions a été développée. Cette fois, les informations issues de la distorsion de forme d'impulsion et de la reconstruction des vertex ont été utilisées. Avec une approche de maximum de vraisemblance, la forme d'impulsion a été comparée à une référence avant et après que le vertex soit placé dans la cheminée. Cela a permis d'estimer la composante restante du bruit de fond des stopping muons parmi les IBD pour la prochaine publication de Double Chooz qui exploitera la capture de neutrons sur l'hydrogène pour identifier les interactions IBD.

En ce qui concerne les neutrons rapides, la présence de protons de recul de faible énergie, suivie d'un plus énergique résulte dans une crête retardé dans les formes d'impulsions enregistrées. Cette caractéristique est exploitée par une sélection des neutrons rapides qui mesure le retard du pic de forme d'impulsion par rapport à son début, et l'utilise pour discriminer les neutrons rapides des événements IBD. Cette sélection fait partie des rejets de fond dans la prochaine publication Double Chooz qui exploite la capture de neutrons sur l'hydrogène pour identifier les IBD.

En plus d'analyser les données, j'ai collaboré, conjointement avec le groupe de Strasbourg et d'autres collègues des États-Unis, sur l'assemblage de l'un des deux détecteurs Double Chooz, à savoir le détecteur proche. Le détecteur a commencé la prise de ses données dans une configuration stable en Janvier 2015. Les données provenant de ce nouveau détecteur permettront d'améliorer considérablement l'efficacité de détection ainsi que la précision des mesures Double Chooz en réduisant les erreurs systématiques associées à l'estimation du flux des neutrinos issus du réacteur.

Pour le montage et la mise en service du détecteur proche, j'ai participé aux tests des photomultiplicateurs de l'Inner Veto, l'un des cylindres qui composent le détecteur, et à l'installation des fibres optiques qui sont utilisés pour l'étalonnage périodique des propriétés des photomultiplicateurs. Cet étalonnage se fait déjà mensuellement pour le détecteur lointain, et permet à la collaboration de surveiller les propriétés électroniques de ces appareils. En outre, j'ai collaboré également dans le montage de l'Outer Veto, un détecteur constitué de scintillateurs plastiques placé sur le dessus du détecteur pour l'indentification des événements induits par les muons cosmiques.

Pour ce qui concerne la communication avec la collaboration Double Chooz, j'assiste régulièrement à distance et en personne aux réunions au cours desquelles je rends compte du progrès de mes analyses. J'étais aussi régulièrement disponible pour les shifts du détecteur, des périodes d'une semaine durant lesquelles les shifters surveillent la prise des données du détecteur, contribuant de manière significative au quota de travail du groupe de Strasbourg.

Un autre sujet important pour lequel j'ai travaillé ces deux dernières années est l'étude de l'ortho-positronium dans Double Chooz, principalement sa caractérisation pour la détection des neutrinos. Ce sujet implique le groupe de Strasbourg par le biais du projet NuToPs, une expérience à petite échelle dont le détecteur est situé ici à Strasbourg sur le campus de Cronenbourg. Ce projet étudie la formation de l'ortho-positronium, mesurant sa fraction et la durée de vie dans divers scintillateurs liquides.

L'importance de l'ortho-positronium en physique des neutrinos est due à la possibilité d'effectuer uns PSD alternative, basée sur l'observation de l'ortho-positronium, pour une discrimination β^{+}/β^{-}-. Le positron émis dans le processus IBD, en fait, avant de s'annihilee avec un électron dans la matière, peut former un état métastable positronium, ce qui conduit à une annihilation retardée. Dans sa configuration avec un spin total de 1 (spins parallèles de l'électron et le positron) ce composé est appelé ortho-positronium.

L'ortho-positronium a une durée de vie moyenne dans le vide de 142 ns. Dans la matière, cependant, divers phénomènes écourtent sa durée de vie de l'ordre de quelques nanosecondes. Bien que la durée de vie de l'ortho-positronium est généralement raccourci dans la matière, la distorsion dans la distribution du temps d'émission de photons peut être encore observable. La collaboration Borexino, par exemple, a exploité la signature fournie par forme d'impulsion de distorsion induite par l'ortho-positronium pour rejeter les désintégrations β^+ des noyaux cosmogéniques.

Dans Double Chooz, les événements IBD sont le signal recherché. Par conséquent, l'identification de l'ortho-positronium ne fournirait pas un grand potentiel en termes de signal sur bruit de fond. En fait, la probabilité de formation de l'ortho-positronium dans les scintillateurs liquides de Double Chooz ne dépasse pas 50%. Par conséquent, un rejet d'événements β^+/β^-- se traduirait par une perte significative de signaux.

Néanmoins, la formation d'ortho-positronium événement par événement n'a jamais été observée jusqu'à présent dans des grandes expériences à scintillateurs liquides, ce qui en fait une découverte intéressante. En outre, l'identification de l'ortho-positronium pourrait être utilisée à l'avenir comme technique supplémentaire dans la sélection de signal pour une expérience des neutrinos de réacteur qui serait spécialement conçue pour exploiter la formation de l'ortho-positronium pour réduire les bruit de fond cosmogéniques des noyaux β^- et celui non corrélé accidentel.

Avec ces motivations, j'ai travaillé sur l'identification de l'ortho-positronium dans Double Chooz en utilisant une analyse basée sur la forme des impulsions. Si l'ortho-positronium ne se forme pas, le temps entre l'ionisation induite par le positron et l'annihilation qui s'en suit est trop court pour les distinguer. Cependant, en cas de formation de l'ortho-positronium, le délai entre les deux processus n'est plus négligeable puisque l'ortho-positronium a une durée de vie d'environ $3,4$ ns dans les scintillateurs liquides de Double Chooz, une discrimination entre les deux signaux devient en principe possible. Cela n'est toutefois pas trivial dans Double Chooz, compte tenu du fait que le temps de décroissance rapide du scintillateur et l'échantillonnage électronique sont du même ordre (quelques ns) que la durée de vie de l'ortho-positronium.

Ensemble avec mon superviseur, nous avons développé un algorithme spécifique pour trouver un double pic dans la forme d'impulsion, le premier correspondant à l'ionisation du positron, et le second à l'émission des deux rayons gamma de 511 KeV de l'annihilation e^+–e^-. Une fonction de fit a été construite en combinant deux formes d'impulsion de référence séparées par un retard correspondant au temps mis par l'ortho-positronium pour se désintégrer. Un fit fait sur la forme d'impulsion de positons d'un IBD donne ainsi la durée de vie possible ortho-positronium de cet événement en sortie.

Nous avons comparé la distribution de retard entre l'ionisation et l'annihilation des neutrinos de l'IBD avec celui d'un échantillon dans lequel on ne prévoit aucune formation de positronium. En conséquence, nous avons vu un net excès d'événements à grand retard pour les IBD, ce qui montre la capacité de cette technique pour identifier la formation de l'ortho-positronium événement par événement dans l'expérience Double Chooz. En outre, cette distribution peut être en ajustée pour extrapoler la formation de l'ortho-positronium et sa durée de vie. Les valeurs que nous avons obtenues pour un échantillon restreint des IBD sont en bon accord avec celles mesurées par NuToPS.

Ce travail sur l'observation de la formation de l'ortho-positronium dans Double Chooz a été traduit en un poster que j'ai présenté à la prestigieuse conférence ICHEP, tenue en Juillet dernier à Valence, en Espagne. Il a également été publié un document de la collaboration Double Chooz entièrement axé sur cette analyse et ses implications dans la physique des neutrinos.

Au total, je compte 7 publications, dont deux de la collaboration OPERA, découlant de la contribution que j'ai apportée au cours de mon mémoire de master, et quatre de Double Chooz, y compris celui que j'ai déjà cité. Un article en dehors de la collaboration mais lié à ce sujet, qui explore la possibilité de détection des antineutrinos en se basant sur le marquage de l'ortho-positronium, a été publié.

En ce qui concerne la progression de ma carrière de doctorat sur le plan académique, j'ai eu l'occasion de participer à divers conférences et séminaires. Les plus pertinents, outre ICHEP déjà mentionné, sont les 3 GDR neutrino à Paris, dans l'un desquels j'ai présenté mes travaux sur la discrimination de forme d'impulsion et de son importance pour la physique des neutrinos. J'ai aussi présenté les derniers résultats de Double Chooz, représentant officiellement la collaboration lors de la conférence internationale sur les neutrinos PPP 2015, tenue à Valdaï. Mes participations aux conférences ICHEP et PPP 2015 ont abouti toutes deux à une contribution dans les proceedings de ces conférences, publiés dans une revue internationale. J'ai également pris part à l'école d'été de l'INSS, tenue à St. Andrews en août dernier, une école riche en contenu spécifiquement dédié à la physique du neutrino. Enfin j'ai participé aux rencontres jeunes chercheurs de la physique des particules réunissant l'ensemble des doctorants en France.

Le dernier travail d'analyse que j'ai mené portait sur l'étude du vieillissement du scintillateur liquide de l'Inner Veto de Double Chooz, pour le détecteur loin. La stabilité du composé scintillateur est une question cruciale dans les expériences modernes comme Double Chooz, qui utilisent un mélange de plusieurs liquides : un solvant et un dispositif de décalage de longueur d'onde, également dopé au gadolinium. En particulier, le veto interne de Double Chooz sert à identifier et à caractériser le bruit de fond corrélé, et donc sa stabilité est importante afin de contrôler de tel bruit de fond.

Afin d'étudier le vieillissement du scintillateur de l'Inner Veto j'ai fait usage des runs d'étalonnage pris hebdomadairement, consistant à la lumière produite par des diodes électroluminescentes et envoyée à l'intérieur du détecteur. Ce système d'étalonnage est sous la responsabilité de l'IPHC au sein de la collaboration, une autre raison pour laquelle j'ai opté pour étudier le vieillissement du veto interne. La lumière collectée par des photomultiplicateurs à distance différente d'une LED a été étudiée pour des runs d'étalonnage produits à différents moments au cours de toute la période de la prise de données. De cette manière, une évolution dans le temps de la longueur d'atténuation du scintillateur a été obtenue en fittant la distribution de la lumière recueillie à différentes distances. Les résultats n'ont montré aucune variation importante de la longueur d'atténuation dans Double Chooz, et donc aucun effet de vieillissement du scintillateur de l'Inner Veto.

Après ma thèse, je continuerai à travailler dans la physique des neutrinos que je considère comme l'un des axes les plus fertiles de la recherche et un sujet clé pour l'avenir de la physique des particules, et devenir un expert dans ce domaine. Je suis particulièrement intéressé par les sujets les plus modernes pour lesquels les expériences futures sont conçues. Je crois que les prochaines recherches dans le secteur des neutrinos vont constituer un point tournant de la physique des particules, et je suis prêt à faire partie du processus qui mènera à ces réalisations.

Il ya beaucoup de questions ouvertes auxquelles les recherches futures dans la physique des neutrinos vont essayer de répondre. Quelle est l'ampleur absolue de la masse des neutrinos, et la physique derrière ces masses est-t-elle différente des autres particules? Quelle est la hiérarchie de ces masses ? Est-ce que les interactions de neutrinos violent la parité CP? Y a-t-il des neutrinos stériles? Y a-t-il une physique des neutrinos au-delà du modèle standard? De nombreuses expériences étudient ces aspects, qui sont tous très intéressants pour moi. En particulier, je me sens très attiré par l'étude de la violation de CP et des neutrinos de Majorana.

Il ya une forte possibilité de voir une découverte révolutionnaire dans l'avenir de la physique des neutrinos, et je pense que ce serait une grande opportunité pour un chercheur de travailler dans ce domaine. Pour ces raisons, j'ai profité de l'occasion d'accepter un poste de post-doc dans le département IRFU du laboratoire CEA-Saclay. Dans les deux ans qui suivent, je vais travailler principalement sur l'expérience de STEREO, une expérience de courte baseline sur les neutrinos issus d'un réacteur qui étudie l'anomalie des neutrinos des réacteurs par la recherche de neutrinos stériles à l'échelle de masse eV. L'anomalie des neutrinos des réacteurs, découverte dans le même laboratoire, consiste en un flux de neutrinos observé en deçà des attentes pour une série d'expériences à courte baseline qui ont été menées ces dernières années. Le déficit dans le flux de neutrinos observé peut être interprété comme la présence d'une famille de neutrinos supplémentaire. Cependant, ce quatrième neutrino doit être essentiellement droit ou stérile, soit avec un couplage fortement réprimé avec les bosons de jauge de l'interaction faible, ce qui rend sa détection plus difficile. STEREO fait partie d'une nouvelle génération d'expériences sur les neutrinos qui visent à résoudre cette anomalie en observant directement l'oscillation des neutrinos classiques vers le neutrino stérile.

L'échelle relativement petite, par rapport à Double Chooz, de STEREO, me permettra d'être impliqué et d'avoir des responsabilités dans un grand nombre d'aspects de l'expérience. Cela aura certainement un impact positif sur ma croissance professionnelle et augmenter les chances de continuer à travailler dans ce domaine. Je sui reconnaissant pour l'opportunité qui m'a été donnée par ce post-doc, je ferai de mon mieux pour augmenter mes compétences scientifiques, avec le projet d'obtenir un poste permanent dans un avenir proche, en France pourquoi pas.

Contents

Introduction

From the remotest parts of the Universe to our atmosphere, from the Sun to the Earth core, neutrinos come from numerous natural sources. It was however from an artificial source, nuclear reactors, that the *poltergeist* have been discovered by Cowan and Reines in 1956. It was the birth of one of the most prolific branches of particle physics, dedicated to the study of these elusive and mysterious objects. One of most salient features of neutrinos is that they change their flavour propagating through space, or *oscillate*, a phenomenon first hypothesized by Pontecorvo that has been since supported by several observations. A large number of studies has been devoted to the characterization of neutrino oscillation, involving the combined efforts of a large number of physicists over more than 40 years. Now that we have understood this phenomenon, it is again reactor neutrinos that open doors to new physics. The size of the θ_{13} mixing parameter, measured by reactor neutrino experiments, allows for the exploration of the mass hierarchy and the CP-violation in the leptonic sector, a key step in understanding unknown aspects of our Universe. In the first chapter of this manuscript we attempt to draw a line between past, present and future of neutrino research, by discussing the main measurements in this area.

One of the modern reactor neutrino experiments, Double Chooz, takes up the legacy of CHOOZ, which first tried to measure θ_{13} with reactor neutrinos. Such neutrinos are detected via their inverse beta decay (IBD) interactions in a liquid scintillator 1 km far from the source. The *disappearance*, that is the deficit in the rate of neutrinos with respect to the predictions, is interpreted as result of their oscillation and used to determine θ_{13}. The principle of this measure and the Double Chooz detector are described in chapter 2.

Double Chooz was the first reactor neutrino experiment to report hints of a non-zero θ_{13} in 2011. More recently, it is giving an important contribution to the increasingly precise determination of this neutrino oscillation parameter. Double Chooz profits from a very well known detector and controlled backgrounds. Errors on the θ_{13} measurement arise predominantly from the neutrino flux prediction. However, data collected by the near detector since December 2014 will dramatically reduce such uncertainties. The strong signature of IBD interactions, given by a delayed coincidence between a positron and a neutron signal, is used to heavily suppress the background. The remaining main sources of background consist in decays of cosmogenic elements, accidental coincidences and correlated events that simulate the IBD coincidence. The Double Chooz sample selection, final analysis, and error evaluation are described in chapter 3.

The Double Chooz correlated background is studied with a pulse shape discrimination (PSD), a technique used to separate signal from background using characteristic light time profile of different particles in liquid scintillators. Stopping muons, a correlated background in which a cosmic muon stops and decays in the detector, are fully analysed with a PSD that exploits the spatial reconstruction of these events. Such study allowed for a dramatic reduction of the stopping muons contribution to the background budget. Fast spallation neutrons that excite protons of the medium constitute another source of correlated background. The signal coming from these protons is used to perform a dedicated PSD that separate this background from the signal. A PSD was also used to study the formation of ortho-positronium, a bound state of electron and positron. The ortho-positronium was tagged using a specific algorithm on an event-by-event basis, for the first time in a large liquid scintillator experiment. Ortho-positronium can be the key for electron-positron separation, and therefore contribute to the enhancement of the signal-on-background ratio for future dedicated experiments. A full description of these PSD applications is given in chapter 4, and represents the main theme of the study presented in this manuscript.

The utilization of liquid scintillators is an experimental technique widely used in the physics of neutrinos, tracing back its first applications to the Cowan and Reines' experiments. One of the main challenges in developing a liquid scintillator experiment is the stability of the compound. As additional subject of discussion, in chapter 5 we present a study made on the ageing of one of the Double Chooz liquid scintillators.

1 Neutrino Physics

Contents

Neutrinos are without any doubt one of the most fascinating physical objects of which we have knowledge. They are among the most abundant particles in our Universe, and yet the most mysterious ones. What we know about neutrinos comes from an 80 years long history of continues discoveries, dilemmas and innovations. What we still don't know, on the other hand, can open new doors for physics beyond our current understanding of subatomic world, as well as answer some of the most pressing opened questions in particle physics and cosmology.

The first sections of this chapter will retrace the discovery and the first measurements made on the three neutrino families, heading on how massless neutrinos are integrated in our current model of particle and interactions, the Standard Model. However, neutrino physics go beyond the Standard Model in the so-called phenomenon of neutrino oscillation, which implies neutrino to have mass, as we will describe in the second part of the chapter. We will focus on the researches of parameters that govern neutrino oscillation, which have been and are of vast importance in the experimental high-energy physics agenda. Particular attention will be given in the second section to the θ_{13} parameter, the measure of which is the motivation of the Double Chooz experiment. The third and last section is instead dedicated to the opened questions about neutrinos and the experimental approaches that are and will be used to uncover them in the years to come.

1.1 Neutrinos in the Standard Model

The history of neutrino physics is strongly linked with the characterization of the weak interaction, one of the three fundamental forces described in the Standard Model. This interaction is responsible for the transmutation of nuclei called β decay, the study of which brought up the hypothesis of neutrino existence.

1.1.1 The neutrino: from hypothesis...

The birthdate of the neutrino can be placed in 1930, year in which W. Pauli first postulated the existence of a particle later identified as the neutrino [1]. With his idea Pauli intended to solve two conundrums of the recently born field of nuclear physics at the same time: the so called wrong spin-statistics and the β decay spectrum problem.

Physicists have been studying the phenomenon of radiation from the end of the previous century. The radiation processes were classified in three different types, α, γ and β, basing on the penetrating power and the deflection by a magnetic field of their products [2, 3]. β particles, high-speed electrons produced in β decays, have been object of study, by the others, of J. Chadwick, during his work under H. Geiger at PTR[1]. Using his mentor's invention, the Geiger counter, he proved in 1913 how these electrons were characterized by a continuous spectrum [4] (see an e.g. in figure 1a or [5, 6]). This was in contrast with the current formulation of the β decay

$$ {}^{A}_{Z}\mathrm{X} \longrightarrow {}^{\;\;A}_{Z+1}\mathrm{Y} + e \,, \tag{1}$$

that implied a fixed electron (e) energy. That was the case in fact of γ and α emissions (see e.g. in figure 1b), which presented narrow spectral lines. Many possible solutions were proposed at the time, some more extreme than others, to explain the continuous spectrum of β particles, but without any favourable result[2].

---

[1] Physikalisch-Technische Reichsanstalt, Berlin.

[2] The L. Meitner's idea of electrons loosing energy in the source [7] was ruled out by the measures with precise calorimeters of C.D. Ellis and W.A. Wooster in 1927 [8]. N. Bohr was prone to give up the dogmatic law of energy conservation, by proposing that it would have been conserved only statistically.

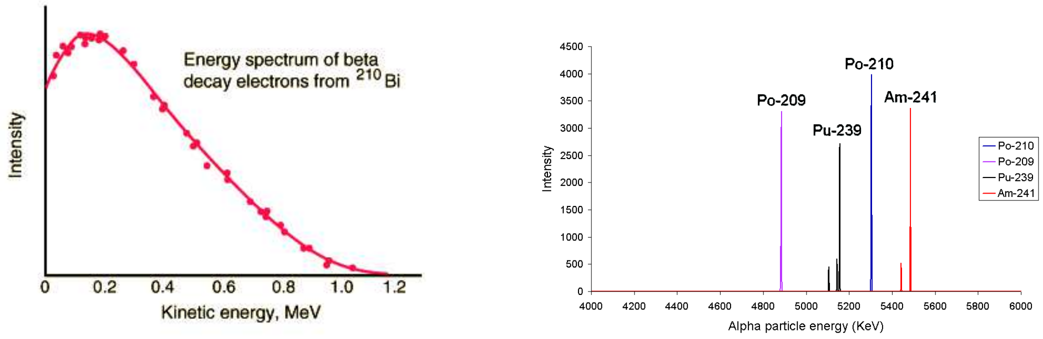

(a) Energy spectrum of β decay electrons of ^{210}Bi; from [6].

(b) Spectral α lines of four isotopes; from [9].

Figure 1: Comparison between e.g. β and α energy spectra.

According to the ’20s knowledge [10–15], an atom $^{A}_{Z}\mathrm{X}$ is constituted by A protons and $A-Z$ electrons. This leads to the inconsistence that an atom (for instance) of $^{14}_{7}\mathrm{Ni}$ would be a fermion[3] (consisting of an odd number of fermions), while experimentally behaves like a boson. This inconsistency was referred as wrong spin-statistics.

In a letter addressed at his fellow physicists participating at a conference held in Tubingen [16], Pauli proposed as “desperate remedy” the existence of a particle that he called *neutron* with the following characteristics:

- electrically neutral (from which the name);
- spin 1/2;
- mass similar to e (and not travel at speed of light).

The production in β decay of such particle would explain the e spectrum, and its presence in the atom lead to the correct number of fermions. However, as Pauli himself remarked, the possible detectability of such particle was questionable[4].

Having been in contact with Pauli’s ideas during the 1933 Solvay conference, in Bruxelles[5], E. Fermi developed his theory of the beta decay. Meanwhile, the neutron, as we mean it in modern physics, had been discovered by Chadwick in 1932 [18, 19],

---

[3] Particles with half-integer spin J^p which follow the Fermi-Dirac statistic, opposed to bosons, which have instead integer spin and follow Bose-Einstein statistic.

[4] Pauli is commonly credited with the statement “I have done a terrible thing; I have postulated a particle that cannot be detected”.

[5] A remarkable event, in which, along with a talk from Pauli on the neutrino, the discoveries of the neutron and of the positron were announced [17].

solving the wrong spin-statistics problem. However, the questions on β decay spectrum were still opened, and Fermi decided to include the Pauli's particle, which he renamed neutrino[6] (ν), in a point-like four body interaction

$$n \longrightarrow p + e + \bar{\nu}^{7} \,. \tag{2}$$

Using the Dirac spinors formalism of the QED theory [20], Fermi proposed as a Lagrangian of the β decay

$$\mathcal{L}_\beta = G_F(\bar{u}_p \gamma_\mu u_n)(\bar{u}_e \gamma_\mu u_\nu)\,, \tag{3}$$

where G_F is the coupling constant, known as Fermi constant, and u_x the operator that creates (destroys) a particle (anti-particle) x [21, 22][8]. In strict analogy with the QED, Fermi used vector-like bilinear forms γ_μ as covariant term, but his Lagrangian terms involved a change of charge. The theory predicts the nucleus lifetime, as well as the shape of the energy spectrum of the emitted electrons, and represents the first step toward the development of a universal theory of weak interaction.

As further consequence, other processes, derived from the β decay, could be explained with the same formalism, i.e.

$$e + p \longrightarrow \nu + n \qquad \mathrm{K-capture}\,, \tag{4}$$

$$\bar{\nu} + p \longrightarrow n + e^{+} \qquad \mathrm{InverseBetaDecay(IBD)}\,. \tag{5}$$

The existence of the IBD interaction makes neutrino detection in principle possible (as first proposed by B. Pontecorvo [23]). However, estimations of that time [24] placed the cross-section far beyond current experimental possibilities.

1.1.2 ...to discovery

Two decades later, however, the experimentalists C. Cowan and F. Reines developed at Los Alamos laboratory an experiment able to bear the challenge of proving neutrino existence. After the initial idea of exploiting the large neutrino flux produced in a nuclear bomb explosion[9] [25, 26], they turned their attention to nuclear reactors. Cowan and Reines designed an experiment which used the newly developed tech-

---

[6] in Italian, little neutron.

[7] We know now that the particle involved is an anti-neutrino, the neutrino anti-particle.

[8] Fermi's article was considered too speculative and refused by Nature in 1933, who admitted its error and belatedly republished his results in 1939.

[9] An idea endorsed by Fermi, with whom Reines collaborated in the Manhattan Project, and H. Bethe.

nique of liquid scintillator counters to detect the positron and the neutron produced in IBD interactions, in a delayed time coincidence (figure 2a). Low-energy neutrons were detected via capture on cadmium (Cd) dissolved in chloride salt form in the organic scintillator (up to $\sim$ 9 MeV released energy and an average capture time of a few ns). The positron-neutron delayed coincidence is still the key technique for anti-neutrino detection in modern reactor neutrino experiments.

In 1953 Cowan and Reine's project moved to the US latest and biggest plutonium-producing reactor of the time, at HEW[10]. There they measured a difference between the flux with the reactor on and off of 0.41 ± 0.20 events per minute [27]. Prompted by these encouraging results, other groups started to explore the same technique [28]. Reines himself developed a re-designed detector able to isolate the IBDs from the cosmic background, the main experimental challenges faced in HEW. The result was a new structure of 2 tanks filled with water and Cd (the target) sandwiched between three tanks of scintillator equipped with 110 photomultiplier tubes (PMTs) each to reconstruct the event topology and better characterize IBD interaction (see a sheme in figure 2b).

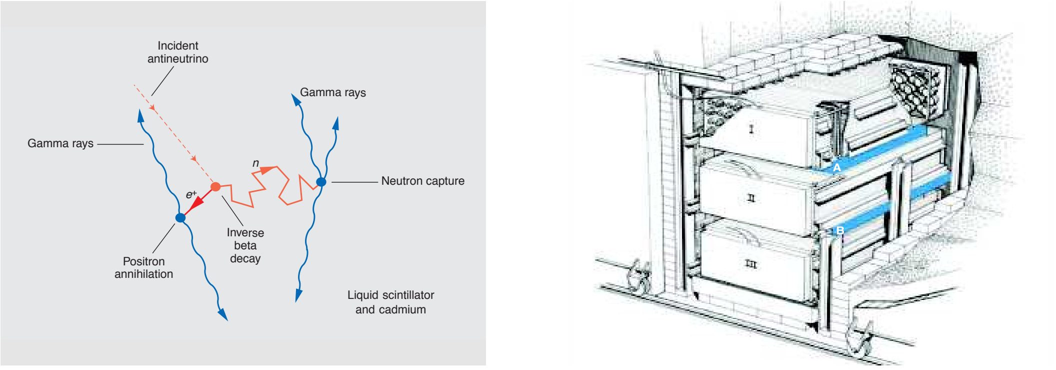

(a) Double signature of an IBD. The positron annihilatio is followed by a delayed neutron capture.

(b) Detector scheme: two 200 l water (with Cd) tanks (A, B) sandwiched between three 1400 l scintillation detectors (I, II, III), equipped with 110 PMTs.

Figure 2: The Cowan and Reine's experiment: neutrino signature and scheme of the Savannah River detector.

The new detector was installed at the Savannah River plant in 1955. After 8 months of data taking, the group claimed the observation of a reactor-power-dependent signal undoubtedly identified as result of IBD interactions, in agreement within 5% with the predicted cross-section [29, 30]. Improved results with a larger data sample

---

[10] Hanford Engineering Works in Hanford, Washington.

appeared in a later article, as well as an almost doubled estimation of the IBD cross-section [31] (due to downward revision of the detection efficiency). Meanwhile the theoretical value of the cross-section had doubled too, thanks to another breakthrough in the subatomic world that changed the prediction of Fermi: the discovery of the parity violation.

1.1.3 Three neutrino families

In the years between the first hypothesis on the β decay and the neutrino discovery, the study of cosmic rays and the use of new detection techniques (preeminently the D. Glaser's bubble chamber) led to the discovery of new particles. One of these particles, the muon (μ), was discovered by C. Anderson[11] and S. Neddermeyer in 1936 [32]. Initially thought to be the Yukawa meson (later discovered as the pion [33]), the μ was proven not to interact with the strong force [34], making it in all respects a massive version of the *e* (we now refer to these particles as leptons). B. Pontecorvo discovered that the phenomenon of muon absorption could be described with the Fermi's formalism, in the form of

$$\mu^- + p \longrightarrow n + \nu \tag{6}$$

On the same basis, he predicted a μ decay (both for particle and anti-particle)

$$\mu^\pm \longrightarrow e^\pm + 2\nu \tag{7}$$

of the same kind of the β decay [35]. When H. J. Steinberg confirmed such predictions measuring a continuous spectrum for Michel electrons[12] [36] (under E. Teller and Fermi), it was clear how the Fermi model was more than just beta decays[13]. It was also questioned whether or not the two neutral particles produced in such interaction were of the same kind than the β decay neutrino. Steinberg himself tested this hypothesis with L. Lederman and M. Swartz at Brokhaven laboratory AGS[14] accelerator by developing an instrumental apparatus able to detect neutrinos produced along with muons in pion decays. Pions were in turn produced by proton beam hit on a beryllium

---

[11] Anderson also had discovered the positron, the first known anti-particle, four years before.

[12] The electron produced in muon decays is also known as Michel electron, honoring the French physicist L. Michel who invented the four parameters used in describing the phase space distribution of leptonic decays of charged leptons.

[13] Steinberg himself will participate in the development of the SU(2)xU(1) theory of electroweak interactions.

[14] Alternating Gradient Synchrotron.

target. The neutrino interactions observed were

$$\nu + n \longrightarrow \mu + p \tag{8}$$

$$\nu + n \longrightarrow e + p \tag{9}$$

The experimental group observed 34 events of long tracks (muons), of which 5 where estimated as background, and only 6 showers (electrons), showing that the neutrino produced along with the μ (ν_μ) was different from the β decay one (ν_e) [37]. Accordingly, equation 7 becomes

$$\mu^- \longrightarrow e^- + \bar{\nu}_e + \nu_\mu \tag{10}$$

$$\mu^+ \longrightarrow e^+ + \nu_e + \bar{\nu}_\mu \,. \tag{11}$$

The need to adapt the Fermi's Lagrangian (equation 3) of a more general theory that includes parity violation[15] pushed towards the so-called V-A theory of weak interaction [40]. However, mathematical difficulties prevent it from being a complete theory. For that we would have to wait the stunning accomplishments of the next decade, which led to one of the greatest achievement of particle physics: the Standard Model. Despite its high predictivity, there are fundamental physical phenomena that the Standard Model does not explain (gravity, dark matter, dark energy, baryon-antibaryon asymmetry). Hints of physics beyond the Standard Model, as well as possible solutions on some of these issues, can be find in neutrino physics, as we will later discuss.

In the Standard Model the weak and the electromagnetic (EM) interactions are unified in the electroweak force, described by the Glashow-Salam-Weinberg theory (GSW), with the introduction of the gauge bosons W^+, W^- and Z^0[16] (see Ref. [41] and included references). Interactions mediated by $W^\pm$ are said to be in charged current (CC), while are in neutral current (NC) if the mediator boson is the Z^0. The electroweak interaction is associated with the gauge symmetry under a SU(2)xU(1) group. For energies below $\sim$ 100 GeV, weak and EM interaction resolve due to a phenomenon known as spontaneous symmetry breaking. With a similar mode, elementary fermions obtain their masses in the so-called Higgs Mechanism, by coupling with

---

[15] The parity violatiion was measured in the Wu experiment [38], confirming the hypotesis of T. D. Lee and C. N. Yang [39].

[16] As gauge bosons, these particles mediate the weak interaction, in the same way that photons mediate the EM one.

the scalar field of the Higgs boson. The weak interaction couples with left-handed[17] particles and right-handed antiparticles. Neutrinos (antineutrinos) are massless, only left-handed [42] (right-handed), and interact via weak force.

The Standard Model includes three lepton and neutrino families. When the third lepton, the tau (τ), was discovered by M. L. Perl in a series of experiments between 1974 and 1977 [43, 44], it appeared natural that the corresponding neutrino, the ν_τ, would have been found. Nonetheless, the τ has a much higher mass and shorter lifetime than μ, which makes harder the implementation of an experiment that directly detects ν_τ from τ produced in CC interaction. For this reason, we have to wait the beginning of this century to see the DONUT experiment proving the existence of the ν_τ. In DONUT a ν_τ beam was produced by the Tevatron accelerator, at Fermilab, colliding 800 GeV protons to a tungsten target, and sent to an emulsion-based[18] detector. Charged current neutrino interaction produce charged daughters, which leave tracks in nuclear emulsion films and are detected by a system of scintillators and drift chambers. Using information on the electronics to reconstruct tracks, involved emulsions are analysed and short tracks reconstructed across subsequent films. The signature of a ν_τ is given by a *kink* a few mm after the primary vertex, indicating decay of a τ. With 4 τ observed decays, DONUT provided a conclusive evidence of the observation of ν_τ CC interactions [46]. The experiment also measured the τ magnetic momentum and interaction cross-section [47, 48].

Is this the end of the story regarding the number of neutrino families? The number of neutrino families N_ν was determined at CERN in the '90s with the use of the four LEP[19] experiments (ALEPH, DELPHI, L3 and OPAL) as [49]

$$N_\nu = 2.9840 \pm 0.0082\,. \tag{12}$$

The number is in agreement with the three families observed so far. However, the measure concerns only neutrinos that couple to the Z^0 boson. There may still be *sterile* neutrinos, whose weak interaction is strongly suppressed but are involved in neutrino oscillation.

---

[17] A particle has right-handed (left-handed) helicity if its spin parallel (anti-parallel) to the motion.

[18] The use of emulsion cloud chamber technique dates back to the '50s [45].

[19] Large Electron–Positron collider.

1.2 Neutrino oscillations

Despite the Standard Model being inherently an incomplete theory, no experimental evidences have been found to date that definitively contradict its predictions. Among the possible keystones that may allow breaking through physics beyond the Standard Model, neutrino physics plays a privileged role. The neutrino oscillation is an irrefutably proven phenomenon that implies neutrino to have non-zero masses, conflicting with the Standard Model (see section 1.3).

The concept of neutrino oscillation, strictly linked to the flavour mixing, was first proposed by Pontecorvo in 1957 [50, 51]. Neutrinos are always produced in weak interactions in correspondence with the creation or the absorption of their respective lepton. However, these weak (or flavour) eigenstates may not correspond to the mass eigenstates - which are the fundamental particles and solutions of the Schrödinger equation[20] - being rather a mix of such states[21]. Every time a weak eigenstate $|\nu_\alpha\rangle$ is created it may correspond to a ν_i mass state, with a probability given by the nature of this mix, or, if neutrino masses are too small to be resolved experimentally (which is the case), to a coherent superimposition of mass eigenstates

$$|\nu_\alpha\rangle = \sum_i U^*_{\alpha i} |\nu_i\rangle \ . \tag{13}$$

Different mass states also propagate at different speed, and the relative phase between states will change with the distance from the source. As a consequence, it is possible to detect a neutrino of a different flavour (say $|\nu_\beta\rangle$) onward, or, in other words, that the flavour component of a neutrino beam may *oscillate* with its propagation.

1.2.1 Experimental evidences

The theory of neutrino oscillation covers a great deal of experimental evidences collected during the last 40 years with different techniques. Anomalies in the observations of solar and atmospheric neutrinos led to the conclusion that neutrinos change flavour.

Solar neutrino anomaly

---

[20] The fundamental equation of the dynamics in quantum mechanics. Mass states are the solutions of such equation, as opposed to flavour states, which are represented in the Lagrangian of weak interaction.

[21] Similarly to what happens in the quark sector [52, Chapter 11.1].

Electron neutrinos are produced in the Sun as result of fusion reactions. The largest component comes from the so-called pp-chain, with a smaller contribution from the CNO cycle [53]. The final spectrum contains continuous and discrete components, and is shown in figure 3.

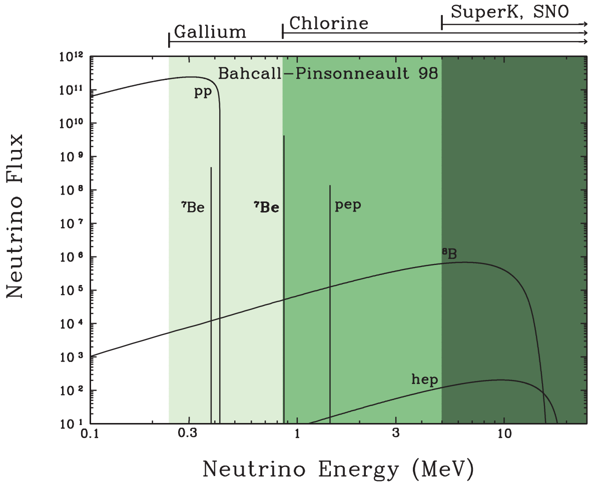

Figure 3: Bahcall's prediction of main solar neutrino flux components. The sensitivity of the different detection techniques used in solar neutrino experiment are shown with different shades of green. Figure borrowed from [54].

The first evidence supporting the hypothesis of neutrino flavour mixing [55] arose concomitantly with the first observation of solar neutrinos made by the Homestake experiment, which was developed in 1965 by R. Davis Jr. and J. N. Bahcall. Their results pointed out an inconsistency between predicted and observed solar neutrino flux, known as *solar neutrino problem* [56]. Davis designed an apparatus consisting of a 380 m^3 tank filled with perchloroethylene, which was placed 1478 m underground in the Homestake gold mine, in South Dakota. Perchloroethylene is rich in chlorine (Cl); neutrinos were detected by means of the inverse electron capture reaction (IEC) on ^{37}Cl

$$\nu_e + {}^{37}\mathrm{Cl} \longrightarrow {}^{37}\mathrm{Ar} + e^- , \tag{14}$$

which has a 0.814 MeV threshold. Argon was then collected by bubbling helium through the tank and filled in a gas counter to measure the ^{37}Ar decays. The observed capture rate was compared to the calculation made by Bahcall: 2.56 ± 0.25 SNU[22] were measured, roughly one third than the expected 8.1 ± 1.2 SNU rate [57].

---

[22] Solar neutrino unit, 1 SNU = 10^{-36} neutrino interactions per target atom per second.

Results from Homestake were initially criticized due to the difficulty of the measure (very low rate) and its reliance on radiochemical techniques, without the possibility of having directional or energetic information about neutrinos. Doubts were also posed on the predictions of the Bahcall's Standard Solar Model (SSM). Bahcall himself continued to develop his model in the following years (see Ref. [58] and included references for details). The nowadays confidence in Bahcall's SSM description of the Sun derives largely on helioseismology studies, which confirm to a 5% precision the SSM predictions on the velocity of sound waves propagation inside the star [59]. More light was shed on Davis' results thanks to the measurements of the Kamiokande and gallium experiments, before the final answer given by SNO.

Kamiokande[23] is a large water Cherenkov[24] experiment initially designed to observe proton decays for GUT[25] physics. In its second phase (Kamiokande II), the experiment turned its attention to solar neutrinos, which were observed via elastic scattering (ES) on free electrons

$$\nu_e + e^- \longrightarrow \nu_e + e^- \,. \tag{15}$$

The electrons are then detected by means of Cherenkov light emission, with a lower experimental energy threshold of $\sim 5\,\mathrm{MeV}$ (mostly ^{8}B neutrinos were observed, as figure 3 suggests) [61]. Kamiokande II measured a ratio between the observed neutrino rate and a SSM-based Monte Carlo simulation of 0.46 ± 0.08 [62]. From the electron reconstruction it was also possible to infer the energy and, for the first time, the direction of neutrinos, which was undoubtedly pointing toward the Sun[26] [63].

Gallium experiments had similar detection technique to Homestake, but they could span a larger solar neutrinos spectrum (which included the pp component, see figure 3), thanks to the lower IEC threshold of ^{71}Ga (233.2 keV). The GALLEX experiment was located in LNGS[27], in Italy, and operated between 1991 and 1997. It observed a solar neutrino flux of $77.5^{+7.5}_{-7.8}$ SNU [64] using a 50 t gallium target, in contrast with a prediction of 129^{+8}_{-6} SNU [65] (more recent predictions provide a similar value of 131^{+12}_{-10} SNU [66]). The joint results from 1991 to 2003 of GALLEX

---

[23] Kamioka (Japan) nucleon decay experiment.

[24] Cherenkov radiation, emitted by charged particle passing through a medium at a speed greater than the speed of light in that medium, is named after P. A. Cherenkov, who first detected it experimentally [60].

[25] grand unification theories.

[26] The precision on the directionality was limited by the experimental resolution and physical reasons like multiple scattering of the electron.

[27] Laboratori Nazionali del Gran Sasso.

and its successor GNO (1998-2003) confirmed the observed deficit with a measured flux of 69.3 ± 5.5 SNU [67]. The SAGE experiment - which operated in parallel in the underground Baksan Neutrino Observatory, in Russia (1990-2007) - measured a similar neutrino flux in 1998 ($67.2^{+8.0}_{-7.6}$ SNU) [68] and with its total data set (65.4 ± 4.1 SNU) [69]. Gallium experiment tested their experimental operation with neutrino sources (e.g in Ref. [70]).

The solution to the solar neutrino problem and proof of the neutrino flavour changing were finally given by the results of the SNO[28] experiment. All experiments quoted so far can only observe charged current (CC) or elastic scattering (ES) neutrino interactions, and hence are sensitive predominantly to electron neutrinos[29]. SNO, on the other hand, uses heavy water (D_2O) and three detection channels: the ES interaction on free electrons (equation 15), the CC interaction on deuterium

$$\nu_e + d \longrightarrow p + p + e^- \tag{16}$$

and the neutral current (NC) interaction on deuterium

$$\nu_x + d \longrightarrow n + p + \nu_x \,. \tag{17}$$

This latter interaction is the key one, being insensitive to the neutrino flavour and therefore allowing for a measure of the total neutrino flux. The SNO detector is located 2100 m underground in the Creighton mine in Subdury, Canada [71]. The neutrino target consists in 1100 t of 99.92% pure heavy water in an acrylic vessel (6 m radius). Outside of the target, in the detector cavity, a geodesic spherical structure (8.5 m radius) serves as a support to the 9600 PMTs used for the light detection. The cavity is filled with normal water that provides hydrostatic support to target (with the help of suspension ropes) and shield it from the radioactivity. The combination of the Cherenkov detection technique of Kamiokande with the detection of the final state neutron provides the signature of the NC interaction. The neutron detection has been performed in a different, improved way for each of the three SNO phases: with capture on deuterium in the first phase (1999-2001), with neutron capture on ^{35}Cl from 2 t dissolved salt in the second phase (2001-2003) [72], and with 300 ^{3}He counters in the third phase (2004-2006) [73]. The first evidence of neutrino oscillation came in 2001 [74] and was followed one year later by final results of phase I [75]. In terms of

---

[28] Sudbury Neutrino Observatory.

[29] The solar neutrino energy end-point ($\sim$ 20 MeV) does not allow the production of heavy leptons.

neutrino fluxes associated with each channel, such results are

$$\phi_{ES} = \phi_{\nu_e} + 0.15(\phi_{\nu_\mu} + \phi_{\nu_\tau}) = (2.39^{+0.27}_{-0.26}) \cdot 10^{-8}\text{cm}^{-2}\text{s}^{-1} \tag{18}$$

$$\phi_{CC} = \phi_{\nu_e} = (1.76^{+0.11}_{-0.10}) \cdot 10^{-8}\text{cm}^{-2}\text{s}^{-1} \tag{19}$$

$$\phi_{NC} = \phi_{\nu_e} + \phi_{\nu_\mu} + \phi_{\nu_\tau} = 5.09^{+0.64}_{-0.61} \cdot 10^{-8}\text{cm}^{-2}\text{s}^{-1} \tag{20}$$

from which one can also derive $\phi_{\nu_\mu} + \phi_{\nu_\tau} = 3.33 \pm 0.63$. The total active neutrinos flux ϕ_{NC} was in agreement with the SSM value $\phi_{SSM} = (5.05 \pm 1.01) \cdot 10^{-8}\text{cm}^{-2}\text{s}^{-1}$. Results of the other two phases were consistent.

The observations of all main solar neutrino experiments are resumed in figure 4. The deficit measured in all CC and ES channels is interpreted as flavour changing of neutrinos. The different ratios between observed and expected rates of the various experiments suggest an energy dependence of this deficit.

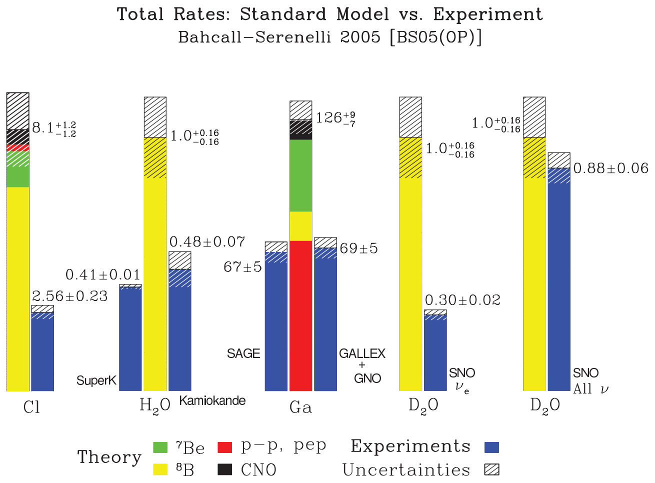

Figure 4: Observed and predicted rates of solar neutrinos. Group of bars represent different detection techniques. For each group, the central bar represents the SSM prediction in which contribution of different flux component are featured with different colours, while the side bars (blue) show results from different solar neutrino experiments. Errors bars for both predictions and measurements are represented in grey.

Atmospheric neutrino anomaly

Neutrinos are also created as result of the decay of secondary particles produced in the interaction of cosmic rays (mostly protons and α particles) with the Earth atmosphere. The ν_μ component of atmospheric neutrinos arises mostly from pion decays, while ν_e are dominantly produced in μ decays; kaon decays also contribute at $\sim$ 1 GeV energies. While flavour components of the flux are known with rather large uncertainties ($\sim$ 20%), the ratio

$$R = \frac{\nu_\mu + \bar{\nu}_\mu}{\nu_e + \bar{\nu}_e} \tag{21}$$

can be estimated with a better precision ($\sim$ 5%). A scheme of a general atmospheric neutrino experiment is shown in figure 5.

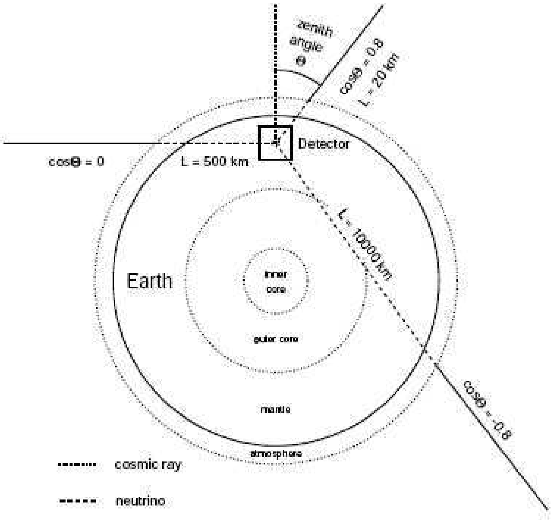

Figure 5: Scheme of an atmospheric neutrino experiment. Neutrinos travel different distances, before reaching the detector, depending on their zenith angle of arrival.

The *atmospheric neutrino problem* originated when several experiment measured a low ratio between observed and predicted R [76–79]. Among these experiments, Super-Kamiokande (SK), a bigger and more sophisticated version of Kamiokande, was able to measure the neutrino energy and zenith angle θ_{zenith}, i.e. the angle at which the neutrino enters the detector. The results, shown in figure 6, clearly point-out how the observed deficit concerns mostly muon neutrinos and depends on θ_{zenith}. These results, as well as the evidences on solar neutrinos, can be easily explained with the neutrino flavour change within the context of neutrino oscillations.

1.2.2 Physics of neutrino oscillation

In the theory of neutrino oscillation Hamiltonian eigenstates are related to weak eigenstates, the states of definite lepton number in which neutrino are produced, by a unitary matrix U. One can in principle imagine an arbitrary number of neutrinos, although experimental results limit the number of active families to three [49]. The

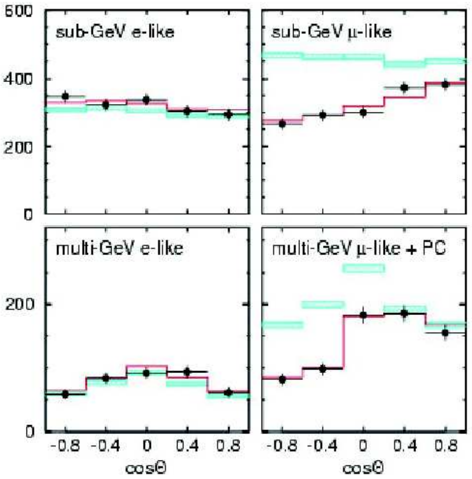

Figure 6: Zenith angle distribution of atmospheric ν_e and ν_μ observed in Super-Kamiopkande, in different energy range, compared with predictions without (turquoise) and with (red) neutrino oscillation. From [80].

general case of three neutrino families can be approximated to a two flavours oscillation in many experimental cases. Moreover, oscillation in matter differs from the one in vacuum due to interaction of electron neutrinos with electrons of the medium.

Two-flavour oscillations

If we consider two mass eigenstates $|\nu_1\rangle$ and $|\nu_2\rangle$ and two flavour eigenstates $|\nu_\alpha\rangle$ and $|\nu_\beta\rangle$, the mixing (see equation 13) is given by[30]

$$\begin{pmatrix} \nu_\alpha \\ \nu_\beta \end{pmatrix} = \begin{pmatrix} \cos(\theta) & \sin(\theta) \\ -\sin(\theta) & \cos(\theta) \end{pmatrix} \begin{pmatrix} \nu_1 \\ \nu_2 \end{pmatrix} , \tag{22}$$

where θ is the mixing angle. A neutrino generated as a flavour eigenstate $|\nu_\alpha\rangle$ is a combination of the two mass states $|\nu_1\rangle$ and $|\nu_2\rangle$

$$|\nu_\alpha\rangle = \cos(\theta)\,|\nu_1\rangle + \sin(\theta)\,|\nu_2\rangle \tag{23}$$

and propagates in space and time (t,$\mathbf{x}$) as the combination of the $\nu_{1,2}$ plane waves,

---

[30] The only unitary 2×2 matrix is the 2D rotation operator.

solution of the Schrödinger equation

$$|\nu_\alpha(\mathbf{x},t)\rangle = \cos(\theta)e^{-iE_1 t}\,|\nu_1(\mathbf{x})\rangle + \sin(\theta)e^{-iE_2 t}\,|\nu_2(\mathbf{x})\rangle \ , \tag{24}$$

where $E_{1,2} = \sqrt{m^2_{1,2} + |\mathbf{p}|^2_{1,2}}$ are the eigenvalues of $\nu_{1,2}$ (with m and $\mathbf{p}$ the mass and momentum). The probability of flavour changing is proportional to the amplitude of the transition between $|\nu_\alpha\rangle$ and $|\nu_\beta\rangle$, or

$$P_{\nu_\alpha\to\nu_\alpha} = 1 - P_{\nu_\alpha\to\nu_\beta} = 1 - |\,\langle\nu_\beta|\nu_\alpha(t)\rangle\,|^2\,. \tag{25}$$

By replacing the complex conjugate of equation 23 in equation 24, and reasonably assuming relativistic neutrinos[31], we obtain the survival probability (see full calculation in Ref. [81])

$$P_{\nu_\alpha\to\nu_\alpha} = 1 - \sin^2(2\theta)\,\sin^2\left(1.27\Delta m^2\frac{L}{E_\nu}\right)\,, \tag{26}$$

where $\Delta m^2 = m_2^2 - m_1^2$ (eV^2) is the mass squared difference of the two states, L (m) the travelled distance, or baseline, and E_ν (MeV) the neutrino energy. In equation 26 the first term, which contains the mixing angle θ, governs the oscillation amplitude, while the oscillation itself, often represented as the L/E_ν ratio, is given by the second term.

If we look at figure 6 we see that for ν_e there is no big discrepancy between data and predictions in absence of oscillation, suggesting that the phenomenon involves mostly ν_μ and ν_τ. Hence, the results on atmospheric neutrinos shown in the previous section can be described with a two flavour oscillation

$$P_{\nu_\mu\to\nu_\tau} = \sin^2(2\theta_{atm})\,\sin^2\left(1.27\Delta m^2_{atm}\frac{L}{E_\nu}\right)\,, \tag{27}$$

where θ_{atm} and Δm^2_{atm} are the atmospheric mixing angle and squared mass difference. For what concerns ν_μ, on the other hand, the ratio between observations and predictions is ~ 1 only for downgoing neutrinos ($\cos\theta_{zen} = 1$), while it decreases with the zenith angle up to $\sim$ 50% for upcoming neutrinos ($\cos\theta_{zen} = -1$). Such behaviour is explained if we assume equation 27 with $\Delta m^2_{atm} \simeq 2\cdot 10^{-3}$ eV^2 and $\sin^2(2\theta_{atm}) \simeq 1$.

We might naively assume that the same sort of analysis can be done for solar neutrinos. The Sun-Earth distance ($L \sim 10^8$ km) and the neutrino energy (around 10 MeV for ^{8}B) would suggest a $\Delta m^2_\odot$ of the order of 10^{-10} eV^2. These values, though,

---

[31] Neutrino masses are below 1 eV, while current experimental low energy thresholds are of the order of hundreds of keV.

are not correct, since matter effects change the solar neutrinos oscillating pattern.

Oscillation in matter

In vacuum, the phase difference responsible for the flavour changing arises from the mass difference between neutrino states. Nonetheless, if neutrinos are propagating through a medium the phase needs to include a potential V given by the interaction of neutrinos with matter. If the interaction and thus the potential is different for different neutrino flavours, with $\Delta V = V_\alpha - V_\beta$, then a further phase difference is introduced. This is known as MSW[32] effect. In the energy range of solar neutrinos, only ν_e can interact with both CC and NC, while ν_μ and ν_τ are limited to NC interactions due to the large mass of their respective lepton. This originates a ΔV between electron and other neutrinos,

$$\Delta V = 2\sqrt{2} G_F E_\nu N_e \,, \tag{28}$$

where N_e is the electron density of the medium. The addition of two different potentials terms V_α and V_β to the Schrödinger equation changes its solutions. The new eigenvalues at rest obtained from the diagonalization of the matter Hamiltonian, m_{1m} and m_{2m}, give a mass splitting of

$$\Delta m_m^2 = \Delta m^2 \sqrt{(\Delta V/\Delta m^2 - \cos(2\theta))^2 + \sin^2(2\theta)} \,. \tag{29}$$

The flavour mixing of equation 22 also changes into

$$\begin{pmatrix} \nu_\alpha \\ \nu_\beta \end{pmatrix} = \begin{pmatrix} \cos(\theta_m) & \sin(\theta_m) \\ -\sin(\theta_m) & \cos(\theta_m) \end{pmatrix} \begin{pmatrix} \nu_1^m \\ \nu_2^m \end{pmatrix} , \tag{30}$$

where $\left|\nu_{1,2}^m\right\rangle$ are the new eigenstates, for an oscillation probability

$$P_{\nu_\alpha \to \nu_\alpha} = 1 - \sin^2(2\theta_m)\, \sin^2\left(1.27 \Delta m_m^2 \frac{L}{E_\nu}\right) , \tag{31}$$

where

$$\sin(2\theta_m) = \frac{\sin(2\theta)}{\sqrt{(\Delta V/\Delta m^2 - \cos(2\theta))^2 + \sin^2(2\theta)}} \,. \tag{32}$$

By looking at equation 32 we notice that, if N_e is such that $\Delta V = \Delta m^2 \cos(2\theta_m)$, the matter oscillation amplitude is maximal; this condition is known as MSW resonance, and such electron density N_e^{res}. It is also interesting to note that for $N_e \ll N_e^{res}$ we go

---

[32] Mikheyev-Smirnov-Wolfenstein.

back to the vacuum case, while if conversely $N_e \gg N_e^{res}$ the oscillation is suppressed.

Neutrinos created in the solar core do not oscillate there due to the high electron density. The oscillation may occur when they reach a region in which $N_e \sim N_e^{res}$, depending on the energy E^{ν}, which makes the MSW effect more or less dominant for different flux components[33]. When neutrinos exit the Sun, we go back to the vacuum oscillation, which, assuming again two flavours, will be

$$P_{\nu_e \to \nu_x} = \sin^2(2\theta_\odot)\,\sin^2\left(1.27\Delta m^2_\odot \frac{L}{E_\nu}\right), \tag{33}$$

Solar data suggest that $\Delta m^2_\odot \simeq 7.5 \cdot 10^{-5}\,\mathrm{eV}^2$ and $\sin^2(2\theta)_\odot) \simeq 0.8$. With such small $\Delta m^2_\odot$, the source dimension and the experimental energy resolution are not negligible with respect to the oscillation period, causing a loss of coherence. Consequently, once solar neutrinos leave the Sun, we do not observe an oscillation but rather an averaged deficit of $0.5\sin^2(2\theta_\odot)$.

The matter mixing angle of equation 32 depends on the sign of the mass squared difference. In particular, the observed resonance is possible only if $\Delta m^2_\odot > 0$.

Three-flavour oscillation

In the general three-flavour case, the mixing is governed by the 3×3 unitary and complex matrix known as PMNS[34]

$$\begin{pmatrix} \nu_e \\ \nu_\mu \\ \nu_\tau \end{pmatrix} = \begin{pmatrix} U_{e1} & U_{e2} & U_{e3} \\ U_{\mu 1} & U_{\mu 2} & U_{\mu 3} \\ U_{\tau 1} & U_{\tau 2} & U_{\tau 3} \end{pmatrix} \begin{pmatrix} \nu_1^m \\ \nu_2^m \\ \nu_3^m \end{pmatrix}. \tag{34}$$

The PMNS matrix is usually paramaterized with 3 rotation matrices that define an

---

[33] For instance, the ^{7}Be flux of ν_e is maximally affected, whereas the opposite is true for the pp flux, explaining the different results of solar neutrino experiments.

[34] Pontecorvo-Maki-Nakagawa-Sakata. This matrix was introduced in 1962 by the latter three [82] to explain the neutrino oscillations predicted by Pontecorvo [50].

equivalent number of sectors

$$\begin{aligned} U = & \begin{pmatrix} 1 & 0 & 0 \\ 0 & c_{23} & s_{23} \\ 0 & -s_{23} & c_{23} \end{pmatrix} \begin{pmatrix} c_{13} & 0 & s_{13}e^{-i\delta_{CP}} \\ 0 & 1 & 0 \\ -s_{13}e^{i\delta_{CP}} & 0 & c_{13} \end{pmatrix} \begin{pmatrix} c_{12} & s_{12} & 0 \\ -s_{12} & c_{12} & 0 \\ 0 & 0 & 1 \end{pmatrix} \\ = & \begin{pmatrix} c_{12}c_{13} & s_{12}c_{13} & s_{13}e^{-i\delta_{CP}} \\ -s_{12}c_{23} - c_{12}s_{23}s_{13}e^{i\delta_{CP}} & c_{12}c_{23} - s_{12}s_{13}s_{23}e^{i\delta_{CP}} & c_{13}s_{23} \\ s_{12}2_{23} - c_{12}s_{13}c_{23}e^{i\delta_{CP}} & -c_{12}s_{23} - s_{12}s_{13}c_{23}e^{i\delta_{CP}} & c_{13}c_{23} \end{pmatrix}, \end{aligned} \tag{35}$$

where $c_{12} = \cos\theta_{12}$, $s_{12} = \sin\theta_{12}$. The parameters θ_{12}, θ_{13}, and θ_{23} can be seen as the angles of a tri-dimensional rotation of the mass base with respect to the flavour base. They govern the mixing, i.e. the amount of $\nu_{1,2,3}$ in the flavour eigenstates and the oscillation amplitudes. The *23-sector* is usually referred as the atmospheric sector, and the *12-sector* to the solar one. The irreducible complex phase δ_{CP} is associated with the *13-sector* and accounts for possible CP violation in the neutrino sector. Basing on equations 34 and 35, the oscillation probability is determined as

$$\begin{aligned} P_{\nu_\alpha \to \nu_\beta} = & \delta_{\alpha\beta} - 4\sum_{i>j} \mathrm{Re}\left\{(U^*_{\alpha i}U_{\beta i}U_{\alpha j}U^*_{\beta j})\right\} \sin^2\left(1.27\Delta m^2_{ij}\frac{L}{E}\right) \\ & + 2\sum_{i>j} \mathrm{Im}\left\{(U^*_{\alpha i}U_{\beta i}U_{\alpha j}U^*_{\beta j})\right\} \sin\left(2.54\Delta m^2_{ij}\frac{L}{E}\right). \end{aligned} \tag{36}$$

With three families, there are also three mass squared differences (of which two independent). The fact, confirmed by data, that a mass squared difference is much smaller than the other two, together with the relative smallness of θ_{13}, allows in many experimental cases approximating the oscillation probability to the one with two families (equation 26). Without going into details, we will just say that we identify ($\Delta m^2_\odot$, $\theta_\odot$) with (Δm^2_{12}, θ_{12}), and (Δm^2_{atm}, θ_{atm}) with ($\Delta m^2_{23} \simeq \Delta m^2_{13}$, θ_{23}).

1.2.3 State of the art in neutrino oscillation

The results in the solar and atmospheric sectors shown in the previous paragraph, which proved the neutrino oscillation, have been investigated by a second generation of experiments.

Given that $\Delta m^2_{23} \simeq 0.002\,\mathrm{eV}^2$, it is possible to develop accelerator experiments (for example with a $\sim$ 1 GeV neutrino beam sent to a $\sim$ 400 km far away detector) to reproduce and further investigate results on atmospheric neutrinos. The main features of an accelerator neutrino experiment are:

- a pure and well known neutrino beam of $\sim$GeV energy;
- a large far detector a few hundred km along the beam to measure the oscillated flux;
- possibly a near detector to check the non-oscillated flux at the source, which has to be as similar as possible to the far one to minimize systematic uncertainties.

The neutrino oscillation can be observed in two modes:

- in disappearance, by observing a deficit in the flux specific flavour (as for actual atmospheric neutrinos);
- in appearance, by observing a neutrino flavour not present in the initial beam.

The precision of a measure in appearance largely relies on the ability to constrain the presence of background in the beam that could mimic the appearance signature. Since the baseline is fixed, the depth of the deficit observed in a spectral analysis is proportional to $\sin^2(2\theta_{23})$, while its position in the L/E space depends on Δm^2_{23}. Accelerator experiment can also detect atmospheric neutrinos.

In order to check the solar oscillation with accelerators ($\Delta m^2_{\odot} \simeq 8 \cdot 10^{-5}\,\mathrm{eV}^2$), say with 1 GeV neutrinos, we would need an experimentally impossible baseline L that is greater than 10^5 km. Neutrinos produced in nuclear reactors, on the other hand, have an average energy of $\sim$ 5 MeV, allowing for the observation of solar oscillation on a $\sim 10^2$ km baseline. Reactor neutrinos were used, 40 years after Cowan and Reines' experiments, to test the solar sector and study the last unknown mixing angle θ_{13}.

Atmospheric sector

MINOS[35] is a long-baseline neutrino experiment whose purpose is to test the oscillation in the atmospheric sector. The 500 kW NuMI[36] beam, located at Fermilab, sends ν_μ of 3 GeV average energy to the 732 km away far detector located in a salt mine in Soudan, Minnesota [83]. A 980 t tracking calorimeter made of interspaced layers of scintillator bars and iron, magnetized to perform $\nu_\mu - \bar{\nu}_\mu$ separation, serves as a near detector. The far detector, also magnetized, is a larger version of the near one, with a mass of 5.4 kt, and it is 716 m underground. The experiment started to take data in 2004 and, one year later, published first results confirming the neutrino oscillation

---

[35] Main Injector Neutrino Oscillation Search.

[36] Neutrinos at the Main Injector

hypothesis with parameters consistent with Super-Kamiokande measurements [84]. Latest results [85] combining data from accelerator and atmospheric neutrinos report $\Delta m^2_{23} = (0.00228 - 0.00246)\,\mathrm{eV}^2$ (68% C.L.) and $\sin^2\theta_{23} = 0.35 - 0.65$ (90% C.L.).

The T2K[37] long-baseline experiment was designed to measure the θ_{13} mixing angle, but can also perform precise measurements in the *23-sector*. The experiment consists in a 600 MeV ν_μ beam produced in the J-PARK facility of Tokai, Japan, directed to the SK water Cherenkov detector at a 295 km distance. SK and the T2K near detector ND280 are placed 2.5° off-axis with respect to the beam in order to have a narrower energy distribution peaked where the mixing is maximal [86]. The T2K collaboration published first results on ν_μ disappearance in 2011 [87]. Latest results include the $\nu_\mu \to \nu_e$ appearance channel, for a measured $\sin^2\theta_{23} = 0.514^{+0.055}_{-0.056}$ and a $\Delta m^2_{23} = (2.51 \pm 0.10) \cdot 10^{-3}\,\mathrm{eV}^2$ [88]. A combination of the most recent results about neutrino oscillation in the atmospheric sector from SK, MINOS and T2K, is depicted in figure 7.

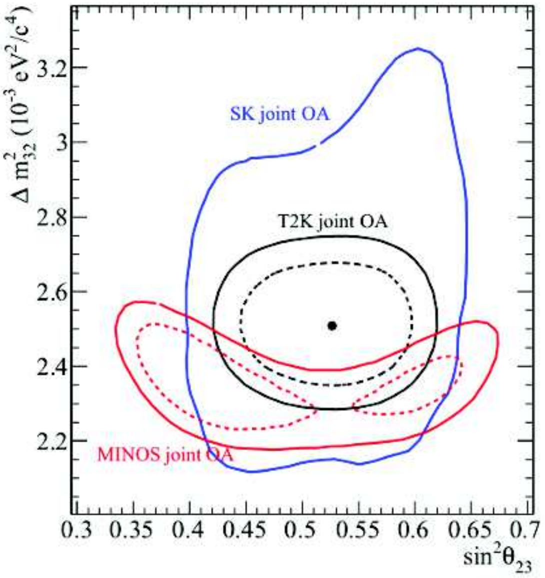

Figure 7: C.L. regions in the ($\sin^2\theta_{23}$, Δm^2_{23}) *space of results from SK [89], T2K [88], and MINOS [85]. Figure borrowed from Ref. [88]*

Unlike MINOS and T2K, the OPERA[38] experiment was designed to look at $\nu_\mu \to \nu_\tau$ oscillation in appearance mode. CNGS[39], a ν_μ beam with a neutrino mean energy $\langle E_\nu \rangle = 17\,\mathrm{GeV}$, was produced at CERN (with the SPS accelerator) and sent

---

[37] Tokai to Kamioka (Japan).

[38] Oscillation Project with Emulsion-tRacking Apparatus.

[39] CERN Neutrinos to Gran Sasso.

to the OPERA detector, in the 730 km far away LNGS laboratory [90]. The ν_τ detection technique is similar to the one used in DONUT (section 1.1.3), with a hybrid detector consisting in emulsion-lead target walls (for a 1.3 kt total mass) sandwiched with plastic scintillators planes, with the addition of muon spectrometers. Including recently published results [91], OPERA collected 5 ν_τ CC interaction candidates analysing data taken between 2008 and 2012, for a total significance of the measure that exceeds 5 σ.

Solar sector

The KamLAND[40] experiment is a liquid scintillator detector located in the Kamioka mine, the former Kamiokande site. It detects $\bar{\nu}_e$ produced in 53 nuclear reactors with a flux-weighted average distance of 180 km via IBD. KamLAND measured a first evidence of disappearance from a deficit in the observed $\bar{\nu}_e$ flux with respect to predictions in 2003 [92]. Figure 8 shows latest KamLAND results in terms of allowed ($\tan^2\theta_{12}$, Δm^2_{12}), in combination with a compilation of solar neutrino experiments. Best-fit results from figure 8 are $\tan^2\theta_{12} = 0.436^{+0.029}_{-0.025}$, $\Delta m^2_{12} = (7.53 \pm 0.18) \cdot 10^{-5}\,\mathrm{eV}^2$ [93]. Notice that KamLAND and solar experiments measures are complementary and consistent: whereas the solar lack in energy resolution but have abundant statistics, determining a better precision on the amplitude of the mixing than on the oscillation itself, KamLAND has opposite conditions and therefore a better precision on Δm^2_{12}. Indeed, KamLAND was the first experiment to report a spectral distortion in the neutrino spectrum, directly observing the oscillating pattern [94].

Another real-time solar neutrino experiment, Borexino[41], started to take data at LNGS in 2007. Solar neutrinos are observed via ES in a 300 t ultra-pure liquid scintillator, with a lower threshold of 250 keV. Borexino observed directly the monochromatic flux of ^{7}Be [95] (0.862 MeV) and pep [96] (1.44 MeV) solar neutrinos, as well as the ^{8}B one [97] (above 3 MeV). The study of single fluxes is important to further check the SSM and to study the MSW effect in the Sun. The MSW effect inside the Earth can be also tested, by looking for a day-night asymmetry in solar neutrino observation [98]. Borexino reported a null day-night asymmetry [99], in contrast with recent hints from SK [100].

The great deal of experimental evidences discussed so far strongly supports a theory

---

[40] Kamioka Liquid scintillator Antineutrino Detector.

[41] BORon solar neutrino EXperiment. The suffix *-ino*, italian for little, was also used by Fermi for the neutrino.

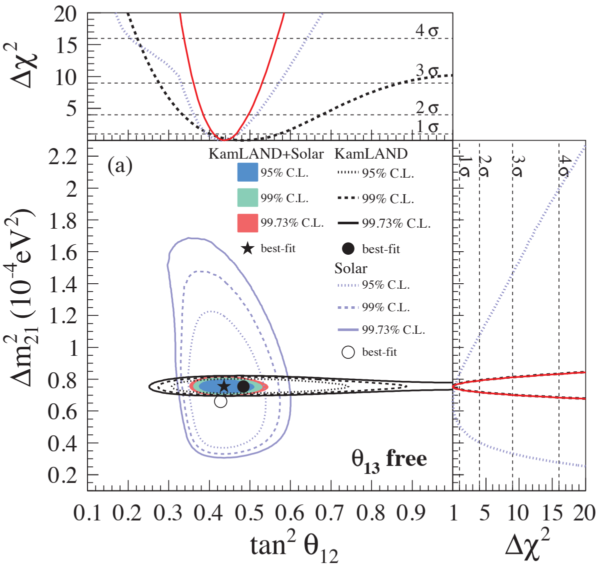

Figure 8: C.L. regions in the ($\tan^2\theta_{12}$*,* Δm^2_{12}*) space of results from KamLAND [93] and solar experiments.*

of three families neutrino oscillation, with the addition of the MSW effect. Global analyses of oscillation data allow determining the three mixing angles and mass squared differences (only absolute values, except for $\Delta m^2_{12} > 0$) [101–103]. Nonetheless, there is still room for an improvement of such measurements, as well as unknown parameters (δ_{CP}), opened questions (sign of Δm^2_{23}, θ_{23} octant, nature of neutrino masses), and unexplained anomalies (reactor anomaly) that need to be addressed. Before going to a brief review of experimental approaches to these issues, we will discuss the measure of the mixing angle θ_{13}.

1.2.4 The race for θ_{13}

The 2010s is neutrino-wise the decade of the θ_{13} mixing angle. In the last four years, we have in fact witnessed a rapid evolution in the knowledge of this parameter, which went from being unknown to fully determined with great precision. Before that, indications of a possible non-zero value came from global analyses (see Ref. [104] results, later confirmed in [105]). The relative smallness of θ_{13} ($\sim 8.5°$) with respect to other mixing angles was the main challenge for its measurement.

The θ_{13} mixing angle has an important role in determination of a possible CP violation in the lepton sector, one of the most ambitious goals in future neutrino researches. It is in fact associated to the δ_{CP} phase in the PMNS matrix (equation 34), determining the magnitude of a possible effect of CP violation. A major contribution to measure

θ_{13} comes from reactor neutrino experiments that followed KamLAND. Early measurements made by the CHOOZ experiment were followed by a second generation of reactor neutrino experiments: Double Chooz, Daya Bay, and RENO. Accelerator experiments such as T2K and MINOS also contributed to the race for θ_{13}. An hystorical summary of the various measurements of reactor and accelerator experiments is shown in figure 9.

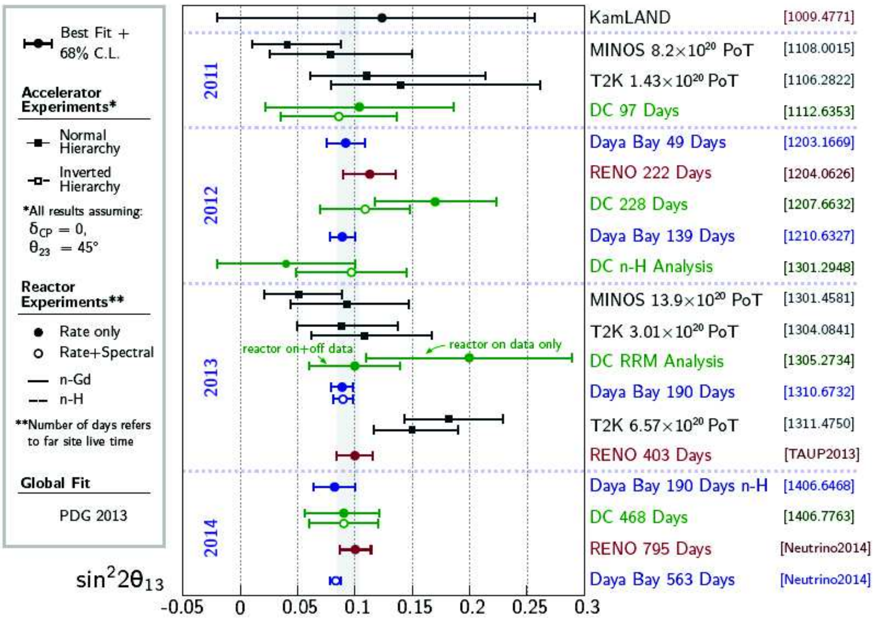

Figure 9: Summary of the various measurements of $\sin^2(2\theta_{13})$ *from reactor neutrino experiments (KamLAND, RENO, Daya Bay and Double Chooz) and accelerator neutrino experiments (T2K, MINOS). A legend explaining the measurement type (on the left) and references to various measurements (on the right, with the arXiv.org number or conference name) are also shown.*

Reactor experiments contribution

We have seen how reactor $\bar{\nu}_e$ ($\langle E_\nu \rangle \sim 5\,\mathrm{MeV}$) observed at a baseline of $\sim 200\,\mathrm{km}$ can be used to study the oscillation driven by $\Delta m^2_\odot$. However, if we place a detector at a $\sim 1\,\mathrm{km}$ baseline the solar oscillation becomes negligible and the small wiggles due to θ_{13} dominate the oscillating pattern (see section 2.1.1 for details). The first experiment that made a measurement in these conditions was CHOOZ. Located 1 km away from the homonymous nuclear power plant, in France, in a 300 mwe[42] under-

---

[42] Meter water equivalent (mwe) are commonly used to measure the cosmics attenuation in under-

ground laboratory, the CHOOZ detector consisted of a target tank filled with 17 t of gadolinium-doped liquid scintillator, surrounded by another tank of 90 t un-doped scintillator. Reactor $\bar{\nu}_e$ were detected via IBD. We already mentioned the use of dopants to enhance the neutron detection for other scintillator experiments. CHOOZ reported inconclusive results on the observation of a $\bar{\nu}_e$ disappearance, setting an upper limit $\sin^2(2\theta_{13}) < 0.14$ [106, 107].

CHOOZ was followed by three other reactor neutrino experiments: Double Chooz, which partially exploits the same facility, Daya Bay in China, and RENO[43] at Yoggwang in South Korea. Similarly to CHOOZ, these experiments use multi-layer detectors, with a gadolinium-doped liquid scintillator target, an un-doped liquid scintillator γ-catcher, a mineral oil Buffer, and an optically isolated external veto. The neutrino flux before the oscillation is monitored with identical near detectors, placed at short distance from the reactors. Among these experiments Daya Bay is the one that benefits from the highest reactor thermal power (17.4 GW_{th} from 6 reactors), as well as the largest number of detectors, which are six and deployed in two near (flux-weighted baseline of 470 m and 576 m) and one far (1648 m) underground facilities. RENO exploits a similar reactor power (17.4 GW_{th} from 6 aligned reactors) and two detectors (294 m and 1383 m from the centre of the reactor array). Double Chooz has also two detectors (400 m and 1050 m baseline), but a lower total reactor power (8.5 GW_{th} from 2 reactors). The chapter 2 of this manuscript is fully devoted to the description of the Double Chooz experiment. The analysis used to determine the θ_{13} mixing angle is described instead in another dedicated chapter, the 3. Double Chooz was the first reactor neutrino experiment to report a hint of non-zero θ_{13} in 2011 [108], followed by stronger evidences with a $5.2\,\sigma$ and $4.9\,\sigma$ significance from Daya Bay [109] and RENO [110] respectively. The current most accurate experimental value of the oscillation amplitude, measured by Daya Bay in 2014, is $\sin^2(2\theta_{13}) = 0.090^{+0.008}_{-0.009}$ [111].

Accelerator experiments contribution

Despite the high accuracy achieved by reactor neutrino experiments, the first experimental indication of a non-zero θ_{13} came from the observation of $\nu_\mu \to \nu_e$ oscillation in T2K [112]. Such appearance measurement came out in 2011, the same year in which Double Chooz published its first result. The collaboration observed 6 candidates of ν_e interaction, while the expectations from the background were 1.5 ± 0.3 events, implying that $\theta_{13} > 0$ with a $2.5\,\sigma$ significance. More recent results [113] reported the

---

ground laboratories.

[43] Reactor Experiment for Neutrino Oscillations.

observation of a 43 events signal with 4.9 ± 0.6 expected background events, which excludes the $\theta_{13} = 0$ hypothesis at $7.3\,\sigma$. The MINOS experiment also observed a signal from $\nu_\mu \to \nu_e$ oscillation (see latest results in Ref. [114]).

1.3 Future researches

The phenomenon of neutrino oscillation, widely discussed in the previous section, is accurately described by the mixing of three neutrino families. Many of the oscillation parameters represented in the U matrix (equation 35) have been measured. However, the sign of the squared mass splitting Δm^2_{23} and the value of the CP-violating phase δ_{CP} are still missing from the puzzle.

The oscillation also implies neutrino to be massive particles, since the interference that causes the flavour changing is due to different propagation of Hamiltonian eigenstates. As a matter of fact, if neutrino masses degenerated, the oscillation probability (equation 36) would inevitably go to zero. Such probability depends only on the mass squared difference, and therefore no information on the absolute masses can be extrapolated for an oscillation measure. At present, only uppers limit are set on neutrino masses, which place them sat least 5 orders of magnitude below charged leptons and quark. Such small masses rise theoretical problems on their inclusion in the Standard Model as well as a debate on the physical mechanism behind their origin [115, 116].

Currently there is no compelling evidence for the existence of predominantly right-handed (left-handed) neutrinos (antineutrinos). Nonetheless, right handed neutrinos may play a crucial role in the

- generation of ν masses;
- understanding of their great difference from charged leptons and quarks masses;
- justification of the matter-antimatter asymmetry in the Universe.

The interaction of a predominantly right handed neutrino is quenched by a factor m/E[44], therefore they are called *sterile*. Thermal leptogenesis with Majorana neutrinos is commonly believed to be the simplest possible extension of the Standard Model to describe the above mentioned phenomena [117, 118]. CP violation in the neutrino sector is considered a necessary input, through the Sakharov conditions [119], to justify such model.

This section contains an incomplete summary of current researches on the opened questions listed above.

---

[44] Right handed neutrinos do not couple with gauge bosons.

1.3.1 Mass hierarchy

Oscillation studies conducted so far allowed measuring the values of Δm^2_{12}, which is positive[45], and $|\Delta m^2_{13}| \simeq |\Delta m^2_{23}|$, with no information on the sign. There are therefore two potential ordering or *hierarchies* for the neutrino mass states: the normal, in which ν_3 is the heaviest, and the inverted, in which it is the lightest. A scheme of the two potential mass hierarchies is shown in figure 10. Unveiling the neutrino mass hierarchy would help to set values for the mixing angles, reduce the uncertainty on future determination of the CP-violating phase, δ_{CP}, and define the horizon of future neutrino-less double beta decay experiments. There are two main approaches to determine the neutrino mass hierarchy. A first one is based on the MSW effect for neutrino crossing the Earth, while the other one relies once again on the study of reactor neutrinos.

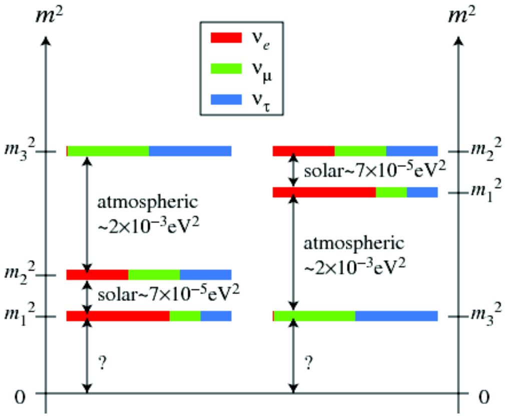

Figure 10: Diagram representing the flavour composition and possible ordering of the three ν mass states. Figure borrowed from [120].

Earth MSW effect approaches

The mass hierarchy can be determined by investigating $\nu_\mu \leftrightarrow \nu_e$ oscillation in terrestrial matter. If we neglect δ_{CP} and oscillating terms related to Δm^2_{12}, and we consider the MSW effect described in section 1.2.2, we have

$$P_{\nu_\mu \rightarrow \nu_e} \simeq P_{\nu_e \rightarrow \nu_\mu} \simeq \sin^2\theta_{23}\sin^2(2\theta_{13,m}) sin^2\left(1.27\Delta m^2_{23,m}\frac{L}{E_\nu}\right) \tag{37}$$

where $\theta_{13,m}$ and $\Delta m^2_{23,m}$ are defined in equations 32 and 29 respectively. The NC

---

[45] We define the state ν_1 as the one having the largest admixture of ν_e.

scattering effective potential has opposite sign for ν_e and $\bar{\nu}_e$; therefore the matter potential ΔV changes accordingly. Hence, the oscillation probability of equation 37 depends on the relative sign of ΔV and Δm^2_{23}, changing between normal and inverted hierarchy and between ν and $\bar{\nu}$. This makes possible for an experiment that collects data for $P_{\nu_\mu \to \nu_e}$ and $P_{\bar{\nu}_\mu \to \bar{\nu}_e}$, such as:

- an atmospheric neutrino experiment capable of separating ν from $\bar{\nu}$[46];
- a long baseline accelerator neutrino experiment with large enough $L \cdot \Delta m^2_{23,m}$ factor, and which profits of a beam that alternates the production of ν and $\bar{\nu}$;

to be able to determine the mass hierarchy. However, such measure is not simple. Besides the oscillation probabilities being suppressed by the small size of θ_{13}, subleading oscillation terms depending on Δm^2_{12} introduce degeneracies between certain values of Δm^2_{23} and δ_{CP} (which also changes between ν and $\bar{\nu}$).

Among the already existing accelerator neutrino experiments, T2K and, to a large extent, NOνA have chances of finding indications of the mass hierarchy via ν_e appearance, provided that the value of δ_{CP} is favourable. NOνA uses an upgraded NuMi beam (8.5° off-axis) and two detectors of fine-grained highly active liquid scintillator tracking calorimeter to distinguish the topology of electron-like and muon-like events [121]. The full operational phase began in late 2014 and, lately, first ν_e appearances have been observed [122].

For atmospheric neutrinos, resonant oscillation occurs either for neutrinos in the case of the normal hierarchy, or antineutrinos for the inverted hierarchy, and for specific patterns of neutrino energies and Earth-crossing paths. PINGU and ORCA are two proposed projects that aim to observe such patterns to unveil the mass hierarchy. Their similar design consists of closely separated vertical strings of digital optical modules for detecting atmospheric neutrinos with energies down to a few GeV via Cherenkov light, installed into water or ice.

The underground India-based Neutrino Observatory (INO) will use a 50 kt magnetic iron calorimeter. The experiments relies on the determination of charge and momentum of muons in CC interactions, and the energy of the hadronic showers, to distinguish atmospheric ν_μ from $\bar{\nu}_\mu$. Civil construction for INO began in 2013, while detector installation and commissioning is foreseen for 2017.

Reactor neutrinos approach

---

[46] This can be done directly, or by measuring the neutrino flavour and relying on the intrinsic difference in atmospheric neutrino flux between ν and $\bar{\nu}$ and in the interaction cross-section.

An alternative measurement technique relies on the interference of two different oscillation frequency components driven by Δm^2_{23} and Δm^2_{13}, which results in small hierarchy-driven wigles in the solar oscillation of reactor neutrino. The observation of this effect is enabled by the large discovered values of θ_{13}, but requires a detector with an unprecedentedly high energy resolution (3% at 1 MeV).

JUNO will be a bigger counterpart of today's reactor neutrino experiments. With a 20 kt high-transparent liquid scintillator target equipped with 15000 PMTs (80% coverage), JUNO aims to reach the energy resolution necessary to explore the mass hierarchy. Civil construction works for the experiment began in Jiangmen, China, where the detector will be located, $\sim$ 58 km from the Yangjiang (17.4 GW_{th}) and Taishan (18.4 GW_{th}) reactor facilities. The JUNO group claims to be able to reach a sensitivity on the mass hierarchy better than 3 σ, which can be improved to more than 4 σ with more precise measurements of Δm^2_{23} [123, 124]. Other scientific goals include the measurement of the oscillation parameters Δm^2_{12}, Δm^2_{23} and $sin^2\theta_{12}$ to a level below 1%.

An overview of the sensitivity of some present and future experiments to a measure of the neutrino mass hierarchy is shown in figure 11.

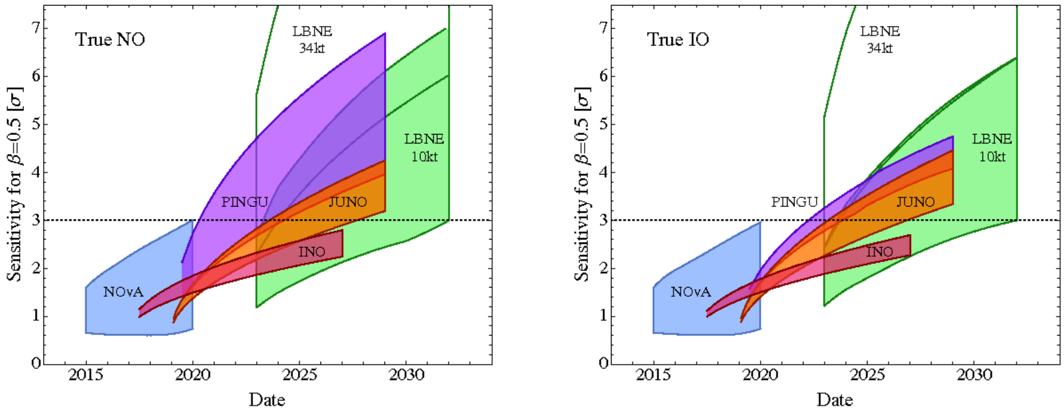

(a) Rejecting the inverted hierarchy if the normal hierarchy is true.

(b) Rejecting the normal hierarchy if the inverted hierarchy is true.

Figure 11: Sensitivity to the mass hierarchy, expressed in terms of 50% rejection probability (β) of the wrong mass ordering, for different experiments as a function of the date. The width of bands corresponds to different values of δ_{CP}. From [125].

1.3.2 Absolute neutrino mass scale

Even assuming a defined neutrino mass ordering, their absolute values would still be unknown. In two limit conditions, it could be that $m_1 \ll m_3$ ($m_3 \ll m_1$) in case of normal (inverted) hierarchy, so that m_3 (m_1) is close to $\sqrt{\Delta m^2_{23}}$, or, conversely, that $m_1 \simeq m_2 \simeq m_3 \gg \sqrt{\Delta m^2_{23}}$. Both cases are compatible with existing constraints on the absolute scale of neutrino masses.

Neutrinos masses affect the large-scale structure of the Universe, as well as the cosmic microwave background radiation (CMBR) [126]. Consequently, upper limits on the sum of all neutrino masses come from a combination of cosmological measurements and model-based assumptions. Measurements on the CMBR from the WMAP probe, combined with other measurements of cosmological parameter, give a limit of [127]

$$\sum_j m_j < 0.44\,\text{eV}\ (95\%\text{C.L.})\,. \tag{38}$$

Similarly, the Planck space observatory measured [128]

$$\sum_j m_j < 0.23\,\text{eV}\ (95\%\text{C.L.})\,. \tag{39}$$

Other authors, basing on observations on CMBR and lensing, suggest [129]

$$\sum_j m_j = 0.32 \pm 0.08\,\text{eV}\ (95\%\text{C.L.})\,. \tag{40}$$

The presence of a massive neutrino in the β decay affects the shape of the electrons energy distribution in the region very close to the end-point (a 10^{-13} effect). Very precise measurements of β decay spectrum of tritium can be used to determine the incoherent sum of mass eigenstates ν_e, as represented in figure 12. Contrary to what is deduced from astronomical data, these measurements have the advantage of being model-independent. The Mainz and Troitsk experiments have set upper limits for $m_{\bar{\nu}_e}$, with the latter experiment having published the most stringent one [130, 131]

$$m_{\bar{\nu}_e} < 2.05\,\text{eV}(95\%\text{C.L.})\,. \tag{41}$$

KATRIN[47] plans to reach sensitivity of $m_{\bar{\nu}_e} < 0.20$ eV, probing at least the second limit case for neutrino masses [132].

---

[47] KArlsruhe (Germany) TRItium Neutrino experiment.

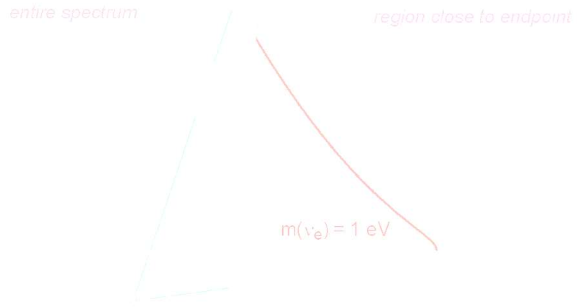

Figure 12: Measurement principle of $m_{\bar{\nu}_e}$ with tritium decay.

1.3.3 Majorana or Dirac neutrino?

A Majorana particle is a particle that is its own antiparticle [133]. All fermions of the Standard Model, with the exceptions of neutrinos, are charged; therefore they cannot be Majorana particles. The nature, Dirac or Majorana, of neutrinos, on the other hand, is not yet settled. Majorana neutrinos can arise from symmetry breaking in the *see saw* mechanism, which explains the smallness of the neutrino masses compared to those of charged leptons [134]. Majorana particles also violate the lepton number conservation.

Important information about the mass hierarchy, the absolute mass scale, and the nature of neutrinos can come from double beta ($\beta\beta$) decay experiments. The $\beta\beta$ decay is a process allowed in the Standard Model that can be observed in nuclei where the single β decay is forbidden. The half-life of the process $\tau_{1/2}^{\beta\beta}$ is in a range of $10^{18} - 10^{22}$ y. The neutrino-less double beta decay ($0\nu\beta\beta$) is instead forbidden in the Standard Model, since it requires the violation of the lepton number. However, if neutrinos are massive Majorana particles, the $0\nu\beta\beta$ is allowed and has a rate that is proportional to coherent sum of real masses [135]

$$m_{\beta\beta} = |\sum_i m_i U_{ei}^2| \, . \tag{42}$$

The value of $m_{\beta\beta}$ depends on the mass ordering, being lower in case of normal hierarchy. $m_{\beta\beta}$ is also related to the $0\nu\beta\beta$ half-life

$$(\tau_{1/2}^{0\nu})^{-1} = G_{0\nu} |\mathcal{M}_{0\nu}|^2 |m_{\beta\beta}|^2 \, , \tag{43}$$

where $G_{0\nu}$ is the reaction phase-space and $\mathcal{M}_{0\nu}$ the matrix element, which depends on the isotope. The signature of a $0\nu\beta\beta$ would be a peak at the end-point of the $\beta\beta$ spectrum. In order to resolve such signal from the natural radioactivity, isotopes with high decay energies[48] and an ultra-clean detectors with high energy resolution are required. Among the different approaches used by current experiments, high-resolution calorimeters select the signal basing on the energy of the decay, while tracking experiments aim to recognise its topology by tracking the two electrons. Example of $0\nu\beta\beta$ experiments are:

- the CUORE and GERDA experiments, in LNGS, which use TeO_2 crystals and Ge crystal diodes respectively as both decay source and particle detector [136, 137];
- KamLAND-Zen, a modified version of KamLAND obtained by equipping the apparatus with 13 t of Xe-loaded liquid scintillator [138] (a similar approach is also used in SNO+);
- SuperNemo, which aims to perform a tracking-calorimetric measurement using thin foils of $\beta\beta$ emitting isotopes surrounded by tracking chambers [139].

At present day, there is no evidence of $0\nu\beta\beta$ decay, and only upper limits on $m_{\beta\beta}$ are set, of which a global picture is given in figure 13. A next generation of forthcoming $\beta\beta$ experiments seeks to expand the sensitivity in the inverted hierarchy region.

1.3.4 Light sterile neutrinos

There have been possible hints for the presence in the neutrino mixing of one or more additional states with masses at the eV scale, namely the LSND anomaly and the reactor anomaly.

LSND anomaly

In 1996, before Kamiokande results, the LSND experiment reported the observation of $\bar{\nu}_e$ appearance in a $\bar{\nu}_\mu$ beam at short (30 m) baseline [141, 142]. The oscillation results favour the presence of an additional mass splitting $\Delta m^2 \simeq 1\,\text{eV}^2$, and therefore at least[49] a fourth sterile (considering $N_\nu \simeq 3$ from LEP) neutrino.

---

[48] Used isotopes include ^{48}Ca, ^{76}Ge, ^{100}Mo, ^{150}Nd, ^{82}Se, ^{130}Te, ^{136}Xe and ^{96}Zr.

[49] Combining LSND results with other short-baseline measurements (from Bugey, CCFR, CDHS, CHOOZ, KARMEN and NOMAD), and atmospheric results, the hypothesis of 2 additional sterile neutrino (with large CP violation) appears more likely [143].

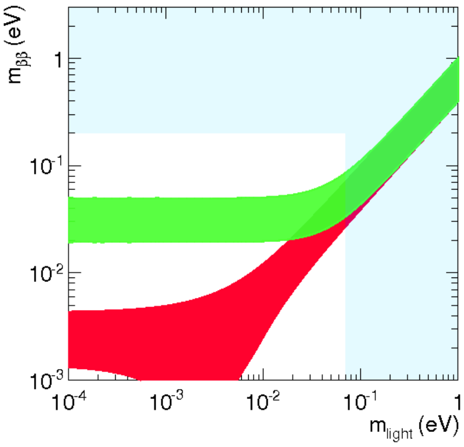

Figure 13: Effective neutrino Majorana mass $m_{\beta\beta}$ as a function of lightest neutrino mass m_{light}. The red band corresponds to the normal hierarchy ($m_{light} \equiv m_1$), while the green band corresponds to the inverted hierarchy ($m_{light} \equiv m_3$). The vertical exclusion band comes from cosmological bounds; the horizontal one from current $0\nu\beta\beta$ limits. See Ref. [140] and included references for details.

Such controversial results were challenged by MiniBooNE, which investigated the LSND mass splitting in the better-understood $\sim$ 1 GeV energy regime of the Booster beam, at Fermilab. Results on the whole data sample [144, 145] showed no excess in the LSND energy region, partially ruling out its oscillation allowed region, but yet another excess at lower energies.

MiniBooNE was superseded by MicroBooNE, whose detector consists of a large (60 t) time projection chamber with ultra-pure liquid argon (LArTPC) [146]. Other than testing the MiniBooNE and the LSND anomalies, MicroBooNE will measure low energy neutrino cross-sections and test the LArTPC technology for future long-baseline experiments. The data taking began in July 2015 [147]. MicroBooNE, along with the other two Fermilab experiments T600 and LAr1-ND, is part of the SBN[50] program, which aims to extend the sensitivity to short-baseline $\nu_\mu \to \nu_e$ oscillation far beyond the LSND allowance region, as shown in figure 14.

Reactor anomaly

Reactor neutrino oscillation experiments rely on accurate predictions of the $\bar{\nu}_e$ flux. Energy spectra of $\bar{\nu}_e$ emitted in the several β branches involved in the decay of fission products (^{235}U, ^{238}U, ^{239}Pu, ^{241}Pu) are converted from precision measurements

---

[50] Short Baseline Neutrino.

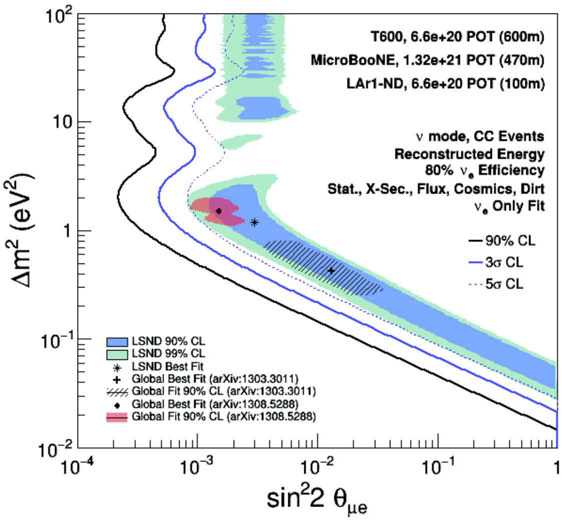

Figure 14: Sensitivity to ν_e appearance of the SBN program [148].

of the β spectrum. A recent improved method for the conversion [149], applied to 19 results from six reactor short baseline (< 100 m) neutrino experiments (Bugey, Geosgen, ILL, Krasnoyarsk, Savannah River, Rovno), revealed a ratio between observed and predicted IBD events of 0.943 $\pm$ 0.023 [150] (also confirmed in Ref. [151]). This 98.6% C.L. deficit can be interpreted as the contribution of a sterile component in the neutrino oscillation, as shown in figure 15.

In order to probe the possible existence of a sterile neutrino at the eV mass scale, which would have deep impact in particle physics and cosmology, different experimental approaches can be used. The E/L distortion induced in the energy spectrum at very short baselines will be used by the STEREO experiment at the ILL reactor facility (Grenoble, France), and the SoLiδ project at the BR2 research reactor (Mol, Belgium). Another approach aims to leave out dependencies on the reactor model by deploying neutrino sources in already existing liquid scintillator experiments (e.g. in Ref. [152]). The eV scale can be also tested by the already mentioned direct measurements of the ν_e combined mass in tritium decays [153].

1.3.5 CP violation

With respect to the mass hierarchy, the CP-violating parameter is a more challenging measurement and will require strong experimental efforts on a longer time-scale. At

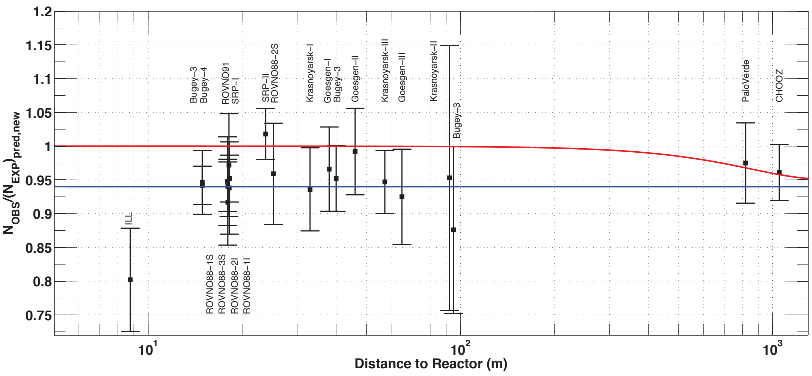

Figure 15: Ratio between predicted and observed neutrino rates measured in Ref. [150]. The results are compared with the standard three-families oscillation mode (red line) and an oscillation with an additional Δm^2 (blue line).

the present day, constraints on the value of δ_{CP} have been put by comparing CP-independent measures of θ_{13} in disappearance, made by reactor experiments, with the CP-dependent measure of θ_{13} with ν_e appearance of T2K [113]. Several large-scale long baseline experiments have been proposed for a direct measure of δ_{CP} through oscillation of a ν_μ beam in matter. Such projects also claim to be able of resolving the mass hierarchy with high sensitivity power. A comparison of expected sensitivities can be found in Refs. [154, 155]. Among these projects, DUNE (former LBNE), which plans to send a neutrino beam produced at Fermilab to a multi-kiloton liquid argon detector on a 1300 km baseline [156], has recently obtained the financial support of the U.S. government and the external support of CERN.

2 The Double Chooz experiment

Contents

Double Chooz is a reactor neutrino oscillation experiment designed to measure θ_{13}, one of the parameters that governs the standard three-families neutrino oscillation. In 2011, Double Chooz published results indicating a first hint of non-zero value of θ_{13}, which by that time was the last unknown of the three mixing angle (see Ref. [108]). Since then, Double Chooz gave a significant contribution to the experimental race to improve the precision on θ_{13} [157–160] along with two other reactor neutrino experiments Daya Bay [109, 111, 161, 162] and RENO [110, 163], and the neutrino accelerator experiments MINOS [114, 164] and T2K [88, 112, 113].

From many points of view, Double Chooz takes up the legacy of the CHOOZ experiment, which first set a limit on the θ_{13} value with an analogous experimental approach [106]. For instance, both experiments use as neutrino source the two N4 pressurized water reactors of the Chooz nuclear plant, which is located in the homonymous town, in the French Ardennes. Nuclear reactors are powerful artificial neutrino sources, and reactor neutrinos energies are ideal to observe the atmospheric oscillation at relatively short baselines ($\sim$ 1 km). The idea of Double Chooz is to use two identical detectors placed at different distance from the source in order to measure the neutrino flux and energy spectrum before and after the oscillation occurs. In disappearance mode, the expected neutrino rate is compared with the observed one, and the deficit is related to the oscillation parameters. The far detector exploits the same facility of CHOOZ, placed at a mean distance of 1050 m from the two reactor cores - near the oscillation maximum - and under a 300 mwe rock overburden. The near detector is hosted in a newbuilt cave at a distance of 400 m on average from the two reactors and under 120 mwe rock overburden. This position meets the requirement of being in the non-oscillation region to logistic considerations. Both detectors are based on the technology of organic liquid scintillators, in which neutrinos are detected via inverse beta decay (IBD). Double Chooz started taking data, with the far detector only, in April 2011. The near detector, whose data taking started in December 2014, will reduce the systematics associated with production and detection of reactor neutrinos. This chapter focuses on the experimental design and working mode of the experiment, while the following one describes in details how the measurement of θ_{13} is performed.

2.1 Experimental design

Double Chooz aims to measure the mixing angle θ_{13} with two detectors at different baselines in order to observe the $\bar{\nu}_e$ disappearance. Antineutrinos are detected using the strong signature of their inverse beta decay (IBD) interactions.

2.1.1 Measuring θ_{13} with reactor neutrinos

In the framework of the standard three-flavours oscillation, the survival probability of $\bar{\nu}_e$ can be expressed as

$$\begin{aligned} P_{\bar{\nu}_e\to\bar{\nu}_e} \simeq 1 &- P^{atm}_{\bar{\nu}_e\to\bar{\nu}_x} - P^{\odot}_{\bar{\nu}_e\to\bar{\nu}_x} \\ = 1 &- \sin^2(2\theta_{13})\sin^2\left(1.27\Delta m^2_{23}\frac{L}{E}\right) \\ &- \cos^4(\theta_{13})\sin^2(2\theta_{12})\sin^2\left(1.27\Delta m^2_{12}\frac{L}{E}\right), \end{aligned} \tag{44}$$

where L(m) is the distance between the neutrino source and the detector, or baseline, E(MeV) the neutrino energy, Δm^2_{23} and Δm^2_{12} the atmospheric and solar mass splitting (eV^2), θ_{12} and θ_{13} two of the three mixing angles. The nature of the two mass splitting is so that the two terms $P^{atm}_{\bar{\nu}_e\to\bar{\nu}_x}$ and $P^{\odot}_{\bar{\nu}_e\to\bar{\nu}_x}$ govern the oscillation at different L/E. A graphic representation of equation 44 is given in figure 16, where the $\bar{\nu}_e$ survival probability is shown as a function of L/E.

In the same figure, the position of the Double Chooz two detectors is shown. The far detector is placed at a baseline of 1050 m, which corresponds to a point of maximal atmospheric oscillation and no solar oscillation. The near detector, on the other hand,

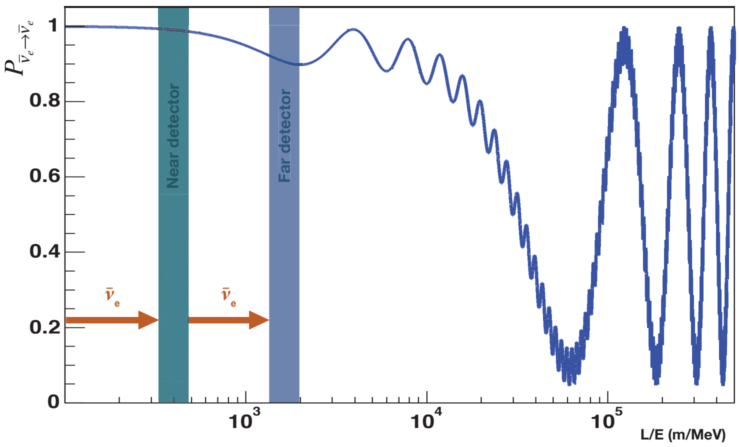

Figure 16: Survival probability of electron anti-neutrinos, according to the three-flavours oscillation theory. The used oscillation parameters are: $\Delta m^2_{12} = 8 \cdot 10^{-5}\, eV^2$, $\sin^2(2\theta_{12}) = 0.9$, $\Delta m^2_{13} = 0.0025\, eV^2$, $\sin^2(2\theta_{13}) = 0.1$.

is placed at shorter baseline of 400 m, where the oscillation probability is almost zero. The disappearance of $\bar{\nu}_e$ happening between the near and the far detectors is proportional to the atmospheric oscillation amplitude of equation 44, i.e. $\sin^2(2\theta_{13})$, which can consequently be inferred from the relative neutrino rates. Furthermore, the oscillation depends on the neutrino energy E, meaning that $\sin^2(2\theta_{13})$ can be also measured by observing a distortion between neutrino spectra measured by the two detectors.

The arrangement of the two detectors and reactors is shown in figure 17. The results published so far [157–160] correspond to a data sample collected only with the far detector. In these analyses, a Monte Carlo simulation normalized on Bugey-4 measurements plays as an effective near detector in terms of non-oscillated $\bar{\nu}_e$ flux and spectrum. While a constant effort was made to refine the accuracy of the reactor $\bar{\nu}_e$ simulation and to reduce the associated systematic, the latter constitutes the major component on the final error, limiting the one-detector precision to the order of 30% on $\sin^2(2\theta_{13})$. The operation of the near detector will lead to a major reduction of such systematics and consequently to a major improvement of the precision. We expect a two-detector analysis to be able to determine $\sin^2(2\theta_{13})$ with a final relative precision nearing the 10%.

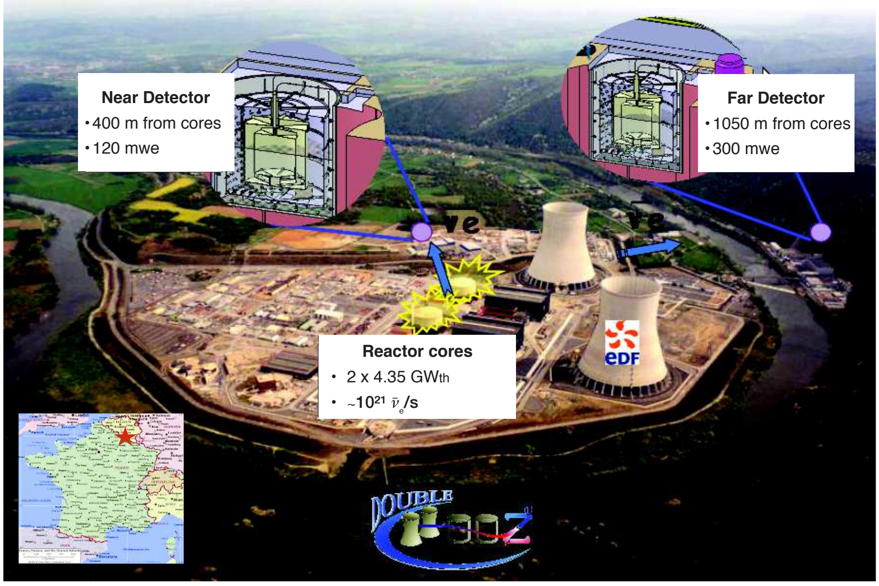

Figure 17: Top view of the Chooz nuclear plant, with the different elements involved in Double Chooz emphatized.

2.1.2 Neutrino detection

Among all CC and NC neutrino interactions, an important role in neutrino detection is played by the inverse beta decay (IBD), or

$$\bar{\nu}_e + p \longrightarrow e^+ + n\,. \tag{45}$$

The minimum energy for a neutrino to interact via IBD, must be so that the lepton mass m_e and the neutron mass m_n are produced in the process. From kinematical assumption, this corresponds to an energy threshold of

$$E_{\bar{\nu}_e}^{min} = \frac{(m_e + m_n)^2 - m_p^2}{2m_p} \simeq 1.806\,\mathrm{MeV}\,, \tag{46}$$

where m_p is the proton mass (neutrino mass is negligible). Moreover, since recoil energy of the neutron is small compared to the neutrino energy, the positron energy is directly linked to the neutrino energy

$$E_{e^+} \simeq E_{\bar{\nu}_e} - \Delta \simeq E_{\bar{\nu}_e} - 1.293\,\mathrm{MeV}\,, \tag{47}$$

where Δ is the mass difference between neutron and proton.

The inverse beta decay is the detection method used in the Cowan and Reines' experiments and - half a century from then - by modern reactor neutrino oscillation experiments. In Double Chooz, as well as for the above-mentioned experiments, $\bar{\nu}_e$ are detected by means of their IBD interaction in an organic liquid scintillator (LS). The LS acts both as target - with the abundant hydrogen nuclei of the organic compound providing the protons - and as detection material for the IBDs. The energy dependence of the hydrogen IBD cross-section matches the one of a free proton and can be represented as [165]

$$\sigma_{IBD} = K \times (E_{\bar{\nu}_e} - \Delta)\sqrt{(E_{\bar{\nu}_e} - \Delta)^2 - m_e^2} \simeq 5 \cdot 10^{-44} \frac{E_{\bar{\nu}_e}}{\mathrm{MeV}} \mathrm{cm}^2 \,. \tag{48}$$

where K is a constant that depends on the neutrino lifetime. The neutrino energy spectrum is a convolution of the reactor flux and the IBD cross section. A graphical depiction of such spectrum is given in figure 18. The energy range goes from the 1.806 MeV threshold to roughly 10 MeV, where the neutrino flux drops off, and it is peaked between 3 and 4 MeV.

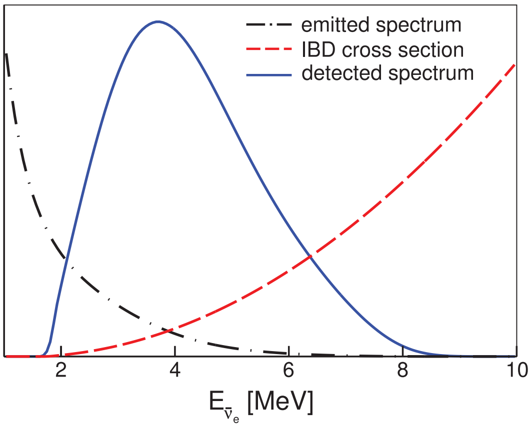

Figure 18: Energy spectrum of detected $\bar{\nu}_e$ as a result of the convolution of the flux and IBD cross-section, as redrawn from [149].

The signature of an IBD interaction in Double Chooz is given by the prompt positron scintillation and annihilation followed by the delayed neutron capture. The time and space correlations between the two distinct signals of the positron and the neutron strongly reduce the background due to radioactivity, enhancing the neutrino detection. A graphical representation of such IBD signature is given in figure 19.

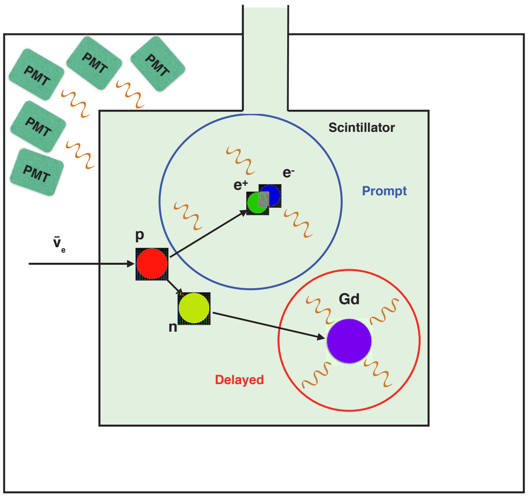

Figure 19: Graphic representation of signal induced by inverse beta decay in a gadolinium-doped liquid scintillator.

Prompt signal

The positron interacts with the scintillating medium, exciting its molecules and loosing its kinetic energy. Subsequently, it annihilates with a surrounding electron, generating two 511 *keV* γ rays. The photons do not produce a direct signal in the scintillator, but are detected by the means of secondary electrons produced in Compton scatterings. Scintillation and annihilation light are delayed by a short time ($\sim$ 100 ps) compared with the detector response and are seen as a single process with total visible energy

$$E_{vis} = E_{e^+} + m_e \simeq E_{\bar{\nu}_e} - \Delta + m_e \simeq E_{\bar{\nu}_e} - 0.782\,\text{MeV}\,. \tag{49}$$

The IBD threshold in terms of E_{vis}, according to equation 46, is $E_{vis}^{min} = 1.022\,\text{MeV}$. Since the oscillation probability depends on the neutrino energy, a measure of E_ν allows to perform a shape oscillation analysis (see section 3.5.2). By measuring E_{vis} it is possible to infer the neutrino energy, which by reversing equation 49 will be $E_{\bar{\nu}_e} = E_{vis} + 0.782\,\text{MeV}$.

Delayed signal

The neutron is detected by the energy released in the process of capture by a nucleus of the scintillator material. The amount of energy and number of γ depends on the capturing nucleus. Double Chooz uses gadolinium (Gd) as a dopant for the liquid scintillator, to enhance the neutron detection. The Gd has a large n-capture cross-section ($\sim 2.5 \cdot 10^{-19}$ cm^2). Moreover, the γ rays produced in the process have a total energy of 8 MeV, which places the delayed signal well-above the natural radioactivity. Neutrons can be captured by hydrogen (H) as well, forming deuterium. The cross section of that process is smaller (8 orders of magnitude lower than for Gd), and the released energy 2.22 MeV, making it a less preferable channel for neutron detection. In any case the capture follows the neutron thermalisation, which is responsible for a time and space separation between prompt and delayed signals. The average time delay of the neutron capture with respect to the positron signal depends on the capturing element, being $\sim$ 30 μs for Gd and $\sim$ 200 μs for H.

2.2 The Double Chooz detectors

Double Chooz is a large liquid scintillator experiment with a total target mass of $\sim$ 20 t. Charged particles are detected by means of light produced in their interaction with the organic liquid scintillator. The light is collected by phototubes (PMTs) which are used to reconstruct the interacting position and released energy.
In this section we will describe the two Double Chooz detectors and their *modus operandi* (see also Refs. [166, 167]). After a description of the apparatus layout, we will discuss the steps that lead from an energy deposit in the liquid scintillator to a fully reconstructed event.

2.2.1 Detector overview

Each of the two detectors mainly consists of four concentric cylindrical volumes of different sizes, nested in an onion-like structure. The volumes are characterized by different hulls and are filled with different liquids, depending on their function. The various components of a detector, specifically for the far one, are shown in figure 20. We will now give a description of each component, starting from the innermost volume and moving progressively to the outside. Note that near and far detectors are designed to be identical, as we already mentioned, thus the descriptions of the various components are valid for both detectors. However, small differences are present and will be mentioned.

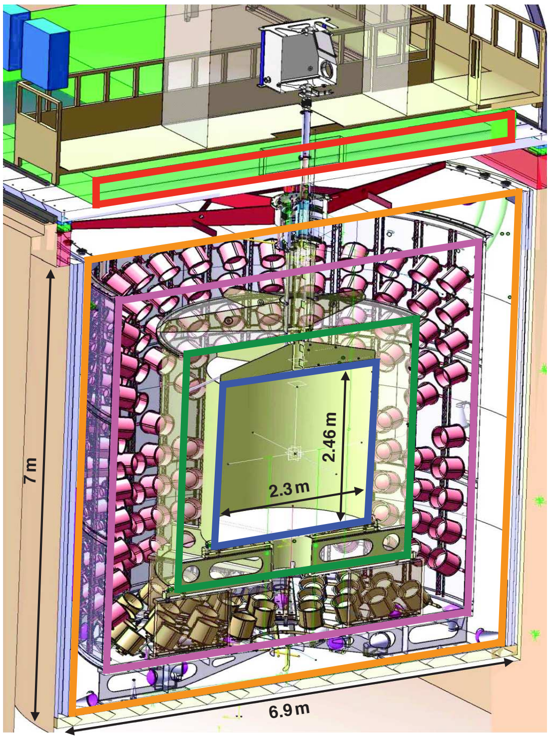

Figure 20: Double Chooz far detector layout represented by the means of its horizontal section. Each detector component is highlighted with a different colour: inner target (blue), gamma-catcher (green), buffer (magenta), inner veto (orange) and outer veto (red).

Inner target

The innermost cylinder is the inner target (IT), which, as its name suggests, is the main target for neutrino interactions. It consists of an 8 mm thick acrylic vessel with a total internal volume of $10.3\,\mathrm{m}^3$ (230 cm diameter $\times$ 246 cm height) filled with liquid scintillator. The chemical properties of the acrylic allow the vessel resisting the mechanical stress and to be transparent to light in the wavelength region of interest (wavelength of scintillation light). The filling liquid consists of a PXE-based LS[51] doped with Gd at 1 g/l [168, 169]. The presence of Gd increases the neutron detection efficiency by providing a large n-capture cross-section and released energy, as discussed in the last section.

Gamma-catcher

---

[51] In the Double Chooz liquid scintillators o-PXE (ortho-Phenylxylylethane) is the solvent, and PPO (2,5-Diphenyloxazole) and bis-MSB (4-bis-(2-Methylstyryl)benzene) the primary and secondary solute.

Outside the IT and surrounding it is the gamma-catcher (GC), a 22.3 m^3 tank in acrylic vessel (339 cm diameter × 357 cm height). The GC is filled with a liquid scintillator that has a similar composition to the one of the IT but is Gd-free. The liquids of the IT and GC are chosen to guarantee an equal light yield (LY) between the two volumes, while the acrylic vessel has an increased thickness of 12 mm to withstand the more intense mechanical stress.

Again the choice of the name is suggestive, as the purpose of the GC is to detect gammas that are produced near the IT borders and escape from it. Nevertheless, the GC works as an effective neutrino target for IBDs with neutron capture on hydrogen.

Buffer

In turn the gamma-catcher is surrounded by the buffer, a 110 m^3 volume (552 cm diameter × 567 cm height) filled with 80 t non-scintillating mineral oil. The buffer is the one of the major improvement with respect to the CHOOZ detector. The 105 cm thick mineral oil layer effectively shields the innermost volumes of the IT and GC - with an identical liquid density - from radioactivity (mostly ^{40}K). The buffer hull is a 3 mm thick stainless steel tank. The resulting optically isolated ensemble formed by IT, GC and buffer is named inner detector (ID). The two identical ID areas of the near and far detector are shown in figure 21.

The buffer tank also serves as support structure for the photomultiplier array, installed in its inner wall, that collects the light from the target and the gamma-catcher. The array consists of 390 low-background 10-inch Hamamatsu R7081 PMTs distributed at regular intervals all over the buffer wall, and it has a total light coverage of 14% [170–172]. The chosen PMTs meet the high Double Chooz required standards in term of performances, low radioactivity and mechanical properties.

Inner veto

The last of the four detector layers is the inner veto, a 90 m^3 tank (659 cm diameter × 664 cm height) hosting a 50 cm thick layer of liquid scintillator. The IV is equipped with 78 8-inch PMTs formerly used in the IMB[52] experiment [76]. They are installed on the steel tank, whose interior surface is coated with reflecting painting to enhance the light collection. The purpose of the IV is to identify and reject events originating

---

[52] Irvine-Michigan-Brookhaven detector, located in Ohio.

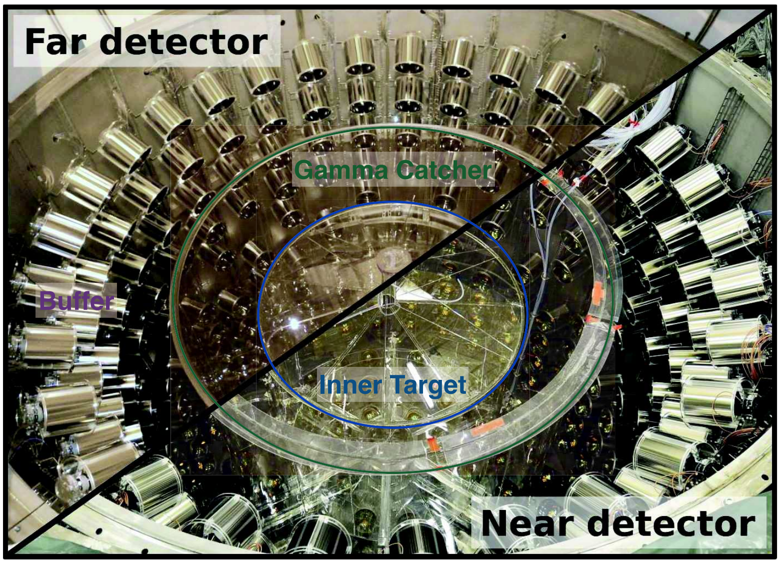

Figure 21: Comparison between the two Double Chooz detectors IDs before each of their filling phases. The IT and GC areas are highlighted in blue and green respectively.

outside the ID, that it surrounds. The PMTs are arranged on three layers (top, bottom, and side of the wall) with a higher density on the bottom part of the IV in order to better track downgoing muons [173].

Shielding

The two Double Chooz detectors are placed in underground laboratories, sheltered from cosmic rays. The far detector is hosted in the CHOOZ pit and can profit of a 300 mwe rock overburden. The neutrino flux in the near detector is a factor of 7 higher thanks to the source proximity; therefore a similar signal-on-background ratio can be kept with its 120 mwe rock overburden.

Furthermore, an extra shielding is put around the whole detector (ID and IV) to screen it from radioactivity produced in the surrounding rock. In the far lab the constrain posed by the existing pit dimensions led to the choice of 150 mm of demagnetized steel for the shielding. In the near lab, on the other hand, a larger pit was excavated, enabling the use of a 50 cm water layer[53].

---

[53] Water has a reduced intrinsic radioactivity with respect to metal.

Outside the inner detector

An array of plastic scintillators is placed horizontally on top of the detector to further reject muon-induced background. This outer veto (OV) provides a crucial contribution in tagging downgoing muons. In the far detector, the OV covers the whole detector upper surface and extends further in all directions, for a total coverage of 13 × 7 m^2. It is also structured on multiple levels to provide further coverage and help to track muons. The near detector OV is a smaller version of the far detector - with a non-full coverage of the detector surface - and is not used as a tracker.

Above the OV is the glove box, a system kept under nitrogen atmosphere and at the detector pressure that is used to deploy calibration sources inside the IT (see section 2.2.2). The detector is attached to the glove box through the chimney, a vertical multi-layer tubular structure that connects the detector volumes with the exterior. A further layer of plastic scintillators, the upper-OV, is placed above the glove box to enhance the coverage on the chimney area. A scheme of the far detector, with a zoom on the chimney area, is given in figure 22.

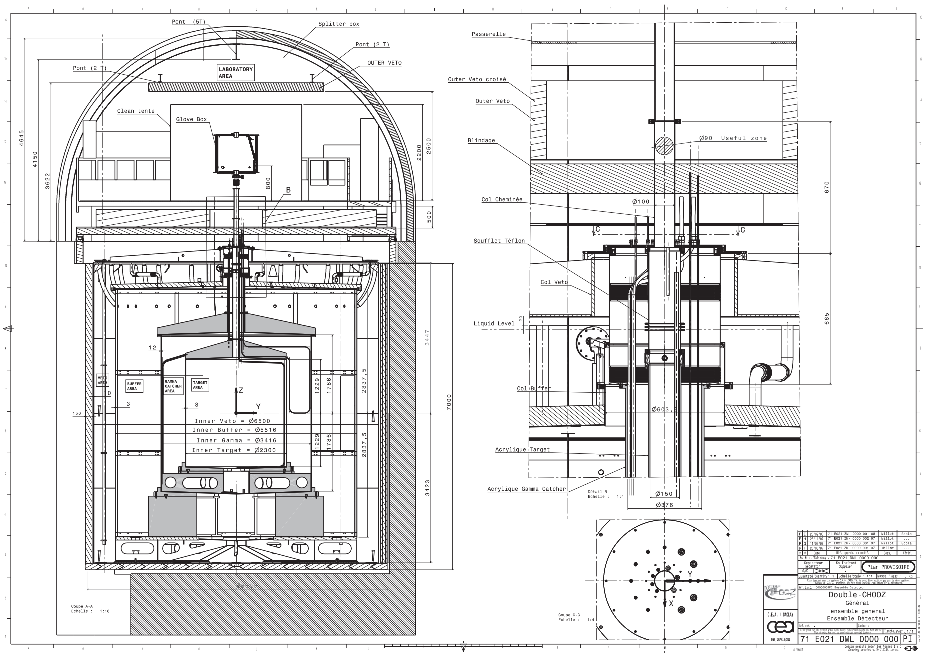

Figure 22: Double Chooz far detector scheme, with a zoom of the chimney.

2.2.2 Calibration systems

Although the functioning of all components have been simulated and tested before and during the installation of each of the two detectors, calibrations are taken on regular basis to further investigate and check the stability of the detectors properties. Two different sets of parameters are tested:

- the detector response, at different energies and positions, to the signal induced by particles involved in the neutrino detection (and of the background);
- the optical response of the liquids (scintillation, light propagation), and the readout (PMTs, electronics).

Calibrations are taken with natural occurring events, sources deployed inside the detector, and direct injection of light.

Natural sources

Natural calibration sources include energy peaks from environmental radioactivity (U/Th decay chains), Bi-Po coincidences, and tracked cosmic μ. Muons also produce a large number of spallation neutrons, whose capture can be studied to characterize the efficiency of the neutron detection, as well as providing a clear energy peak.

Deployed sources

Radioactive sources can be deployed in different positions inside the detector by the means of two different systems:

- the Z-axis deploying system, consisting in pulley system located inside the glove box, that allows deploying sources directly inside the IT liquids along the vertical axis with a $\sim$ 1 mm precision;
- the guide-tube, a rigid tube shaped in the form of a loop that goes in the upper half of one side of the GC, along which the sources are deployed with $\sim$ 1 cm precision.

Up to now, four different sources have been deployed using both systems. The choice of these sources is such to guarantee a full energetic coverage in the prompt signal energy region, as well as a neutron source for the delayed signal:

1. ^{137}Cs emits a 667 keV γ ray (energy near the trigger threshold);

2. ^{68}Ge decays via electron capture to ^{68}Ga, and the subsequent ^{68}Ga β^+ decay eventually leads to two 0.511 MeV annihilation gammas (total energy close to IBD threshold);

3. ^{60}Co emits two γ rays of 1.17 MeV and 1.33 MeV (total energy near the prompt energy peak and the n-H capture);

4. ^{252}Cf is a neutron emitter, with the neutron capture used for the energy scale (conversion between photoelectrons and MeV), detector stability and systematics evaluation.

Light injection systems

In addition to radioactive sources, a laser ball is deployed in the IT using the z-axis system. A blue (λ = 470 nm) and a UV (λ = 380 nm) light emitting diodes (LEDs) are used to test the light propagation and readout response.

Besides the laser ball, a light injection system consisting of LEDs connected to the detector interior through optical fibres is permanently installed in both inner detector and inner veto. LEDs operate in pulsed mode to minimize background through scintillation light, with pulse width, flashing frequency and light intensity varied remotely.

In the light injection system of the inner detector (IDLI), each of the 32 Teflon fibres with diffusers (for diffused light) and 14 quartz fibres (for narrow beams) are attached to the support structure of one PMT inside the ID. Three different wavelengths are used: 385, 425 and 475 nm. Only the first two wavelengths excite the scintillator, allowing for a study of the absorption of target and gamma-catcher liquids. The unabsorbed 475 nm light is used instead to study the light propagation. The IDLI system is used to:

- monitor the PMTs, measuring their gain and time response;
- monitor the liquids, checking the LY and the general response.

Like the IDLI, the light injection system of the IV (IVLI) disposes of multiple-wavelength LEDs, namely 375 nm and 475 nm, in order to test different aspects of the IV response, and 96 fibres. A more detailed description of the IVLI will be given in section 5.2.

2.2.3 Electronics and data acquisition

The signals of the 468 total ID and IV PMTs are collected, digitalized and stored by the Double Chooz electronics and data acquisition system (DAQ) [174]. Each PMT is connected to the readout system by a single cable, which carries both the $\sim 1.3\,\mathrm{kV}$ high voltage (HV) and the few mV signal. Customized HV-splitters separate the two components, allowing the signal to be amplified and processed. This is done in multiple steps: a front end electronic (FEE) filters and amplifies the signal before sending it to the flash-analog-to-digital converter (FADC) for the digitalization and, in parallel, to the trigger system. A schematic representation of this process is shown in figure 23. The OV information is stored independently utilizing a different DAQ system and then merged with the main DAQ.

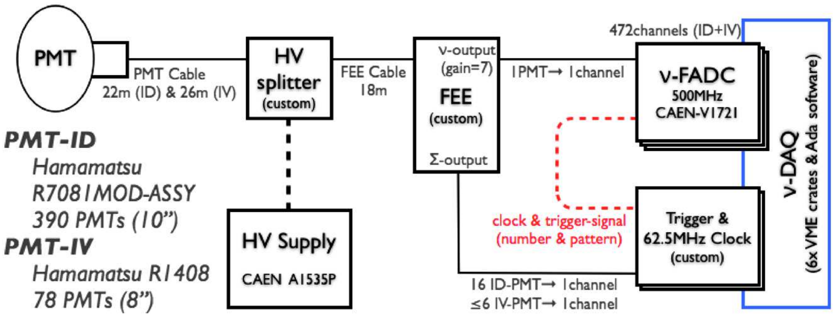

Figure 23: Diagram showing the readout and DAQ system used in Double Chooz (from [157]). PMT signals are separated from the HV by splitter boxes, pre-processed by custom made FEE modules, and sent to the FADC modules and the trigger system.

FADC

The ν-FADC, designed to process signals in the IBD energy range, consists of 64 CAEN-Vx1721 8-channels waveform digitizers [175]. Each channel processes and records the waveform of a PMT in a 8-bit temporary memory, corresponding to a signal sampling of 500 MHz or, equivalently, 2 ns. Waveforms are then moved in a buffer memory region before being sent to the readout when a trigger signal comes, in a completely deadtime-free way. As a result of the whole process, for each trigger a 256 ns digitalized waveform is recorded for every PMT (with 1 ADC count corresponding to $\sim 4\,\mathrm{mV}$).

Trigger system

The trigger system consists of three trigger boards (one for the 78 IV PMTs, two for the 390 ID PMTs) and a trigger master board [176]. Each trigger board is connected either to half of the ID PMTs, either to all IV PMTs. In the ID the grouping has been made such that for every PMT, its neighbour PMTs belong to the opposite board. In this way the two ID boards trigger independently on the same volume, allowing cross-monitoring. The FEE processes the sum of the signal of groups of either 16 ID PMTs, or 3 to 6 IV PMTs. The amplitude of that signal is proportional to the total integrated charge of the group. A positive trigger is sent to the master board if a certain threshold is passed by a minimum amount of groups in a given board. This threshold corresponds to a charge equivalent to $\sim 350\,\mathrm{keV}$ for an ID group, and $\sim 10\,\mathrm{MeV}$ for an IV group. Both the ID and IV channels are read out in case any of the two sub-detectors create a trigger. This enables to tag background events entering the ID from outside, as they often also deposit energy in the IV. When the master board receives the decisions of the trigger boards (an 8-bits word), it allows the FADCs storing the event in their internal memory. The master board also distributes a 62.5 MHz clock signal to all the FADCs for synchronization. Each stored events is then read by read out processors and transferred to the event builder, which create binary files ready to be processed offline.

2.3 Event reconstruction

The processing of recorded events is handled by the dedicated Double Chooz Offline Group Software (DOGS). DOGS is a software framework that has external dependencies on ROOT[54] (data analysis) [177], GEANT4[55] (physics simulation) [178, 179], and MySQL[56] (database management) [180].

After the event building operated by the local machines, recorded events are arranged in runs - typically corresponding to 1 hour of data taking - and formatted as binary files. These files are sent with little manipulation to the CC-IN2P3[57] computing cluster and storage system, in which all offline operations are made. These *raw* files are then converted in ROOT files including triggers, run and data taking conditions in what

---

[54] An object-oriented data analysis framework, developed by CERN.

[55] GEometry ANd Tracking, developed by CERN.

[56] Structured Query Language, an open source relational database management system.

[57] Computing centre of the IN2P3, or Institute National de Physique de Particules et de Physique Nucleaire, hosted in Lyon.

is called DOGSification process. During the Double Chooz one-detector phase the DOGSified files used to include the waveforms for all recorded events and the reconstruction of channel pulses was done in a further step. Due to the increased amount of data coming from two detectors, the pulse reconstruction is now integrated in the DOGSification and only a small amount of waveforms is kept. For the Monte Carlo (MC) simulation, specific *raw* files are produced and processed in a similar way.
The bulk of the analysis is performed in the so-called Common Trunk (CT), which processes DOGSified files and produces other ROOT files, the CT ones. In this second-level event processing various algorithms are applied for different tasks, including the vertex reconstruction, muon tracking, the ortho-positronium characterization, and background-reducing algorithms. At this stage, calibration data of the IDLI and IVLI serve also as input, providing the PMT gains (PMT current amplifications) μ and time offsets (transit times) t_0.
Finally, the energy reconstruction is performed in a further data processing step, the ROOT Light Trees (LT) production. To reconstruct each event, energy calibration from deployed sources and energetic peaks are used.

While a schematic representation of the whole process is shown in figure 24, a description of some of the reconstruction algorithms is given in the rest of this section (see also Ref. [157, Section IV] or [160, Section 3]).

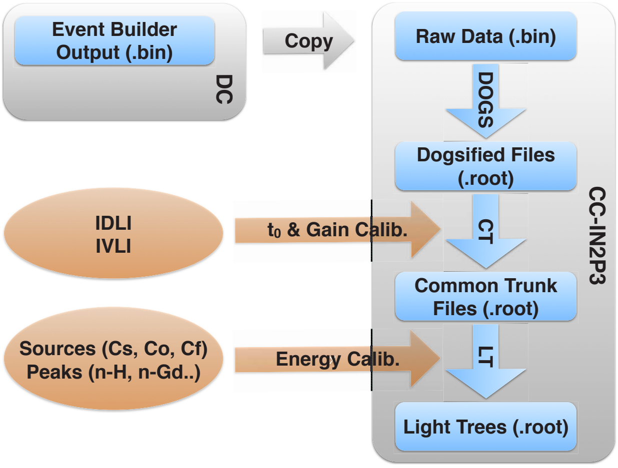

Figure 24: Diagram showing the data processing of recorded events in Double Chooz. Data processing steps are featured in blue and the operation platforms in grey, while calibration inputs are represented in orange.

2.3.1 Pulse reconstruction

The first step in the characterization of an event is the calculation of starting times and integrated charges of PMT waveform pulses. This is the purpose of the dedicated DCRecoPulse algorithm.

For each channel, DCRecoPulse estimates the integrated charge q by integrating the waveform over a 112 ns sub-window and subtracting the mean baseline B_{mean}. The integrating window starting point is chosen so that q is maximal. B_{mean} and its root mean square B_{RMS} are evaluated channel-by-channel for a given run with periodic 1 Hz triggers. For events depositing up to a few MeV (like the typical prompt and delayed signals) the majority of PMTs collects one photoelectron (p.e.), corresponding to a pulse amplitude of $\sim$ 6 ADC counts. Once values of q are calculated, the number of p.e. are retrieved for the energy reconstruction using the gains μ, which are calculated during IDLI and IVLI calibrations

$$N_{pe} = q/\mu \tag{50}$$

In order to avoid any contribution arising from baseline fluctuations, only pulses with a maximum bin with more than 2 ADC and with

$$q - B_{mean} \geq B_{rms}\sqrt{N_S}\,, \tag{51}$$

where N_S is the number of integrated waveform samples[58], are considered.

DCRecoPulse is also used to evaluate the starting time of each pulse, which is assumed to be the time where the pulse reaches 20% of its maximal amplitude. It is then corrected for the PMT offset obtained from IDLI and IVLI calibrations. An alternative pulse starting time measurement is given by the DCRecoTimePulse algorithm with a fit on the waveform shape. This method is used to implement pulse shapes in Double Chooz; it will be described in the dedicated section 4.1.2.

2.3.2 Vertex reconstruction

Pulses integrated charges and starting times are used to evaluate the event vertex. The RecoBAMA algorithm[59] uses a likelihood approach to retrieve the event position basing on the prediction of the detector optical model, assuming a point-like isotropic source.

---

[58] N_S = 56, i.e. 112 ns divided by the 2 ns sampling.

[59] In Double Chooz vertex reconstructing algorithms peculiarly owe their name to the place where they are developed. RecoBAMA was developed in the University of Alabama.

For a given set of variables $\mathbf{X} = (\mathbf{x}_0, t_0, \phi)$ - which includes not only the vertex position $\mathbf{x}_0$, but also the event time t_0 and the light intensity per unit solid angle ϕ (photons/sr) - the expected amount of charge q_i^{th} collected by a PMT i located at a distance r_i from $\mathbf{x}_0$ is given by

$$q_i^{th} = \frac{\epsilon_i}{\mu_i}\phi_i\Omega_i((\mathbf{x}_0)e^{-r_i/\lambda}\,, \tag{52}$$

where ϵ and Ω are the quantum efficiency and angular coverage of the PMT, which depends on the event position, and λ the characteristic attenuation length of the scintillator. The expected arrival time t_i^{th} of the light collected by the same PMT i is given by

$$t_i^{th} = t_0 + \frac{r_i}{c_n}\,, \tag{53}$$

where c_n is the speed of light in the scintillator medium[60].

For each set of $\mathbf{X}$, the predicted charges q_i^{th} and starting times t_i^{th} are compared with the respective reconstructed q_i and t_i to find the best-likelihood vertex. The likelihood function is defined as

$$L(\mathbf{X}) = \prod_{q_i=0} f_q(0, q_i^{th}) \prod_{q_i>0} f_q(q_i, q_i^{th}) f_t(t_i, t_i^{th}, q_i^{th})\,, \tag{54}$$

where f_q and f_t are the charge and time probability functions, representing the probability to observe a charge q_i and a time t_i when expecting q_i^{th} and t_i^{th}, and are obtained from Monte Carlo simulations and calibration with laser source. The first part of equation 54 accounts for PMT not recording a pulse in the event 256 ns window. The event vertex is obtained by maximising $L(\mathbf{X})$ or, equivalently, minimizing its inverse logarithm

$$\mathrm{FuncV} = -\ln L(\mathbf{X}) = -\sum_i \ln f_q(q_i, q_i^{th}) - \sum_i \ln f_t(t_i, t_i^{th})\,. \tag{55}$$

2.3.3 Energy reconstruction

In Double Chooz, the measurement of θ_{13} relies on rate and energy spectrum comparison between observed and non-oscillating expected $\bar{\nu}_e$, with the latter given by MC simulations or, in the future, by near detector data. A thorough understanding of the detector energy response is therefore crucial for its physics goal. The event energy reconstruction has seen major improvement through the Double Chooz history. In our first publication n-Gd [108] the energy was obtained from the charge using a scaling factor and then corrected for space and time dependencies using data-MC

---

[60] 0.299792458 cm/ns divided by the refraction index $n = 1.53$.

comparison of calibration data. The latest n-Gd publication [160], on the other hand, uses a step-by-step construction of the event visible energy E_{vis} using multiple scaling/correction factors. In particular, E_{vis} is given in polar detector coordinates by

$$E_{vis} = N_{pe}^{tot}(\rho, z, t) \times f_u(\rho, z) \times f_{MeV} \times f_s(E_{vis}^0, t) \tag{56}$$

for data and

$$E_{vis} = N_{pe}^{tot}(\rho, z, t) \times f_u(\rho, z) \times f_{MeV} \times f_{nl}(E_{vis}^0) \tag{57}$$

for Monte Carlo, where N_{pe}^{tot} is the global number of photoelectrons, f_u a space uniformity correction, f_{MeV} the p.e.-to-MeV energy scaling, f_s the time stability correction (applied on data only) and f_{nl} the time non-linearity correction (applied for MC only).

Linearised p.e. calibration

The number of photoelectrons is obtained from the sum over contributions of all channels, i.e. by

$$N_{pe}^{tot} = \sum_i \frac{q_i}{\mu_i(q_i, t)} . \tag{58}$$

The time variation and non-linearity of the gains μ_i, with the latter originating by the baseline sampling and affecting especially low charges, are obtained for each channel from IDLI (or IVLI for the IV) calibrations.

Uniformity correction

The uniformity correction accounts for the variation of the detector response with the event position. It consists of a 2D map which converts the total number of p.e. of an event in a given location (ρ, z) in the IT or GC to the corresponding value as the event was in the centre of the target $(\rho = z = 0)$. The 2D maps for data and MC, shown in figure 25, are obtained by fitting the energy peak given by captures on hydrogen of spallation neutrons, which are simulated for the MC. An energy uniformity within 5% is observed for the data in the IT, and the data-MC point-to-point variation used to evaluate the associated systematics.

Absolute energy scaling

The absolute conversion factor between p.e. and MeV is estimated again from the energy peak of neutron captures on H, but using neutrons from a ^{252}Cf source de-

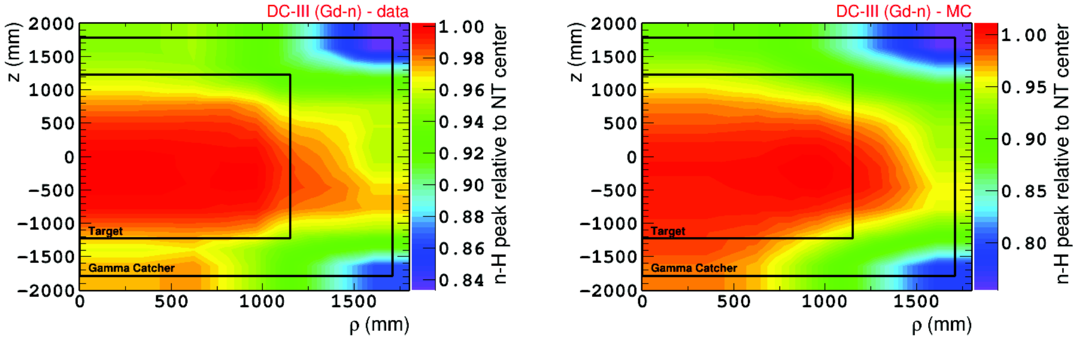

Figure 25: Maps of the uniformity correction for data (left) and MC (right), from [160].

ployed at the centre of the target ($1/f_{\mathrm{MeV}}$ = 186.2 p.e./MeV for data and $1/f_{\mathrm{MeV}}$ = 186.6 p.e./MeV for MC).

Stability correction

The stability correction factor accounts for time fluctuation of the channels mean μ and for residual detector response time variations. It is measured at various energies using spallation neutrons captured on Gd (8 MeV) and H (2.22 MeV), as well as ^{212}Po α decays from ^{212}Bi–^{212}Po coincidences (1 MeV visible energy after quenching). First, the mean μ is obtained imposing the PMT multiplicity (number of PMT recording a pulse) to be equal to the p.e. number. The gain fluctuation is then evaluated using neutrons captured on H and its energy dependence using neutrons captured on Gd and the ^{212}Po α emitter. Residual effects observed in the n-H peak are assumed to be due to detector response variations and are further corrected. The systematic uncertainty associated with the time stability correction was estimated from lingering variations after correction, rescaled to the full prompt energy range.

Non-linearity correction

The non-linearity correction factor (first introduced in Ref. [160]) represents energy dependent discrepancies between data and MC. It consists of two terms: the charge non-linearity (applied to data) and light non-linearity (applied to MC and only in the n-Gd analysis).

The charge non-linearity is associated with the readout modelling and the charge integration and is applied to all events. It is estimated as the discrepancy in the energy response between ^{252}Cf-emitted neutron capture on Gd and H, for which the single-gamma energy is similar[61].

The remaining non-linearity effect due to scintillator modelling is studied generating sets of MC simulations with different Birks' quenching parameters and light yields, varied within their experimental uncertainties, and comparing with the nominal set to extract a correction factor and systematics. This light non-linearity effect is particle dependent and is studied and applied only on positrons (prompt) events in the n-Gd analysis. It is conversely left as a free parameter for the energy shape fit in the n-H analysis.

The final visible energy and the resolution for different sources at different energies is shown in figure 26 as a comparison between data and MC, which are consistent. The resolution (σ) is fitted with a function of the statistical fluctuation (a), a constant term (b), and a noise (c), as

$$\frac{\sigma}{E_{vis}} = \sqrt{\frac{a^2}{E_{vis}} + b^2 + \frac{c^2}{E_{vis}^2}}. \tag{59}$$

The best fit values published in Ref. [160] are $a = 0.077 \pm 0.002\,\mathrm{MeV}^{1/2}$, $b = 0.018 \pm 0.001$ and $c = 0.017 \pm 0.011\,\mathrm{MeV}$ for data, while the same values are obtained for MC excepted $c = 0.024 \pm 0.006\,\mathrm{MeV}$.

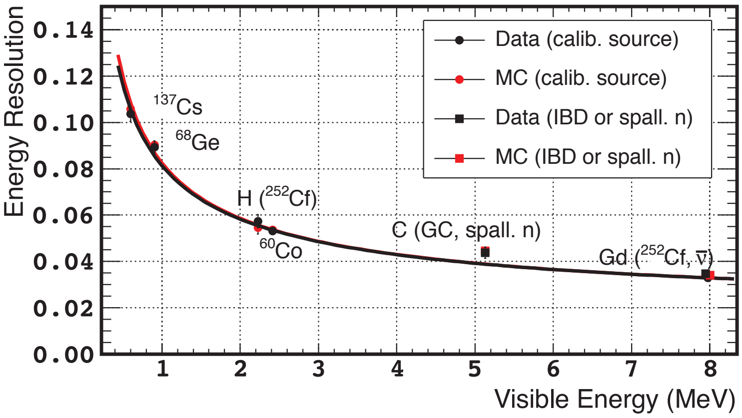

Figure 26: Data-MC comparison of the visible energy resolution from [160]. The values measured with different energy peaks are fitted with the fit function of equation 59.

---

[61] Although 8 MeV are released in the neutron capture on Gd, the single γ has an average energy of $\sim 2.2\,\mathrm{MeV}$.

2.3.4 Muon track reconstruction

The identification and tracking of muons is used in Double Chooz to characterize cosmogenic $\beta - n$ emitters, which are the main source of background in the n-Gd analysis (see section 3.3). Muon tracking algorithms rely on patterns of PMT hits in the ID and IV, as well as on the OV signal (see Ref. [181]).

3 Measuring θ_{13} with the Double Chooz far detector

Contents

The Double Chooz results published so far rely on data coming from the far detector only. In such condition, the oscillation analysis is performed by comparing the estimated non-oscillating spectrum of $\bar{\nu}_e$ with the prompt E_{vis} IBD spectrum observed in the far detector. The mixing angle θ_{13} is measured by fitting the distortion of the observed spectrum, or the rate deviation, from the non-oscillating one.

In this chapter we will describe the Double Chooz θ_{13} analysis. After discussing the flux estimation process, we will focus on the selection of IBD candidates. The main backgrounds and systematic errors are also discussed, before getting to the final analyses for the measurement of θ_{13}.

3.1 Neutrino flux prediction

The build-up of the expected non-oscillating IBD spectrum consists in a simulation of the reactor conditions, a study of the physics of the reactions and the replication of the detector response to $\bar{\nu}_e$ interactions (see Ref. [160, Section 2] for further details). The predicted number of $\bar{\nu}_e$ produced in the two reactors R and detected in absence of oscillation is parametrized as

$$N_{\nu}^{exp}(E,t) = \sum_{R=1,2} \frac{N_p \epsilon}{4\pi L_R^2} \times \frac{P_{th,R}(t)}{\langle E_f \rangle_R(t)} \times \langle \sigma_f \rangle (E,t)\,. \tag{60}$$

The first term of equation 60 is a normalization factor given by the number of proton in the detector target N_p, the detection efficiency ϵ, and divided by the solid angle $4\pi L_R^2$, where L_R is the baseline. The second member represents the number of fissions, as it comes from the reactor thermal power $P_{th,R}$ divided by the mean energy released per fission $\langle E_f \rangle_R$, and it varies with time basing on the fuel composition. Finally, the last term of equation 60 represents the cross-section weighted to the total flux, of which each component is normalized for a given fissile.

Reactor simulation

$\bar{\nu}_e$ are produced in β-decays of unstable secondary fragments generated in the fission of the main fuels. At the beginning of a cycle, the fuel consists in enriched uranium, 99.99% of which being ^{235}U and ^{238}U[62]. As the ^{235}U burns in fission chains, ^{238}U captures neutrons producing the two other plutonium fissiles ^{239}Pu and ^{241}Pu [182]. The evolution of the fuel composition, or burn-up, is accurately simulated in Double Chooz using a Monte Carlo based on a combination of the MURE [183] and DRAGON [184] codes. With informations on the reactor geometry, fuel positions and replacements as inputs, a daily-sampled burn-up is calculated. The time evolution of fission rate fractions α_k of fissiles k (with $k = {}^{235}\text{U}, {}^{238}\text{U}, {}^{239}\text{Pu}, {}^{241}\text{Pu}$) is shown in figure 27a. The accuracy of the simulation is estimated by varying input parameters and by comparing the two codes, and has an impact on the systematic uncertainties of $\sim 0.8\%$.

The thermal power of each of the two reactors is provided regularly by EDF with time intervals of $\sim 30\,\text{s}$ and a $1\,\sigma$ precision of $\sim 0.5\%$, and is shown in figure 27b. The average energy released per fission depends on the fissile fission fractions α_k

---

[62] Natural uranium have $\sim 0.7\%$ of the ^{235}U isotope, while such component typically reaches 5% in enriched uranium.

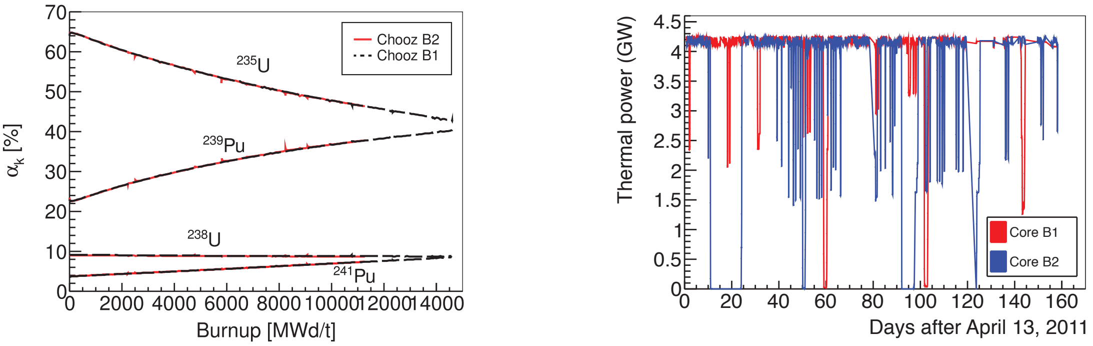

(a) Simulated fission fractions time evolution. The initial rate of ^{235}U decreases during the burn-up and Pu rates increase, until the two components decay at equal rate.

(b) Time variation of the thermal power of the two Chooz cores. Provided by EDF.

Figure 27: Time evolution of the fissile fractions and thermal power of the Chooz cores.

Isotope	$\langle E_f \rangle_k$ (MeV)	$\langle N_{\bar{\nu}_e} \rangle$	$\langle E_{\bar{\nu}_e} \rangle$ (MeV)
^{235}U	201.92 ± 0.46	1.92	5.226 ± 0.051
^{238}U	209.99 ± 0.60	2.38	7.040 ± 0.326
^{239}Pu	205.52 ± 0.96	1.45	3.799 ± 0.033
^{241}Pu	213.60 ± 0.65	1.83	4.956 ± 0.049

Table 1: Neutrino production associated with the four main fissiles. For each fissile the average released energy $\langle E_f \rangle_k$, the average number of neutrinos $\langle N_{\bar{\nu}_e} \rangle$ and their average energies $\langle E_{\bar{\nu}_e} \rangle$ are shown.

and the average energy released per fissile $\langle E_f \rangle_k$

$$\langle E_f \rangle = \sum_k \alpha_k \langle E_f \rangle_k \, . \tag{61}$$

$\langle E_f \rangle_k$ values for the four main fissiles, along with informations on produced neutrinos, are shown in table 1.

Flux estimation

The flux-normalized cross-section per fission $\langle \sigma_f \rangle$ can be similarly expressed as

$$\langle \sigma_f \rangle = \sum_k \alpha_k \langle \sigma_f \rangle_k \, , \tag{62}$$

where $\langle\sigma_f\rangle_k$ is now the flux-normalized cross-section per fissile k. If we consider the whole energetic spectrum, for a given fissile k, $\langle\sigma_f\rangle_k$ is given by the convolution of the IBD cross section σ_{IBD} and the neutrino spectrum S_k, i.e.

$$\langle\sigma_f\rangle_k = \int dE\, S_k(E)\sigma_{IBD}(E)\,, \tag{63}$$

where σ_{IBD} is retrieved analytically from [185].

For what concerns S_k values, ^{235}U, ^{239}Pu and ^{241}Pu neutrino spectra are deduced from their respective β spectra measured at ILL and normalized to each fission [186–188]. ^{238}U neutrino spectrum is instead calculated with a method described in Ref. [149, 189]. The uncertainties on $S_k(E)$ are energy dependent and of the order of 3%.

Instead of directly measuring $\langle\sigma_f\rangle_k$, an anchoring to the value measured by the Bugey-4 experiment is used [190], with a correction for the different fuel composition of the Bugey-4 reactor

$$\langle\sigma_f\rangle = \langle\sigma_f\rangle^{Bugey} + \sum_k(\alpha_k - \alpha_k^{Bugey})\langle\sigma_f\rangle_k \tag{64}$$

The positive impact of this method on the systematics is mentioned in section 3.4.1.

Detector response simulation.

The electronics and PMT response of Double Chooz is modeled with a dedicated DOGS package, the Readout System Simulation (RoSS), which produces MC files of the same structure used for data. The detector geometry is implemented in the Geant4 enhanced package DCGLG4sim [191], which handles the detector simulation.

3.2 IBD selection

In section 2.2 we discussed the functioning of the Double Chooz far detector, covering all steps that intercurr between an energy deposition in the liquid scintillator and the full reconstruction of the event, with trigger time, visible energy E_{vis}, and spatial vertex. The principle of IBD (equation 45) identification relies in the search of a coincidence between a prompt and a delayed signal, with the prompt given by the positron scintillation and annihilation, and the delayed by the neutron capture (see paragraph 2.1.2). We can summarize the process that leads from individual triggers to IBD candidates in three steps:

1. single events are required to be *valid triggers* for the IBD selection;
2. then a coincidence of two *valid triggers* with certain conditions is required in order to identify IBDs candidates among all possible events;
3. finally vetoes are applied to remove the remaining background.

Background vetoes are used, along with specific analyses, to characterize the different backgrounds, whose rates and energy shapes are used as imput for the θ_{13} fit.

3.2.1 Single events selection

IBD interactions contribute only for a small fraction of recorded events (of the order of 10^{-9} for the far detector), with the main sources of triggers given by natural radioactivity, cosmic muons, and the so-called light noise, i.e. spontaneous flashes of the PMT bases. The identification of *valid triggers* for the IBD candidates selection aims to significantly reduce the contribution of light noise and muon induced events. To be a *valid trigger*, a single event must:

- have $E_{vis} > 0.4\,\mathrm{MeV}$;
- not be identified as a μ;
- not be recorded in a 1 ms (1.25 ms) after-μ time window in the n-Gd (n-H) analysis;
- not be identified as a light noise event.

The first condition ensures a 100% trigger efficiency on *valid triggers*. μ and light noise events are identified using specific conditions. *Valid triggers* energy spectrum before and after light noise reduction is shown in figure 28.

Light noise

A PMT base can occasionally experience spontaneous discharges in a light flash that is detected by neighbour PMTs after reflection on the buffer tank surface. This light noise (LN), or dark noise, is a background observed in many experiments that make use of photomultipliers. It can be identified basing on the peculiar topology of the distribution of collected charges and times of the PMTs [192, Chapter 4]. The main variables used to discriminate light noise are the ratio between the maximum charge collected by a single PMT and the total one, i.e. q_{max}/q_{tot}, and the RMS of the

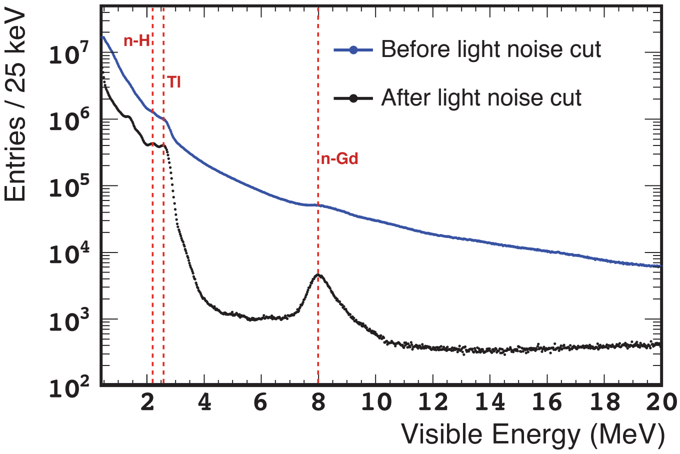

Figure 28: Visible energy of single events before (blue) and after (black) the light noise cuts are applied. Energy peaks for neutron capture on Gd and H, as well as ^{208}Tl γ *decay, are highlighted (red dashed lines). From [160].*

distribution of the recorded pulse times t_{RMS}. A more sophisticated LN rejection (first introduced in Ref. [160]) makes also use of the PMT charge distribution RMS q_{RMS} and of q_{dev}, which is defined as the relative variance of charges q_i collected by PMTs i within 1 m from the one that collected the q_{max}. An event that satisfies the conditions

$$\begin{aligned} q_{max}/q_{tot} &< 0.12 \\ q_{dev} \equiv \frac{1}{N}\sum_i^N \frac{(q_{max}-q_i)^2}{q_i} &< 30000\,\mathrm{DUQ} \\ t_{RMS} < 36 \quad \text{or} \quad q_{RMS} &< 464 - 8t_{RMS}\,. \end{aligned} \tag{65}$$

is kept, otherwise it is identified as LN [157, Section D]. Charges are measured in integrated ADC counts, or DUQ (100 DUQ $\sim$ 1 p.e.).

Muons

A μ is identified basing on the large amount of energy that releases when crossing the IV and/or the IT. In the IV an energy calibration of the same precision of the one used in the IT is not possible (see section 2.2.1). For this reason, while the reconstructed E_{vis} is used in the IT, for the IV we consider the total charge collected by IV PMTs, i.e.

q^{IV}_{tot}. An event is defined as a μ if at least one of these two conditions is satisfied

$$\begin{aligned} E_{vis} &> 20\,\text{MeV} \\ q^{IV}_{tot} &> 30000\,\text{DUQ}\,, \end{aligned} \tag{66}$$

with 30000 DUQ corresponding approximately to 16 MeV in the IV.

3.2.2 IBD candidates

The IBD candidate selection is based on requiring a coincidence between two *valid triggers* corresponding to the prompt positron scintillation and annihilation and the delayed neutron capture. Such coincidence strongly suppresses the natural radioactivity contribution. The criteria on which the IBD selection is based are:

- a prompt energy window;
- a delayed energy window;
- a prompt-delayed correlation time Δt;
- a prompt-delayed correlation distance ΔR;
- an isolation time window around the prompt.

Double Chooz measures θ_{13} using two different analysis samples, basing on the neutron capture reaction taken into account:

- the gadolinium analysis, or n-Gd, which considers IBD with neutron captured on Gd and the IT as target, since only the IT scintillator is doped with Gd;
- the hydrogen analysis, or n-H, which considers instead IBD with neutron captured on hydrogen and the whole of IT and GC as target.

Given the Gd higher neutron capture cross-section, only 13% of IBD neutrons are captured by hydrogen in the IT. As a consequence, the n-H data sample has 95% of delayed signals located in the GC. The n-Gd and n-H analyses have identical IBD selection criteria but different conditions because of the different target volumes, as well as the different neutron capture lifetime and released energy of Gd and H, which are resumed in table 2. Energetic peaks of neutron captures on H and Gd are also visible among single events in figure 28.

	^{157}Gd	^{1}H
Cross-section	259 kb	0.33 b
Lifetime	30 μs	200 μs
Released energy	8 MeV	2.22 MeV
$\langle N_\gamma \rangle$	~ 3	1

Table 2: Physical properties of neutron capture by gadolinium and hydrogen, as measured in Ref. [193].

Prompt energy window

The IBD rate, as represented by the energy spectrum of $\bar{\nu}_e$ interacting via IBD, drops below 1 MeV and above 8 MeV (figure 18). However, using a larger prompt energy window in the IBD selection gives some advantages in the θ_{13} measurement. Indeed, the oscillation probability is higher at low neutrino energies (peaking at $E_{vis} \sim 1$ MeV), making that region more significant for the oscillation analysis. Moreover, energies higher than 8 MeV are dominated by the correlated background (see section 3.3.2) making that energy region crucial for the characterization of such background and for the final fit that determines the background rates along with θ_{13}.

Delayed energy window

The delayed signal is given by the neutron capture and the signal window is therefore tuned on the energetic peak of the interaction (table 2). An extended lower limit of the energy window can include events for which part of the energy is not reconstructed (as for escaping n-Gd γ rays), but introduce also a background component due to accidental coincidences (see section 3.3.3). In the n-H analysis the accidental contribution becomes dominant given the lower neutron capture released energy.

Correlation time

The time correlation between prompt and delayed signals, Δt, depends as well on the capturing nucleus and therefore varies basing on the chosen sample. The presence of a lower boundary on the Δt IBD window serves to avoid the contamination of the stopping muons background, which will be described in section 3.3.2. Moreover, an upper limit is necessary to avoid an excess of accidental coincidences and to suppress systematic uncertainties associated with the spill-in spill-out effect (described in section 3.4.2), while the induced inefficiency can be kept as negligible.

	n-Gd	n-H
Prompt E_{vis}	$[0.5, 20]$ MeV	$[1, 20]$ MeV
Delayed E_{vis}	$[4, 10]$ MeV	$[1.3, 3]$ MeV
Correlation time Δt	$[0.5, 150]$ μs	$[0.5, 800]$ μs
Correlation distance ΔR	< 1 m	< 1.2 m
Isolation window (before prompt)	$[-200, 0]$ μs	$[-800, 0]$ μs
Isolation window (after prompt)	$[0.5, 600]$ μs	$[0.5, 900]$ μs

Table 3: IBD candidate selection criteria for the n-Gd and n-H analyses.

Correlation distance

A selection on the prompt-delayed vertices distance ΔR was introduced in the latest candidate selection [160] to help suppressing the accidental background. This allowed to relax other IBD selection conditions with an overall positive effect on the signal-on-background ratio. With respect to the n-Gd, the n-H analysis uses a more relaxed condition for the longer neutron capture lifetime.

Isolation window

Finally an isolation window around the prompt allows reducing the contribution of correlated background. Such selection requires that no valid trigger is recorded within a time interval before the prompt, and that no signal excepted the delayed one is recorded in a time window following the prompt.

The latest Double Chooz analysis [160] has shown major improvements in the background rejection with respect to previous results [157, 158], allowing for a safely widening of most of the cuts. In addition, the n-H selection has seen a dramatic background reduction, especially in its accidental component, which is crucial in the n-H analysis. This was made possible thanks to a newly-developed multi-variable neural network cut, and a veto based on pulse shapes (see below). Consequently the IBD selection was widened, simultaneously improving the signal-on-background ratio. The improved IBD selection for the n-H analysis is used in the upcoming dedicated publication, and is summarized, together with the one of the latest n-Gd analysis [160], in table 3.

3.2.3 Background vetoes

The inner veto (IV) and outer veto (OV) described in section 2.2.1 are used in combination with analysis tools to reduce backgrounds. Background vetoes are applied along with the IBD selection, leading to the final IBD candidates. A summary of vetoes applied to the n-Gd and n-H analyses is given in table 4. Here we briefly describe the various veto. The associated deadtimes and inefficiencies are treated as a correction factor for the MC, and the uncertainties as part of the systematics, as we will discuss in section 3.4.

Inner veto tagging

The IV identifies events originating outside the inner detector by using information from:

- the number of IV PMTs recording a pulse, or PMT multiplicity, N_{PMT}
- the total charge collected by those PMTs q_{tot}^{IV};
- the reconstructed event time t_{IV} and vertex $\mathbf{x}_{IV}$.

The IV vertex reconstruction algorithm used for t_{IV} and $\mathbf{x}_{IV}$ is based on a neural network approach.
Since one (or more) high energetic γ released in the neutron capture on Gd can exit the ID and interact in the IV, this veto is only applied on prompt signals in the n-Gd analysis.

Outer veto tagging

The OV is used to remove events generated by down-going muons that are tagged by its plastic scintillators array. The chimney - which is used to deploy calibration source - is a critical spot for cosmic muons. The coverage of that area by the OV has been improved by the installation of the upper OV, a smaller and uplifted part that covers the area around the chimney. The OV is used in a simple veto way by removing events for which the prompt is in time coincidence with an OV trigger. This allows removing muon-induced events while the inefficiency due to the induced deadtime is kept below 0.1%.

Goodness of the vertex

The functional value, or FuncV, was defined in equation 55 as the negative logarithm of the likelihood function used for vertex reconstruction. FuncV characterizes the goodness of the vertex reconstruction algorithm for a given event. An event that does not satisfy the conditions on which the vertex reconstruction is based, i.e. a point-like source of isotropic light, results in a large FuncV value. Such is the case for stopping muons, as first pointed out by a pulse shape analysis (see section 4.2), and also for accidental coincidences with light noise events, making possible to remove these events with a FuncV cut.

^{9}Li+^{8}He likelihood

A likelihood function is used as a tool to identify cosmogenic background from ^{9}Li and ^{8}He. The probability density functions (PDF) are obtained from another cosmogenic emitter, the ^{12}B, which produces similar results and is available with higher statistics. The parameters used for the PDF building are:

- the lateral distance between the parent muons track and the daughter event vertex;
- the number of neutrons created along with the daughter event in a 1 ms window after the parent μ.

Artificial neural network

The artificial neural network (ANN) is a new technique developed to deal with the accidental background in n-H analysis. Instead of use harder selection criteria on ΔR, Δt and the delayed E_{vis}, with the inevitable signal loss, these three variables are considered together in a multi-variable approach. This was done with a multilayer perception neural network, based on the TMVA package in ROOT. The neural network was first trained on MC simulation before being applied on data.

Pulse shape selection

The multiple pulse shape (MPS) cut identifies fast neutrons thanks to the pulse shape distortion induced by the overlapping of a proton recoil with the neutron capture in the same trigger window. A detailed description of the cut is given in section 4.5, in the pulse shape analysis chapter.

	n-Gd	n-H
IV cut	$N_{PMT} \geq 2$ $q_{tot}^{IV} > 400$ DUQ $\lvert\mathbf{x}_{ID} - \mathbf{x}_{IV}\rvert < 3.7$ m $t_{ID} - t_{IV} \in [-110, -10]$ ns	$N_{PMT} \geq 2$ $q_{tot}^{IV} > 400$ DUQ $\lvert\mathbf{x}_{ID} - \mathbf{x}_{IV}\rvert < 4$ m $t_{ID} - t_{IV} \in [-110, -20]$ ns
OV cut	no OV-coincidence	
FuncV cut	$E_{vis} < 0.068\, e^{FuncV/1.23}$	$E_{vis} < 0.2755\, e^{FuncV/2.0125}$
^{9}Li + ^{8}Helikelihood	^{9}Li – likelihood > 0.4	
ANN	–	ANN < –0.23
MPS cut	–	see table 19

Table 4: Background vetoes for the n-Gd and n-H analyses. The FuncV cut is applied only on the delayed signal, while the IV cut is applied only on prompt signal for n-Gd and on prompt and delayed signals for n-H. IBD candidates that satisfy the conditions required by one of the vetoes are removed. See the text for details.

3.3 Backgrounds

The IBD selection described in the previous section strongly reduces the initial event rate. Background events that can mimic the prompt-delay coincidence of an IBD and pass the candidates selection are rejected using suitably developed vetoes. However, there is a residual component of background contamination in the IBD candidate sample. We distinguish three categories:

- cosmogenic background;
- correlated background;
- accidental coincidences.

The residual fraction of each of these categories is estimated, along with its spectral shape information, and used in the final fit for the determination of θ_{13}. The estimated background rates are resumed in table 5.

Background	Rate in n-Gd (day^{-}1)	Rate in n-H (day^{-}1)
^{9}Li–^{8}He	$0.97^{+0.41}_{-0.16}$	$0.95^{+0.57}_{-0.33}$
Correlated	0.604 ± 0.051	1.55 ± 0.15
Accidental	0.070 ± 0.003	4.334 ± 0.011

Table 5: Estimated rates of main backgrounds after full IBD selection with vetoes.

Isotope	Decay Mode	Decay Energy	Daughter
^{9}Li	β^{-}– *n* (50.8%)	11.94 MeV	2×^{4}He
	β^{-} (49.0%)	13.61 MeV	^{9}Be
^{8}He	β^{-} (83.0%)	10.65 MeV	^{8}Li
	β^{-}– *n* (16.0%)	8.62 MeV	^{7}Li
	β^{-}– *n* (0.9%)		^{3}H+^{4}He

Table 6: Main decay modes of ^{9}Li and ^{8}He, as obtained from Ref. [194]. β^{-}– n decays are responsible for the cosmogenic background.

3.3.1 Cosmogenic background

Cosmogenic background consists in long-lived β-*n* decaying isotopes, such as ^{9}Li or ^{8}He. They are produced by cosmic muons spallation on ^{12}C, which is abundant in the organic molecules that form the Double Chooz liquids. Such isotopes easily survive the muon isolation window (1 ms) given their long lifetime, which is of the order of hundreds of milliseconds (257 ms for ^{9}Li, 171 ms for ^{8}He). The β-*n* decay is under all detection aspects identical to an IBD interaction, and the released energy is comparable with the prompt energy window, making impossible the rejection of those events basing on their topology. The decay modes of ^{9}Li and ^{8}He are listed in table 6. Contributions from daughter atoms or recoil protons to the promot signal energy, although quenched, are also possible.

The ^{9}Li and ^{8}He contributions are reduced by the application of the ^{9}Li-likelihood to the IBD selection, which was introduced in the last n-Gd publication [160]. The remaining component rate and shape, shown in figure 29, is estimated using the correlation with the parental μ and given as input of the final fit. In particular, the correlation time between a high energy μ and any IBD event recorded in a 80 cm cylinder along the reconstructed track is fitted to evaluate the cosmogenic background rate (figure 29a), which is then corrected for the selection inefficiency. For what concerns the background shape, with the introduction of the ^{9}Li-likelihood it is possible to measure it directly on selected events (figure 29b), while it was simulated before [157].

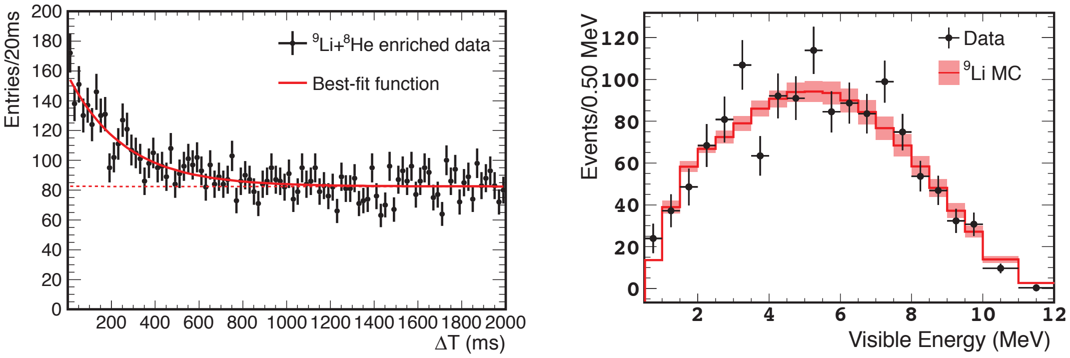

(a) Δt from last μ distribution of a cosmogenic background enriched sample. The fit (red curve) includes a flat component of μ accidental coincidences (dashed line).

(b) Energy spectrum of cosmogenic background prompt signal, for data (black points) and for MC normalized to data (red line).

Figure 29: Characterization of the cosmogenic background, from [160].

3.3.2 Correlated background

For correlated background we mean muon-induced processes that produce a prompt-delayed coincidence. In Double Chooz this includes fast spallation neutrons and muons stopping and decaying in the chimney.

Fast neutrons

Fast spallation neutrons are produced by cosmic μ in the surrounding rock and thermalize in the detector before being captured. The neutron thermalization consists in energy loss via multiple scattering on the nuclei of the material. For a neutron of energy E_n scattering on a nucleus of atomic number A, the average energy loss per collision is

$$2E_n\frac{A}{(A+1)^2}\,, \tag{67}$$

meaning that for light nuclei the energy loss is higher ($E_n/2$ for H) and the thermalization requires a small number of collisions (which is usually of the order of 10^1). In case of scattering on hydrogen nuclei, abundant in the scintillator organic compounds, the resulting recoil protons loose their kinetic energy ionizing the scintillator. Although protons are strongly quenched due to their mass, the energy released by one or more protons may be sufficient to be detected as a prompt signal, with the following neutron capture providing the delayed signal to fake an IBD.

The prompt energy shape is estimated on a fast neutron sample selected by applying an IV-based tag that is similar to the IV cut described before (section 3.2.3). This selection is applied on a sample of IBDs extended at higher energies to include a region in which the correlated background dominates. Once the shape is assessed, the rate for all correlated background is estimated by calculating the selection efficiency for events in a $E_{vis} > 20$ MeV region, and rescaling the rate estimated in the prompt energy window accordingly. Figure 30 shows the estimated shapes for the n-Gd (figure 30a) and n-H (figure 30b) analyses. The extended energy window used in the two cases differs, and so does also the estimated energy shape of correlated background: flat for n-Gd, exponential for n-H. A similar method based on OV tagging was also used as a cross-check in the n-H analysis, which give similar results (see figure 30b). The parameters of the shape fit and the estimated rate are given as inputs for the final fit.

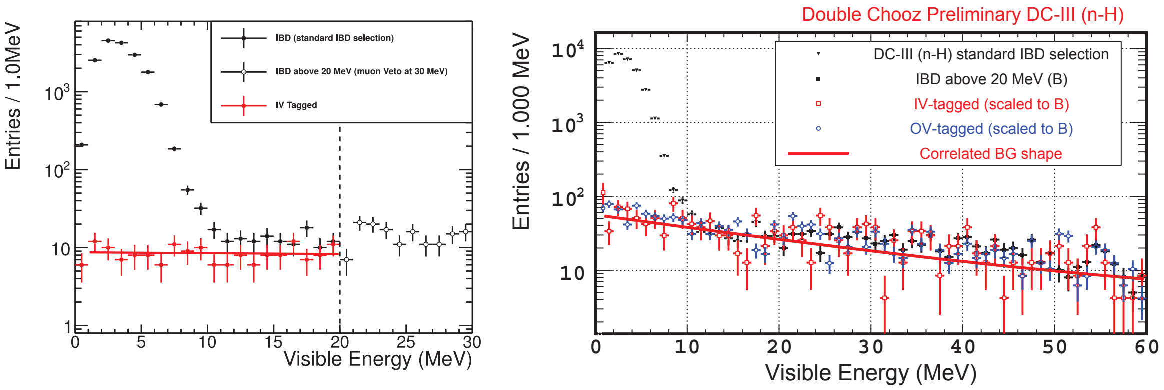

(a) Extended IBD spectrum, n-Gd.

(b) Extended IBD spectrum, n-H.

Figure 30: Prompt energy spectrum of IBD candidates (black filled dots), events tagged using the IV (red points), and coincident signals above 20 MeV (black empty dots), for n-Gd and n-H analyses. The best fit (redline) to rescaled IV tagged events (red dots), and rescaled OV tagged events (blue dots, only for n-H) are also shown.

Stopping muons

Cosmic muons could also enter the detector from the chimney and stop there, giving a small signal that could fake a prompt positron one. The Michel electron coming from the μ decay has a large energy spectrum that includes also the energy window selected for the neutron capture and can therefore fake an IBD delayed signal. These stopping muons are characterized by an exponential prompt-delayed Δt distribution, with the time constant given by the μ lifetime (2.197 μs).

Correlated background is vetoed by the OV and IV, and stopping muons are further removed by the FuncV cut. The FuncV cut can be also used, together with an analysis based on pulse shapes, to estimate the residual stopping muons component in the IBD sample. The estimation of residual stopping muons will be treated in details, for the n-H analysis, in section 4.3.

3.3.3 Accidental background

The accidental background, as its name suggests, arises from two uncorrelated events that are incidentally in time and spatial coincidence. Given the wide prompt energy window, the prompt signal is typically given by low-energy radioactivity originated in the surrounding rock or the PMTs. The delayed signal usually corresponds to a fast spallation neutron that gets absorbed on Gd (or H) within the allowed time and space window from the prompt signal.
The energy spectrum of single events, shown in figure 28, is dominated at low energies by the radioactive decays that contribute to the accidental background. In the figure we can see the 2.614 MeV peak of a ^{208}Tl γ decay, just above the n-H capture. Smaller contribution at higher energies, not clearly visible in the figure, are given by β-decays of ^{214}Bi (decay energy 3.27 MeV) and ^{208}Tl (decay energy 5.00 MeV). Whereas the accidental background represents the lowest component in terms of residual rate for the n-Gd analysis, it dominates in the n-H analysis. This reflects the importance of Gd in the neutron detection that was already pointed out in section 2.1.2.

The estimation of the accidental component left in neutrino candidates is performed with off-time coincidences. The off-time windows method consists in looking for a prompt-delayed coincidence with the IBD selection applied but with the delayed signal with 1 s offset from the prompt. The accidental rate estimated in this way is then corrected for veto-induced dead time. Figure 31 shows how the off-time window accidental selection well reproduces the data, as well as the importance of the cut on ΔR to remove such background.

3.4 Systematic uncertainties

In this section we discuss the different categories contributing to the overall budget of systematics affecting the θ_{13} measurement. Reactor flux uncertainties represent together the dominant component for both n-Gd and n-H analysis. Regarding the

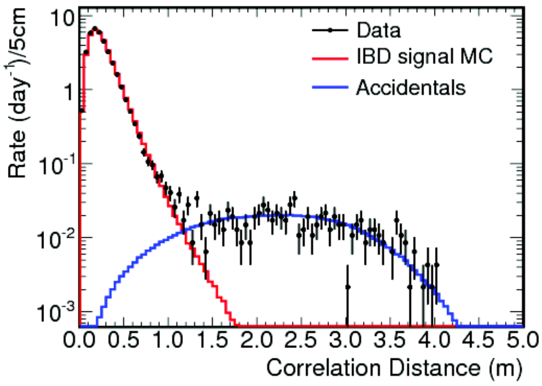

Figure 31: Data ΔR distribution (n-Gd), which is well reproduced by a MC IBD simulation (red) and a distribution of accidentals obtained with the off-time window method (blue).

	n-Gd		n-H	
Inefficiency	MC correction	Uncertainty	MC correction	Uncertainty
DAQ & trigger	1.000	negligible	1.000	negligible
After muon deadtime	0.955	negligible	0.946	negligible
Background vetoes	0.993	0.001	0.994	0.002
Isolation window	0.989	negligible	0.978	negligible
Number of protons	1.000	0.003	1.002	0.010
Neutron detection	0.975	0.005	1.015	0.003
Total detection	0.914	0.006	0.935	0.010

Table 7: MC correction factor and associated detection systematic uncertainties balance [160, 195].

neutrino detection efficiency, the dead-time free data acquisition and the high trigger efficiency - which reaches 100% at the 0.5 MeV low prompt energy threshold - results in a full prompt signal detection efficiency. However, the neutron detection efficiency is less trivially determined and in general lower, being sensitive to the modelling of the event reconstruction. The associated systematic uncertainty is evaluated - using ^{252}Cf source calibration data and IBD candidates - as the error on the MC correction factor obtained from a data/MC comparison. Correction factors are also calculated for deadtime introduced by *valid trigger* and IBD selection, and the associated errors added to the systematic budget. A summary of the normalization uncertainties is given in table 7, and each component will be discussed in a dedicated paragraph.

Source	Uncertainty (%)
Bugey-4 measurement	1.4
Fractional fission rate of each isotope	0.8
Thermal power	0.5
IBD cross section	0.2
Mean energy released per fission	0.2
Distance to reactor core	negligible
Total flux estimation	1.7

Table 8: Summary of flux estimation systematics.

3.4.1 Reactor flux uncertainties

Systematic uncertainties are associated with the measurement of each component used in equation 60 to estimate the IBD rate. Among these reactor flux uncertainties, which are summarized in table 8, the highest contribution is given by the Bugey-4 shapes measurement. However, the anchoring to the Bugey-4 values allows reducing significantly the overall uncertainty from 2.7% to 1.7%.

3.4.2 Neutron detection uncertainties

The MC correction factor associated with the detection of the delayed signal c_n can be parameterized as the combination of three other factors, corresponding to the capturing nucleus fraction correction (c_N), the IBD selection inefficiency (c_{IBD}), and the spill-in spill out current modelling correction ($c_{\phi_{spill}}$); i.e.

$$c_n = c_N \cdot c_{IBD} \cdot c_{\phi_{spill}} \,. \tag{68}$$

The three factors and their errors are evaluated independently. The ^{252}Cf provides a high statistics neutron source for such purpose (3.5 neutrons on average per fission). The γ emitted in coincidence with the neutrons is used as prompt signal, further enhancing the neutron selection purity. IBD candidates, on the other hand, are not limited by deployment positions (along the z axis in the IT, or in the guide tube in the GC). The deadtime associated with the prompt isolation window is not included in these factors and instead computed analytically. Gd fraction, IBD detection, and spill corrections, with their respective errors, are combined together to get the detection efficiency correction and associated systematic uncertainty (listed as last item in table 7).

Capture fraction

Using ^{252}Cf events selected requiring a prompt $E_{vis} > 4\,\mathrm{MeV}$ and a neutron multiplicity $N_n > 1$, we identify the number of neutrons captured by H (N_H) and Gd (N_{Gd}) using different delayed E_{vis} intervals[63]

$$\begin{aligned} N_{Gd} &= N(3.5\,\mathrm{MeV} < E_{vis} < 10\,\mathrm{MeV}) \\ N_H &= N(0.5\,\mathrm{MeV} < E_{vis} < 3.5\,\mathrm{MeV}) \\ N_{Gd+H} &= N(0.5\,\mathrm{MeV} < E_{vis} < 10\,\mathrm{MeV})\,. \end{aligned} \tag{69}$$

In the target, the fraction f_{Gd} of neutrons captured by Gd depends on the Gd concentration and can be measured as N_{Gd}/N_{Gd+H}, while the fraction f_H^{IT} of neutrons captured by H will be $1 - N_{Gd} = N_H/N_{Gd+H}$. Similary, f_H^{GC} in the GC is evaluated as N_H/N_{Gd+H}. The MC correction factor for the capture fractions c_{Gd} and c_H are obtained by comparing f_N values measured with data and with MC simulation. Systematic uncertainties on each factor, evaluated by varying the delayed E_{vis} windows defined in equation 69, are also accounted.

$$c_{Gd} = \frac{f_{Gd}^{\mathrm{data}}}{f_{Gd}^{\mathrm{MC}}} = \frac{85.30 \pm 0.08\%}{87.49 \pm 0.04\%} = 0.9750 \pm 0.0011(stat.) \pm 0.0041(syst.) \tag{70}$$

$$c_H^{IT} = \frac{f_H^{\mathrm{data}}}{f_H^{\mathrm{MC}}} = \frac{14.70 \pm 0.08\%}{12.51 \pm 0.04\%} = 1.1750 \pm 0.0078(stat.) \pm 0.0265(syst.) \tag{71}$$

$$c_H^{GC} = \frac{f_H^{\mathrm{data}}}{f_H^{\mathrm{MC}}} = 1.0020 \pm 0.0007(stat.) \pm 0.0003(syst.)\,. \tag{72}$$

In the n-H analysis c_H^{IT} and c_H^{GC} are applied separately in the rate and spectral fit (section 3.5.2), while the global correction factor 1.015 shown in table 7 is obtained by combining the two values weighted for the respective fraction of IBD events in the two volumes and used in the rate analysis (section 3.5.3). All results for n-Gd and n-H have been cross-checked using IBD candidates, for which compatible values are obtained.

IBD selection

The detection efficiency of the IBD selection for neutron captures is measured with IBD candidates, with some further cuts on the prompt signal to limit the background

---

[63] Neglecting the fraction of n-C captures, which is 0.1%.

contribution. In a similar way on what done for the capture fraction, the efficiency of the IBD selection is evaluated by comparing events selected with the standard IBD selection and with an extended version obtained by relaxing the conditions on the delayed signal and correlation Δt and ΔR. Again the correction factor c_{IBD} is calculated by comparing data and MC

$$c_{IBD} = \frac{\epsilon_{IBD}^{\mathrm{data}}}{\epsilon_{IBD}^{\mathrm{MC}}} \, . \tag{73}$$

The results are $c_{IBD} = 0.9996 \pm 0.0021$ for the n-Gd analysis and $c_{IBD} = 1.0000 \pm 0.0022$ for the n-H analysis.
An independent method relies on the ^{252}Cf source deployed along the z axis in the IT and the guide tube in the GC (only for the n-H analysis) to obtain a map of the detection efficiency $\epsilon_{IBD}(\rho, z)$ in the volume of interest. While for the n-H analysis this method is used only as a cross-check, for the n-Gd one the value obtained $c_{IBD} = 1.0003 \pm 0.0032$ was used in combination with the one calculated using IBD candidates to get a combined value of $c_{IBD} = 1.0000 \pm 0.0019$.

Spill current

Neutrons produced in IBD interactions can travel distances up to the order of 10 cm before being captured. Thus, there is a possibility that the prompt and the delayed signal of the same IBD interaction are detected in different detector volumes. For instance, a neutron resulting from an IBD interaction in the GC can be captured by Gd in the IT (spill-in), or *vice-versa* a neutron from an IBD interaction in the IT escape it (spill-out). These two effects do not cancel, resulting in a spill current that affects the IBD rate prediction. Since it is not possible to identify spill events in the data, the correction factor associated with the spill current must be obtained with MC simulations. This was done with two different codes: NeutronTH-Geant4 (a patched version of Geant4 [178]) and TRIPOLI-4 (accurate low-energy neutrons physics); the discrepancy in their outputs is used as error on the correction factor. The resulting spill correction factor and uncertainties are $c_{spill} = 1.0000 \pm 0.0027$ for the n-Gd and $c_{spill} = 1.0000 \pm 0.0025$ for the n-H analysis.

3.4.3 Deadtimes

Each background veto described in section 3.2.3 introduces a deadtime in the data acquisition, for which the MC must be corrected. The after-μ veto and the light noise cuts act at the level of single events. The deadtime introduced by the after-μ veto is estimated to be 4.49% (with negligible error) for the n-Gd analysis, while the rejection of light noise introduces a loss of 0.012 ± 0.001% of the livetime. For the n-H analysis these numbers are respectively 5.43% for the after-μ veto and (0.060 ± 0.001)% for the LN cut. The prompt isolation window deatime amounts in 1.06% for the n-Gd and 2.25% for the n-H analysis.

The combined deadtime of the OV, IV, Li+He, FV vetoes, which are applied in the IBD selection of the n-Gd analysis, results in a correction of 0.9930 ± 0.0011. For the n-H analysis, the same vetoes with the addition of the fast neutrons MPS veto (see section 4.5.1) are considered, and the total deadtime results in a 0.9938 ± 0.0018 correction factor. The deadtime is included in the MC as an additional correction factor and the errors contribute to the final systematic budget.

3.4.4 Number of protons

The number of free protons in the neutrino target is used to calculate the expected IBD rate (equation 60). For each of the Double Chooz volumes the proton number is estimated using the hydrogen fraction, determined from chemical formulas of the scintillator individual components, and information of the amount of liquids, obtained from a combination of direct measurements and calculations. In the n-Gd analysis the target consists in the liquid scintillator of the IT and the corresponding correction factor is unitary, with an error given by the accuracy of the measurement of N_p in the target

$$c_{N_p}^{Gd} = 1.0000 \pm 0.0030\,. \tag{74}$$

Conversely, for the n-H analysis the correction factor includes a small contribution ($\sim$ 0.5%) of the target acrylic vessel events, and the contribution of each volume (IT and GC) is weighted for the number of IBD interaction expected in it

$$c_{N_p}^{H} = 1.0022 \pm 0.0095\,. \tag{75}$$

Moreover, as for the capture fraction, $c_{N_p}^{H}$ is used in the rate analysis while corrections are applied separately for the IT (1.39 ± 0.23) and other volumes (1.00 ± 0.03) in energy spectral fit. Errors on N_p are included in the detection systematics rather than

	n-Gd (on)	n-Gd (off)	n-H (on)	n-H (off)
Livetime (days)	460.67	7.24	455.57	7.15
IBD candidates	17351	7	31835	63
Reactor $\bar{\nu}_e$	17530 ± 320	1.57 ± 0.47	30051	2.34 ± 0.70
Correlated bck	278 ± 23	3.84 ± 0.64	706 ± 68	10.4 ± 1.4
Accidental bkg	32.3 ± 1.2	0.508 ± 0.019	1974.4 ± 4.8	30.9 ± 0.4
Cosmogenic bkg	447^{+189}_{-74}	$7.0^{+3.0}_{-1.2}$	433^{+260}_{-150}	$6.8^{+4.1}_{-2.4}$
Total prediction	18290^{+370}_{-330}	$12.9^{+3.1}_{-1.4}$	$33164.3^{+268.6}_{-165}$	$50.4^{+4.4}_{-2.9}$

Table 9: Data set used in the n-Gd and n-H analyses. The number of IBD candidates is determined basing on the selections described in section 3.1. The numbers of expected neutrino events are evaluated with the reactor simulation described in section 3.2, while backgrounds are estimated according to the different analyses described in section 3.3.

in the flux estimation systematics.

3.5 θ_{13} measurement

In Double Chooz the observation of a deficit in the measured neutrino rate with respect to the predictions is attributed to the oscillation of reactor $\bar{\nu}_e$. The amplitude of such oscillation allows to retrieve $\sin^2(2\theta_{13})$ basing on equation 44. The value of Δm^2_{13} is given as an input in the analysis and taken from MINOS latest results [85]. The analysis performed in the first publication [108] used the total number of observed IBD candidates to determine the deficit. Currently, two main analyses based on a χ^2 minimization have replaced this rate-only fit: the *Reactor Rate Modulation* (RRM) analysis and the *Rate + Shape* (RS) analysis. Both analyses, described in this section, are applied to the full Double Chooz data sample. A summary of the estimated and observed values for IBD candidates and backgrounds, for the full Double Chooz livetime and for both n-Gd and n-H analyses, is shown in table 9. These values and errors are the main ingredients for the analyses fit.

With respect to the previous publications [157, 158], we profit of an extended livetime, which corresponds to a factor ~ 2 statistics. Moreover, thanks to an improved background reduction, it was possible to widen the IBD selection and still have positive effect on the signal-on-background ratio. The uncertainties, which are resumed in table 10, were also reduced by roughly 20%. The amount of stopping muons in the IBD sample has been suppressed mostly thanks to the FuncV cut, which is based on the effect on the vertex reconstruction of the typical topology of such events. Moreover, the n-H analysis has seen a dramatic reduction of the accidental component, the main background for this analysis, with respect to previous n-H results. This

Uncertainty	n-Gd (%)	n-H (%)
Reactor flux	1.73	1.73
Detection	0.63	1.09
Cosmogenic bkg	+1.08/-0.42	+0.86/-0.50
Correlated bkg	0.13	0.23
Accidental bkg	0.01	0.02
Statistics	0.76	0.55
Total	+2.3/-2.0	+2.28/-2.18

Table 10: Summary of systematic uncertainties from flux estimation (discussed in section 3.1), neutrino detection (evaluated in section 3.4) and background estimation (from the analyses shown in section 3.3).

improvement was mostly due to the newly developed artificial neural network cut, which disentangles the accidental coincidences with a multi-variable approach. The fast neutron component was also reduced significantly thanks to the MPS selection. Concerning the systematics, the reactor flux estimation carries the larger error, as already mentioned.

The number of selected IBD candidates per day follows with a very good agreement the reactor power, as shown for the n-Gd analysis in figure 32. In the figure, the two configurations with only one reactor on, and two reactors on are highlighted, as well as two small periods of time in which both reactors were off, to which we refere as off-off period.

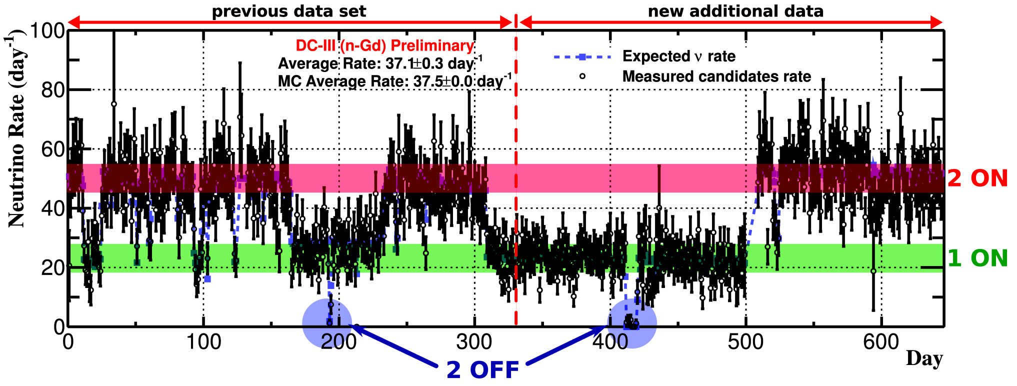

Figure 32: Selected number of neutrino candidates day by day.

A comparison of the different analyses and samples, in terms of fitted $\sin^2(2\theta_{13})$ values, is represented in table 11.

Analysis	$\sin^2(2\theta_{13})$	Background rate
Rate + Shape (n-Gd)	$0.090^{+0.032}_{-0.029}$	$1.38 \pm 0.14\,(\text{day}^{-1})$
Rate + Shape (n-H)	$0.124^{+0.030}_{-0.036}$	$7.55 \pm 0.00\,(\text{day}^{-1})$
RRM_{UB} (n-Gd)	0.060 ± 0.039	$0.93^{+0.43}_{-0.36}\,(\text{day}^{-1})$
RRM_{UB} (n-H)	$0.098^{+0.038}_{-0.039}$	$7.29 \pm 0.49(\text{day}^{-1})$
RRM_{CB} (n-Gd)	$0.090^{+0.034}_{-0.035}$	$1.56^{+0.18}_{-0.16}\,(\text{day}^{-1})$
RRM_{CB} (n-H)	$0.123^{+0.042}_{-0.043}$	$8.28 \pm 0.87(\text{day}^{-1})$
RRM_{CB} (Gd+H)	0.090 ± 0.033	

Table 11: Results, in term of oscillation amplitude $\sin^2(2\theta_{13})$ *and background rate, of the different Double Chooz analyses: the RS analysis, and the RRM analysis with constrained (CB) and unconstrained (UB) background.*

3.5.1 Off-off data

The off-off period is a unique feature of Double Chooz among other contemporary reactor neutrino experiments. It allows studying the background in a direct mode by counting the IBD candidates that are recorded in absence of the reactor neutrino flux. Residual neutrinos are produced in beta decay of fission products that are still present when the nuclear chain reaction is stopped. The number of residual neutrinos is simulated with dedicated codes and subtracted from the observed candidates to correctly evaluate the background. The off-off data collected so far come from two different periods (in 2011 and 2012) for a total of roughly 7 days of data taking. The number of IBD events and predicted backgrounds recorded during these times are resumed in table 9. These data are used in both RRM and RS analyses.

3.5.2 Rate + Shape analysis

In the *Rate + Shape* analysis, the energy spectrum (shape) of each components is used, with data divided in energy bins, to characterize the oscillation as a function of E_{vis} and statistically separate the signal from the background. The major improvements of the *Rate + Shape* analysis of the last n-Gd publication [160] are a wider energy range (0.5–20 MeV), a finer binning, which was possible thanks to the improved statistics, and a better energy reconstruction for IBD events. The off-off data is included in the fit as an extra bin (pull term).

Figure 33 shows the prompt visible energy spectrum used for the *Rate + Shape* fit, for the n-Gd (figure 33a) and for the n-H (figure 33b) analyses. The oscillation pattern is clearly visible in the energy distribution of the observed-on-predicted rates, shown for both analyses in figure 34, which deviate clearly from the non-oscillation pattern. An excess of event is also visible around $E_{vis} \sim 5\,\text{MeV}$, which has been object of different studies, and has also been observed by other reactor neutrino experiments. Evidences of the dependence of such excess on the reactor power [160, Section 9] suggest that it may be related to an unaccounted component that contributes to the neutrino flux in that energy region. The solidity of the θ_{13} measurement, however, has been proven by dedicated studies [196].

3.5.3 Reactor Rate Modulation analysis

The RRM relies the unique feature of Double Chooz experiment of having the direct background measurement given by the off-off period. This background model independent method for measure θ_{13} compares the observed and expected IBD rate for different reactor power conditions in order to determine θ_{13} and total background at same time. A RRM analysis applied to the livetime of Ref. [160] was first reported in a dedicated publication [159]. Two different approaches have been used: in the first one the background is treated as a total free parameter, while in a second approach the background is constrained using the estimated value. The combined results fo the RRM fit on the n-Gd and n-H samples is shown in figure 35.

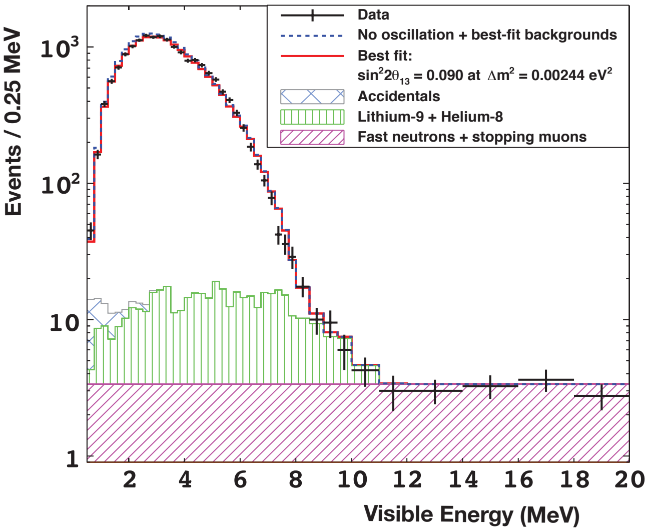

(a) n-Gd, 460.67 days livetime.

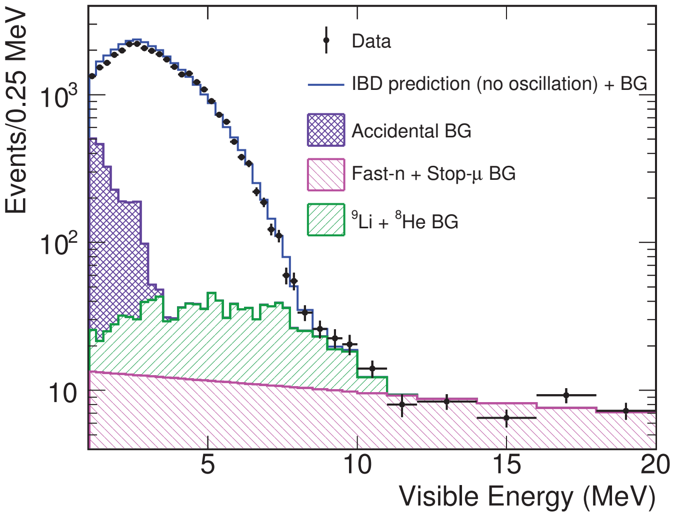

(b) n-H, 455.57 days livetime.

Figure 33: Energy spectrum, for the prompt signal in the n-Gd and n-H analyses, of data (black points), accidentals (grey for n-Gd and purple for n-H), ^{9}Li+^{8}He (green), and fast neutron + stopping muons (magenta). These are compared with predictions without neutrino oscillation (blue dashed line), and the n-Gd rate + shape best-fit with $\sin^2(2\theta_{13}) = 0.090$ *(red line, only for n-Gd).*

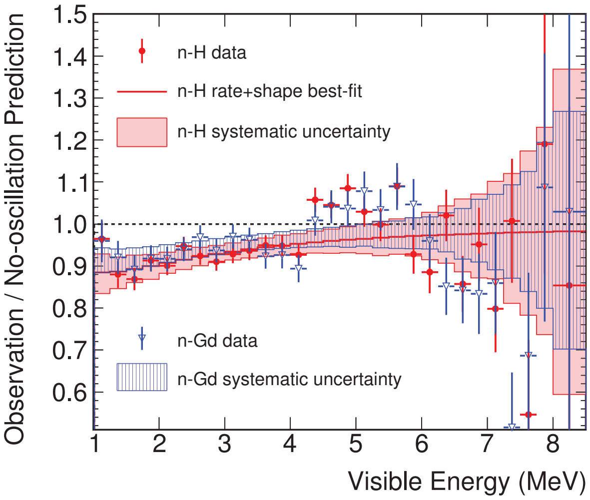

Figure 34: Ratio of background-subtracted data on non-oscillating prediction (points), and systematics uncertainties (bands) for n-Gd (blue) and n-H (red) analyses. These are compared with predictions without neutrino oscillation (dashed line), and the n-H rate + shape best-fit with $\sin^2(2\theta_{13}) = 0.124$ *(red line).*

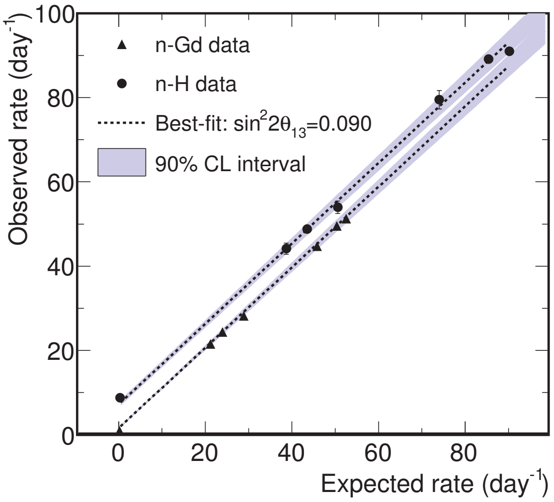

Figure 35: Combined RRM fit to the n-H and n-Gd data sets, assuming no correlations between the background uncertainties of the two data sets and full correlation of the reactor flux and residual neutrinos uncertainties. The observed rate vs the rate expected as a function of reactor power. The fit (dotted lines) is compared to the n-Gd (triangles) and n-H (circles) data sets.

4 Pulse shape analysis

Contents

In the process of light emission that follows the passage of a charged particle through a liquid scintillator compound, a key feature lies in its time response. The notion of time response of a scintillator is closely related to the one of pulse shape. In an ideal detector in which all emitted light is collected by a photomultiplier (PMT), the time response directly translates into the profile of the current pulse observed in the PMT readout, i.e. the pulse shape. The main application of the study of the time response is the so-called pulse shape discrimination, or PSD. The aim of a PSD is to separate different particles based on the characteristic time profile of scintillation light that they induce.

In addition to the nature of the charged particles crossing the scintillator media, several other effects may influence the light time profile. For a large liquid scintillator experiment like Double Chooz, the path that scintillation light travels from its production to its collection has a distorting effect on the light profile. The transit time inside the photomultipliers themselves may be of the same order of magnitude of the typical prompt scintillation light emission times and has to be taken into account. It has also been proven that scintillators suffer deterioration of their molecular structure due for instance to oxidation or exposure to high amount of radiation. These phenomena - which generally go under the name of scintillator ageing - will be addressed in another chapter, specifically for the Double Chooz inner veto liquid scintillator.

The Double Chooz apparatus employs several (390) PMTs; hence the concept of pulse shape differs from the one we just defined. However, a combination of each PMT response is possible, and a global light profile can be computed. By investigating the global light profile of events detected in Double Chooz, we have been able to carry out different studies with many applications that take the form of a PSD. The motivation, description, and results of these applications are the subject of discussion of this chapter. The attempt to perform a traditional PSD was the incentive and the first idea that brought us to the observation of pulse shapes; however, the applications derived by this study divert from the classical PSD, as they cover a good range of topics and pave the way for future analyses.

Since, as we mentioned, a PSD is the motive of the work represented here, a brief description of the principle on which such discrimination is based will open the chapter and its first part. Before moving to the actual PSD, we will focus on the Double Chooz case, with particular regard for the efforts made to build a pulse shape in a large and multi-channel detector. The remaining parts of the chapter are dedicated to the description of each application of the pulse shape studies we carried out. A PSD will be used to address the stopping muon background, in both the n-Gd and n-H capture analyses of Double Chooz, the fast neutrons background in the n-H analysis, and the formation of ortho-positronium.

In particular, we will start by discussing a pulse shape analysis of the stopping muon background. This extensive study represents the main building block of this chapter; covering different applications that involve both the Double Chooz n-Gd capture analysis, and the more recent n-H one. For the latter, a PSD based analysis provides a powerful tool to estimate the remaining component of stopping muons in the final sample.

Fast neutrons, the other main Double Chooz correlated background, have also been addressed with a PSD, as we will discuss afterwards. With an approach similar to the one used for stopping muons, we disentangled a significant part of the fast neutrons background using some pulse shapes features.

Another important achievement that made possible thanks to the use of pulse shapes in Double Chooz is the tagging of the ortho-positronium, a bound state of positron and electron. The identification of ortho-positronium, besides representing a new feature *per se* in a large liquid scintillator, is the starting point for a positron/electron separation and its study can prompt future applications.

Finally, to wind up the chapter, we will discuss the applications of the pulse shape studies to the new-built Double Chooz near detector.

4.1 Pulse shape discrimination in Double Chooz

Pulse shape discrimination is a key technique with many applications in liquid scintillator experiments. It is very often used to separate signal from background. The PSD is based on the distinctive ionization process and consequent emitted light profile, namely the pulse shape (PS), of different charged particles. Traditional PSD exploits the different slow decay component in the light profile of different particles to perform particle identification (PID). It is particularly effective in separating heavy particles, for example protons and alpha, from electrons and photons. It is conversely ineffective in separating muons from electrons and photons. Furthermore, it is not possible in principle to distinguish between electrons and positrons with a traditional PSD. However, the formation of ortho-positronium, and the induced delay in the positron annihilation, can be used to identify a significant part of positrons interacting in liquid scintillator, basing on the different PS topology, assuming a fine enough time sampling.

Double Chooz is a multiple-channel detector and therefore pulses are produced in each PMT. The global light time profile must therefore be constructed taking into account each contribution. It is more correct, then, in an experiment like Double Chooz, to refer to global light time profile rather than using the term PS. However, in the rest of this chapter, we will use the terms PS and light time profile indistinctively, provided that we now made the difference clear for the reader.

In this first section we will describe the principle behind the traditional PSD and how the pulse shape of an event is constructed in Double Chooz. The feasibility of a PSD is investigated by comparing cumulative pulse shapes, i.e. the sum of PSs of a particular sample, of different samples. We will see how the attempt to perform a PSD led to the observation of a distortion in the PSs of stopping muons (described in section 3.3.2). This distortion represents the basic feature on which a PID on this Double Chooz background can be performed, and it has been exploited in different ways. On one hand, the correlation between the PS distortion and the goodness of the vertex reconstruction was exploited to develop a stopping muons separation criteria based on the latter. This cut, the functional value cut (FuncV), has been discussed in section 3.2.3 and it is part of the Double Chooz candidates selection since the last published results, in which IBDs with n-captures on gadolinium are analysed (n-Gd, see [160]). On the other hand, two analysis strictly based on PS are used in the forthcoming Double Chooz publication, which exploits instead the n-capture on hydrogen (n-H).

4.1.1 Scintillation and pulse shape discrimination

The observation of scintillation light is one of the oldest and yet more widely used techniques to detect ionizing radiation. The conversion of a fraction of the particle kinetic energy into fast-emitted detectable light allows in fact detecting, tracking, and measuring the energy of high rates of charged particles, while it is relatively affordable to produce and manage a large amount of scintillator. For organic liquid scintillators, fast fluorescence light, and, on a smaller extent, slow phosphorescence light, are emitted corresponding to the decay of singlet and triplet excited states of the scintillator molecule respectively. The phosphorescence is usually much slower than the typical prompt fluorescence. However, triplet states can be promoted thermally to singlet ones, resulting in an intermediate slow component of fluorescence light, as extensively described by J. B. Birks in his book [197]. The amount of visible energy deposit in the scintillator depends on the particle nature and energy, with heavy particles being more quenched[64] than light ones. Nonetheless, not only the light output, but the time response as well, is influenced by the particle nature.

In general, the time response of a liquid scintillator depends on the various process involved. If we imagine that luminescent states are formed instantaneously and consider only singlet excited states, the time response would be a simple exponential. However, this is not a realistic case, as instead the finite time to populate an excited state and the slow component of the de-excitation due to the decay via triplet state influence the final PS as well. In modern liquid scintillators like the ones used in Double Chooz, the population of excited states occurs in a few ns, while the de-excitation employs times of the order of tens of ns. By assuming that the population of electronic levels follows an exponential law as well, a simple mathematical model of the whole process can describe the evolution of scintillation light intensity I with time as

$$I(t) = I_0(e^{-t/\tau} - e^{-t/\tau_{rise}})\,, \tag{76}$$

where the rise characteristic time τ_{rise} distinguishes the population of the optical state, the fall characteristic time τ the fluorescence emission, and I_0 is a constant. If we disentangle the slow component due to indirect de-excitation of triplet states from the prompt fluorescence, the total light profile will instead be

$$I(t) = I_0(e^{-t/\tau_{fast}} + e^{-t/\tau_{slow}} - e^{-t/\tau_{rise}})\,. \tag{77}$$

A graphical representation of a PS with these three components is given in figure 36. The phosphorescence light due to direct de-excitation of triplet states is usually several orders of magnitude slower (and not compatible with data acquisition times) and will not be taken into account in our simple model. Other observations suggest that the effect of the excitation on the time profile is rather represented by a Gaussian $f(t)$ and therefore the total profile

$$I(t) = I_0 f(t)(e^{-t/\tau_{fast}} + e^{-t/\tau_{slow}})\,. \tag{78}$$

An important observation, made since the first applications of liquid scintillators and for a wide deal of different compounds, is that the relative amount of slow component, represented by the decaying time constant τ_{slow}, depends on the nature of the charged particle. In particular, it is ascertained that heavy particles, like alphas and protons, have typically a larger slow component with respect to gammas and elec-

---

[64] The quenching happens when high vibrational states of the excited electronic level decay radiationless to the ground state.

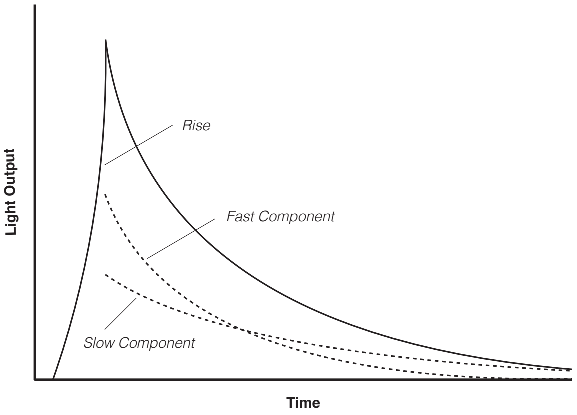

Figure 36: Graphic representation of the light time profile, as a result of the combination of the excitation and the two-component de-excitation of molecular states of a liquid scintillator.

trons, as shown in figure 37. A profitable use of this difference is to separate different particles depositing the same energy in the scintillator, allowing for a PSD [198–200].

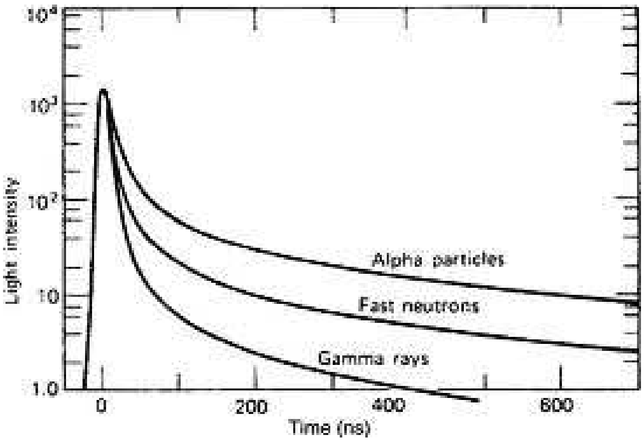

Figure 37: De-excitation times in stilbene (1,2-diphenylethene isomer) for various particles, as represented in the Birks [197]. Fast neutrons (i.e. recoil protons) and, more significantly, alpha particles, have a larger tail in the PS with respect to γ rays.

As Birks first suggested, a moderate slow component arises from the recombination of two molecules excited in the triplet state. One of the molecule goes to the excited S1 state, decaying consequently, while the other goes back to the ground state. The number of molecule doublets goes with the square of the excitation density $(dE/dx)^2$, while the fast component is simply proportional to dE/dx. This, in first approximation, explains how particles with a higher excitation density, i.e. with a low $|\mathbf{p}|/m$, are characterized by a larger slow component in the light profile.

4.1.2 Pulse shape reconstruction in a multi-channel large detector

In Double Chooz, IBD interactions of neutrinos are detected by means of the scintillation light that is induced by the positron and by the gammas arising from the n-capture. The light coming from the inner target and the gamma catcher scintillators is collected by the PMT array installed on the inner wall of the stainless steel buffer tank (see section 2.2.1 for detector details). In each of the 390 PMTs, the current produced by incident light is multiplied in multiple dynode stages and recorded by flash-ADC (FADC) [175]. A single photon-like incident signal results in a sizeable pulse in the baseline PMT current, whose size is proportional to the number of collected photo electrons (p.e.). For each energy deposition, namely an event, occurring inside the detector, a 256 ns waveform with 2 ns sampling is recorded for every PMT and the pulses extracted. Different pulses recorded by the same PMT during the 256 ns window are accounted separately if distant more than 25 ns, otherwise they are merged together. The time-spatial distribution and sizes of pulses over the whole PMT array are used to reconstruct energy and vertex of the event (see section 2.3 for details).

Double Chooz uses multiple channels; therefore the global light profile of an event must be the combination of the contribution of every PMT. For the purposes of this analysis, it will be consider as a pulse shape the time distribution of PMT pulses for one event occurring in the detector. The first step to build such a distribution is to extrapolate the pulses times from the PMTs current profiles. The pulse reconstruction described here is performed by the suitably-developed RecoTimePulse package of DOGS, the Double Chooz analysis framework. A linear fit has been developed for that purpose, with an example given in figure 38. When the waveform of a PMT goes under a threshold of 2 FADC counts (approximately 0.3 p.e.), a linear fit is performed on the rising part of the current profile. The intercept of the fit line with the PMT baseline provides the pulse starting time. The baseline may fluctuate in time, and must be precisely extrapolated in each physics run; this is done by looking at the first thousand events in which no signal over threshold was recorded by the PMT. Once the pulses times are computed, a series of corrections is made on each time separately and on the final combination to account for specific effects and allow properly comparing different PSs. Specifically, a time of flight (TOF) correction, a transit time correction, a spurious pulses removal, and a final PS aligment, are applied.

Time of flight correction

Let us consider the interaction of electrons, positrons, and γ rays within the scintillator.

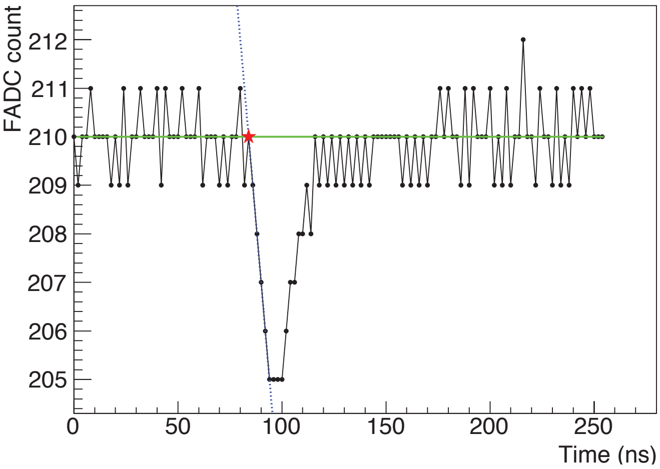

*Figure 38: Example of the time determination of the pulse of one PMT. The green solid line represents the pedestal value (*FADC = 210*), the blue dashed line shows the fit of the pulse edge. The pulse starting time (*84 *ns) is represented by a red star.*

For an e^- with energy of a few MeV, the dominant energy loss process is the ionization. The energy released per unit of travelled distance is significantly more than a MIP[65] ($\sim$ 2 MeV/cm) and therefore its interaction in the liquid scintillator is nearly point-like. The behaviour of a e^+ is slightly different, because of the different spin and the possibility of forming bound states with electrons of the medium, but without a sizeable influence on its free path (see section 4.4.5). For a γ emitted in the n-capture process or as result of positron annihilation, on the other hand, the scintillation light is triggered only via production of secondary charged particles, and consequently its attenuation length is bigger (10-15 cm for few MeV and the density of the DC scintillator).

These mentioned particles cover a rather short distance before being completely absorbed in the liquid scintillator. Conversely, the emitted scintillation light travels a few meters before reaching and being collected by the PMTs. By moving the interacting point within the target, the time of flight of the scintillation light can change by a few nanoseconds[66]. Such variation is of the same order of the scintillation characteristic fast decay time, i.e. the τ_{fast} of equation 77, which is 2.6 ns in the inner target and 5.4 ns in the gamma catcher. As a result, the same event in two different positions can produce different light profiles.

In order to avoid that, a TOF correction is applied to each pulse individually. The

---

[65] Minimum ionizing particle

[66] Light travels one meter in 5 ns in a material with refractive index $n = 1.5$.

distance between the interacting point and each involved PMT is used to calculate the time of flight. Such TOF is then subtracted to the fitted time of pulses recorded by that particular PMT. It is easy to see how the vertex reconstruction is crucial in this correction, since the TOF calculation relies precisely on the event vertex. The accuracy of such vertex measurement is close to 20 cm.

Transit time correction

Since PMTs are accounted individually, any other effect that may differ the time recording of pulses from PMT to PMT must be corrected. In Double Chooz, a specific calibration is performed regulary with the IDLI and IVLI systems in order to compute the transit time t_0, i.e. the elapsing time between the formation of a p.e. in the photocathode and the final current pulse at the end of the multiplication process (see section 2.3). t_0 are measured with a $\sim$ 1 ns precision. Like the TOF, the transit time of each PMT is subtracted to the time of pulses it records for every event. Once pulse times are corrected for the TOF and the PMT t_0, they are combined together to form the PS.

Spurious pulses removal and PS alignment

Before analysing the PS, two further corrections are applied.

The presence of spurious pulses uncorrelated to the observed event but recorded in the same time window may result in an overall shift of the PS at higher times. To avoid that, the first spurious pulses are removed if too isolated. The condition used is to recursively skip the first pulse until at least 3 pulses are present in the following 4 ns window. Finally, after the spurious pulses, if present, are removed, the first recorded pulse time is subtracted to all the others. This aligment has the purpose of allowing for a correct comparison between different PS.

An example of PS for a single event resulting for the aforesaid steps is given in figure 39. In the energy ranges of a prompt or a delayed signal of an IBD (1 – 10 MeV), the number of pulses is of the same order of the number of PMTs. The number of p.e. per pulse, on the other hand, tends to increase with energy; each PMT generally collects one or a few photo electrons. For instance, the PS of figure 39 represents the time distribution, with all mentioned corrections, of 386 pulses of an event with a visible energy of 4.74 MeV.

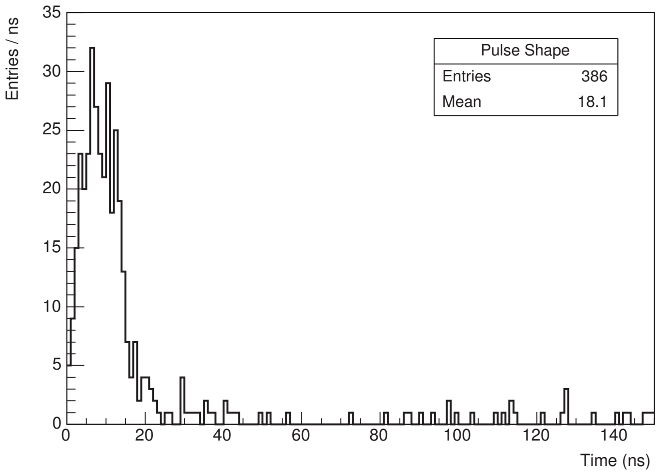

Figure 39: Example of a PS reconstructed in Double Chooz for a single event of 4.74 *MeV.*

4.1.3 Cumulative pulse shapes comparison

The effect of having a larger tail in the PS of high ionizing particles, on which the PSD is based, is reproducible in the combination of multiple PMT contributions. More specifically, we can have for instance a larger number of pulses at longer times for a proton PS with respect to an electron one. However, provided that this difference is noticeable, PSs can have other dependences than the particle nature, such as the event vertex position, the energy, and may also be affected by random fluctuations due to the statistical nature of the scintillation and light propagation processes.

A reliable and statistically significant representation of the mean PS of a particular sample is given by the cumulative pulse shape, i.e. the sum of the PS of all events of that sample. Figure 40 shows the cumulative PS of calibrations made with three different sources located at the centre of the detector. The sources are ^{60}Co, ^{137}Cs and ^{68}Ge, and the PSs are normalized to one to correctly compare different statistics. The difference between the cumulative time profiles is due to the different energy of the respective source decays (see section 2.2.2), which are conveniently resumed in table 12. This discrepancy is reproduced by neutrino candidates in different energy ranges, and it is confirmed to be small over the whole range $1-10$ MeV.

Thereafter, in order to explore the possibility of a PSD, first step is to compare the cumulative PS of the signal with the ones of the backgrounds that need to be discriminated. Figure 41 shows the cumulative PSs of different samples, all normalized to 1, for the prompt and the delayed signal separately. These samples are selected using the Double Chooz candidates selection of the second n-Gd publication [157],

Source	Decay mode	γ energy
^{60}Co	$\beta-\gamma$	2.506 MeV
^{68}Ge	β^{+}	1.022 MeV
^{137}Cs	$\beta-\gamma$	0.667 MeV

Table 12: Energy values of three of the four Double Chooz calibration sources.

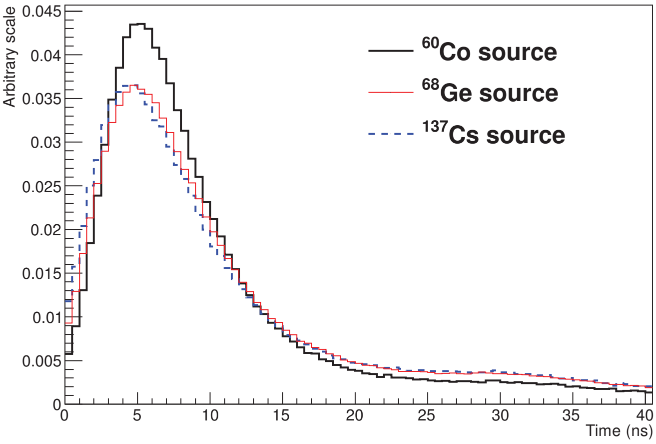

Figure 40: Time profile distribution for ^{60}Co (thick black line), ^{137}Cs (dashed blue line) and ^{68}Ge (thin red line) events in the centre of the target. The distributions are normalized to one.

the outer veto (OV) tag information, and the correlation time Δt between the prompt and the delayed signals. Three samples are studied:

- neutrino IBD candidates (selection after official cuts);
- OV sample, i.e. events passing all the selections for the IBD candidates but in coincidence with an OV trigger, subsequently divided into:
    - stopping muons, with a Δt < 10 μs;
    - fast neutrons, with a Δt $\geq$ 10 μs;
- a ^{60}Co calibration run, with the source deployed in the centre of the target.

The ^{60}Co cumulative PS is a key feature in the studies presented in this chapter as it will be used as a reference for neutrino PSs for different analysis. It is built collecting events of the calibration runs and requiring these events to have a vertex reconstructed close to the deployment position (maximal distance of 20 cm) and a reconstructed energy in the range of the ^{60}Co decay (1.3–3 MeV). Additional cuts are also applied to reject background contaminations and therefore select a pure sample of ^{60}Co decays.

Let us now go into details of figure 41. First of all, we notice that for the prompt signal (figure 41a), neutrino candidates and ^{60}Co cumulative PS are almost identical. For the delayed signal (figure 41b), candidates are also very similar to ^{60}Co, with a small peak-to-tail ratio mismatch arising from the difference in the energy range (^{60}Co decay is at 2.824 MeV, close to the prompt mean visible energy, while the delayed energy is 8 MeV for neutron capture on Gd). However, the effect is small, in agreement with the remark that PSs are stable over our energy range of interest. Coming to fast neutrons, we see how in the delayed the cumulative PS matches perfectly the one of candidates, as their delayed are both given by a neutron capture on Gd. On the other hand, by looking at the prompt signal, it is clear how fast neutrons have a different PS with respect to neutrinos. This is expected, since for fast neutrons the prompt signal is given by the ionization of recoil protons, which, as we mentioned, have a different light emission profile (see again figure 37). Finally, stopping muons have different PS in both prompt and delayed signals. This is unexpected, since the muon and the Michel electron have similar energy loss density and therefore produce in principle similar PS with respect to positrons and gammas. This entire next section of this chapter is focused on the study of this latter discrepancy. The main goal is, in fact, to exploit the difference in stopping muon PSs for a background. Fast neutron will be studied as well in another following section, and the nature of the discrepancy

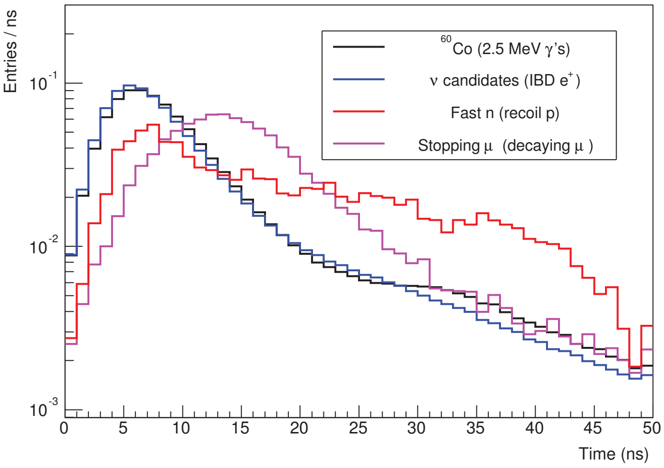

(a) Cumulative PS of the prompt signals.

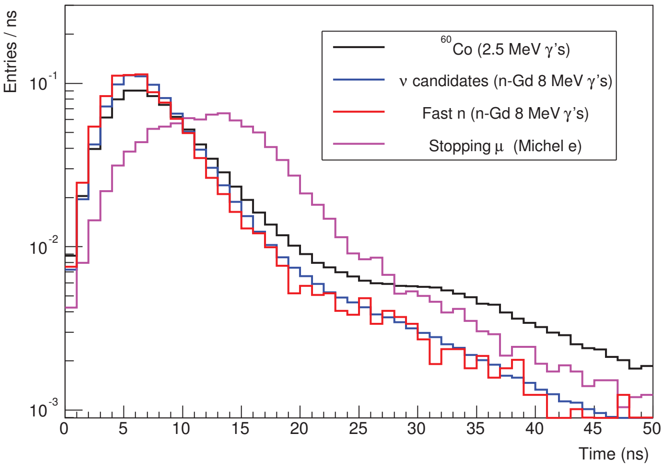

(b) Cumulative PS of the delayed signals.

Figure 41: Cumulative pulse shape of the prompt (a) and delayed (b) signal of neutrino candidates (blue), stopping muons (magenta) and fast neutrons (red) samples, all from the DC-II (n-Gd) selection, and of a ^{60}Co calibration source run (black). For a correct comparison, PSs are all normalized to one and shown in log-scale.

in the prompt PS will be further investigated and exploited to separate some of these events from candidates.

4.2 Study of the stopping muon background in the n-Gd analysis

In this section, an application of pulse shape discrimination in the Double Chooz experiment will be examined. Stopping muons, background events in which a cosmic muon decays after being passed through the chimney of the detector, are separated from the neutrino IBD sample with two different analysis based on PS (see section 3.3 for a detailed description of the Double Chooz backgrounds). The former PSD analysis (section 4.2.2) is performed on IBD events that are selected with the criteria described in Ref. [157] for the n-Gd analysis and [158] for the n-H one up to March 2012 (DC-II). It is a direct application of the Gatti's method [201], and led to the implementation of a cut based on the goodness of the vertex reconstruction to remove stopping muons. Such cut was applied to the latest IBD candidates selection, which involves a longer livetime and is described in chapter 3 of this manuscript (and in Ref. [160] for n-Gd only). This is the sample on which is applied the latter of the PSD analyses, which is based on a likelihood approach. The goal for this analysis is to contribute to a further background reduction and the estimation of its residual component.

4.2.1 Stopping muon pulse shape distortion

As already mentioned, the explanation for the different PS of stopping muons does not lie in the scintillation process; instead, as will be demonstrated, it is due to the vertex reconstruction of such events. The importance of the vertex position on the PS reconstruction has been remarked in section 4.1.2.

By observing the distribution of the reconstructed vertices for the stopping muon sample defined before (in section 4.1.3), as by looking at figure 42, it appears how they are located in the top area of the inner target. A muon entering the inner target without travelling mostly through the chimney crosses the inner veto and the gamma catcher. A series of condition on the inner veto signal reject events originating outside the detector (as discussed in section 3.2.3 of this manuscript, or Ref. [160, Section 4.3]). Furthermore, the minimum distance to travel in the gamma catcher to reach the inner target would imply an energy loss of $\sim 260\,\mathrm{MeV}$ [202, Section 32.2]. Thus, a muon crossing the gamma catcher would be clearly identified as such by the conditions imposed for muon identification on the released energy (section 3.2.1). In order to be mistaken for a neutrino IBD interaction, conversely, a muon must decay in the chimney.

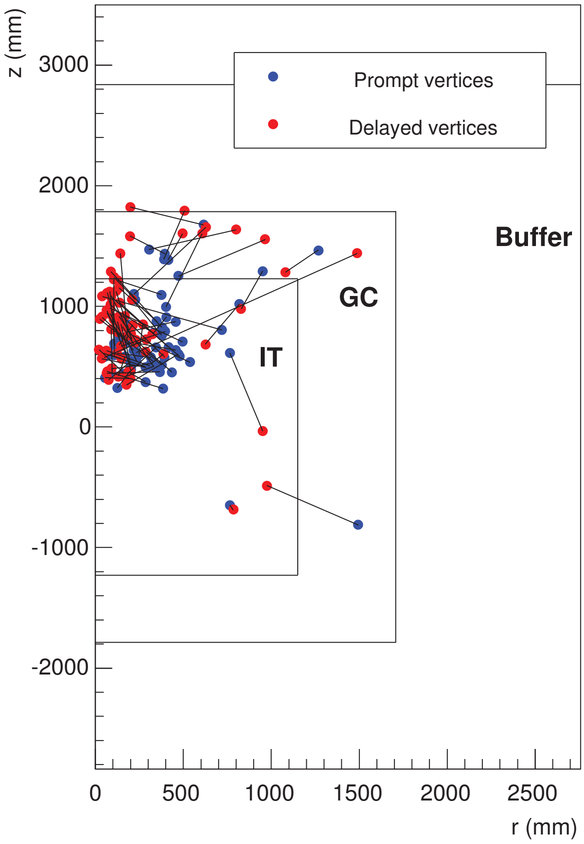

Figure 42: Detector schematic section showing the vertex distribution of stopping muons (with a small component of fast neutrons) selected using the OV tag and the prompt-delayed correlation time (Δt < 10 μs). The black lines represent the borders between the inner target (IT), the gamma catcher (GC) and the buffer. Every set of a blue and a red dot connected by a solid line represents the prompt and the delayed vertex position of the event.

The algorithm we use in Double Chooz, which is described in section 2.3.2 of this manuscript (or Ref. [157, Section 4.B]), has been tuned to reconstruct events well located in the inner detector, while stopping muons are located in the chimney. Consequently, for stopping muons, the prompt (the decaying muons) and the delayed (the Michel's electron) vertices are typically mis-placed in the upper-central part of the inner detector (figure 42) and their pulse shape distorted accordingly for the wrong TOF correction. In figure 43, the prompt (43a) and the delayed (43b) PSs of a typical stopping muon are represented by a blue curve. The figure shows how the discrepancy is noticeable at single event level, as the PSs differ from the reference ^{60}Co one.

It is possible to compute the PS with a vertex in a different position with respect to the one predicted by the algorithm, by simply correcting pulses starting time for the TOF from the chosen vertex. This has been done to probe the vertex mis-reconstruction for stopping muons. When re-computing the PS of stopping muons after placing the vertex in the chimney, e.g. 2500 mm above the centre of the target, the distortion is no longer observable. As example, re-computed PS for a stopping muon are shown by the red curves in figure 43. These PSs look now more in agreement with the reference (^{60}Co) once the vertex is moved 2500 mm above the centre of the target, which is reasonably close to the point where muons are actually stopping. Once more, this happens both for the prompt (43a) and the delayed (43b) PS.

As mentioned before, the stopping muons PS discrepancy will be exploited to disentangle this background with two different techniques and for different candidates selection, as shown in the sections below.

4.2.2 Stopping muon selection with the Gatti's method

The *Optimum Gatti's Method* is a sample separation technique especially developed to be utilized with pulse shapes [201]. It requires two different PSs as references; then, given a single event PS, it determines to which reference it is closer. This is expressed by the sign of the Gatti's parameter, which is returned as an output. In order to compute the Gatti's parameter, first, a bin per bin weight is built as

$$P_i = \frac{\alpha_i - \beta_i}{\alpha_i + \beta_i}\,, \tag{79}$$

where α_i and β_i are the ith bin content of the α and β reference PSs respectively. Then, given the pulse shape S with ith bin content S_i, the output parameter is computed as

$$G_S = \sum_i S_i \times P_i\,. \tag{80}$$

The Gatti's parameter G_S is positive for an α-like event, and negative for a β-like one.

The Gatti's method has been applied to identify stopping muons exploiting their delayed PSs. The main reason why the delayed signal is preferred to the prompt one is that in the delayed the cumulative PS of stopping muons is the only one which differs significantly from the one of neutrinos (figure 41). Other than that, as we will see in section 4.4, the formation of ortho-positronium may distort the prompt PSs as well. The two distributions used as references are the ^{60}Co PS, corresponding to positive output, and the stopping muons delayed cumulative PS, for negative output (both from

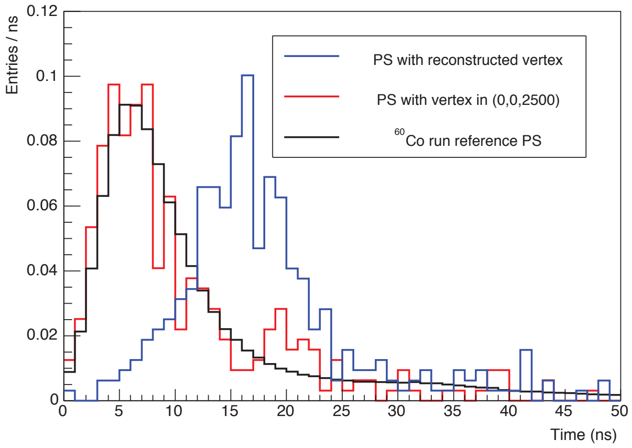

(a) Stopping muon PS (prompt signal).

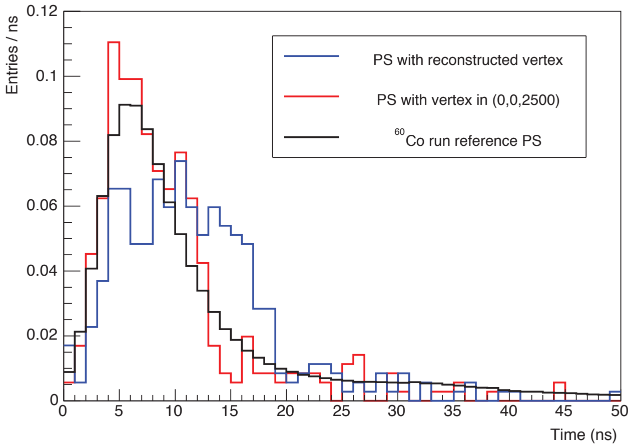

(b) Stopping muon PS (delayed signal).

Figure 43: Comparison between the PS computed using the reconstructed vertex (blue) and the PS computed using a vertex 2500 *mm above the centre of the target (red) with a* ^{60}*Co PS (black) taken as reference.*

figure 41b). The sample studied in this section is selected with the candidates selection of DC-II (n-Gd), corresponding to the first 251.25 days of Double Chooz livetime, for a total amount of 9021 events. In addition, data collected in the spans in which the OV was operating and during the remaining part of the livetime are considered separately.

In order to check the reliability of the method, the Gatti's parameter is first computed for the OV sample, which includes stopping muons and fast neutrons. The results (figure 44a) emphasize a clear separation between stopping muons - which have short prompt-delayed Δt- and fast neutrons. On a total sample of 100 OV events, 60 are selected as stopping muons, for a round fraction of 60% and a stopping muons on fast neutrons ratio of 1.5. The Gatti's method is then applied on the neutrino candidates, to directly look for a stopping muon untagged component.

The results of the same analysis on the sample corresponding to the DC-II (n-Gd) selection of Ref. [157], for the phases with a working OV, i.e. 173.03 days of livetime, are shown in figure 44b. 75 events out of 5894 are found to have a negative Gatti's parameter, corresponding to a rate of 0.43 ± 0.05[67] events per day. The two samples of figure 44 correspond to the same livetime period, since an active OV is needed to select OV stopping muons. The same study, but for the phase without the OV of DC-II (n-Gd), with 78.22 days livetime, gives a number of events with a negative Gatti's parameter of 65 out of 3027, for a rate of 0.83 ± 0.10 events per day. This is shown in figure 45.

An important thing to clarify at this stage, is that the events selected in this way may not only include stopping muons, but also events for which a bias in the vertex reconstruction induce a distortion of the PS that is similar to the one occurring for the events of such background. This is evidenced by the presence of events with negative Gatti's output values and a large prompt-delayed time correlation in figures 44b and 45. On the other hand, we can use the information of the PS re-computed with the vertex in the chimney, like the ones with red curves in figure 43, to distinguish between these two events categories. In particular, it is reasonable to expect that stopping muons will have a positive Gatti's output for the PS with the vertex imposed in the chimney, while other events will keep having negative values.

In figures 46 we can see the distributions of Gatti's parameters of PSs re-computed with a vertex in the chimney, for events which had negative values for the original PS, in the with-OV (figure 46a) and without-OV (figure 46b) phases. We see how in both

---

[67] Unless specified otherwise, errors on calculated rates are statistical only.

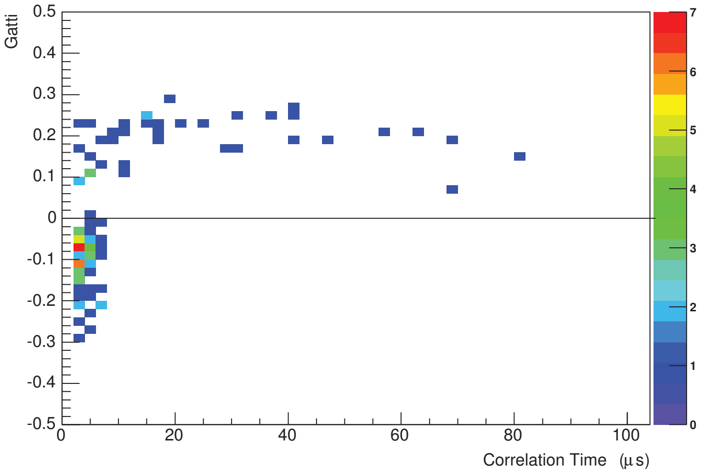

(a) Gatti's parameter for the OV tag sample.

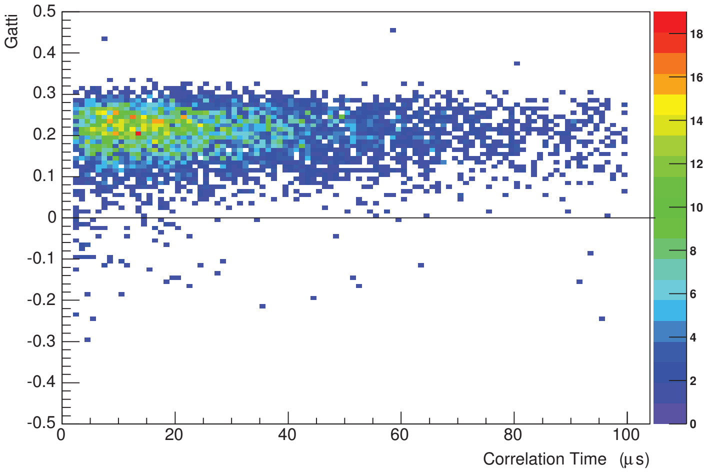

(b) Gatti's parameter for the neutrino sample.

Figure 44: Values of the Gatti's parameter, as a function of the prompt-delayed Δt, for neutrino candidates and the candidates with a coincident OV trigger on the prompt signal, of the DC-II (n-Gd) selection in the with-OV phase (173.03 days livetime). Events with a negative parameter (below the black line) have a stopping-muon like PS according to the Gatti analysis.

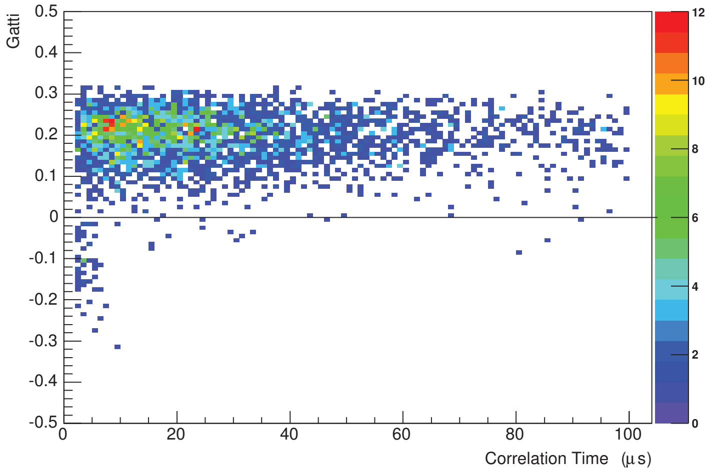

Figure 45: Values of the Gatti's parameter, as a function of the prompt-delayed Δt, for neutrino candidates, of the DC-II (n-Gd) selection in the without-OV phase (78.22 days livetime). Events with a negative parameter (below the black line) have a stopping-muon like PS according to the Gatti analysis.

cases a subsample shows now positive values, meaning that the new PSs are now neutrino-like, and it is characterized by a short Δt. The number of such events is 24 for the with-OV phase and 45 in the without-OV phase, for a rate of 0.139 ± 0.028 and 0.575 ± 0.086 events per day respectively. The rate of these stopping muon events differs for the two OV periods, being higher in the latter case, as we expect since the OV tags most of these events. This difference is, in fact, compatible with the stopping muons selection rate of the OV, which can be estimated using the number of OV coincidences and the fraction of tagged stopping muons in Ref. [157, Section 5D], and is 0.35 ± 0.04 events per day. A summary of the various rates is given in table 13.

Sample	Stopping muons rate (day^{-1})
IBD (with-OV)	0.139 ± 0.028
OV tagged	0.35 ± 0.04
Total (with-OV)	0.49 ± 0.05
IBD (without-OV)	0.575 ± 0.086

Table 13: Comparison of stopping muons rates obtained with the Gatti analysis and the OV tag for different samples.

The study of the stopping muons PS discrepancy conducted so far, has shown how the vertex reconstruction affects the PSs of this background. On the other hand, the vertex reconstruction itself is based on the pulses arrival time and charge. It is therefore plausible that the study on the PS is related to the vertex reconstruction

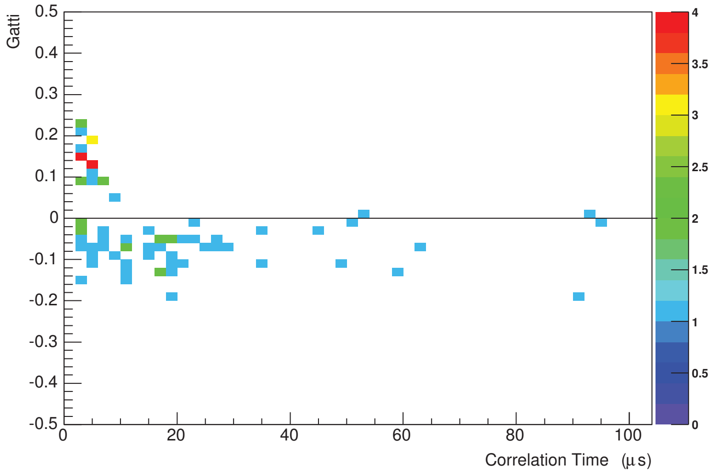

(a) with-OV phase (173.03 days livetime).

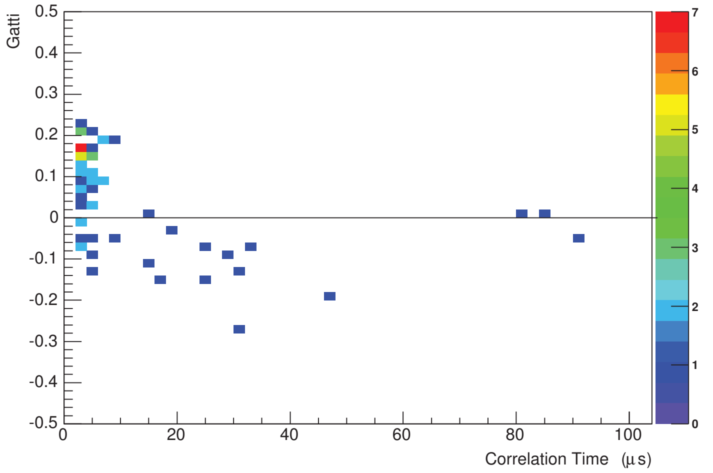

(b) without-OV phase (78.22 days livetime).

Figure 46: Values of the Gatti's parameter, as a function of the prompt-delayed Δt, for neutrino candidates, of the DC-II (n-Gd) selection in the two OV phases (with-OV and without-OV), once the PS is re-computed with a vertex 2500 mm above the centre of the detector. Events that now display a positive parameter (above the black line) have a neutrino-like PS with the vertex in the chimney.

algorithm; and this is in fact what is observed. The goodness of the vertex reconstruction is represented by a functional value, or FuncV, defined in equation 55, section 2.3.2. Not only the FuncV is generally higher for the delayed signal of stopping muons with respect to the one of IBD events, but it is also strongly correlated with the results obtained with the Gatti's method. A representation of this correspondence is given in figure 47, where the two variables are compared for the OV sample. Events with large FuncV have a negative Gatti's output as well, and are characterized by the typical short correlation time of stopping muons.

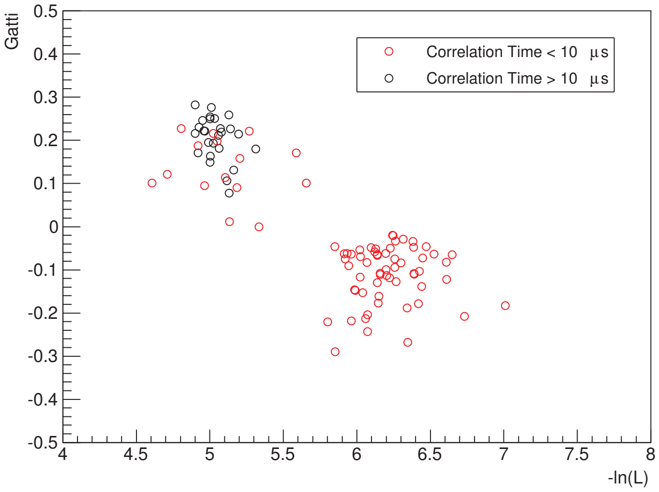

Figure 47: Correlation between the Gatti's method output and the FuncV (–ln(L)) *for the OV sample. Events with a short prompt-delayed* Δt *are featured in red, the others in black.*

The results shown in this section proved the capability of the Gatti's method to disentangle stopping muons in the neutrino candidates selection. The tagged stopping muons rate in agreement with the expectations, combined with the correlation of the Gatti's method with the FuncV, led to a big effort in terms of study of this latter variable. Figure 48 shows the energy as a function of FuncV of the delayed signal of the DC-II (n-Gd) IBD sample. In the plot, the most populated band on the left, with FuncV $\sim$ 5, represent the IBDs, while stopping muons appear to form another band at higher FuncV values ($\sim$ 6). The last events scattered on the right (FuncV > 7) are part of another background, the light noise (described in section 3.2.1), which has not been addressed by the Gatti analysis but will be object of study later in this chapter.

A cut based on the delayed visible energy and the FuncV on the delayed vertex reconstruction has been proved to have a capability in disentangling stopping muons comparable to the one of the Gatti's method. On the other hand, the vertex recon-

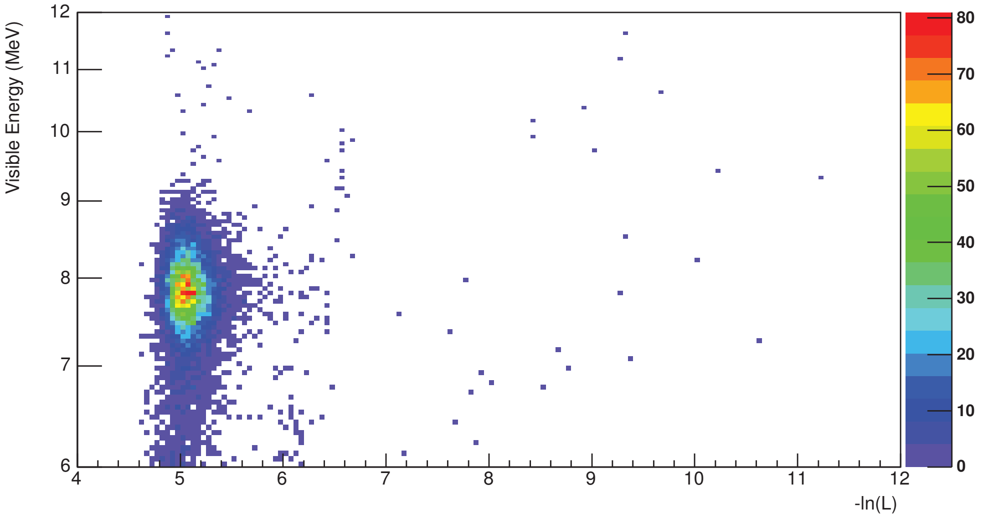

Figure 48: Energy of the delayed signal, in log scale, as a function of the delayed vertex FuncV (–ln(L)) *of the DC-II (n-Gd) candidates selection.*

struction, as well as the FuncV, was already embedded in the Double Chooz offline software, while the Gatti analysis had to be implemented. For these reasons a FuncV-based cut has been included in the candidates selection of the third Double Chooz gadolinium publication, or DC-III (n-Gd) [160].

4.2.3 Stopping muon selection using a likelihood approach

From now on, for the rest of this section 4.2, we will study the sample corresponding to the DC-III (n-Gd) candidates selection [160]. The entire livetime of DC-III will be studied, i.e. 467.90 days, for a total amount of 17358 neutrino candidates for the n-Gd analysis. On this selection, the FuncV cut discussed before had a strong impact, being responsible for the removal of 666 background events, i.e. 1.42 ± 0.06 events per day. The largest fraction of the sample of candidates rejected by the FuncV cut ($\sim 80\%$) consists of stopping muons, the rest being accidental coincidences with light noise single events. This number must not be compared with stopping muon rates we found in the previous section 4.2.2, which were estimated for DC-II (n-Gd) sample. In fact, as mentioned on multiple occasions in the description of the Double Chooz analysis (chapter 3), DC-III uses a wider IBD selection with respect to the antecedent DC-II, with backgrounds eliminated by more efficient vetoes.

In this and the next sections, however, we will provide a new PS-based background study on the DC-III candidates. In fact, a cross check on the FuncV cut with an independent analysis may lead to a more solid understanding of the stopping muons background. Furthermore, an improvement of the previous analysis could give better results in terms of stopping muons separation with respect to the FuncV cut, enhancing the signal-on-background ratio. A second analysis has therefore been developed; it is a pulse shape analysis that uses a likelihood approach, comparing the PS with a reference one. That reference is the ^{60}Co calibration run cumulative PS used so far.

Figure 43 shows how the PS of a stopping muon depends on the reconstructed vertex, and, in particular, how moving the vertex in the chimney, in that case 2500 mm above the centre of the target, results in a better agreement between the PS and the one expected for an electron/gamma event. The agreement can be measured with a negative log-likelihood, with the reference PS used as probability density function, or PDF, $f_{PS}(t)$. In particular, the likelihood that the PS is electron-like can be calculated as follows: first, the ^{60}Co cumulative PS, normalized to one, is taken as a discrete PDF $f_{Co}(t)$ (because of the binning); then, the additive inverse of the log-likelihood is computed as:

$$L = -\frac{\sum_i^n \ln f_{Co}(t_i)}{n}\,, \tag{81}$$

where $f_{Co}(t_i)$ is the bin content of the ^{60}Co reference PS corresponding to the t_i pulse time, and n the total number of pulses, of the PS. A lower value of L represents a better correspondence between the given PS and the reference one[68].

A comparison between the PS with the reconstructed vertex and the one with the vertex set in the chimney could therefore be given by the confrontation of the log-likelihood computed in the two cases. We call L_{reco} the value L of equation 81 for the PS with the vertex reconstructed by the official algorithm, and L_{chm} the value L for the PS re-computed with the vertex set 2500 mm above the centre of the detector target. For a stopping muon, a better agreement with the reference for the latter PS is expected, meaning a L_{chm} lower than L_{reco}. Such is the case of the PSs in figure 43, for which the values obtained are $L_{chm} = 3.83$ and $L_{reco} = 4.20$ for the prompt signal (43a) and $L_{chm} = 4.03$ and $L_{reco} = 5.02$ for the delayed signal (43b). Positions other than 2500 mm above the centre of the target and inside the chimney have been alternatively used to compute L_{chm}, giving similar results in all the analyses based on this approach showed in this chapter.

This method is in principle more reliable than the Gatti's one. In fact, a misreconstructed vertex for a non stopping muon event can in principle produce a de-

---

[68] Since the PDF has integral = 1, the logarithm gives negative numbers. So, for a PS that is in good (bad) agreement with the reference, the sum of negative numbers, with small (large) absolute values, gives a small (large) L.

formation in the PS comparable with one occurring for the stoppping muons, resulting in a negative output in the Gatti's method. By requiring instead a lower L_{chm} than L_{reco}, i.e. a L_{chm}/L_{reco} ratio lower than one, we intrinsically demand the event actual vertex to be more likely located in the chimney. This fact, other than providing a stronger hint of a stopping muon PS behaviour, is also valid for the prompt and delayed signal indifferently, meaning that the same information on the prompt PS can be exploited as well. The Gatti's method, as well as the FuncV cut, instead, are applied only on the delayed signal, since the effect that they exploit (the PS distortion in the case of the Gatti's method) can have different causes, being not solely a stopping muons feature (fast neutrons, ortho-positronium).

Considering this, for the purpose of this likelihood analysis, the sum of the L_{chm}/L_{reco} ratio of the prompt ($(L_{chm}/L_{reco})_p$) and the delayed ($(L_{chm}/L_{reco})_d$) will be studied. For a stopping muon, this sum is expected to be less than 2. This is done in figure 49, in which $(L_{chm}/L_{reco})_p + (L_{chm}/L_{reco})_d$ is shown as a function of the prompt-delayed correlation time Δt for the DC-III (n-Gd) neutrino candidate sample, with and without the FuncV cut applied. By looking at this distribution for IBD candidates (figure 49a), it is possible to distinguish three populations:

1. a population of stopping muons, with $(L_{chm}/L_{reco})_p + (L_{chm}/L_{reco})_d < 2$ and the typical short Δt;
2. a small amount of events with $(L_{chm}/L_{reco})_p + (L_{chm}/L_{reco})_d < 2$ and large Δt values;
3. the whole cluster of neutrinos at $(L_{chm}/L_{reco})_p + (L_{chm}/L_{reco})_d > 2$.

Further light on the nature of these populations will be shed in the next section. Before going into that, we will apply a simple cut based on the assumptions made on the $(L_{chm}/L_{reco})_p + (L_{chm}/L_{reco})_d$ value, which are supported by what represented in figure 49. In particular, we observe that a stopping muons selection with the requirement:

$$(L_{chm}/L_{reco})_p + (L_{chm}/L_{reco})_d < 2 \tag{82}$$

identifies 47 stopping muons in the DC-III (n-Gd) neutrino candidates selection (figure 49a). This corresponds, given the total livetime of 467.90 days, to a rate of 0.100 ± 0.015 events per day. If we include in the sample the events removed by the FuncV cut discussed before, the total number of events selected by the likelihood cut is 648 (figure 49b), for a rate of 1.385 ± 0.053 events per day. The impact of the likelihood analysis on events removed by the FuncV cut will be discussed in further details later, in order to compare the two different stopping muons selections.

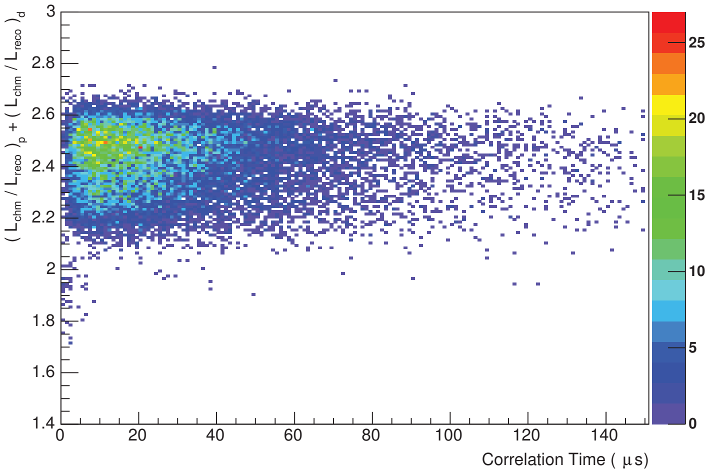

(a) DC-III (n-Gd) IBD candidates selection, including FuncV cut.

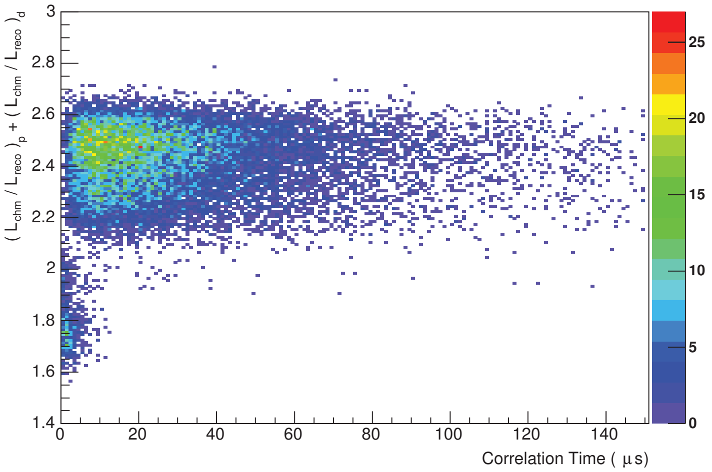

(b) DC-III (n-Gd) IBD candidates selection without FuncV cut.

Figure 49: Sum of the prompt and the delayed ratio between L_{chm} and L_{reco}, as a function of prompt-delayed Δt, for neutrino candidates of the DC-III (n-Gd) selection with and without the FuncV cut applied.

4.2.4 Improved likelihood analysis using vertex position

A reasonable assumption about the behaviour of the L_{chm}/L_{reco} variable is that it depends on the distance between the reconstructed vertex and the one in which L_{chm} is computed. In fact, a vertex of a stopping muon event reconstructed far from the chimney (its actual position) will result in a higher L_{reco} value, thus in a lower L_{chm}/L_{reco} ratio, than a vertex reconstructed close to the chimney. Conversely, for a neutrino event located far from the chimney, the value of L_{chm} will be higher, meaning a higher L_{chm}/L_{reco}, with respect of a neutrino interacting close to the chimney.

To see this effect, the $(L_{chm}/L_{reco})_p + (L_{chm}/L_{reco})_d$ distribution of the neutrino candidates is shown in figure 50 as a function of the distance of the reconstructed prompt vertex from the chimney $\mid\left(\bar{X}_{reco}\right)_p - \left(\bar{X}_{chm}\right)_p\mid$, plus the distance of the reconstructed delayed vertex from the chimney $\mid\left(\bar{X}_{reco}\right)_d - \left(\bar{X}_{chm}\right)_d\mid$, with

$$\left|\left(\bar{X}_{reco}\right) - \left(\bar{X}_{chm}\right)\right| = |x_{reco}{}^{\smile}x_{chm}|^2 + |y_{reco}{}^{\smile}y_{chm}|^2 + |z_{reco}{}^{\smile}z_{chm}|^2 . \tag{83}$$

By looking at the distribution, it is possible to see how neutrino events have higher (L_{chm}/L_{reco}) as the distance of their vertices from the chimney increase. Another smaller population of events characterized by a small Δt has instead an opposite behaviour, decreasing in (L_{chm}/L_{reco}) when reconstructed further from the chimney, as expected for stopping muons. These events also correspond to the 1^{st} population (stopping muons) in figure 49a. The separation in $(L_{chm}/L_{reco})_p + (L_{chm}/L_{reco})_d$ between neutrinos and stopping muons vanishes when $\mid\left(\bar{X}_{reco}\right)_p - \left(\bar{X}_{chm}\right)_p\mid + \mid\left(\bar{X}_{reco}\right)_d - \left(\bar{X}_{chm}\right)_d\mid$ approaches 2500 mm. In this region, we can observe events with high Δt and $(L_{chm}/L_{reco})_p + (L_{chm}/L_{reco})_d < 2$. These events correspond to the 2^{nd} population in figure 49a. In order to avoid to select such events, a conservative cut on $(L_{chm}/L_{reco})_p + (L_{chm}/L_{reco})_d$ (1.9 rather than 2) is needed.

Another aspect shown by the distribution of figure 50 is that the cut proposed before in equations 82 inevitably select neutrino events, characterized by a higher Δt, in the region where $\mid\left(\bar{X}_{reco}\right)_p - \left(\bar{X}_{chm}\right)_p\mid + \mid\left(\bar{X}_{reco}\right)_d - \left(\bar{X}_{chm}\right)_d\mid$ approaches to 2000 mm. Such limit can be overcame by replacing, in the space of figure 50, a straight line cut with a diagonal one that preserves events close to the chimney with high Δt from being selected as stopping muons.

A two-dimensional cut on the $(L_{chm}/L_{reco})_p + (L_{chm}/L_{reco})_d$ vs $\mid\left(\bar{X}_{reco}\right)_p - \left(\bar{X}_{chm}\right)_p\mid + \mid\left(\bar{X}_{reco}\right)_d - \left(\bar{X}_{chm}\right)_d\mid$ phase-space will be discussed later on, applied to the IBD sample, and compared with the FuncV cut. For the sake of compactness of this text, we will exploit the peculiar shape of the plot in figure 50 to nick-name the distribution *chili*

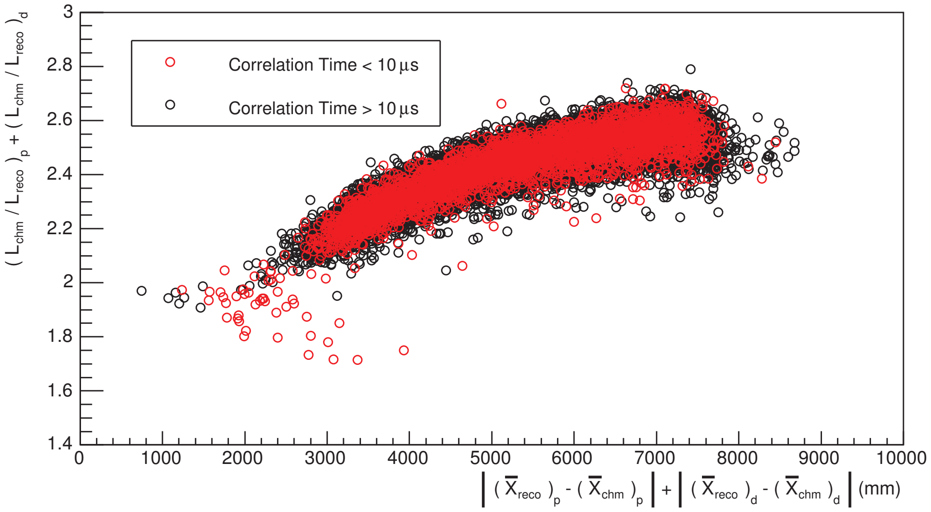

Figure 50: Chili plot, or sum of the prompt and the delayed ratio between L_{chm} and L_{reco}, as a function of the sum of the prompt and the delayed vertices distance from the chimney $\left|(\bar{X}_{reco}) - (\bar{X}_{chm})\right|$, for neutrino candidates of the DC-III (n-Gd) selection. Events with short prompt-delayed Δt are featured in red.

plot, as we will do from now on.

4.2.5 An extension of the likelihood approach: the vertex scan

The likelihood approach examined so far compares the PS with the reconstructed vertex with the PS with the vertex in the chimney, in order to identify stopping muons, for which the vertex is systematically poorly reconstructed. This approach can be extended from the chimney to the whole target by scanning it with a certain step, re-computing the PS in each position i of the scan, and calculating the negative log-likelihood L_i. We can then define a best likelihood vertex (X_{best}) as the position in the target that gives the smallest value of L_i, i.e. the vertex that gives the best agreement between the event PS and the reference.

Vertices computed in this way have a lower resolution (25 cm) with respect to the ones reconstructed with the Double Chooz algorithm (12 – 17 cm, depending on the event energy)[69]. On the other hand, the PS best likelihood vertex can be a relevant information in case the normal reconstruction algorithm does not work properly, such as for stopping muons.

Figure 51 shows the values of X_{best} for the 47 events that have been selected

---

[69] Vertex resolutions are evaluated on one axis using calibration sources.

with the log-likelihood cut discussed in section 4.2.3. As expected, most part of the X_{best} are located in the chimney, i.e. the position in which these events actually occur. The scanning area used to obtain the results of figure 51 has been chosen to match the contour of the inner target, with the addition of the chimney area. A scheme representing the chimney can be found in figure 22 of section 2.2.1. Other scanning area have been tested as well, for example, by relaxing its boundaries to include a larger region. In all cases the resulting values X_{best} are not significantly far from the ones of figure 51, providing further confirmation of the assumptions made so far on stopping muons.

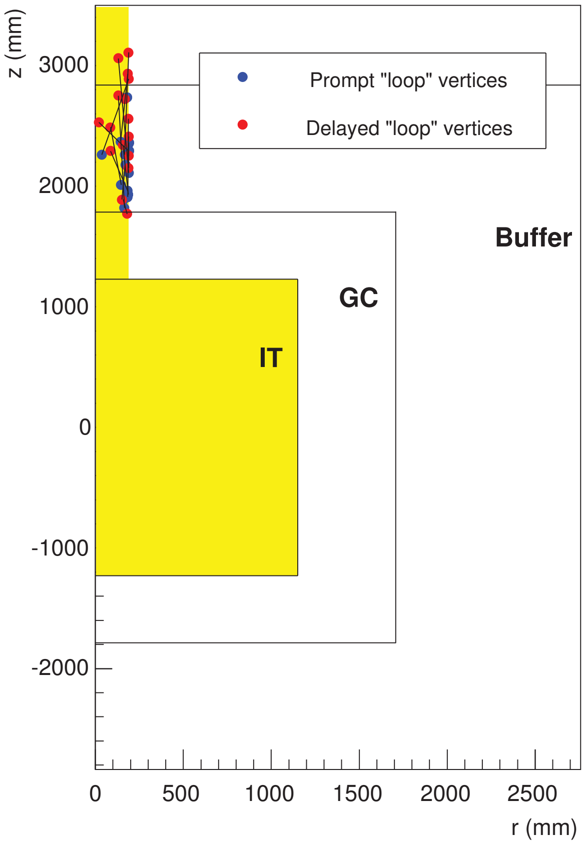

Figure 51: Best likelihood vertices, based on the PS analysis, for the 47 stopping muons selected with the PS log-likelihood cut. The scanned area is coloured in yellow.

4.2.6 Cross-check on the FuncV cut

We applied the likelihood-based stopping muon selection on the full live time of the DC-III (n-Gd) candidates selection (467.90 days), which has most of the stopping muons removed by the FuncV cut. However, 47 additional events are removed, corresponding to a rate of 0.100 ± 0.015 events per day. This in addition to the 666 events (1.42 ± 0.06 per day) already removed by the FuncV cut, of which however only 80% consists of stopping muons.

In order to fully compare the PS log-likelihood and the FuncV cut, we want to test the former on the stopping muons population removed by the latter. As a first step, only events removed by the FuncV cut are taken into account, corresponding to a sample of 666 events. The distribution of $(L_{chm}/L_{reco})_p + (L_{chm}/L_{reco})_d$ as a function of $|\left(\bar{X}_{reco}\right)_p - \left(\bar{X}_{chm}\right)_p| + |\left(\bar{X}_{reco}\right)_d - \left(\bar{X}_{chm}\right)_d|$ for such sample is shown in figure 52. The distribution shows three distinct populations, separated in the figure by rectangular outlines:

1. a substantial population (507 events) of stopping muons, all characterized by a short Δt;
2. another isolated cluster (128 events) with high $\left|\left(\bar{X}_{reco}\right) - \left(\bar{X}_{chm}\right)\right|$ and middle L_{chm}/L_{reco} values, which can be identified as light noise (corresponds to the light noise band in figure 48);
3. a small population (31 events) in the position of the phase-space occupied by neutrinos.

A characterization of these samples is given in figures 53 and 54, where the prompt-delayed correlation time Δt (figure 53), and the prompt visible energy (figure 54) of the three populations are shown. An exponential fit made on the stopping muon sample returns a value of the mean lifetime of $2.022 \pm 0.100\,\mu$s that is in reasonable agreement with the muon mean lifetime ($2.197\,\mu$s), and a reduced χ^2 of 0.55.

The large amount of stopping muons with a $(L_{chm}/L_{reco})_p + (L_{chm}/L_{reco})_d \leq 1.9$ (1^{st} population) shows the possible agreement on stopping muons identification between the PS log-likelihood cut proposed before and the FuncV cut. Furthermore, it is interesting to see how in the phase-space of figure 52 the light noise background (2^{nd} population) - which corresponds to the light noise band in figure 48 - is clustered in a specific position at high $\left|\left(\bar{X}_{reco}\right) - \left(\bar{X}_{chm}\right)\right|$ values. By comparing figures 50 and 52 this position looks distant from the neutrino cluster. It is therefore possible to select light noise with a cut based on the likelihood analysis. However, this cut must be

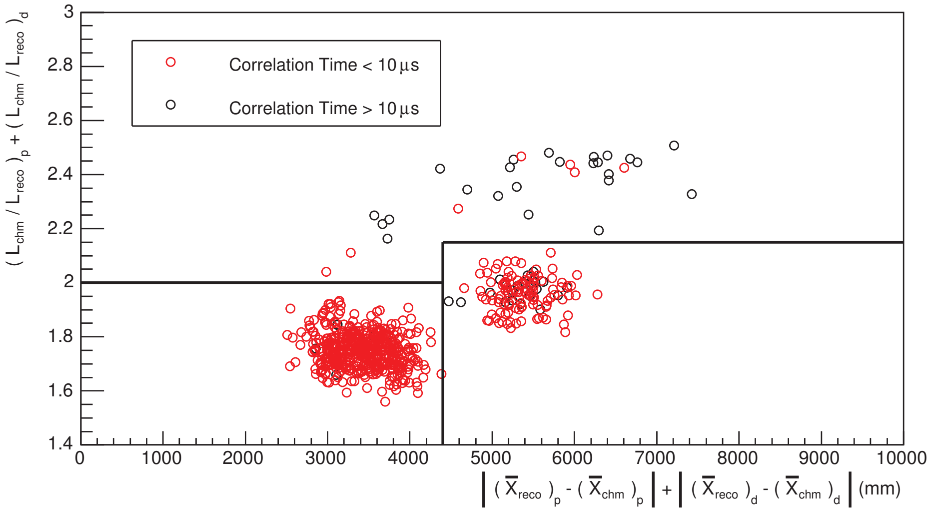

Figure 52: Chili plot of candidates selected by the FuncV cut, with events characterized by a short prompt-delayed Δt featured in red. Stopping muons (bottom left box) and light noise (bottom right box) are clearly visible, as well as a third population in the neutrino (upper) phase-space position (see figure 49a).

different from the one developed in the previous section, since these events have higher L_{chm}/L_{reco} values than stopping muons. Finally, there is a third population of events in the position occupied by neutrinos in figure 50. The small size of this family (31 events) is not sufficient to make any conclusive statement about its nature, although the Δt distribution suggests they are not stopping muons (figure 53) and the energy spectrum is similar to the IBD one (figure 54). Nonetheless, the number of these events is fully compatible with the FuncV cut inefficiency of IBD events, which is estimated to be 32.1 ± 6.0 events [160, Section 4.3]).

The observations made so far, based on figures 50 and 52, can be resumed in these statements:

- a cut on $(L_{chm}/L_{reco})_p + (L_{chm}/L_{reco})_d$ can separate some stopping muons from the neutrino sample, as well as tag the stopping muons already removed by the FuncV cut;
- in the region of low $\left|(\bar{X}_{reco}) - (\bar{X}_{chm})\right|$ the populations of neutrinos and stopping muons are more mixed, making that cut less powerful,
- a different cut on $(L_{chm}/L_{reco})_p + (L_{chm}/L_{reco})_d$ could also tag the light noise already removed by the FuncV and other cuts.

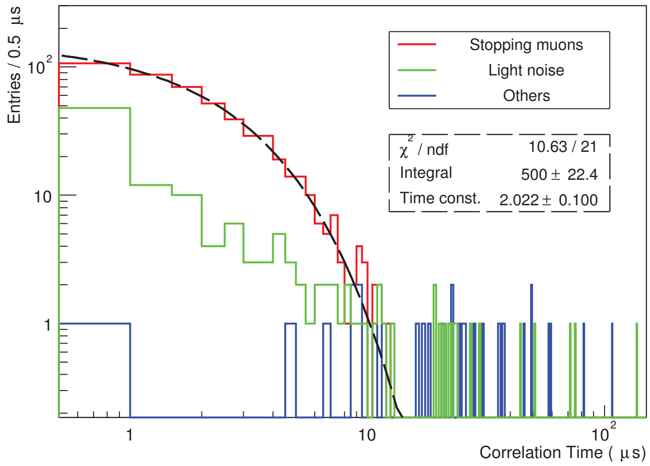

Figure 53: Δt distributions of events selected by the FuncV cut, separated in the three sub-samples previously observed in figure 52: stopping muons (red), light noise (green) and other events located in the neutrinos position (blue). An exponential fit on stopping muons (dashed black line) returns a mean lifetime of 2.022 ± 0.100 *μs.*

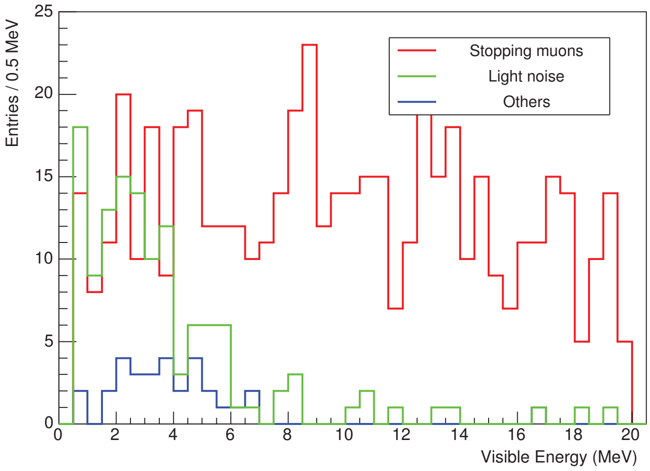

Figure 54: Prompt energy distributions of events selected by the FuncV cut, separated in the three sub-samples previously observed in figure 52: stopping muons (red), light noise (green) and other events located in the neutrinos position (blue).

That being so, we can build a cut in the *chili plot* to select light noise and stopping muons at the same time. Figure 55 shows the distribution of $(L_{chm}/L_{reco})_p + (L_{chm}/L_{reco})_d$ as a function of $|\left(\bar{X}_{reco}\right)_p - \left(\bar{X}_{chm}\right)_p| + |\left(\bar{X}_{reco}\right)_d - \left(\bar{X}_{chm}\right)_d|$ for all neutrino candidates, including events removed by the FuncV cut. A PS log-likelihood cut defined as

$$\begin{array}{ll} y < x/12500\,\text{mm} + 1.75 & x \leq 5000\,\text{mm} \\ y < 2.15 & x > 5000\,\text{mm}\,, \end{array} \tag{84}$$

with

$$\begin{array}{c} y = (L_{chm}/L_{reco})_p + (L_{chm}/L_{reco})_d \\ x = |\left(\bar{X}_{reco}\right)_p - \left(\bar{X}_{chm}\right)_p| + |\left(\bar{X}_{reco}\right)_d - \left(\bar{X}_{chm}\right)_d| \quad , \end{array} \tag{85}$$

which is represented in figure 55, removes a number of 657 events. The selected sample consists in stopping muons and light noise, for a rate of 1.40 ± 0.06 events per day. These numbers are in perfect agreement with the removed events number and rate of the FuncV cut, as shown in table 14.

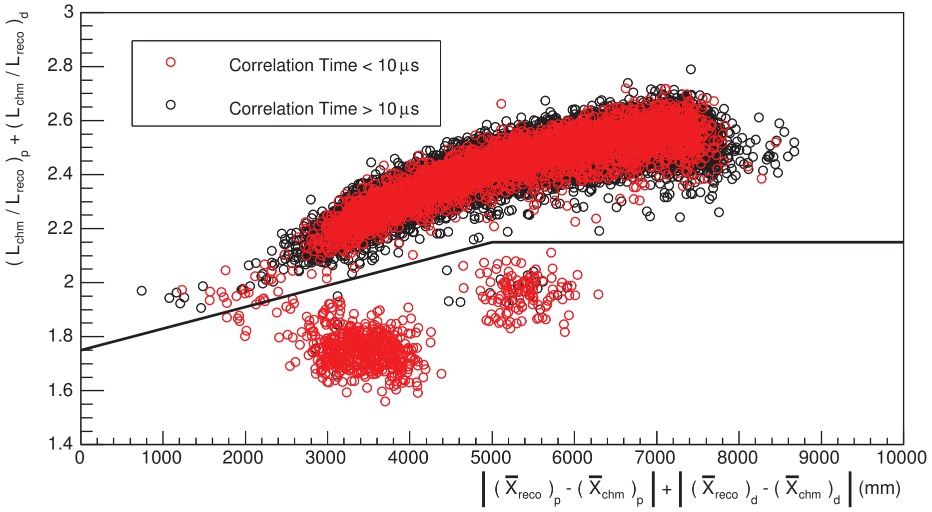

Figure 55: Chili plot of all DC-III (n-Gd) neutrino candidates, including events removed by the FuncV cut. A 2D cut (black solid line) disentangles stopping muons and light noise from neutrinos.

Another depiction of the FuncV and PS log-likelihood comparison is given in figure 56. The picture shows the FuncV variable on the delayed events as a function of the event delayed visible energy, as for figure 48. In addition, events selected by the

Cut	Removed events	Rate (day^{-1})
FuncV	666	1.42 ± 0.06
PS log-likelihood	657	1.40 ± 0.06

Table 14: FuncV and PS log-likelihood cut comparison in terms of removed events on DC-III (n-Gd).

PS log-likelihood cut discussed here are featured with a different colour. In figure 56 appears that:

- events in the light noise band are fully selected by the likelihood;
- events in the stopping muon band are also selected, excepted the 31 events in the upper part of figure 52;
- 22 events in the neutrino band are selected with the PS log-likelihood over the FuncV cut.

The discrepancy of 9 events between the two selections showed in table 14 is therefore given by the 31 events removed by the FuncV cut but not by the likelihood cut minus the 22 for which occurs the opposite condition. This discrepancy is entirely located in the stopping muons sector, since for the light noise the number of events removed by the two cuts perfectly matches. Given this, a detailed comparison can be made by looking at the stopping muons selection made by the two respective cuts. In particular we compare the stopping muon band of figure 48, which is selected by requiring the delayed visible energy E_d to be

$$0.068 \cdot e^{FuncV/1.23} > E_d > 0.038 \cdot e^{FuncV/1.23} \,, \tag{86}$$

and the stopping muons cluster at low L_{chm}/L_{reco} and low $\left|\left(\bar{X}_{reco}\right) - \left(\bar{X}_{chm}\right)\right|$ in figure 55, which we obtain from equation 84 limiting to events that satisfy

$$|\left(\bar{X}_{reco}\right)_p - \left(\bar{X}_{chm}\right)_p| + |\left(\bar{X}_{reco}\right)_d - \left(\bar{X}_{chm}\right)_d| < 4400\,\text{mm}\,. \tag{87}$$

This corresponds to figure 57, in which the two populations of stopping muons selected by the FuncV (57a) and the PS log-likelihood two-dimensional cut (57b), are shown in terms of their Δt distributions, which are fitted with an exponential function. The results of the two fits, given in table 15, are both in agreement with the muon mean lifetime, as expected for stopping muon events. On the other hand, some events selected by the FuncV cut have a large Δt, resulting in a higher χ^2 for the fit made on this population. These events obviously correspond to the 31 possible neutrinos selected by the FuncV cut.

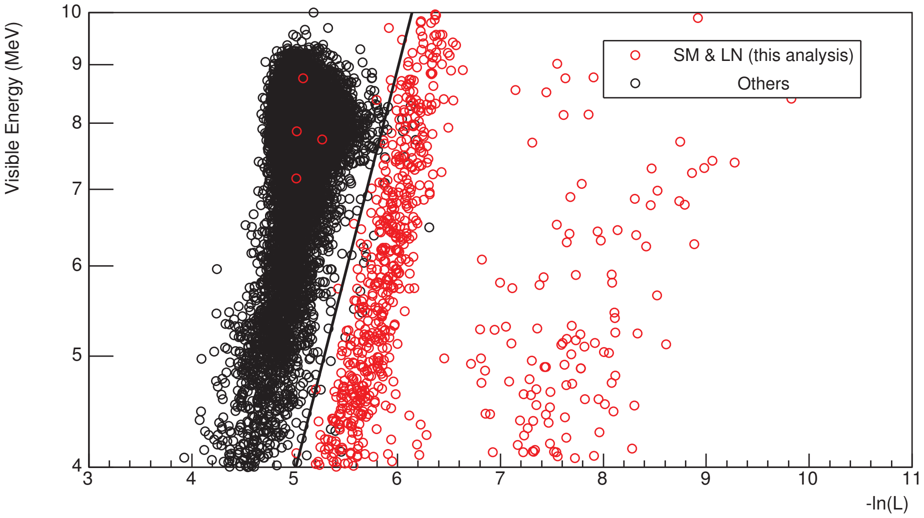

Figure 56: Delayed energy, in log scale, as a function of the delayed FuncV (–ln(L)) *of the neutrino candidates obtained from the DC-III (n-Gd) selection excluding the FuncV cut (solid line). Events tagged by the PS log-likelihood cut are shown in red, the rest being in black. This selection tags the entire light noise band, as well as a large fraction of the stopping muons band (657 total events). 22 events in the neutrino band are also tagged as stopping muons.*

	μ lifetime	χ^2/ndf
Fit on FuncV cut SM	$2.08 \pm 0.11\,\mu$s	0.89
Fit on PS log-likelihood SM	$2.06 \pm 0.10\,\mu$s	0.41
Measured in Ref. [202]	$2.197\,\mu$s	

Table 15: Results of the fits made on the stopping muon populations selected by the FuncV and the log-likelihood cuts, compared with the muon mean lifetime.

4.2.7 Final considerations

In conclusion, the likelihood approach provides a broad understanding of the stopping muons background. These events can be clearly identified by looking at the agreement of the PS with a reference. On the full livetime of the DC-III (n-Gd) candidates selection a cut based only on the log-likelihood ratio between the PS with the reconstructed vertex and the one with the vertex placed in the chimney selects 47 events, with a good degree of confidence. However, such selection induces inefficiency due

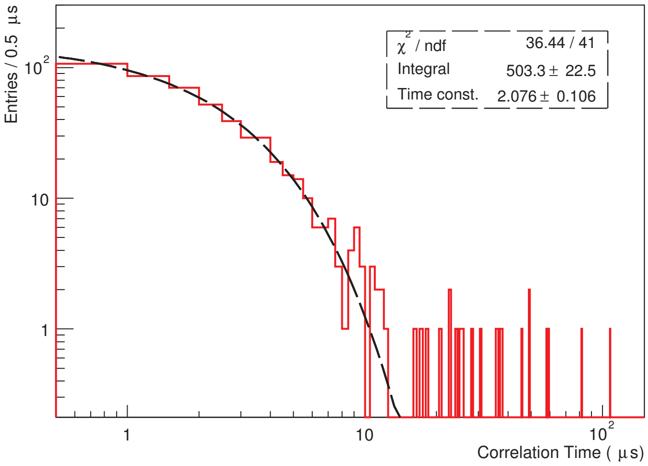

(a) FuncV cut stopping muons selection

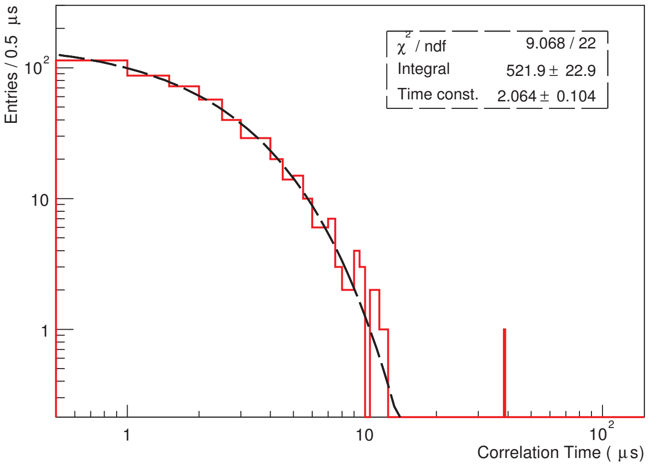

(b) PS log-likelihood stopping muons selection

Figure 57: Δt log-scale distribution of the two stopping muon populations selected by the FuncV and the log-likelihood cuts. Each population is fitted with an exponential curve.

to its limit in separating events that are close to the chimney. A more precise cut can be developed by taking into account the distance between the reconstructed vertex and the chimney. This cut not only provides a better separation of the stopping muon contamination in the neutrino sample, but is also able to disentangle the light noise background. On the full candidate sample, excluding the FuncV cut, it is capable to removes 657 events. This analysis is fully compatible with the FuncV one: the results of the two analyses perfectly match on light noise events, and are very similar for stopping muons, although the PS log-likelihood cut selects a purer sample of stopping muons. In the next section, we will see how the application of a similar analysis on the hydrogen sample can be used to estimate the number of stopping muons left in the candidates.

4.3 Study of the stopping muon background in the n-H analysis

We now apply the arguments discussed so far to the Double Chooz n-H analysis, i.e. the selection of candidates in which the neutron from the IBD is captured on hydrogen. The studied sample corresponds to the DC-III livetime and the candidate selection that uses the neutron capture hydrogen. We already described the different IBD candidate selections in section 3.2. In a few words, the n-H selection differs from the n-Gd one in many ways, the most important being the different vertex distribution (mostly in the gamma catcher), delayed energy (2.22 MeV for the n-capture on hydrogen), and Δt window. Accordingly, to separate stopping muons from neutrinos, we would need slightly different criteria than the ones used for the Gd analysis. In this section, we derive a stopping muons selection similar to the one given by equations 84, tuned on the n-H analysis. The goal is to make a precise estimation of the number of stopping muons left in the neutrino sample once the candidates selection of DC-III (n-H) is applied. In order to do that, we will first tune a selection on a sample of events tagged by the OV; then test it on a series of other samples; and finally apply it to neutrino candidates. The number of estimated stopping muons, i.e. the number of events that we will select with a PS log-likelihood analysis, is used to validate the cuts and as input value for the final fit of the forthcoming DC-III (n-H) publication. An evaluation of the errors on the stopping muons estimation, which will be calculated by studying the efficiency and inefficiency of the selection, will be shown here as well.

4.3.1 The likelihood approach applied to the H sample

The first step to estimate the number of stopping muons left in the candidates sample of DC-III (n-H), is to tune a selection based on the PS log-likelihood variables introduced previously. To do that, we study stopping muons separation criteria on an OV sample similar to the one of section 4.1.3; in other words, we look at all events passing the IBD selection, but with an OV trigger in coincidence with the prompt signal. This sample is composed by stopping muons and fast neutrons, with the second component being dominant due to the fact that a FuncV cut is applied in DC-III (n-H) as well. Once the variables L_{chm} and L_{reco} are computed using the ^{60}Co reference PS, a *chili plot* is built for such events, as shown in figure 58. In order to separate stopping muons and fast neutrons, a cut in the phase-space of the *chili plot*, similar to the one discussed in section 4.2.6, is consequently fashioned. This cut is represented by the black line in the plot, and by equations

$$\begin{aligned} & y < x/10000\,\mathrm{mm} + 1.6 && x \leq 5000\,\mathrm{mm} \\ & y < 2.1 && x > 5000\,\mathrm{mm}\,, \end{aligned} \tag{88}$$

where x and y are defined in equations 85. It isolates a stopping muon population, characterized by a short prompt-delayed Δt and located in similar area of the equivalent population in figure 55, from fast neutrons (which instead are located in the region occupied by neutrinos). The horizontal cut in the high-x region is kept above 2 in order to address the possible presence of light noise in the n-H sample.

4.3.2 Improved precision using the absolute likelihood values

As additional criterion to improve the precision of the stopping muons selection, we require L_{chm} to be in a range of good values. This is made to exclude events for which both the PS with the reconstructed vertex and the PS with the vertex in the chimney are distorted, meaning a high L_{reco} and L_{chm}, with the latter being smaller for small fluctuations in the first bins.

In order to set a range for L_{chm}, we look at the distribution of L_{reco} values for the prompt and the delayed signals of IBD candidates. This is shown in figure 59a. The two distributions differ, due to the different energy windows, but are both characterized by a dominant Gaussian-like shape followed by a lower tail at higher L_{reco} values. This tail involves a small fraction of events, and represents cases in which the agreement with the ^{60}Co reference, and therefore the vertex reconstruction, is poor. From these distributions, it is possible to infer a maximum value that excludes the tail. The

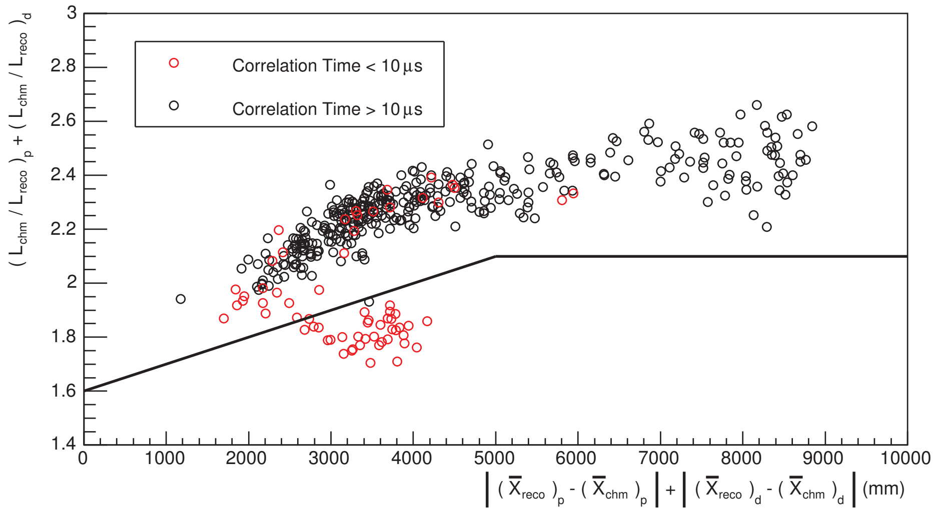

Figure 58: Chili plot of an OV sample in DC-III (n-H). Events with prompt-delayed Δt < 10 μs are featured in red. Stopping muons are separated from fast neutron with a 2D cut represented by the black line.

asymmetry, clearly visible in the log-scale of figure 59a, starts from values around 4.6; therefore, we assume this value as upper limit for the range of good values we wanted to assume.

Neutrino candidates represent a good sample to study a L_{chm} upper limit, since they are isotropically distributed in space and in the energy range of interest. However, as a further cross-check, we can look at the distribution of L_{reco} for ^{60}Co calibration events. The distribution of L_{chm} of events selected from three ^{60}Co calibration runs, with the source deployed in different positions inside the gamma catcher, is shown in figure 59b. A Gaussian fit on ^{60}Co L_{reco} distribution gives a value of $\mu + 3\sigma = 4.57$. Such value is very closed to 4.6, confirming the goodness of the value inferred with the IBD sample.

To sum up, we want to build a stopping muons selection that uses the distribution of the *chili plot* and the absolute values of L_{chm}. To do that, we use the criteria represented by equation 88 with the addition of

$$\begin{aligned} (L_{chm})_p &< 4.6 \\ (L_{chm})_d &< 4.6 \,. \end{aligned} \tag{89}$$

The results of the stopping muons selection made by applying equations 88 and 89 on the OV sample previously defined are the following: 37 events out of 422 are selected

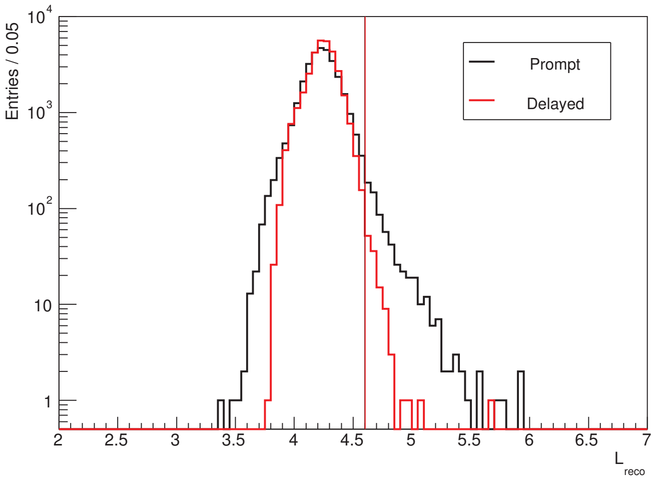

(a) IBD candidates.

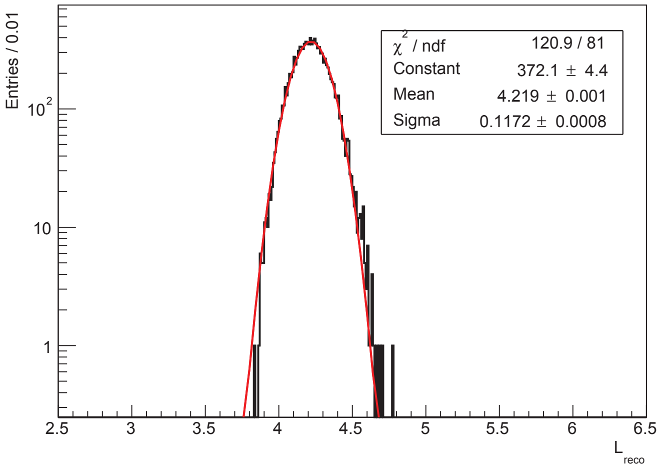

(b) ^{60}Co in the gamma catcher.

Figure 59: Log-scale distribution of absolute values of L_{reco}, for neutrino DC-III (n-H) candidates (top), and of 3 calibration runs with a ^{60}Co source in the gamma catcher (bottom). A Gaussian fit is superimposed on the latter.

as stopping muons, with the remaining 385 being therefore FN. Figure 60 shows the prompt-delayed Δt distributions of the OV sample and its splitting into stopping muons and fast neutrons according to the present analysis. The stopping muons are characterized by a short Δt, as expected. Their distribution is fitted with a double exponential, with the purpose of evaluating the inefficiency of the selection, as will be better explained in the next section. Furthermore, the stopping muons selection has been applied for cross-check purposes to different samples, giving similar results.

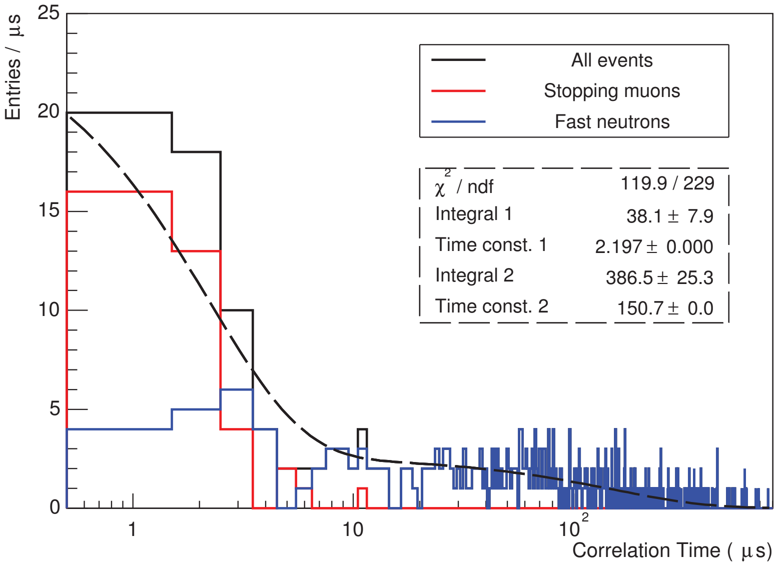

Figure 60: Δt of an OV sample of DC-III (n-H), separated into total events (black), stopping muons (red) and fast neutrons (blue) according to the PS log-likelihood analysis. The total distribution is fitted with a combination of two exponentials, with fixed time constants and integrals left free.

4.3.3 Measurement of the stopping muon contamination

We now apply equation 88 and 89 to the full DC-III (n-H) IBD sample to identify and count stopping muons. The results, as shown in the *chili plot* of figure 61, are 11 stopping muons out of 32768 neutrino candidates; this will be the central value of our estimation. In the figure, events below the line of equation 88, but rejected by equations 89, are not shown. The prompt-delayed correlation times Δt of the 11 selected stopping muons are all below 10 μs.

We now evaluate the errors on the stopping muons estimation. Upper and lower confidence intervals are calculated separately, by using two different criteria. In order

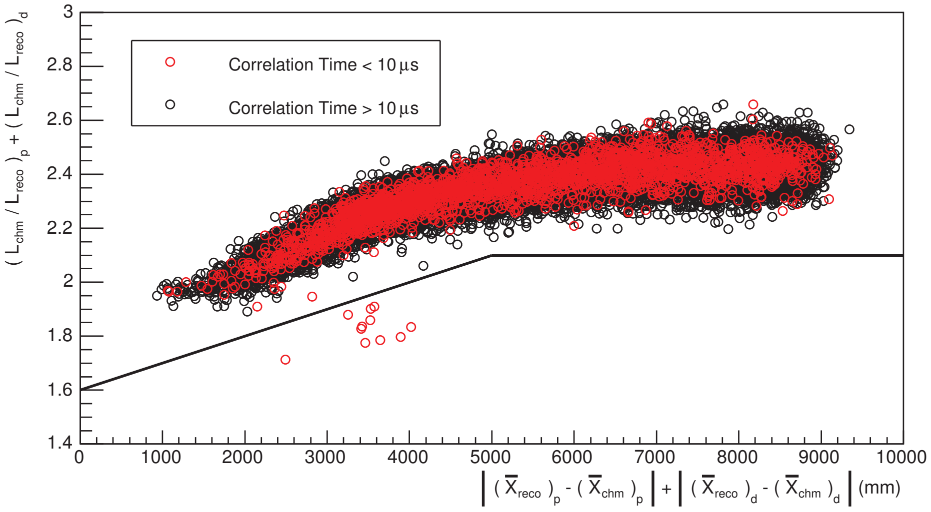

Figure 61: Chili plot of DC-III (n-H) IBD candidate events, with short prompt-delayed Δt events featured in red. The stopping muons selected with the PS log-likelihood analysis are the events below the black polyline.

to compute the lower confidence interval, we study the purity of the stopping muons selection by looking at IBD candidate events with $\Delta t > 10\,\mu s$, virtually excluding every stopping muon[70]. As we mentioned, none of the 11 selected events respond to such conditions, meaning that the stopping muons selection on this sample gives 0 events. This, assuming a Poissonian distribution, corresponds to a maximum amount of contamination of 1.15 (2.30) events that are not stopping muon, at 68% (90%) confidence level. This number, once rescaled to the total number of IBDs (including the ones with $\Delta t < 10\,\mu s$), gives a maximum inefficiency of 1.26 (2.52) events at 68% (90%) CL.

The upper confidence interval, on the other hand, is obtained from the efficiency of the selection on the OV-cut sample. Figure 60 also shows a double exponential fit on the Δt distribution of the total OV sample candidates. The fit uses two fixed time constants of $2.197\,\mu s$, for the muon lifetime, and $150.7\,\mu s$, for the neutron capture lifetime, and has the two exponential integrals left free. The output of the integral of the first exponential, i.e. the number of stopping muons according to the fit, is equal to 38.1 ± 7.9. We assume that the central value plus $1\,\sigma$ (46 events) corresponds to the maximum amount of stopping muons at 68% confidence level. Accordingly, the minimum efficiency of our selection at the same confidence level will be given by the ratio between this number and the 37 stopping muons identified in the OV sample, i.e. 80.43%. The upper confidence limit at 68% on the stopping muons estimation

---

[70] the fraction of muons surviving $10\,\mu s$ is 1.05%

on the IBD candidates is therefore given by the 11 selected events rescaled at 100% efficiency, i.e. 13.7.

In conclusion, the final number of stopping muons estimated in the candidates sample of the DC-III (n-H) selection, and the corresponding rate, with errors, are:

$$\begin{aligned} \text{Events} &= 11.0^{+2.7}_{-1.3} \\ \text{Rate} &= 0.0238^{+0.0058}_{-0.0028}\,\text{day}^{-1}\,. \end{aligned} \tag{90}$$

A consistency check on the number of estimated stopping muons can be made by comparing the rates of such events for the periods with and without the OV running. The with-OV and without-OV phases and livetimes are defined in the same way as did in section 4.2.2. To do that, we sum the number of stopping muons identified in the OV sample (37) with the 1 event out of the 11 SM in the IBD sample which is in a with-OV run, and divide this number for the with-OV total livetime. This rate has to be compared with the without-OV one, which is obtained dividing the 10 remaining stopping muons in the candidates sample by the without-OV phase livetime. In this simple exercise, the errors are evaluated purely statistically assuming they are normal-distributed. The results, resumed in table 16, confirm the goodness of the selection, with the two numbers in agreement within the errors.

	With OV	Without OV
Events	37 (OV) + 1 (IBD)	10 (IBD)
Rate	$0.094 \pm 0.015\,\text{day}^{-1}$	$0.114 \pm 0.036\,\text{day}^{-1}$

Table 16: Stopping muons rate comparison (OV-cut excluded) for the periods with-OV and without-OV.

4.3.4 Cross-check on the FuncV cut

Finally, we compare again the PS log-likelihood analysis and the FuncV, not only in terms of stopping muons (and light noise) selection, but also for the residual stopping muons estimation. In figure 62 the energy as a function of the FuncV of the delayed signal is shown, for the candidates obtained with the DC-III (n-H) selection excluding the FuncV cut. As for the n-Gd (figure 48), the two analyses are compared, with the events selected by the present analysis marked in a different colour. In particular, on the left side of the FuncV cut red events correspond to the ones selected using equations 88 and 89. These 11 events identified are clearly close to the FuncV cut, showing the agreement between the two analyses. On the right side of the FuncV cut, on the other hand, events selected by equation 88 only are marked in red, in order to include the light noise. In that band, a slight disagreement between the two cuts is present, represented by the black dots in the high-FuncV region.

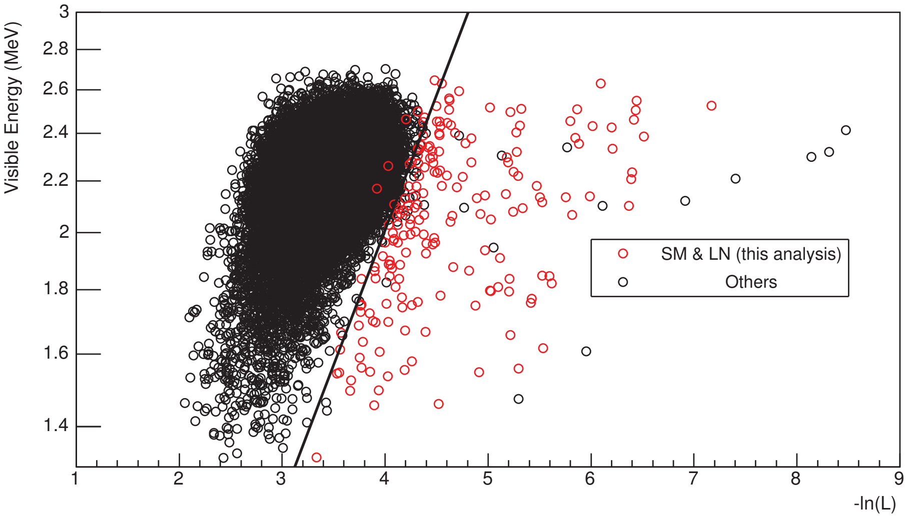

Figure 62: Energy of the delayed events, as a function of FuncV (–ln(L)), of an enriched IBD sample obtained by applying full candidate selection with the exclusion of the FuncV cut, which is represented by the black line. Events selected with the PS log-likelihood analysis are featured in red.

The number of stopping muons left in the candidates sample was evaluated also using a study based on the FuncV cut. The result of such analysis, which corresponds to $9.0^{+3.7}_{-3.2}(stat.)\pm1.4(syst.)$ events, or $0.0195^{+0.0080}_{-0.0069}(stat.)\pm0.0030(syst.)$ event per day, is in agreement with the one of the PS log-likelihood (equation 90).

4.4 Study of the ortho-positronium formation in Double Chooz

As introduced in section 4.1.1, the standard PSD is effective in discriminating protons and alphas from gamma and electrons that emit the same amount of scintillation light, but ineffective for an electron/positron separation. However, the formation of ortho-positronium (o-Ps) may induce a sizeable distortion in the PS due to the induced delay between the scintillation light of the positron ionization and the $e^+ - e^-$ annihilation.

Double Chooz uses the time correlation between the prompt signal of the positron and the delayed signal of the neutron capture to detect neutrino IBD interactions with a strong background reduction. The most consistent remaining source of background is given by cosmogenic β^{-}-n emitting isotopes like ^{9}Li or ^{8}He. Electron-positron discrimination, if possible, could therefore bring a further enhancement to the background rejection.

In the previous section, we applied a non-standard PSD to disentangle stopping muons from neutrino candidates. In this section, we will focus to another alternative PSD based on the o-Ps formation, with the aim to explore the possibility of a e^{+}/e^{-} separation. This has been first proposed for organic liquid scintillators in Ref. [203]. By using a dedicated fit on the PS, we will be able not only to tag o-Ps on an event-by-event basis, but also to measure its formation probability and livetime in the Double Chooz liquid scintillators. This represents the first observation of o-Ps formation in a large liquid scintillator experiment, and could be an input for future aimed studies. The analysed data set corresponds to the IBD selection of DC-II (n-Gd) which was defined at the beginning of section 4.2.

4.4.1 Ortho-positronium enhanced PSD

Positronium is an unstable bound state of electron and positron, whose formation is a competitive process with respect to direct annihilation. Its formation probability depends on the material in which the positron is created. o-Ps is the triplet state of positronium, i.e. the state with parallel electron and positron spins (total spin of 1). It has a branching ratio of 75% and decays in three γ rays in vacuum with a lifetime of 142 ns. However, in matter, the o-Ps lifetime is quenched to a value that depends on the material and is usually of the order of a few ns [204]. The effects responsible for the o-Ps lifetime shortening can be chemical (formation of compounds or oxidation), magnetic (spin-flip) or due to the interaction with electrons of the medium (pick-off). All these processes lead to a two-γ decay. Nonetheless, an induced delay in the annihilation of a few ns can be observed in the photon emission time distribution, if the time sampling is small enough, and used as a signature of the o-Ps formation.

The other positronium state, the one in which positron and electron have anti-parallel spins (total spin 0), is called para-positronium (p-Ps). This singlet state has a 25% branching ratio and a much shorter lifetime of 125 ps in vacuum. Such lifetime is an order of magnitude shorter than the Double Chooz time resolution and therefore cannot be used for an enhanced e^{+}/e^{-} PSD. A scheme of the different positronium states formation and decay is shown in figure 63.

In an o-Ps enhanced PSD, the fraction of positrons that forms o-Ps can be disentangled by using the difference in PS due to the induced delay in the positron annihilation. The Borexino collaboration has already successfully applied this technique in the

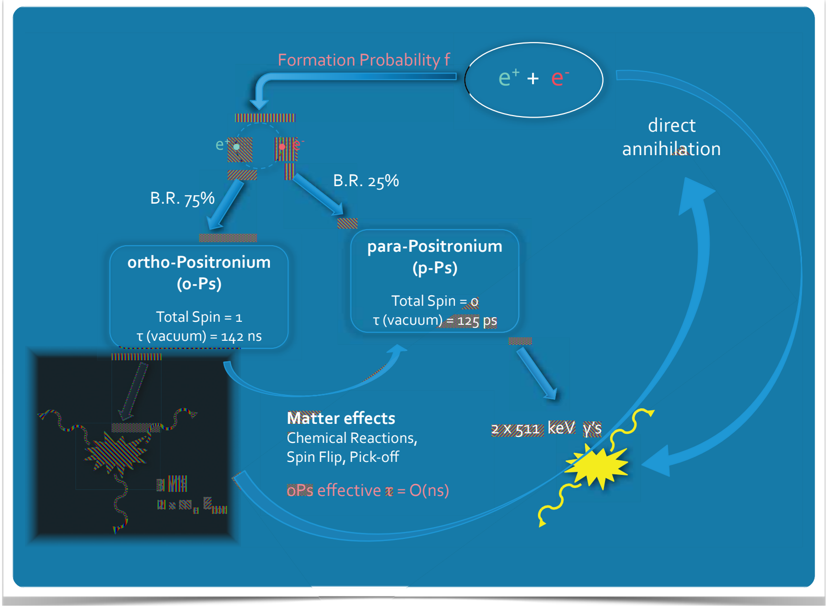

Figure 63: Scheme representing the possible formation of positronium, with decay modes and lifetimes of the two states: the o-Ps and the p-Ps. Figure borrowed from [205].

observation of solar pep neutrinos. In Borexino, cosmogenic ^{11}C β^+ decays, the main background in the pep neutrino rate measurement, have been separated statistically by using a e^+/e^- discrimination parameter that exploits the o-Ps formation [206].

4.4.2 Ortho-positronium properties in the Double Chooz liquid scintillator

The Double Chooz liquid scintillators of the target and the gamma catcher differ in composition but not in light yield, with the target being a mixture of n-dodecane, PXE, PPO, bis-MSB and 1 g Gd/l as a beta-diketonate complex, and the gamma catcher being gadolinium free but with an additional main component of mineral oil. The o-Ps properties, formation probability and effective lifetime, have been measured for the most commonly used organic liquid scintillator compounds, including the Double Chooz scintillators main components [203, 207], and as a function of the dopant concentration [208]. Another specific measurement of the o-Ps fraction and lifetime for the Double Chooz liquid scintillators has been performed with a dedicated setup located at the IPHC laboratory, in Strasbourg. The apparatus, a standards PALS[71] system, is very similar to the one described in details in Ref. [208]. A ^{22}Na positron source of 1 MBq, immersed in a liquid scintillator sample, produces with 90% probability a 1.27 MeV γ ray in association with the positron ($E_{e^+}^{max}$ = 544 keV). Two plastic scintil-

---

[71] Positron Annihilation Lifetime Spectroscopy.

lators (BaF_2), tuned at different energy windows, detect the coincidence between the 1.27 MeV γ and one of the two 511 keV annihilation gammas produced in the o-Ps decay. The time between these two signals is then used to calculate the o-Ps lifetime. In particular, the measured time distribution is fitted with a combination of three exponentials $A_i \cdot e^{-t/\tau_i}$ - two short ones for the direct annihilation or p-Ps formation and decay into the source ($i = 1, 2$) and a long one for the o-Ps decay ($i = 3$) - and a constant C (noise, pile-up). All exponential terms are convoluted with a Gaussian spread to model the detector resolution (180 ps):

$$F(t) = \sum_{i=1}^{3} A_i \cdot e^{-t/\tau_i} + C\,. \tag{91}$$

The o-Ps lifetime is given directly by τ_3, whereas the o-Ps formation fraction is obtained from A_i after some corrections (all details are given in Ref. [209]). A schematic depiction of the system is shown in figure 64, while the results of the analysis for the Double Chooz liquids, including systematic uncertainties, are resumed in table 17.

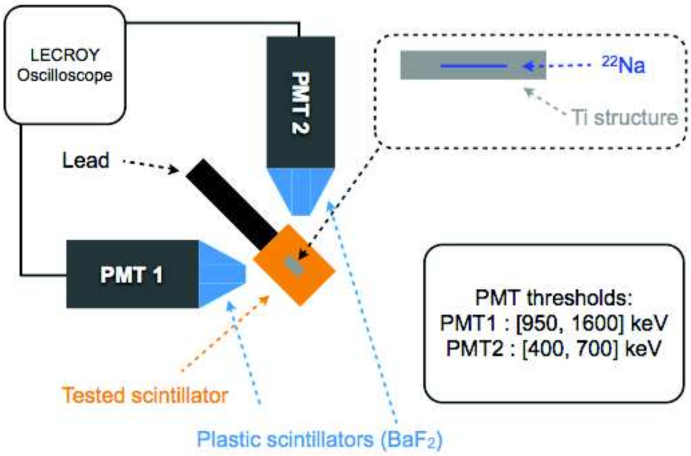

Figure 64: Cartoon of the PALS setup used for characterizing o-Ps in the different scintillators.

DC scintillator	o-Ps lifetime (ns)	o-Ps fraction (%)
Target	3.42 ± 0.03	46.6 ± 1.3
Gamma catcher	3.45 ± 0.03	45.6 ± 1.3

Table 17: o-Ps formation fraction and lifetime in Double Chooz scintillator of target and gamma catcher, measured with a dedicated PALS setup [208].

4.4.3 Ortho-positronium tagging algorithm and results

If, following an IBD interaction, o-Ps is formed, three distinct signals are produced instead of two, the first two being the positron scintillation and the o-Ps decay, and the third represented by the neutron capture. The delay between the positron scintillation and its annihilation is too short for the two events to be resolved as separate triggers in Double Chooz (trigger window of 256 ns). However, such delay may be observed as a distortion in the PS recorded in the prompt signal window. Nonetheless, it is not trivial for Double Chooz to resolve this distortion giving the o-Ps lifetime of 3.4 ns in its liquid scintillators. First of all, the scintillators characteristic fast decay times are of the same order of magnitude, being 2.6 ns and 5.4 ns for the target and gamma catcher respectively. The time sampling of the electronics, which is 2 ns, is also of the same magnitude and represents a limit to the ability to resolve the two signals.

Nevertheless, on an eye check on PSs of prompt IBD signals, we noticed how some events were characterized by a double structure, with sometimes two separate peaks in the pulses time profile. In oreder to explore the possibility of this to be related with the o-Ps formation, we looked at IBD candidates of the DC-II (n-Gd) sample with the idea to tag o-Ps by looking at this double peak in PSs. For this purpose, a fit function was built combining two reference PSs with identical shape but different normalization. The first reference PS is meant to represent the time distribution of pulses arising from the positron ionization light, while the second one reproduces the following light coming from the two 511 keV annihilation gammas. The used PS for both references is again the cumulative PS of a ^{60}Co source calibration run, the same used in previous analyses. The respective normalization of the two references is based on the visible energy E_{vis} and the total number of pulses in the PS N_{tot}, and it is chosen as follow:

1. the number of pulses ot the second reference N_2 has to correspond to the annihilation energy of 1.022 MeV, i.e.

$$N_2 = N_{tot} \cdot (1.022\,\text{MeV}/E_{vis})\,; \tag{92}$$

2. the number of pulses of the first reference N_1 has to correspond to the remaining energy $E_{vis} - 1.022$ MeV, i.e.

$$N_1 = N_{tot} \cdot (1 - 1.022\,\text{MeV}/E_{vis})\,. \tag{93}$$

The two references are then shifted in time by an interval Δt_{e^+}, which is left as the free parameter of this fit.

The normalization of the two references assumes that the number of pulses is proportional to E_{vis}, which is not always true. As a matter of fact, at high energies, when the number of p.e. per PMT increase, it is more likely for a pulse to be formed by two or more photo electrons. Figure 65 shows the distribution of the number of pulses that correspond to 1 MeV of visible energy for some IBD prompt events. The values fluctuate around the average, with a root mean square spread of $\sim$ 25 %. Consequently, in order to account for this energy non-linearity of the number of pulses, the two normalization factors N_1 and N_2 are let as free parameters, allowed to vary in a range of $\Delta N \in [-0.6 \cdot N, +0.6 \cdot N]$.

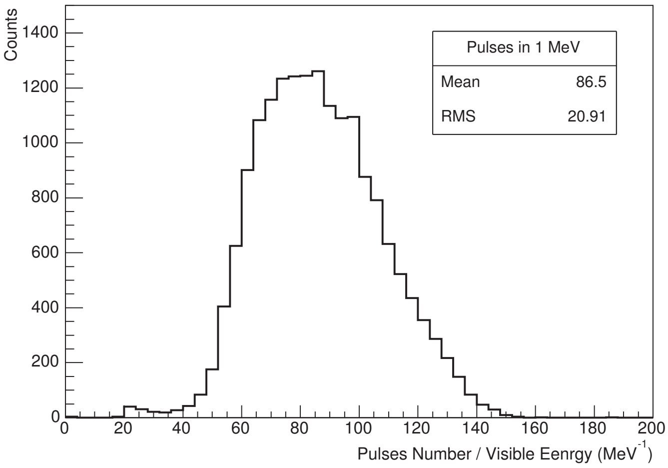

Figure 65: Number of pulses corresponding to 1 *MeV visible energy for the prompt signal of DC-III (n-Gd) IBD candidates.*

Furthermore, an additional fit parameter is added to account for the possible shift of the first peak with respect to the beginning of the PS window. The presence of spurious pulses, discussed in section 4.1.2, as well as random fluctuations, may in fact slightly shift the PS peak. This parameter, λ, can vary within a range going from –10 ns to the time of the first pulse time that is represented in the event PS, in order to correctly match the first peak.

If found more than zero, the parameter Δt_{e^+} may be a signature of o-Ps formation, and interpreted as the lifetime of the o-Ps for that particular event. A maximum limit is set for Δt_{e^+}, with the minimum one obviously being 0, that corresponds to no o-Ps formation. We require that the maximum allowed Δt_{e^+} for an event is the shortest time for which the number of pulses in the following 50 ns is lower than 70% of the number of pulses corresponding to the 1.022 MeV signal. This can be also seen as a lower limit on N_2.

Putting all together - if we recall the previously defined (section 4.2.3) notation for which $f^{PS}_{Co}(t)$ is the function that describes the ^{60}Co cumulative PS normalized to one - a fit function $f_{o-Ps\,fit}(t)$ is given by the equation

$$f_{o-Ps\,fit}(t) = (N_1 + \Delta N_1) f^{PS}_{Co}(t-\lambda) + (N_2 + \Delta N_2) f^{PS}_{Co}(t - \lambda - \Delta t_{e^+}) \, . \tag{94}$$

We already mentioned that the number of pulses of a typical PS is a few hundreds. For this fit, we have chosen a 0.5 ns binning and a PS window of 150 ns, meaning that the number of pulse per bin is relatively small and follows a poissonian distribution. The chosen χ^2 definition is given by equation:

$$\chi^2 = 2 \sum_{i=1}^{N} \left[\nu_i - n_i + n_i ln \left(\frac{n_i}{\nu_i} \right) \right] + \sum_{j=1}^{2} \frac{\Delta N_j^2}{\sigma_j^2} \, , \tag{95}$$

where n_i and ν_i are the number of pulses in the i^{th} bin for the PS and the fit function respectively (only bins with $n_i > 0$ are summed up), N the total number of bins (300), and σ_j a 20% normalization error on the normalization variations ΔN_j ($j = 1, 2$). The fit was performed with the ROOT package and a minimization algorithm of the MINUIT libraries [210, 211]. An example of fit for three prompt IBD events is shown in figure 66, corresponding to a fitted o-Ps lifetime of 0.2 ns (figure 66a), 8.4 ns (figure 66b), and 16 ns (figure 66c).

Results of this analysis have been published by the Double Chooz collaboration [209]. The o-Ps analysis was performed on a subsample of the DC-II (n-Gd) candidates selection. The choice of the studied sample aims to maximize the fit capability to select o-Ps events. In particular, we noticed that the fit efficiency tends to degrade both at high and low energies for reasons attributable to the behaviour of the N_1/N_2 ratio. In order to understand this, we remind that the energy of the second peak corresponds to the energy released in the $e^+ - e^-$ annihilation, i.e. 1.022 MeV. This means that if we have an event with $E_{vis} = 1$ MeV the second peak has all the energy, while if $E_{vis} = 2$ MeV the two peaks roughly shares the energy equally. Now each time we add 1 MeV to E_{vis}, the first peak becomes one time bigger than the second one. As a result, at high energy the second peak could then be covered by the first one. At low energies, on the other hand, the first peak becomes too small for the fit to converge properly. For these reasons, only candidates with a visible energy range between 1.2 MeV and 3 MeV are taken into account. With the same purpose, events with a reduced χ^2 higher than 2 are discarded, as well as events in which the ratio between the integral of the fitted function and the number of pulses of the peak is

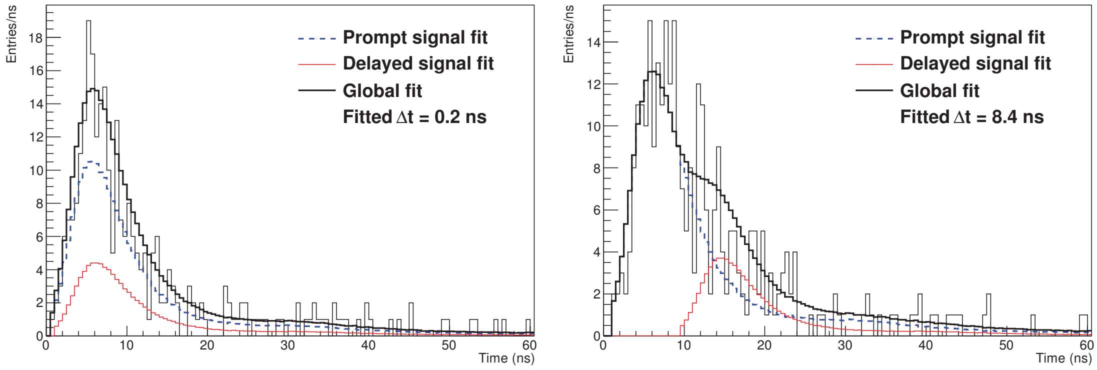

(a) Δt_{e^+} = 0.2 *ns.*

(b) Δt_{e^+} = 8.4 *ns.*

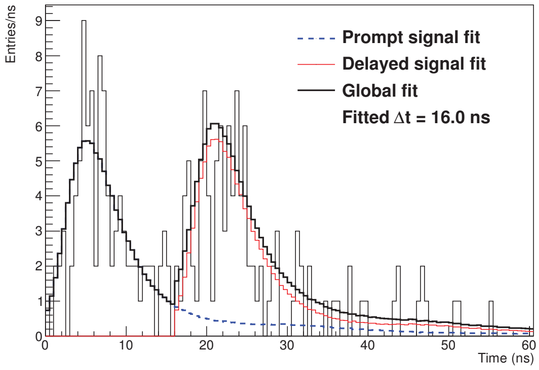

(c) Δt_{e^+} = 16 *ns.*

Figure 66: Three examples of o-Ps fit. The dashed blue line represents the fit of the first time profile, the thin red line the fit of the second one and the thick black line is the total fit.

larger than two in at least one of the two peaks.

The results are shown in term of the distribution of fitted Δt_{e^+} for the subsample of IBDs we have defined, compared with the same distribution for a pure ^{60}Co sample, as shown in figure 67. The latter is selected from a calibration run with the source in the centre of the target, in a way similar to the one described in section 4.1.3. The idea is to compare the Δt_{e^+} distribution for IBD candidates, for which we expect formation of o-Ps, to a sample for which no o-Ps is foreseen. The distribution of the neutrino candidate sample clearly shows an excess of events at large Δt_{e^+}, enforcing the hypothesis of o-Ps. This clearly proves the capability of Double Chooz to observe o-Ps formation with the algorithm that we presented. On the other hand, while most of the ^{60}Co events have $\Delta t_{e^+} = 0$ a smearing in the distribution is visible. Such smearing represents the limit of the algorithm when dealing with small fluctuations in the tail, which can mimic a second peak, or with fluctuations in the first bins, which sometimes result in an underestimated value of the parameter λ. However, this effet is limited statistically and also in the Δt_{e^+} range, since it is not observed for values above 7 ns.

The o-Ps properties have been measured fitting the Δt_{e^+} distribution with an exponential. In figure 68a the distribution is fitted above 5 ns to exclude the region populated by the smearing observed in the ^{60}Co sample. Values of o-Ps lifetime and formation probability are extracted from the fit.

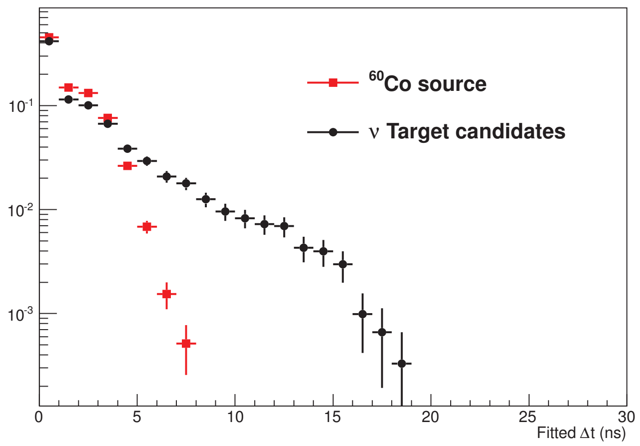

Figure 67: Distribution of the Δt_{e^+} value determined by the fit of equation 94, for the ^{60}Co sample (red squares), and for the neutrino sample (black dots).

4.4.4 Choice of the reference and systematics

We mentioned several times that there is an energy dependency in pulse shapes. Such dependence may influence the results of the o-Ps tagging algorithm, which relies on a reference PS of events with a well-defined energy. In the energy range chosen for the IBD sample studied in this analysis the mean visible energy is 2.237 MeV. In case of o-Ps formation, such energy would be split between the two processes resulting in a 1.215 MeV mean positron prompt energy, and a 1.022 MeV mean o-Ps decay energy. Such values are intermediate between the energy of ^{60}Co events and the one of ^{137}Cs (see table 12).

A o-Ps fit using ^{137}Cs as reference can be obtained by simply replacing f_{Co} with f_{Cs} in equation 94, with f_{Cs} being the ^{137}Cs cumulative PS normalized to one (from figure 40). The resulting Δt_{e^+} distribution is shown in figure 68b and fitted to obtain the o-Ps lifetime and formation probability.

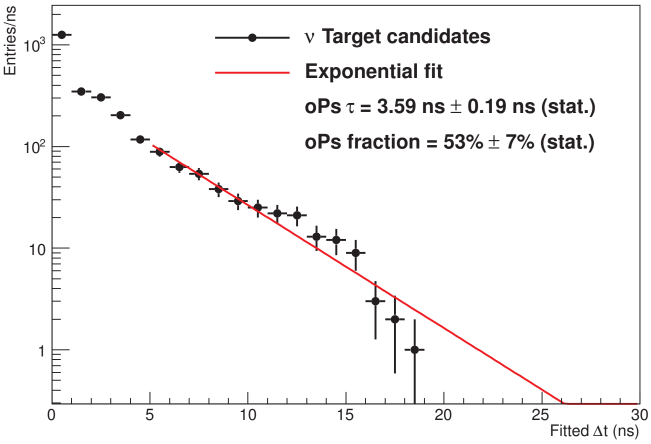

(a) Δt_{e^+} distribution obtained using ^{60}Co reference PS.

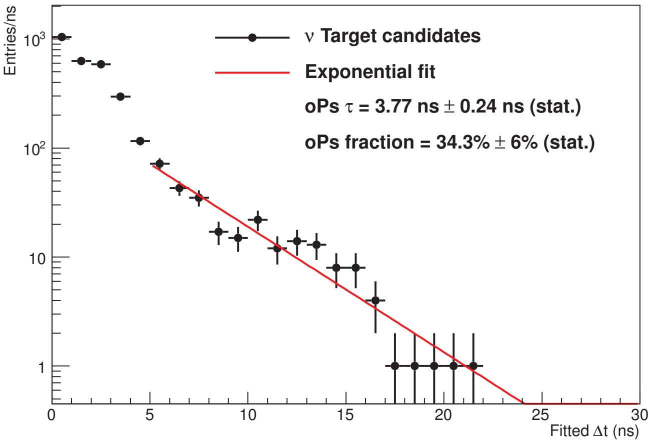

(b) Δt_{e^+} distribution obtained using ^{137}Cs reference PS.

Figure 68: Fit of the Δt_{e^+} distributions of the neutrino sample (above 5 ns) obtained using two different reference PS.

The difference between such values in the two distributions obtained with the two references is thus interpreted as an energy effect. In order to correctly represent the sensitivity of fit results on the reference PS, we proceeded in the following way:

- the o-Ps lifetime and formation probability are chosen from the mean value between the ones measured using the Δt_{e^+} distribution obtained with the ^{137}Cs (figure 68b), and the ones measured using the Δt_{e^+} distribution obtained with the ^{60}Co (figure 68b), i.e.

$$X = \frac{X_{Co} + X_{Cs}}{2} \,; \tag{96}$$

- a systematic uncertainty associated with the result dependency on the reference energy is evaluated as the half-difference between two results, i.e. as

$$X = \frac{X_{Co} - X_{Cs}}{2} \,, \tag{97}$$

  where X is either the o-Ps lifetime, or its fraction.

Other contributions to the systematics come from variations in the method of building the reference curves, which depends on how events are selected in the calibration run. The fit interval, which is chosen to start at 5 ns, is also varied, and the associated discrepancies in the results are taken as systematic uncertainties. Finally, different calibration runs with the source placed in various positions in the target are taken into account to evaluate an associated systematic uncertainty. All these contributions, together with the statistic uncertainty, are resumed in table 18. Such errors are attributed to the values obtained in the manner described previously, in order to achieve a final value of

$$3.68 \pm 0.17(syst.) \pm 0.15(stat.)\,\mathrm{ns} \tag{98}$$

for the o-Ps lifetime, and

$$44 \pm 12(syst.) \pm 5(stat.)\% \tag{99}$$

for the formation probability in the Double Chooz target liquid scintillator. These values can be compared with the measures of the dedicated setup of table 17.

4.4.5 Simulation of detector response to ortho-positronium formation

The formation of o-Ps may not only have an effect on the PS, but also on the vertex reconstruction, which is also based on pulse times (see section 2.3.2). In principle, the induced delay in the positron annihilation allows the e^+ to travel a certain distance inside the detector. If such distance is big enough, the vertex-reconstructing algorithm

Error source	o-Ps lifetime error (ns)	o-Ps fraction error (%)
Reference type	0.09	9
Reference position	0.55	5
Reference building	0.019	1.25
Fit interval	0.14	7
Total systematics	0.17	12
Statistics	0.15	5

Table 18: Summary of the different statistical and systematic uncertainties associated with the o-Ps tagging algorithm.

may be applied separately on the pulses belonging to the two PS peaks. In this way we could resolve the positions of two separate events: the e^+ ionization of the medium, and its annihilation with the resulting γ rays.

In order to investigate this possibility, a simulation of o-Ps formation and detector response has been performed using the GEANT4 [178] simulation package included in DOGS. Various positrons of different energies have been produced through the detector. The value of o-Ps lifetime as well as the formation probability from table 17 have been given as an input for the simulation. The results have shown that the possible disentanglement of the two signals was limited compared to the reconstructing algorithm resolution, which is roughly 20 cm.

4.4.6 Final considerations

In conclusion, although the Double Chooz detector was not conceived for such a measurement, it has been possible to observe the o-Ps formation in its liquid scintillator. This was done with a fit on the single PS, therefore tagging the o-Ps on an event-by-event basis. Unlike Borexino, in which a e^+/e^- separation based on an o-Ps enhanced PSD performed statistically, positron events represent the Double Chooz (prompt) signal to detect IBD interactions. Consequently, a e^+/e^- separation based on o-Ps formation, given the o-Ps formation fractions in the Double Chooz scintillators, cannot be effectively used for a signal-on-background ratio enhancement. On the other hand, the possibility of identifying single ortho-positronium events represents a unique feature for a large liquid scintillator experiment. Moreover, the capability of the technique discussed here to tag o-Ps represents a novelty per se, as well as being a possible benchmark in the development of scintillators for specific future neutrino experiments (see for instance Ref. [212]). From identified events it was also possible to estimate the formation probability and lifetime; the values obtained with the analysis presented here are in perfect agreement with independent experimental measurements.

4.5 Study of the fast neutron background in the n-H analysis

In section 4.1.3 we studied different samples of events of Double Chooz, in terms of their cumulative PS, in order to explore the possibility of a PSD. For fast neutrons, a correlated background, we expect the prompt signal to have a different PS with respect to an IBD prompt signal, given the fact that its scintillation light arises from the ionization of the scintillator medium by a recoil proton rather than by a positron. In figure 41a, we saw how indeed fast neutrons differ from candidates or ^{60}Co events in terms of PS. Nonetheless, this difference is not due only to the different ionization density of recoil protons, but is rather given by multiple effects that will be addressed in this section.

By looking at single events PSs of fast neutrons tagged by the OV, we noticed that for a significant part of them the main peak of the PS was shifted at higher times and preceded by a few other pulses. An example of such PS is given in figure 69. We know that fast neutrons can undergo multiple proton recoil before being captured in the liquid scintillator. Consequently, the shift can be interpreted as the effect of multiple proton recoil, with the first pulses being the result of the scintillation light of one (or more) first low energetic proton, followed in time by a more energetic proton responsible for the remaining pulses.

This shift is used to tag fast neutrons. The main peak is fitted with a Gaussian distribution and the shift extrapolated as the distance of the peak from the beginning of the PS window. A selection based on the value of this shift is described here, and is used as an effective veto, the multiple pulse shape (MPS) cut, in the IBD selection of the forthcoming DC-III (n-H) publication.

4.5.1 Fast neutrons selection

For each event, the PS shift is computed from a Gaussian fit around the main PS peak as the fitted mean minus 1.8 times the σ (see red line in Fig. 69 as example). The idea is to identify a MPS cut on the measured shift that allows selecting the highest possible amount of fast neutrons, limiting at the same time the inefficiency on IBD candidates. As we did many times before at this point of the chapter, we test the method by applying the fit to the IBD candidates, and to a ^{60}Co sample, in which no fast neutron is foreseen, and by comparing the results, as shown in figure 70. The shift values distribution of the DC-III (n-H) candidates is shown in figure 70a, while the

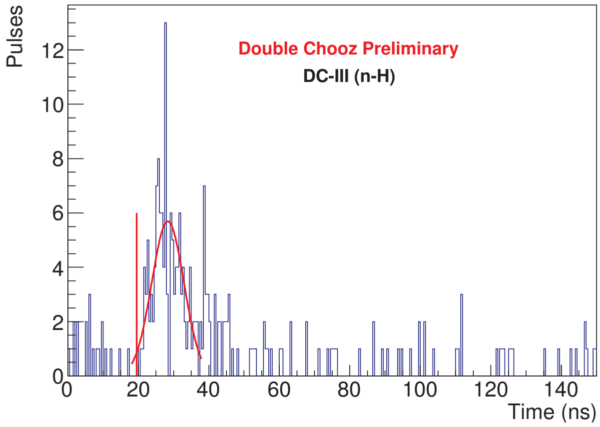

Figure 69: Example of a shifted PS. The red curve represents the Gaussian fit around the maximum to compute the shift. The shift value of 19 ns is represented by the vertical red line (1.8 σ on the left with respect to the fitted mean). The pulses on the left side of the vertical red line are interpreted as the result of a low energy proton recoil.

same distribution but for a sample of ^{60}Co can be seen in figure 70b. By confronting the two distributions, we notice that no event of the ^{60}Co sample has a fitted shift that is above 5 ns while, on the other hand, a statistically significant tail of events above such value is present in the IBD candidates distribution.

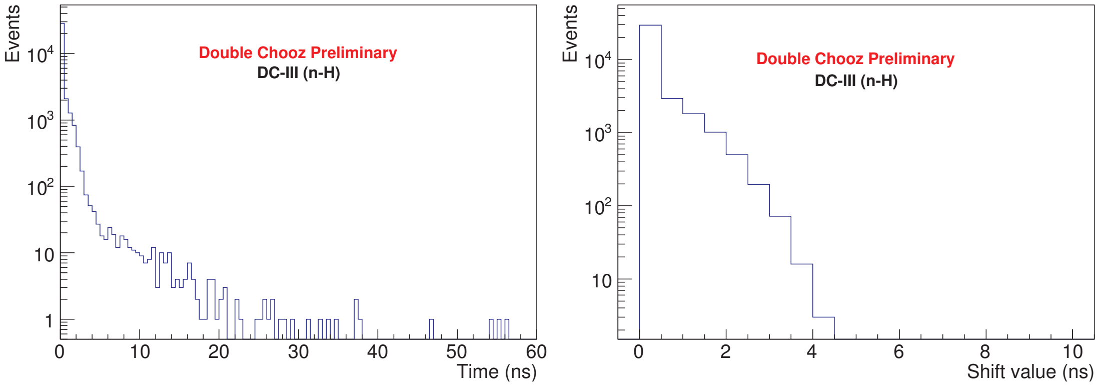

(a) DC-III (n-H) candidates selection.

(b) ^{60}Co (multiple runs with the source in different positions inside the GC).

Figure 70: Distribution of shift values obtained for two different samples.

Consequently a cut on the shift variable above 5 ns has been added in order to tag fast neutrons in the neutrino sample without introducing inefficiencies. However, we saw in the last section that a similar multi-peak structure in the PS is observed for IBD events with o-Ps formation, which we don't want to select with this analysis. Therefore, we need to ensure that the o-Ps tagging algorithm will not conflict with the fast neutrons selection we want to implement. Reminding that the o-Ps tagging algorithm is applied in the energy range of 1.2 – 3 MeV, we distinguish three possible cases, basing on the range of interest.

1. For visible energies below 1.2 MeV, the o-Ps selection is not applied; however, if o-Ps is formed, the first peak is very small (less than 200 keV) and such event can be identified as a fast neutron from the shift of the second peak.
2. Conversely, in the 1.2 – 3 MeV energy range, the o-Ps tagging is done, and it is sufficient to ask that the o-Ps algorithm fails in order to apply the fast neutrons selection safely.
3. Finally, for energies above 3 MeV, if o-Ps is formed the first peak would be bigger than the second, and no fast neutron can be wrongly identified among o-Ps events.

To summarize, a MPS selection criterion is based on a 5 ns cut on the measured shift and tuned for each of the three different energy ranges, as represented in table 19. Note that the *no o-Ps* condition is equivalent to demanding that the o-Ps selection algorithm fails - which typically happens when the two found peaks don't match the energy requirements - for how they are imposed in section 4.4.3.

Energy range	Fast neutrons selection
$E_{vis} \geq 3\,\text{MeV}$	Shift > 5 ns
$1.2\,\text{MeV} < E_{vis} < 3\,\text{MeV}$	Shift > 5 ns & no o-Ps
$E_{vis} \leq 1.2\,\text{MeV}$	No cut

Table 19: Summary of the PS shift cut to select fast neutrons.

4.5.2 Results

On the full DC-III (n-H) candidates sample, with the above conditions, the fast neutrons selection based on MPS disentangles 265 background events. This number corresponds to about 0.824% of the total sample of 32163 candidates, and to a rate of 0.566 events per day. Figure 71 shows the prompt event vertices distribution of the selected events, with the vertices being mostly concentrated in the gamma catcher, as expected for fast neutrons. In figure 72 the prompt event energy is shown as well.

The spectrum is rather flat, with fluctuations that are compatible with statistical errors. Finally, the prompt-delayed Δt distribution is shown in figure 73. The distribution is fitted with an exponential returning a time constant of $(151.7 \pm 10.1)\,\mu$s, which is in agreement with what expected for fast neutrons (150.7 μs).

The fraction of background rejected by the MPS cut can be evaluated by applying the selection on a pure sample of fast neutrons. Two samples are looked at, in order to test the selection efficiency:

- the OV sample, excluding events with Δt larger than 10 μs and with $E_{vis} < 1.2\,$MeV;
- neutrino candidates that have a prompt visible energy above 12 MeV.

The latter sample includes also stopping muons. However, as we discussed in section 4.2.3, the fraction of these events is very poor in DC-III thanks mostly to the application of the FuncV cut. The results, resumed in table 20, show an efficiency in the order of 25%, that is the rejection power of the MPS analysis. Once evaluated, the algorithm tagging efficiency is rescaled to the 265 events selected in the IBD sample, in order to obtain the estimated total number of fast neutrons, which is shown in the table as well.

Sample	Cut efficiency (%)	Total FN in DC-III (n-H)
$E_{vis} > 12\,$MeV	27.2 ± 2.8	973 ± 101
OV tag ($E_{vis} > 1.2\,$MeV and Δ t > 10 μs)	24.9 ± 2.3	1062 ± 101

Table 20: Fast neutron selection efficiency on two almost pure samples, and rescaled number of fast neutron in the DC-III (n-H) IBD candidate sample. The errors are normal distributed.

A series of cross-checks have been made on different samples in order to evaluate the impact of a cut based on the PS shift on neutrino candidates. All these tests confirmed a rejection fraction in the same range of the one shown in table 20, as well as the absence of an impact on the energy spectrum of fast neutrons, which is a crucial input for the final θ_{13} fit.

The inefficiency of a cut based on the MPS cut is also evaluated. This has been done by studying events selected in an altered IBD sample obtained by relaxing the prompt energy upper limit to 20 MeV, but limiting to events with the prompt vertex reconstructed in the bottom half of the detector, where less fast neutrons are expected. From this sample, the high energetic part ($E_{vis} > 12\,$MeV) is used to calculate the fast neutron rate, which is then extrapolated to the low energy part ($E_{vis} < 10\,$MeV) basing

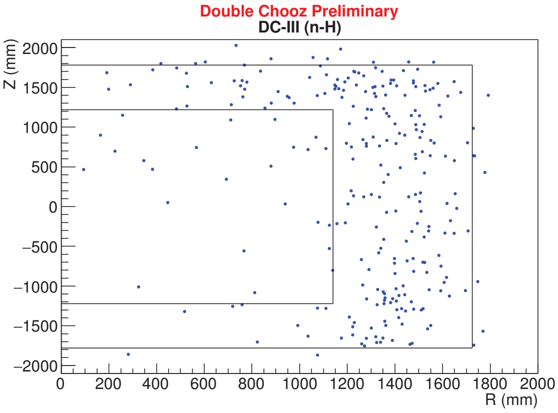

Figure 71: R-Z vertex distribution of the fast neutrons selected events. The inner box shows the target volume whereas the other one shows the gamma catcher volume.

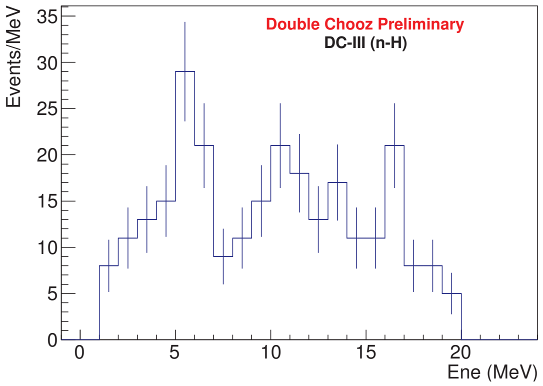

Figure 72: Visible prompt energy of the fast neutron selected events.

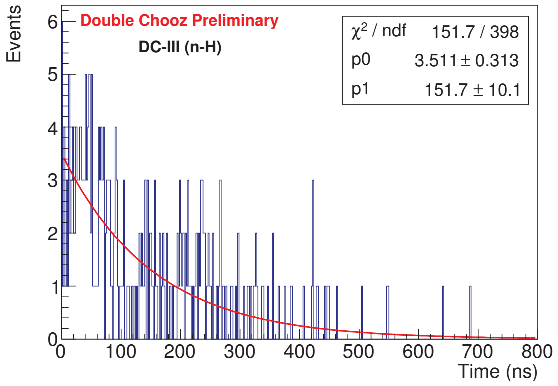

Figure 73: Prompt-delayed Δt of the PS shift selected events.

on the background spectrum evaluated in section 3.3.2. This estimated number of fast neutrons is compared to the observed one, in order to evaluate a possible inefficiency. The result is a difference that is compatible with zero within the statistical errors. A different method uses instead ^{60}Co source calibration runs. In a similar way with respect to what we did for the residual stopping muons evaluation, we obtain the inefficiency from the number of events selected in the ^{60}Co sample rescaled to the whole DC-III (n-H) sample. The results are 5.3 IBD events rejected by the PS shift selection at 90% C.L. i.e. an inefficiency below 0.016%. These numbers are compatible within the errors with the zero inefficiency hypothesis tested with the rate extrapolation method.

4.6 Perspectives on the background characterization in the near detector

The near detector is taking data in a stable configuration since January 2015. Near detector data are crucial to the experiment and have been subject of several studies from early stages. We present here a first application of the PS studies of correlated background on near detector data. The sample studied includes one week of data in which the OV was working, in April 2015, and one month without the OV, in January 2015, i.e. right after the commissioning. Our goal is to test the capability of the selections previously shown in this chapter to identify their respective background in the near detector with the same degree of efficiency that we achieved in the far detector.

In order to carry out the physics goal associated to its construction, the near detector was built identical to the far one. Nevertheless, the different distance from the reactors and depth of the two laboratories result in a different IBD and background rate respectively. In particular, as the neutrino flux goes with L^{-2} (L is the baseline), we expect a near-to-far ratio of the IBD rate that in first approximation is

$$\frac{\phi_\nu^{ND}}{\phi_\nu^{FD}} = \frac{L_{FD}^2}{L_{ND}^2} \simeq \left(\frac{1050\,\mathrm{m}}{400\,\mathrm{m}}\right)^2 \simeq 6.9\,. \tag{100}$$

Moreover, the reduced rock overburden of the near lab (120 mwe) with respect to the far one (300 mwe) results in a muon flux that is roughly 20 times more in the former [213, 214]. This translates, after considering energy and angular effects, in a larger correlated background in the near detector with respect to the far one that is estimated to be roughly 10 times more. Given such higher rate of backgrounds, a measure and understanding of stopping muons and fast neutrons becomes even more important.

The near detector OV also contributes to the reduction and characterization of backgrounds. The OV was installed in the second half of February 2015. However the commissioning and some technical problems prevented it from being fully operating for most part of the livetime ranging from the near detector first data taking to the present day. Having a solid analysis that can reject correlated background gains therefore even greater importance, especially for the portion of livetime in which the OV is not working. In these very last days, an upper part of the OV, similar to the one already present in the far lab, was installed, with the main purpose of controlling the stopping muon background. The decision to promptly improve the OV configuration was motivated also by the results shown here.

In this near detector early stage, neutrino candidates have been identified with a not yet refined selection, which emerged from the first studies on collected data. This selection is based on that of the far detector, with a few small differences in particular in the muon tagging for the selection of single events. The near detector was not yet calibrated with sources deployment. For this reason the full energy reconstruction discussed in section 2.3.3 was not possible. Instead, a simpler version was applied to correct the total charge in visible energy, in the form of an energy scale conversion.

The absence of calibration data influences the PS analysis as well. The stopping muons selection using the likelihood approach and the fast neutrons selection using the shift are in fact based on reference PSs of calibration sources runs. To temporary bypass this issue, we used the same reference PS of the far detector for the near detector analysis. However, a more accurate version of the results shown here will be possible once calibrations campaigns will be performed for this detector.

In figure 74 we can see the *chili plot* of one week of near detector data, where n-Gd IBDs are selected, in which the OV was functioning. The distribution is represented in two variants. In figure 74a we have featured the distinction between events with short and large Δt. A population of events characterized by the typical short Δt of stopping muons is located in a region very similar to the one occupied by such background events for the far detector analysis (see figures 50, 52, and 55). IBDs are in the usual cluster in the upper part of the plot. In figure 74b, on the other hand, we see that most of the stopping muons are tagged by the OV, with such events featured differently. Nonetheless, a significant amount of this background remains untagged. From the figure appears clear that it is possible to remove these events with a selection on the *chili plot*, in similar way that what proposed for the far detector.

If we now look at the *chili plot* distribution for a month of data taking in the near

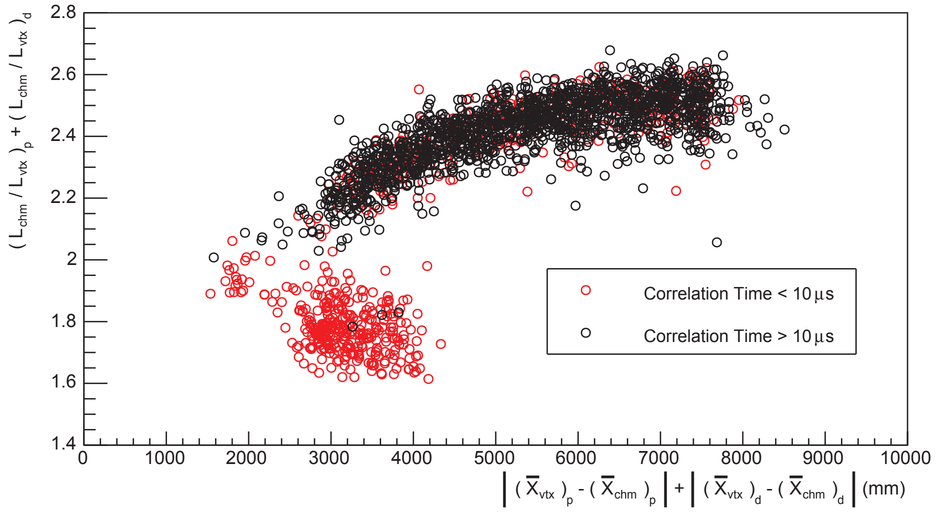

(a) Events characterized by a short prompt-delayed Δt are featured in red.

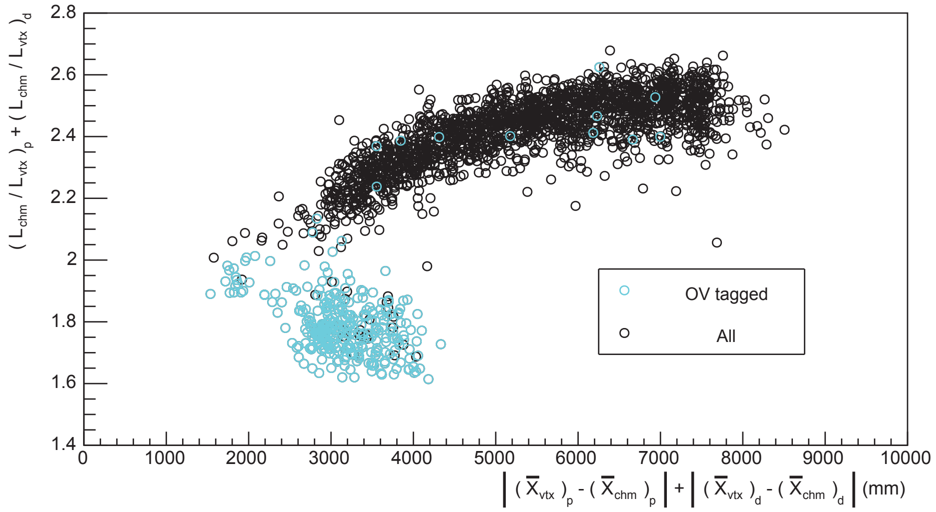

(b) Events with an OV coincidence on the prompt signal are featured in turquoise.

Figure 74: Chili plots of candidates selected in a week of near detector data taking in which the OV was working. As for the far detector, stopping muons are clearly separated from neutrino events.

detector, but without the OV, in figure 75,we can see again a large amount of stopping muons that are placed in a distinct area of the plot phase-space. By applying a simple separation for comparison purposes, made by assuming that events with

$$(L_{chm}/L_{reco})_p + (L_{chm}/L_{reco})_d < 2 \tag{101}$$

are stopping muons, while the rest are neutrinos, we obtain a rate of

$$44.82\,\text{events/day} \tag{102}$$

for the former population and 113.44 events/day for the latter. The already mentioned imperfections in the selection of events in the ND make a direct comparison of these number with the rates of the far detector not entirely reliable. Nonetheless, for a similar livetime in the far detector, with similar selection conditions (no OV, no FuncV cut), we obtain a rate of 5.57 events per day for stopping muons and 50.27 events per day for neutrinos. The neutrino rate is directly influenced by the reactor power, which was modest (only one reactor on) in the month corresponding to near detector data. This explains how the relative rate of IBDs does not match the expectation given by equation 100. The stopping muon rate, on the other hand, does not depend on external conditions but only on the selection. By comparing the 44.82 events/day near detector rate with the 5.57 events/day far detector rate, we obtain the factor of ~ 10 we expected.

To sum up, we have seen how the near detector collects roughly 10 time more stopping muons than the far. Although most of these events can be tagged by the OV, a significant amount remains untagged. Furthermore, the OV is not present for a significant portion of the near detector current livetime. In order to implement a near-far analysis, which is crucial to reduce the main component of the Double Chooz systematics, that is the one associated with flux prediction, a stopping muons efficient selection represents a key feature. We have seen here that with a simple selection on a non-calibrated sample it is still possible to disentangle stopping muons. This proves the importance that the PS-likelihood analysis on stopping muons will have in the future of the Double Chooz experiments.

Finally, the distribution of the shifts calculated with the MPS analysis, for the same month of near detector data, is shown in figure 76. As for the analysis on stopping muons, this is a preliminary study. Moreover, it is not possible to directly compare the distribution with a Co^{60} one, for the already mentioned absence of calibrations. Nevertheless, the distribution appears compatible with the one shown for the far detector,

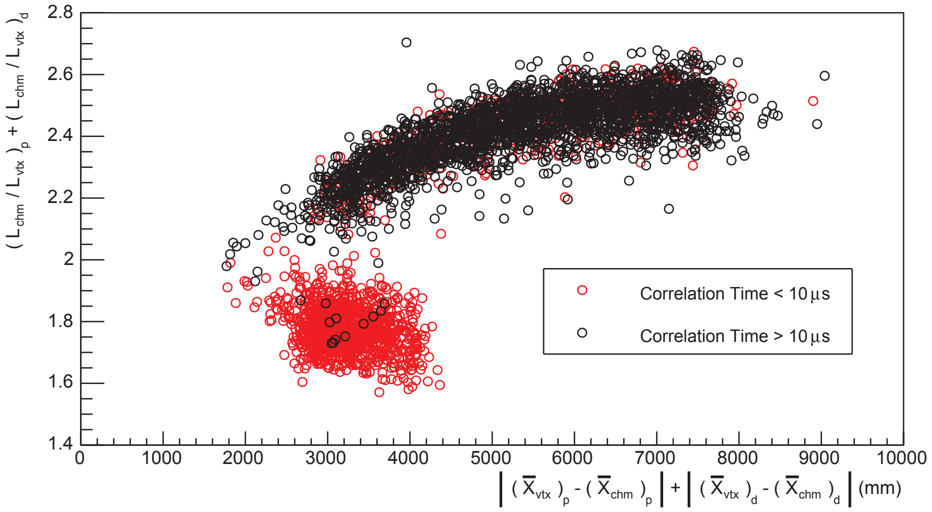

Figure 75: Chili plots of candidates selected in a month of near detector data taking in which the OV was not working.. Events characterized by a short prompt-delayed Δt are featured in red.

and the capability of a fast neutrons tagging in the near detector appears promising.

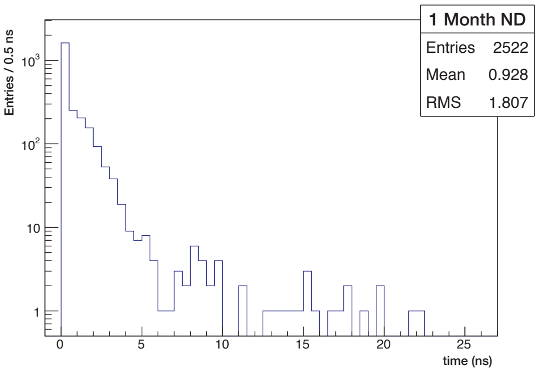

Figure 76: Distribution of shift values obtained for one month of near detector data.

5 Measurement of the inner veto scintillator ageing

Contents

By scintillator ageing we mean the degradation of the properties of a scintillating material with time. This rather general definition actually conceals a big deal of processes with different nature and effects, with the common ultimate outcome of diminishing the overall scintillator response. Various observable characteristics of the scintillator, like its light yield, the attenuation length of the emitted light, the decay times, and chemical properties, determine the scintillator response to electromagnetic processes happening within it. The ageing is observable when one or more of these characteristics changes as a result of the action of internal or external factors.

The effects that are responsible for the scintillator ageing differ in nature and impact basing on the type of scintillator and its use. Environmental ageing effects include the oxidation of the scintillator compound, which represents a threat for many types of scintillators. The oxygen, in fact, absorbs in the region of the scintillating radiation, quenching the fluorescence and consequently reducing light yield and decay times. Plastic scintillators may as well undergo mechanical degradation and surface crazing, which weakens the light transmission by compromising the total internal reflection at the surface. The diffusion of other external molecular components in the scintillator includes the effect of solvents or fingerprints in a plastic, as well as metals diffused from a tank containing a liquid scintillator. Modern liquid scintillators are typically a combination of several liquids, sometimes loaded with metals. The stability of the mixture may degrade with time, with a negative effect on the propagation of the fluorescent light. Last but not least, scintillator calorimeters exposed at high radiation may perish due to the induced chemical reactions.

This chapter is dedicated to a study on the ageing of the Double Chooz inner veto (IV) liquid scintillator. In the first section, we will go into details of the processes involving organic liquid scintillators. In order to tackle two main processes regarding this type of scintillators, namely the stability of the compound and the oxidation, we will monitor the time evolution of the attenuation length of the IV liquid. The study of the ageing of the IV scintillator exploits calibration runs taken with the inner veto light injection system (IVLI). This system is described in a dedicated section of this chapter, the second one, while the actual description of the ageing study is hosted in the third and last section. By using the IVLI system, we will perform an analysis to check the transparency of the inner veto liquid of Double Chooz during the whole livetime of the experiment.

5.1 Ageing of organic liquid scintillators

For the sake of this analysis, we consider two main processes that are commonly responsible for the ageing of an organic liquid scintillator. Firstly, the presence of oxygen can directly or indirectly induce scintillators to de-excite without fluorescence. For this reason the amount of oxygen or other impurities must be constantly checked in liquid scintillator experiments in order to ensure the stability of the energy response. A brief description of such phenomenon, known as quenching, is preliminary to the arguments of this section.

Secondly, we will discuss how a degradation of the compound due to internal chemical reactions can affect the light yield by impairing the transparency of the liquid that is subject to ageing, providing some historical examples. This is of particular importance in modern reactor neutrino experiments, like Double Chooz, where the used liquid is usually a cocktail of different scintillators and other solvents loaded with Gd. The stability of the mixing to keep a constant light attenuation length is certainly among the most challenging tasks during the development of such scintillating cocktails.

5.1.1 Quenching, light propagation and the role of oxygen

The scintillation light is the result of prompt radiative relaxation of the lower vibrational level of the excited state S_1 of the scintillator molecule. Nonetheless, non-radiative or slow decays normally occur, competing with fluorescence decays. An important distinction can be made among such decays, which can be due to the nature of the compound or induced by external effects [197]. For the former, the shape of the energy potential curves of the different states involved in the process may be such as to allow overlaps between high vibrational states of the ground level S_0 and the excited level S_1. As a result, non-radiative transitions due to the $S_0 - S_1$ states mixing are possible. This is obviously an intrinsic characteristic of the scintillator, but is influenced by external aspects as well. Rise in temperature, with increased thermal agitation, or molecular interactions and collisions, may result in a broadening of the potential curves, and increase this effect. The fluorescent quantum yield, i.e. the ratio between the radiative decays total rate and total decay rate, is typically of the order of or greater than 0.8 for high-standard liquid scintillators used in modern applications [197, 215]. The latter category of non-radiative decays, that is the ones not attributable to the nature of the vibrational levels, is commonly referred as quenching. A more dated nomenclature wants the word quenching to refer instead to all non-radiative processes, internal and external.

High ionization densities may also result in a quenching effect. We already discussed how the excitement of singlet and triplet electronic states results in multi-component scintillation decay time profile (see section 4.1.1). High ionization density results in a saturation of available ionization centres, causing an interference effect that quenches the scintillation for high dE/dx particles. As a result, the light yield depends not only on the energy, causing an energy non-linear response, but also on the particle nature.

Among external quenching effects, a crucial role is played by oxidation. An excited scintillator molecule may return radiation-less to the ground state following the collision with another non-fluorescent molecule in the solution. Peroxides that can be formed inside the liquid due to oxidation are strongly electron-deficient and therefore good candidates to participate in such process. This effect may greatly reduce the light yield, as well as impacting the decay time of the scintillator, even at levels of a few ppm [216]. Moreover, in scintillator cocktails the presence of oxygen can cause an indirect quenching by competing with the secondary scintillators, or fluors, in the energy transfer from the excited primary scintillator, or solvent, again reducing the light yield. Other observed effects due to the presence of oxygen include the reduction of ortho-positronium formation fraction [217], as well as a negative effect on a pulse shape discrimination [218], both of which have been treated for Double Chooz in this manuscript. The effect of oxygen on PSD is due to its peculiar electronic levels structure, for which the triplet state coincides with the ground state, rather than the singlet one. This allows excited singlet states of scintillating aromatic molecules to de-excite via a non-forbidden transition within the oxygen levels [194].

Oxygen-induced quenching can be monitored by studying the light yield of the liquid scintillator. In this chapter, however, we will focus on the effects on light propagation. Excited scintillator molecules emit certain wavelengths of UV or visible light in the process of de-excitation, and they can also undergo energy transition when colliding with other particles. These fluorescent photons go through several elastic processes (Rayleigh scattering [219], refraction, reflection) before reaching the PMT photocathode [220]. The presence of oxygen, as well as any other impurity, impairs the propagation of the fluorescent light, by absorbing or scattering inelastically the photons. The effect of impurities may result therefore not only in a lower light yield (up to a total loss of signal), but also in a decreased attenuation length for fluorescence light. This latter characteristic, the attenuation length, will be object of our ageing study for the IV liquid.

5.1.2 Stability of the compound

The advantages of using Gd dopant in the liquid scintillators to enhance the neutron detection have been already stressed in the chapter dedicated to the Double Chooz experiment (section 2.1.2). Nevertheless, the process of loading a scintillator compound with Gd presents some technical challenges. Pure Gd is not soluble in the non-polar aromatic compounds that constitute the scintillator, and must be dissolved in the form of inorganic salts like $GdCl_3$ or $Gd(NO_3)_3$. The development of such complexes is a non-trivial process. The stability of the final doped mixes is another crucial issue, especially for long-term experiments.

The CHOOZ experiment measured a degradation in time of the light yield and attenuation length of its liquid scintillator. Such degradation has been attributed to oxidation by nitrates of the organic liquid, as shown in the final publication of the experiment [107]. A plot from the same reference, showing the evolution of the attenuation length of the liquid with time, is shown in figure 77.

The Palo Verde collaboration, which used a scintillating cocktail similar to the one of CHOOZ, experienced the same degradation problems, also measuring a time evolution of the attenuation length, as shown in Ref. [221].

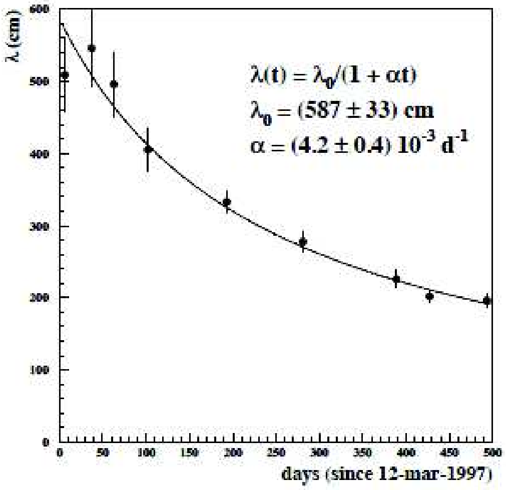

Figure 77: Evolution with elapsed days of the attenuation length λ measured by the CHOOZ collaboration in Ref. [107].

5.2 The IVLI calibration system

In the section dedicated to calibrations in Double Chooz (2.2.2), we introduced two similar systems that inject light inside the detector, one for the inner detector (IDLI) and one for the inner veto (IVLI). Our ageing study of the IV liquids is based on data collected using the IVLI system, of which a brief description is now given.

The IVLI flashes multiple wavelengths light pulses inside the inner veto. When describing the IV (section 2.2.1), we remarked that the PMTs arrangement and direction in the IV, shown schematically in figure 78, are more densely arranged in the bottom part in order to better track downgoing muons. The IVLI permits to calibrate the IV (measure PMTs gain μ and transit time t_0) other than studying its scintillator properties (light transmission, light yeld), in a similar way to what the IDLI does for the inner detector.

5.2.1 IVLI characteristics

The IVLI and its usage in Double Chooz are accurately described in Ref [222, Part-II] as well as in its manual [223]. The system core corresponds to the board pictured in figure 79, which holds a matrix of 8 × 12 LEDs. The board is hosted in the IVLI plastic box, outside the detector (figure 80a). 90 of the 96 LEDs pulse blue light (475 nm), with the remaining 6 emitting UV radiation (375 nm). The UV light excites the wavelength-shifting component of the inner veto liquids, allowing the monitoring of its light yield. The scintillators are conversely transparent to blue light, which normally

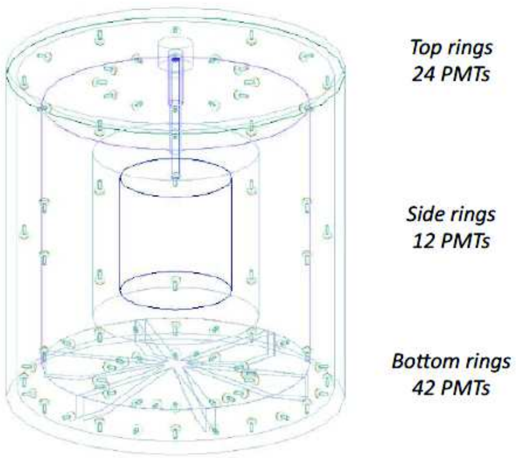

Figure 78: Schematic representation of the disposition and orientation of the photomultipliers of the Double Chooz inner veto. The 78 tubes are arranged in 3 rings, with the bottom one being the more populated.

arrives unabsorbed to the PMTs. For this reason, blue LEDs are used to measure PMT gains and time responses, as well as study the light propagation. The 96 LEDs are activated by a fast pulse generator. They are attached individually to 25-m long quartz fibres that drive the light inside the detector (figure 80b), and in group of 12 to wavelength shifting fibres (WLS, Kuraray Y11) that carry the light to an external reference PMT mounted in a separate dark box inside the IVLI box, which is used to monitor the system. All cables, both those directed into the IV and those holding the fibres that go to the PMT, are of the same length to match light arrival times. On their other end, quartz fibres are attached to the PMTs supporting structures (figure 80c). The fibres materials respond to high standards in term of durability and compatibility with the liquids. Finally, since there are more fibres than PMTs, some of them host two fibres. In such cases, the two fibres on the same PMT are oriented in opposite directions. This redundancy is motivated by the fact that it is less easy to illuminate multiple PMTs in the IV than in the ID given the hull-like structure of the former.

5.2.2 Running modes

The commissioning of the IVLI began in August 2010. Since then, different running modes have been tuned in order to perform all the different measurements the system is designed for. While running, the IVLI system receives from the PC the parameters to send to the pulse generator (pulse height, width and rise time, pulsing rate), as well

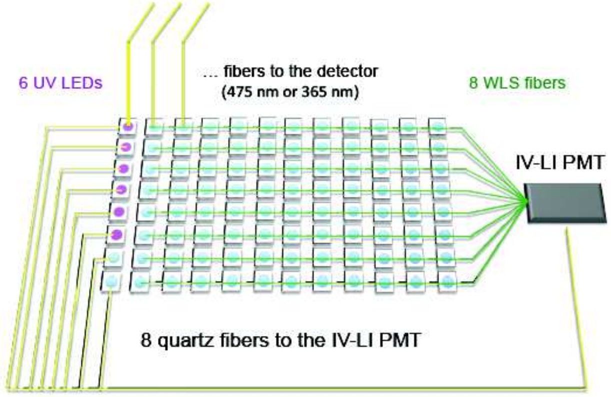

Figure 79: Sketch of the IVLI system.

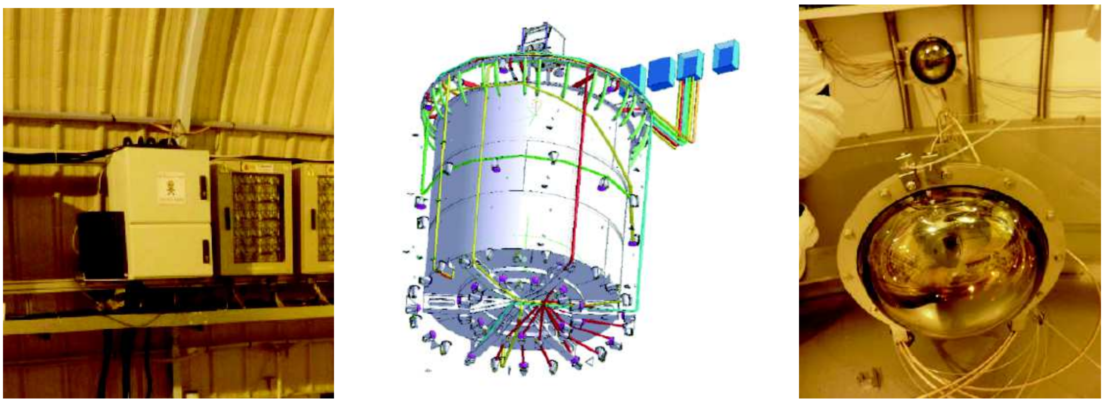

(a) The IVLI box.

(b) Scheme of the fibres connected to the IV.

(c) A PMT with two fibres attached.

Figure 80: Some pictures and schemes of elements of the IVLI system.

as the number of the LED to be switched on. In the IVLI final running configuration, two different modes are used:

- a single-p.e. mode, labelled D19, is used to measure values of μ, to monitor the stability of the PMTs;

- a second type of runs, with a much higher light intensity, labelled D20, is used instead to study PMTs timing and characteristics of the liquid.

D20 runs with UV LEDs are also used to monitor the scintillator light yield. Both kinds of runs are currently taken weekly, in sequences that span all the LEDs.

In this analysis, we exploit data taken using D20 sequences. In D20 runs, each LED is pulsed individually for a total time of one minute. A pulsing rate of 150 Hz is applied, with a 256 ns trigger window opened on all PMTs at each pulse, in a similar way on what is done for the trigger of physics data taking.

5.3 Inner veto scintillators ageing study

In order to evaluate a possible ageing effect, we want to measure the evolution in time of the attenuation length of the IV liquids. IVLI calibration runs are well suited for this purpose. In these runs, the light emitted by a fibre attached to a PMT support structure can be collected by PMTs that are in a cone that has the fibre PMT as vertex. The amplitude of this cone depends on different factors such as the fibre orientation and diffusion, the PMTs light detection threshold, and the structure of the IV itself. The IV is in fact optically isolated from the ID, making each side of the IV virtually blind to another.

The attenuation length is measured by looking at the light collected by PMTs at different distances from the fibre. To achieve a precise measurement of the light collected by each PMT, with multiple distances involved, we need a sufficient amount of light for a certain number of PMTs. For this purpose, IVLI runs with the D20 configuration, in which the light intensity is well above the 1 p.e. per PMT level, are more suitable. On the other hand, saturation effects are also to be considered, as we will see later on. Also, we want to look at direct light propagation, without involving the scintillator absorption and re-emission. Blue light emitting LED are therefore considered. IVLI D20 runs are taken on a regular basis in Double Chooz (weekly in the far detector full operation phase). Wee can therefore measure the attenuation length at different times and evaluate its ageing.

5.3.1 Photomultipliers light collection

In the D20 configuration, each of the 96 LEDs is pulsed in a single run of one minute length. Giving the mentioned flashing rate and the run length, a number of triggers of the order of 10000 is expected for each PMT. In figure 81, the distribution of collected charge in one PMT, for a D20 run, is shown. The particular PMT chosen is the reference PMT of the IVLI system, and the LED the number 53 (blue light). For each run, a distribution like the one in figure 81 is built for every PMT illuminated by the involved fibre. The probabilistic nature of the p.e. production in the photocathode and of the dynode multiplication are responsible for the dispersion of the charge distribution. Such distribution is well fitted with a gaussian curve, shown by a black line in figure 81. Figure 82 represents the same distribution for two other PMTs inside the IV, collecting a different amount of light, during the same IVLI run. The first bin, or pedestal, represents triggers in which no light is collected, and is excluded from the fit. We assume as collected charge for a given run and PMT (q) the fitted mean of the mentioned gaussian fit. q is expressed in ADC counts. In order to convert the measured charge into detected light, it must be transformed into the number of photo electrons N_{pe} using equation 50.

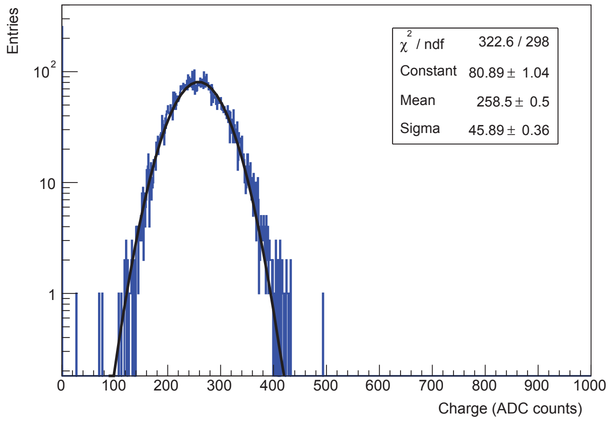

Figure 81: Charge collected by the reference PMT during a calibration run with the LED number 53 of the IVLI system. A gaussian fit on the distribution is represented by the black solid line.

Each of these variables carries its error, which must be taken into account. The error on the charge, or σ_q, is extracted directly from the fit, as the error on the fitted mean. On the other hand, the gain μ of each PMT is reconstructed with a dedicated analysis in Double Chooz (using IVLI sequences D19) and the evaluation of its error needs a separate treatment. In this analysis, we measure the error on the gain σ_μ

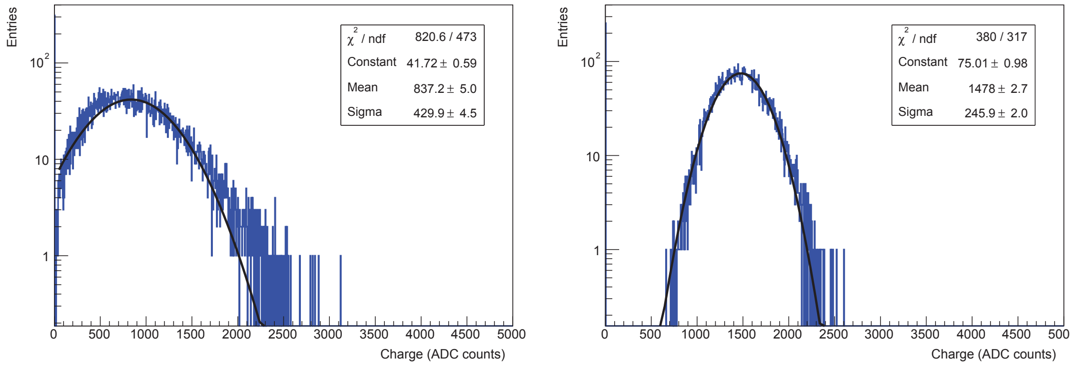

(a) PMT 398 *(b) PMT 399*

Figure 82: Charge collected by two inner veto PMTs during a calibration run with the LED number 53 of the IVLI system. A gaussian fit on the distribution is represented by the black solid line.

basing on short-term fluctuations of the values of μ. To evaluate such fluctuations, we compute for each PMT the distribution of μ measured during one month, and extract from it the value of mean and RMS. The percentage variation of the gain will be therefore given by the ratio RMS/mean. The distribution of μ variations, for 75 of the 78 IV PMTs and for the month between 12 May and 12 June 2011, is shown in figure 83. From the figure, we see how the mean variation is of the level of 3.2 %. Similar short periods at different dates return values in a range between 3 and 4 %. Basing on such observations, we assumed a conservative 5% error on every gain used in this analysis to convert q into N_{pe}. The error on N_{pe} is then propagated from the other two using equation 50

$$\sigma_{N_{pe}} = \sqrt{\frac{\sigma_q^2}{\mu^2} + \frac{q^2\sigma_\mu^2}{\mu^4}} = \frac{1}{\mu}\sqrt{\sigma_q^2 + \frac{q^2}{\mu^2}\sigma_\mu^2}\,, \tag{103}$$

where σ_q is extracted from the fit on the charge distribution and $\sigma_\mu = 0.05\mu$.

5.3.2 Calculation of the attenuation length evolution

Once the number of collected p.e. for different PMTs and different LEDs is computed, we can calculate the attenuation length. The attenuation length λ characterizes the light intensity $I(x)$ at a certain distance from a source of intensity I_0, which is expressed as

$$I(x) = I_0 e^{-x/\lambda}\,. \tag{104}$$

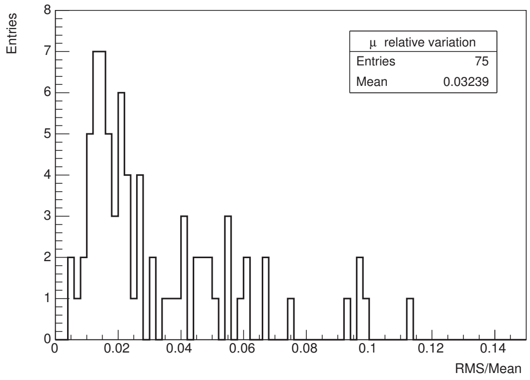

Figure 83: Relative variation of the gain measured during one month of regular calibrations for 75 IV PMTs.

One can reasonably assume that $I(x)$ is proportional to the number of p.e. produced in a PMT α placed at a distance x_α from a LED of a light intensity I_0, i.e.

$$N_{pe}(\alpha) = A \cdot I_0 e^{-x_\alpha/\lambda} \,. \tag{105}$$

In such case, λ could be directly calculated from a fit on N_{pe} values.

However, the coefficient of proportionality A is not constant, as it depends on geometrical factors, like the PMT orientation and the fibre orientation, which is not known a-priori to the desidered level and can also vary with time (long-term mechanical motions, ageing of the fibre end). In figure 82, for instance, the PMT number 398[72] (82a) is closed to the fibre number 53, but gets less light than PMT 399 (82b), which is at higher distance and has the same μ. Moreover, the light intensity of the fibre I_0 also depends on the time, being related to the ageing of the fibre, as well as small fluctuation of the liquid conditions (temperature, pression, etc.). The relation of equation 105 is therefore more realistically represented by

$$N_{pe}(\alpha, t) = A(\alpha, t) \cdot I_0(t) e^{-x_\alpha/\lambda} \,, \tag{106}$$

fact that makes a direct calculation of λ less trivial.

To measure a variation of λ with time, we adopted a different approach: we looked at the relative variation of N_{pe} at different times t_i on the single PMT, in order to isolate the contribution of $A(\alpha, t)$ and $I_0(t)$. The relative percentage variation of collected p.e. between a time t_i and a reference time t_0, for a given PMT (α) located at a distance

---

[72] The numbering system of PMTs include those of the ID; IV ones start from number 390.

x_α from the fibre, is given by

$$N_{pe}^{rel\%}(\alpha, t_i) = 100 \cdot \frac{N_{pe}(\alpha, t_i) - N_{pe}(\alpha, t_0)}{N_{pe}(\alpha, t_0)} \ . \tag{107}$$

The number of p.e. at a given time t_i for a PMT α at a distance x_α from the fibre end is taken directly from equation 106

$$N_{pe}(\alpha, t_i) = A'(\alpha, t_i) e^{-x_\alpha/\lambda_i} \ , \tag{108}$$

where $A'(\alpha, t_i)$ incorporates the terms $A(\alpha, t)$ and $I_0(t)$, including all effects not related to the scintillator ageing, while λ_i represents the attenuation length at the time t_i.

To evaluate λ_i, we calculate N_{pe} at a given time t_i for several PMTs α in order to get a distribution $N_{pe}(\alpha, t_i)$ as a function of x_α. λ_i is then extracted with a fit on such distribution. The fitting function is given by replacing equation 108 in 107, i.e. by

$$N_{pe}^{rel\%}(\alpha, t_i) = 100 \cdot \left(\frac{A'(\alpha, t_i)}{A'(\alpha, t_0)} e^{-x_\alpha \left(\frac{1}{\lambda_i} - \frac{1}{\lambda_0} \right)} - 1 \right) = 100 \cdot \left(A'_{\Delta t_i} e^{-x_\alpha \tau_i} - 1 \right) \ , \tag{109}$$

where $A'_{\Delta t_i}$ represents the ratio between the two factors A' and therefore only depends on the considered times. τ_i is the difference of inverse attenuation lengths at the times t_i and t_0, i.e.

$$\tau_i = \frac{1}{\lambda_i} - \frac{1}{\lambda_0} \ . \tag{110}$$

From the fitted values of τ_i, and the value of λ_0, it is finally possible to obtain λ_i

$$\lambda_i = \frac{\lambda_0}{\tau_i \lambda_0 + 1} \ . \tag{111}$$

5.3.3 Studied sample and results

The Double Chooz liquids have been monitored constantly during the phase antecedent to the installation and filling, showing no significant effects of degradation. A detailed description of these studies can be found in Ref. [224, Section 4.7]. A reference time, or t_0, is defined as the point from which we want to evaluate the ageing. In this analysis we took as t_0 the time corresponding to the first D20 calibration sequence that follows the IVLI commissioning. The studied times t_i that we picked correspond to 4 different dates with regular intervals during the whole data taking. To sum up, the t_0 and other four times t_i are:

- 25 July 2011 (t_0);

- 8 April 2012 (t_1);
- 26 February 2013 (t_2);
- 22 March 2014 (t_3);
- 12 February 2015 (t_4).

For what concerns the attenuation length, a value of λ at t_0 is obtained from a combination of measures taken during tests on the scintillating cocktail of the IV made before and after the filling. Such measurement return values of the attenuation length, measured at the radiation wavelength of 430 nm, for the IV liquid, that span a range going from 8 to 9 m [225]. Accordingly, for the present analysis we use $\lambda_0 = 8.5 \pm 0.3$ m.

During the Double Chooz livetime, several aspects of the far detector hardware, of the PMTs readout, and of the IVLI calibration sequences, have been improved. For instance, in August 2013 an upgrade of the front end electronics took place. As results, the PMT μ values improved by roughly 50%, and the ADC current baseline was raised. Furthermore, the light intensity of D20 runs was increased, of a factor of two, between August and September 2014. The values of measured N_{pe} may therefore present big differences among the studied times. In particular, we expect a significant improvement in the amount of collected light between t_2 and t_3, and again between t_3 and t_4. However, all those effects are included in the factor $A'_{\Delta t_i}$ of equation 109, which sets the scale of the equation and is left as a free parameter in the fit together with λ_i.

Ageing effects, especially if associated with inhomogeneity of the liquid, can be more or less localized in specific areas of the detector. We therefore studied the evolution of λ with different LEDs placed at various positions inside the IV, in order to scan different portions of its volume. According to the geometrical consideration made so far about the IV structure (cylindrical, blinded by the ID), there are three possible kind of areas to scan, that is looking at the light propagation alongside the IV, in its upper part or in its bottom part. However, we found out that the light propagation in the bottom part of the IV was dramatically reduced on long distance (IV side to side) due to the presence of the support structure of the ID. Fibres pointed horizontally in the bottom of the IV are therefore excluded from the analysis shown here. A schematic depiction of the two remaining configurations is shown in figure 84.

We present here the results of our ageing study on a subsample of all observed LEDs. This subsample is selected following some robustness criteria on the data analysed. In particular, we want the fibres to:

- illuminate a portion of liquid as large as possible to maximise the range of the $N_{pe}^{rel\%}(\alpha, t_i)$ distribution;
- illuminate different areas of the IV (top, bottom, vertical slices);
- induce a sizeable signal in the highest possible number of illuminated PMTs;
- do not saturate most of the PMT involved.

Some PMTs, in fact, have their flash-ADC current saturated during one or more triggers for a D20 calibration run. This happens especially for latest calibrations, in which the PMT μ values are higher as a result of a new front-end installed, and in most of the PMTs that get more direct light from the fibre (the PMT on which the fibre is installed, for instance, often saturates). The saturation of PMTs has been a major issue in the choice of the LEDs and in the analysis in general.

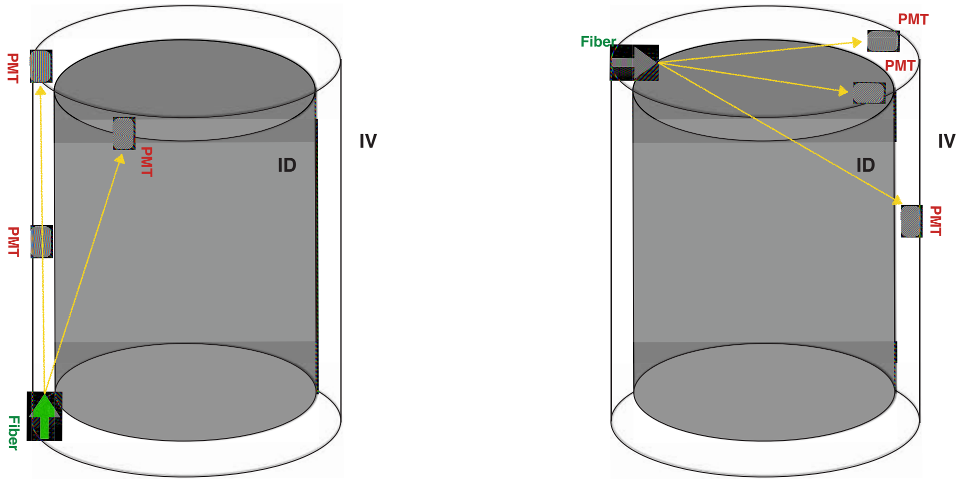

(a) Fibre pointed up from the bottom-side of the IV.

(b) Fibre pointed horizontally in the the top-side of the IV.

Figure 84: Grafic representation of two areas of the IV scanned with pulsed LED light. The light emitted from the LED (green), represented by golden arrows, reaches PMTs at different distances (red).

To sum up, we computed the variation of the attenuation length for 4 LEDs, namely:

- LED 53, 22, and 30, with the fibre pointing up from the bottom-side of the IV (figure 84a);

- LED 92, with the fibre pointing horizontally in the the top-side of the IV (figure 84b);

With LEDs 53, 22 and 30 we studied 3 different vertical portions of the IV, while LED 92 was used to examine its upper part.

The values of $N_{pe}(\alpha, t_i)$ as a function of x_α, for LED 92, are shown as example in figure 85. Each of the four sub-figures (85a, 85b, 85c, and 85d) represents the values at a specific t_i. In the plot are depicted only the PMTs that do not saturate and get at least 4 p.e. at every t_i, with the others being excluded from the λ_i calculation. A fit made with equation 109 on each sub-figure allows to obtain a value for $A'_{\Delta t_i}$ and τ_i. The four λ_i obtained from the respective τ_i (equation 111) are plotted in figure 86, along with λ_0, as a function of time. Errors on λ_i are similarly propagated from the ones of the fitted τ_i

$$\sigma_{\lambda_i} = \frac{\sqrt{\sigma^2_{\lambda_0} + \lambda^4 \sigma^2_{\tau_i}}}{(\tau_i \lambda_0 + 1)^2} . \tag{112}$$

Figure 86 represents the time evolution of λ, and consequently a measure of the ageing based on such parameter. Similar results for the other 3 LEDs analysed and discussed in this section are shown in figure 87 (LED 53), 88 (LED 30), and 89 (LED 22). In all those plots, we see that we are not sensitive to variations of λ, whose value fluctuate within the errors at every considered time.

The same analysis described up to now was performed using LEDs that emit in the UV. The UV light excites the wavelength-shifter component of the liquid scintillator, enabling a study of the scintillator ageing that takes into account absorption effects of the compound. However, we observed that very often the involved PMTs collected an amount of light that does not exceed 2 p.e., fact that inevitably makes the analysis discussed above more difficult. Nevertheless, after accurately selecting the PMT to involve in the fit and the runs to study, a measure of the evolution of λ was performed. The results, which are not explicitly shown here, confirm the non-sizeable deterioration of the attenuation length that has been proven with the analysis on blue LEDs.

5.3.4 Final considerations

In conclusion, we studied the ageing of the IV liquid scintillators by looking at the evolution of light collected by PMTs at different distance from a LED, in different times, using IVLI calibration runs. The attenuation length is extracted from a fit at different times picked in the last 4 years of Double Chooz livetime. As a result of this analysis, we see no appreciable ageing effect, within the errors, over all the data taking period.

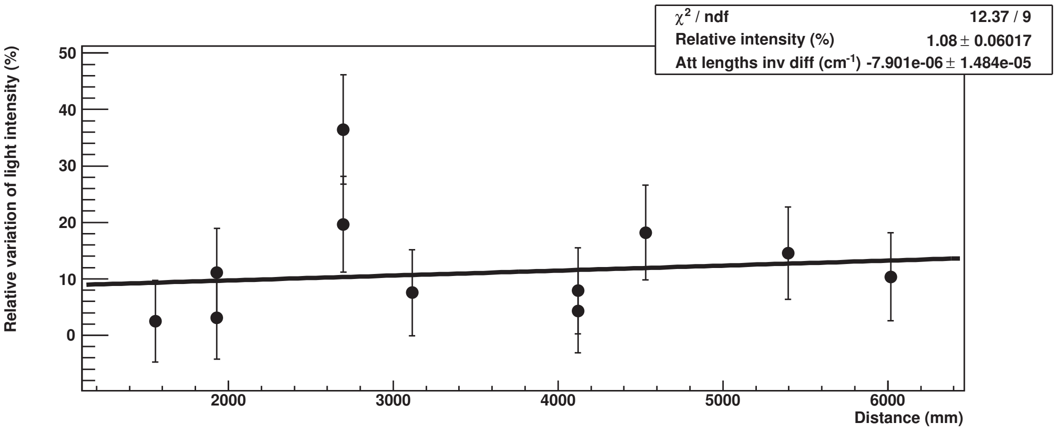

(a) $N_{pe}(\alpha, t_1)$ vs x_α

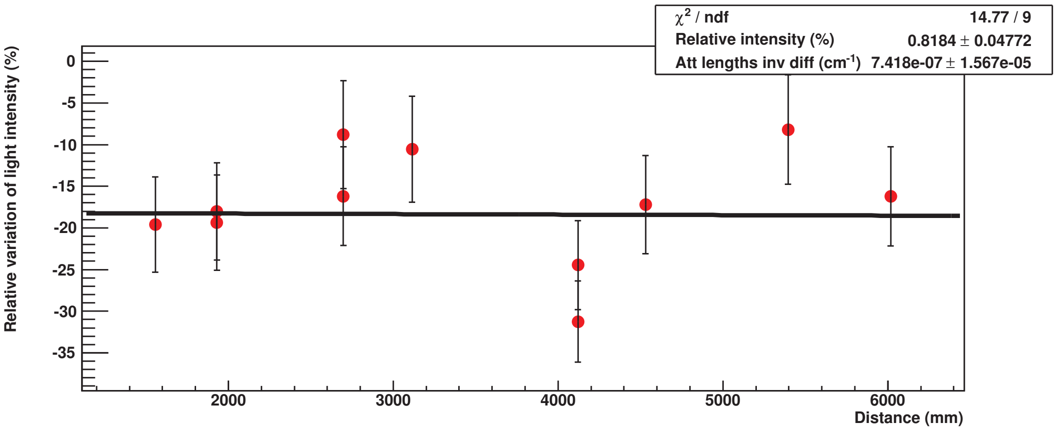

(b) $N_{pe}(\alpha, t_2)$ vs x_α

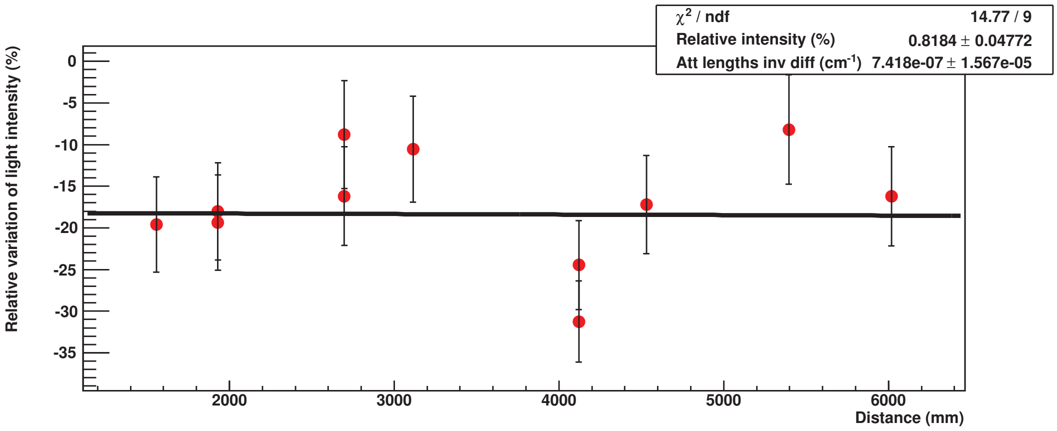

(c) $N_{pe}(\alpha, t_3)$ vs x_α

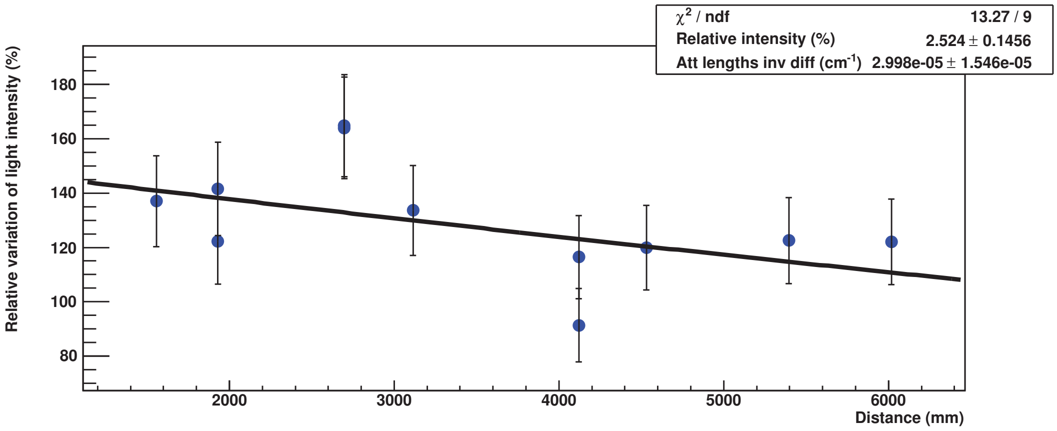

(d) $N_{pe}(\alpha, t_4)$ vs x_α

Figure 85: Relative variation of the number of collected $N_{pe}(\alpha, t_i)$ for different PMTs α, for an IVLI calibration run with LED 92, as a function of the PMT distance from the fibre x_α. Each plot corresponds to a different variation at time t_i with respect to a reference time t_0. Only PMTs that collect a minimum of 4 p.e. and do not saturate at every t_i are considered. In each plot, a fit (equation 109) returns values of $A'_{\Delta t_i}$ and τ_i.

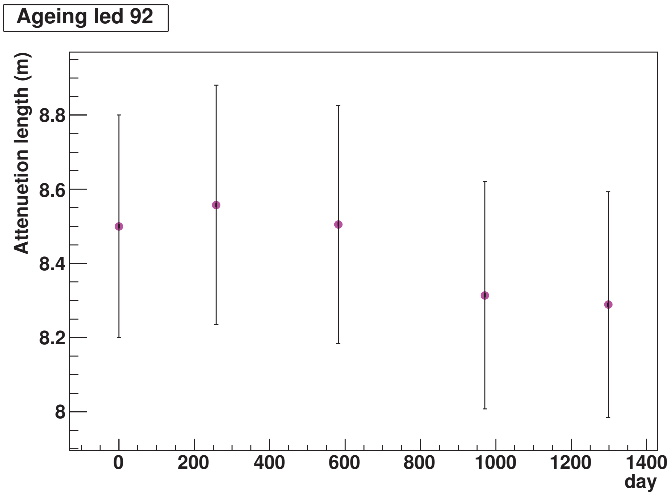

Figure 86: Evolution of the attenuation length with time for LED 92. The four λ_i obtained from the fits, and the λ_0, are plotted as a function of the elapsed days, starting from t_0.

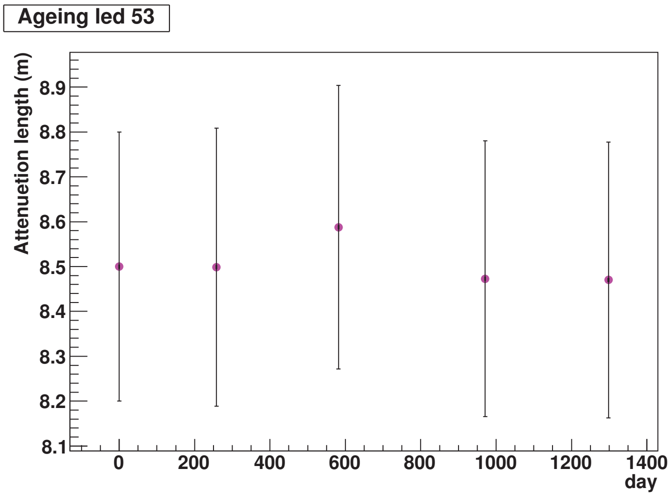

Figure 87: Evolution of the attenuation length with time for LED 53. The four λ_i obtained from the fits, and the λ_0, are plotted as a function of the elapsed days, starting from t_0.

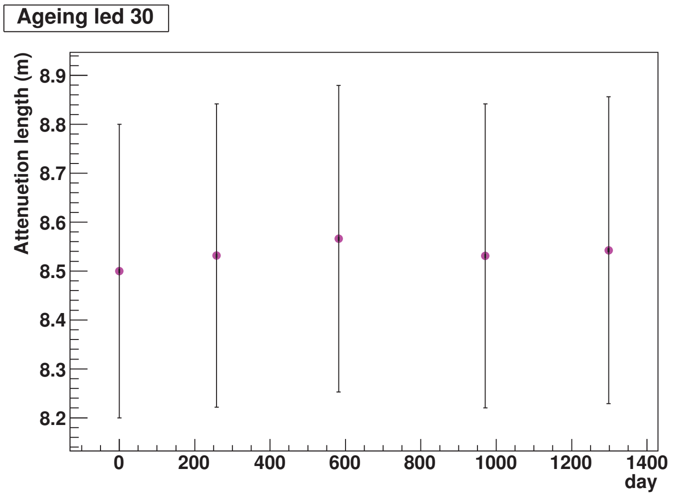

Figure 88: Evolution of the attenuation length with time for LED 30. The four λ_i obtained from the fits, and the λ_0, are plotted as a function of the elapsed days, starting from t_0.

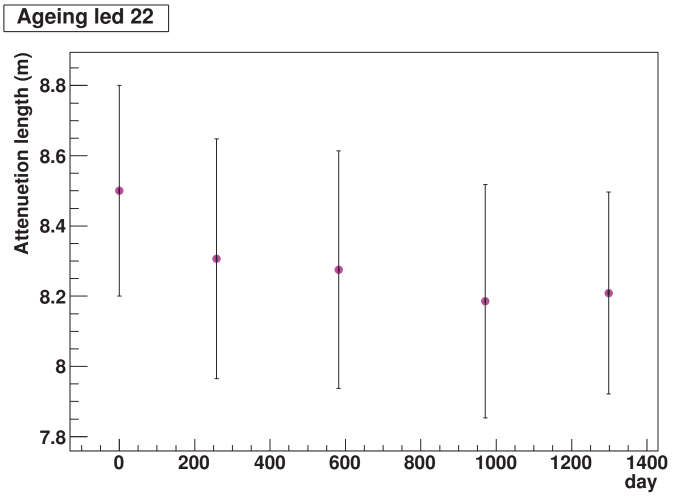

Figure 89: Evolution of the attenuation length with time for LED 22. The four λ_i obtained from the fits, and the λ_0, are plotted as a function of the elapsed days, starting from t_0.

Conclusion

Double Chooz is a reactor neutrino experiment whose goal is to measure the mixing parameter θ_{13}. It is designed to perform this measure in disappearance, by comparing the observed rate and energy shape of reactor $\bar{\nu}_e$ at different distance from the source, with two identical detectors.

The Double Chooz collaboration achieved an excellent understanding of the detector response. Double Chooz features a large signal-on-background ratio, with the latter being contained, well studied, and understood with the help of different tools. The data analysis of the experiment has seen many improvements over its history, with many analyses developed for the reduction of background noise.

The reconstruction and study of pulse shapes has proven to have useful applications in many aspects concerning the Double Chooz experiment. In the dedicated chapter, the main core of the work presented in this manuscript, we have seen how the use of a PSD can lead to a significant reduction of correlated backgrounds, i.e. stopping muons and fast neutrons, and to the characterization of ortho-positronium.

The distortion of a stopping muon prompt and delayed signal PS, arising from the vertex mis-reconstruction, can be exploited to select these background events. On one side, a PS-based stopping muon selection was constantly refined in order to efficiently separate stopping muons from neutrino events. In particular, a first application of the Gatti's method evolved into a likelihood approach, which consists in measuring the agreement of the PS with respect to a reference with a negative log-likelihood, and comparing this value for the PS with the reconstructed vertex (L_{reco}) and for the PS re-computed with the vertex in the chimney (L_{chm}). The information on the reconstructed vertex position was exploited to improve the efficiency of the stopping muons selection, leading to a selection in the *chili plot*. On the other side, the results featured by the PS analysis led to the development of a cut based on the goodness of the vertex reconstruction itself, which dramatically reduced the stopping muons background contribution in [160]. The two selections can work in parallel with similar efficiency, and also be used to estimate the remaining background component. In the forthcoming Double Chooz publication, which exploits the neutron capture on hydrogen for the IBD selection, a pulse shape analysis is used to precisely estimate the amount of stopping muons in the neutrino sample.

As for stopping muons, a characteristic feature of fast neutrons in their PS was also used to tag and reduce the fast neutrons background. In particular, the presence of low-energetic proton recoils before the main one creates a structure in the pulse shape that can be identified by looking for a shift in the main peak. This technique has proven to be an efficient tool to reject a significant amount of this background in the IBD sample.

A PS structure with multiple peaks is similarly used as a signature for the ortho-positronium. Ortho-positronium is a bound state of electron and positron, the formation of which induces a distortion in the PS. Although the two signals of the ortho-positronium, i.e. the positron scintillation and annihilation, cannot be resolved, the associated delay that is created can be enough to be distinguished by a dedicated fit on the PS. Such fit allowed to observe the ortho-positronium formation in the Double Chooz liquid scintillator on an event-by-event basis, for the first time for a large neutrino experiment. Moreover, the distribution of measured delays was used to calculate a lifetime and formation probability of the compound, which are in agreement with independent measurements made on the Double Chooz liquid scintillator.

All pulse shape analyses we discussed have been performed on data collected for the livetime of the last Double Chooz publications. Nevertheless, the experiment is still collecting data and other analyses will come. It is therefore important to keep developing all PS-based studies, tuning them for future Double Chooz analyses. This is true especially for data collected in the newly built near detector, which are of great importance for the future of the experiment. With respect to the far detector we expect an increased amount of muon-induced background due to the different depths of the two laboratories. This increases the importance of having precise and effective cuts on the background. First data from the near detector were recently analysed. Although the lack of a full calibration limits the accuracy in the reconstruction of the events, first analyses were already possible on a preliminary IBD selection. The stopping muon selection with likelihood approach has been tested on near detector data, showing a strong separation power of the analysis and confirming the expectations of a larger background component with respect to far detector data.

A crucial aspect to ensure the stability of data taken during the whole Double Chooz livetime is a constant and precise calibration of the response of the channels and of the liquid scintillator. For this reason LEDs are used to pulse light through fibres inside the detector on regular basis. The analysis of these light injection runs (IDLI and IVLI) is used to monitor the functioning and to calibrate the PMTs, as well as survey the state of the liquid scintillator.

Among the many effects that result in a deterioration of the optical characteristics of the organic compound that constitutes the scintillator, the oxidation is one of the most critical. The main problem encountered in the case of aging of the scintillator is a loss of response characterized by a reduction in the efficiency of production of scintillation light and by a relaxation of the attenuation length.

We presented a study of the scintillator ageing using IVLI runs. The attenuation length was considered as parameter for the stability of the scintillator of the Double Chooz inner veto. In order to study this parameter, we took into account runs in which it was emitted an amount of light sufficiently high to be observed by PMT at large distance from the fibre. The charge collected at various distance was used to estimate the attenuation length. In order to isolate the ageing of the scintillator from fibre-related or external effects, we considered a PMT-by-PMT evolution of the recorded light. By looking at calibration runs at different times we have built a time variation of the attenuation length. Such variation was shown to be included within the estimated uncertainties, supporting the hypothesis of no sizeable ageing effect.

References

[1] Laurie M Brown. ‘The idea of the neutrino’. In: *Physics Today* 31.9 (2008), pp. 23–28.

[2] Ernest Rutherford. ‘VIII. Uranium radiation and the electrical conduction produced by it’. In: *The London, Edinburgh, and Dublin Philosophical Magazine and Journal of Science* 47.284 (1899), pp. 109–163.

[3] James Riddick Partington. *A history of chemistry*. Macmillan, 1970.

[4] James Chadwick. ‘Intensitätsverteilung im magnetischen Spectrum Der β-Strahlen von radium B+C’. In: *Verhandl. Dtsc. Phys. Ges.* 16 (1914), p. 383.

[5] John S O’Conor et al. ‘The beta-ray spectrum of radium E’. In: *Physical Review* 52.4 (1937), p. 303.

[6] GJ Neary. ‘The β-Ray Spectrum of Radium E’. In: *Proceedings of the Royal Society of London. Series A, Mathematical and Physical Sciences* (1940), pp. 71–87.

[7] Lise Meitner. ‘Über die Entstehung der β-Strahl-Spektren radioaktiver Substanzen’. In: *Zeitschrift für Physik A Hadrons and Nuclei* 9.1 (1922), pp. 131–144.

[8] Charles D Ellis and WA Wooster. ‘The average energy of disintegration of radium E’. In: *Proceedings of the Royal Society of London. Series A, Containing Papers of a Mathematical and Physical Character* (1927), pp. 109–123.

[9] Wikipedia. *Alpha spectroscopy - Wikipedia, The Free Encyclopedia*.

[10] .

[11] E. Rutherford. ‘The scattering of alpha and beta particles by matter and the structure of the atom’. In: *Phil.Mag.* 21 (1911), pp. 669–688.

[12] E. Rutherford. ‘The structure of the atom’. In: *Phil.Mag.* 27 (1914), pp. 488–498.

[13] .

[14] Henry GJ Moseley. ‘XCIII. The high-frequency spectra of the elements’. In: *The London, Edinburgh, and Dublin Philosophical Magazine and Journal of Science* 26.156 (1913), pp. 1024–1034.

[15] Ernest Rutherford. 'LIV. Collision of α particles with light atoms. IV. An anomalous effect in nitrogen'. In: *The London, Edinburgh, and Dublin Philosophical Magazine and Journal of Science* 37.222 (1919), pp. 581–587.

[16] ETH-Bibliothek. *Pauli's letter of the 4th of December 1930*. 2015. URL: http://www.pp.rhul.ac.uk/~ptd/TEACHING/PH2510/pauli-letter.html (visited on 30/08/2015).

[17] Roger H Stuewer. 'The Seventh Solvay Conference: Nuclear Physics at the Crossroads'. In: *No Truth Except in the Details*. Springer, 1995, pp. 333–362.

[18] James Chadwick. 'The existence of a neutron'. In: *Proceedings of the Royal Society of London A: Mathematical, Physical and Engineering Sciences*. Vol. 136. 830. The Royal Society. 1932, pp. 692–708.

[19] James Chadwick. 'Possible existence of a neutron'. In: *Nature* 129.3252 (1932), p. 312.

[20] Paul AM Dirac. 'The quantum theory of the emission and absorption of radiation'. In: *Proceedings of the Royal Society of London A: Mathematical, Physical and Engineering Sciences*. Vol. 114. 767. The Royal Society. 1927, pp. 243–265.

[21] Enrico Fermi. 'An attempt of a theory of beta radiation. 1'. In: *Z. phys* 88.161 (1934), p. 10.

[22] Enrico Fermi. 'Tentativo di una teoria dei raggi β'. In: *Il Nuovo Cimento* 11.1 (1934), pp. 1–19.

[23] B Pontecorvo. 'Report PD-205, Chalk River Laboratory, 1946. see B. Pontecorvo "Selected scientific work" p. 21'. In: *Societa Italiana di Fisica, Bologna, Italia* (1997).

[24] Hans Bethe and Rudolph Peierls. 'The *neutrino*'. In: *Nature* 133.3362 (1934), p. 532.

[25] Frederick Reines. 'The neutrino: from poltergeist to particle'. In: *Reviews of Modern Physics* 68.2 (1996), pp. 317–327.

[26] HR Crane. 'The energy and momentum relations in the beta-decay, and the search for the neutrino'. In: *Reviews of Modern Physics* 20.1 (1948), p. 278.

[27] F. Reines and Jr. C. L. Cowan. In: *Phys.Rev* 90 (1953), p. 492.

[28] Raymond Davis Jr. 'Attempt to Detect the Antineutrinos from a Nuclear Reactor by the Cl 37 ($\bar{\nu}$,e^-) A 37 Reaction'. In: *Physical Review* 97.3 (1955), p. 766.

[29] C. L. Cowan Jr. et al. ‘Detection of the Free Neutrino: A Confirmation’. In: *Science* 124 (July 1956), pp. 103–104.

[30] Frederick Reines and Clyde L Cowan. ‘The neutrino’. In: *Nature* 178.4531 (1956), pp. 446–449.

[31] F. Reines et al. ‘Detection of the Free Antineutrino’. In: *Phys. Rev.* 117 (1 1960), pp. 159–173.

[32] Carl D Anderson and Seth H Neddermeyer. ‘Cloud chamber observations of cosmic rays at 4300 meters elevation and near sea-level’. In: *Physical Review* 50.4 (1936), pp. 263–271.

[33] Cesare Mansueto Giulio Lattes, GPS Occhialini and Cecil Frank Powell. ‘Observations on the tracks of slow mesons in photographic emulsions’. In: *Nature* 160.4066 (1947), pp. 453–456.

[34] Marcello Conversi, Ettore Pancini and Oreste Piccioni. ‘On the disintegration of negative mesons’. In: *Physical Review* 71.3 (1947), p. 209.

[35] Bruno Pontecorvo. ‘Nuclear capture of mesons and the meson decay’. In: *Physical Review* 72.3 (1947), p. 246.

[36] J Steinberger. ‘On the range of the electrons in meson decay’. In: *Physical Review* 74.4 (1948), p. 500.

[37] Gaillard Danby et al. ‘Observation of high-energy neutrino reactions and the existence of two kinds of neutrinos’. In: *Physical Review Letters* 9.1 (1962), p. 36.

[38] Chien-Shiung Wu et al. ‘Experimental test of parity conservation in beta decay’. In: *Physical review* 105.4 (1957), p. 1413.

[39] Tsung-Dao Lee and Chen-Ning Yang. ‘Question of parity conservation in weak interactions’. In: *Physical Review* 104.1 (1956), p. 254.

[40] Rodger M Walser. ‘ECG Sudarshan: Quantum catalyst’. In: *Journal of Physics: Conference Series*. Vol. 196. 1. IOP Publishing. 2009, p. 012001.

[41] Chris Quigg. ‘The electroweak theory’. In: *arXiv preprint hep-ph/0204104* 571 (2000).

[42] Maurice Goldhaber, L Grodzins and AW Sunyar. ‘Helicity of neutrinos’. In: *Physical Review* 109.3 (1958), p. 1015.

[43] J-E Augustin et al. ‘Discovery of a Narrow Resonance in e+ e- Annihilation’. In: *Physical Review Letters* 33.23 (1974), p. 1406.

[44] Martin L Perl et al. ‘Evidence for anomalous lepton production in e+- e- annihilation’. In: *Physical Review Letters* 35.22 (1975), p. 1489.

[45] Ml F Kaplon and DM Ritson. ‘Emulsion Cloud-Chamber Observations on the Interactions of High Energy Primary Cosmic Radiation’. In: *Physical Review* 88.2 (1952), p. 386.

[46] K Kodama et al. ‘Observation of tau neutrino interactions’. In: *Physics Letters B* 504.3 (2001), pp. 218–224.

[47] TD Collaboration. ‘A first measurement of the interaction cross section of the tau neutrino’. In: *Phys. Rev. D* 78 (2007), p. 052002.

[48] Reinhard Schwienhorst et al. ‘A new upper limit for the tau-neutrino magnetic moment’. In: *Physics Letters B* 513.1 (2001), pp. 23–29.

[49] D Decamp et al. ‘A precise determination of the number of families with light neutrinos and of the Z boson partial widths’. In: *Physics Letters B* 235.3 (1990), pp. 399–411.

[50] Bruno Pontecorvo. ‘Mesonium and antimesonium’. In: *Zhur. Eksptl’. i Teoret. Fiz.* 33 (1957).

[51] Bruno Pontecorvo. ‘Inverse β processes and non-conservation of lepton charge’. In: *Zhur. Eksptl’. i Teoret. Fiz.* 34 (1958).

[52] Ian Simpson Hughes. *Elementary particles*. Cambridge University Press, 1991.

[53] EG Adelberger et al. ‘Solar fusion cross sections. II. The p p chain and CNO cycles’. In: *Reviews of Modern Physics* 83.1 (2011), p. 195.

[54] John N Bahcall. ‘Solar neutrinos: Where we are, where we are going’. In: *The Astrophysical Journal* 467 (1996), p. 475.

[55] V Gribov and B Pontecorvo. ‘Neutrino astronomy and lepton charge’. In: *Physics Letters B* 28.7 (1969), pp. 493–496.

[56] John N Bahcall and Raymond Davis Jr. ‘Solar neutrinos: A scientific puzzle’. In: *Science* 191.4224 (1976), pp. 264–267.

[57] Bruce T Cleveland et al. ‘Measurement of the solar electron neutrino flux with the Homestake chlorine detector’. In: *The Astrophysical Journal* 496.1 (1998), p. 505.

[58] John N Bahcall and MH Pinsonneault. ‘What do we (not) know theoretically about solar neutrino fluxes?’ In: *Physical review letters* 92.12 (2004), p. 121301.

[59] John N Bahcall, MH Pinsonneault and Sarbani Basu. ‘Solar models: Current epoch and time dependences, neutrinos, and helioseismological properties’. In: *The Astrophysical Journal* 555.2 (2001), p. 990.

[60] Pavel A Cherenkov. ‘Visible emission of clean liquids by action of γ radiation’. In: *Doklady Akademii Nauk SSSR* 2 (1934), p. 451.

[61] Kohji S Hirata et al. ‘Observation of ^{8}B solar neutrinos in the Kamiokande-II detector’. In: *Physical Review Letters* 63.1 (1989), p. 16.

[62] K_S Hirata et al. ‘Results from one thousand days of real-time, directional solar-neutrino data’. In: *Physical Review Letters* 65.11 (1990), p. 1297.

[63] KS Hirata et al. ‘Real-time, directional measurement of B 8 solar neutrinos in the Kamiokande II detector’. In: *Physical Review D* 44.8 (1991), p. 2241.

[64] Wolfgang Hampel et al. ‘GALLEX solar neutrino observations: Results for GALLEX IV’. In: *Physics Letters B* 447.1 (1999), pp. 127–133.

[65] John N Bahcall, Sarbani Basu and MH Pinsonneault. ‘How uncertain are solar neutrino predictions?’ In: *Physics Letters B* 433.1 (1998), pp. 1–8.

[66] JN Bahcalf. ‘Solar models and solar neutrinos’. In: *Physica Scripta* 121 (2005), pp. 46–50.

[67] *G.N.O. Gallium Neutrino Observ*. `http://web.lngs.infn.it/lngs_infn/contents/lngs_en/research/experiments_scientific_info/library_publications/preprint_reports/report04/gno.pdf`. Accessed: 2015-08-30.

[68] JN Abdurashitov et al. ‘Measurement of the solar neutrino capture rate with gallium metal’. In: *Phys. Rev. C* 60.astro-ph/9907113 (1999), p. 055801.

[69] JN Abdurashitov et al. ‘Measurement of the solar neutrino capture rate with gallium metal. III. Results for the 2002–2007 data-taking period’. In: *Physical Review C* 80.1 (2009), p. 015807.

[70] W. Hampel et al. ‘Final results of the Cr-51 neutrino source experiments in GALLEX’. In: *Phys. Lett.* B420 (1998), pp. 114–126.

[71] J Boger et al. ‘The Sudbury neutrino observatory’. In: *Nuclear Instruments and Methods in Physics Research Section A: Accelerators, Spectrometers, Detectors and Associated Equipment* 449.1 (2000), pp. 172–207.

[72] SN Ahmed et al. ‘Measurement of the Total Active B 8 Solar Neutrino Flux at the Sudbury Neutrino Observatory with Enhanced Neutral Current Sensitivity’. In: *Physical review letters* 92.18 (2004), p. 181301.

[73] B Aharmim et al. ‘Independent Measurement of the Total Active B 8 Solar Neutrino Flux Using an Array of He 3 Proportional Counters at the Sudbury Neutrino Observatory’. In: *Physical Review Letters* 101.11 (2008), p. 111301.

[74] QR Ahmad et al. ‘Measurement of the Rate of $\nu_e + d \rightarrow p + p + e^-$ Interactions Produced by B 8 Solar Neutrinos at the Sudbury Neutrino Observatory’. In: *Physical Review Letters* 87.7 (2001), p. 071301.

[75] QR Ahmad et al. ‘Direct evidence for neutrino flavor transformation from neutral-current interactions in the Sudbury Neutrino Observatory’. In: *Physical Review Letters* 89.1 (2002), p. 011301.

[76] D Casper et al. ‘Measurement of atmospheric neutrino composition with the IMB-3 detector’. In: *Physical Review Letters* 66.20 (1991), p. 2561.

[77] K Daum et al. ‘Determination of the atmospheric neutrino spectra with the Frejus detector’. In: *Zeitschrift für Physik C Particles and Fields* 66.3 (1995), pp. 417–428.

[78] WWM Allison et al. ‘Measurement of the atmospheric neutrino flavour composition in Soudan 2’. In: *Physics Letters B* 391.3 (1997), pp. 491–500.

[79] Y Fukuda et al. ‘Evidence for oscillation of atmospheric neutrinos’. In: *Physical Review Letters* 81.8 (1998), p. 1562.

[80] Kate Scholberg et al. ‘Atmospheric neutrinos at Super-Kamiokande’. In: *arXiv preprint hep-ex/9905016* (1999).

[81] A Upadhyay and M Batra. ‘Phenomenology of neutrino mixing in vacuum and matter’. In: *ISRN High Energy Physics* 2013 (2013).

[82] Ziro Maki, Masami Nakagawa and Shoichi Sakata. ‘Remarks on the unified model of elementary particles’. In: *Progress of Theoretical Physics* 28.5 (1962), pp. 870–880.

[83] AG Abramov et al. ‘Beam optics and target conceptual designs for the NuMI project’. In: *Nuclear Instruments and Methods in Physics Research Section A: Accelerators, Spectrometers, Detectors and Associated Equipment* 485.3 (2002), pp. 209–227.

[84] DG Michael et al. ‘Observation of muon neutrino disappearance with the MINOS detectors in the NuMI neutrino beam’. In: *Physical Review Letters* 97.19 (2006), p. 191801.

[85] P Adamson et al. ‘Combined analysis of ν_μ disappearance and $\nu_\mu \to \nu_e$ appearance in MINOS using accelerator and atmospheric neutrinos’. In: *Physical review letters* 112.19 (2014), p. 191801.

[86] K Abe et al. ‘The T2K experiment’. In: *Nuclear Instruments and Methods in Physics Research Section A: Accelerators, Spectrometers, Detectors and Associated Equipment* 659.1 (2011), pp. 106–135.

[87] K Abe et al. ‘First muon-neutrino disappearance study with an off-axis beam’. In: *Physical Review D* 85.3 (2012), p. 031103.

[88] K Abe et al. ‘Measurements of neutrino oscillation in appearance and disappearance channels by the T2K experiment with 6.6×10^{20} protons on target’. In: *Physical Review D* 91.7 (2015), p. 072010.

[89] Alex Himmel. *Recent Results from Super Kamiokan*. 2013. URL: `http://research.dsu.edu/ppc/2013/talks/2013/Talk-40-Alex.pdf` (visited on 31/08/2015).

[90] G. Giacomelli. ‘The CNGS Neutrino Beam’. In: *J.Phys.Conf.Ser.* 116 (2008). 2nd Latin American School on Cosmic Rays and Astrophysics, Puebla, Mexico, 30th August - 8th September 2006, p. 012004. arXiv: `physics/0703247`.

[91] N Agafonova et al. ‘Discovery of tau neutrino appearance in the CNGS neutrino beam with the OPERA experiment’. In: *arXiv preprint arXiv:1507.01417* (2015).

[92] KamLAND& Eguchi et al. ‘First results from KamLAND: evidence for reactor antineutrino disappearance’. In: *Physical Review Letters* 90.2 (2003), p. 021802.

[93] A Gando et al. ‘Reactor on-off antineutrino measurement with KamLAND’. In: *Physical Review D* 88.3 (2013), p. 033001.

[94] T Araki et al. ‘Measurement of neutrino oscillation with KamLAND: Evidence of spectral distortion’. In: *Physical Review Letters* 94.8 (2005), p. 081801.

[95] Gianpaolo Bellini et al. ‘Precision measurement of the Be 7 solar neutrino interaction rate in Borexino’. In: *Physical Review Letters* 107.14 (2011), p. 141302.

[96] G Bellini et al. ‘First Evidence of p e p Solar Neutrinos by Direct Detection in Borexino’. In: *Physical Review Letters* 108.5 (2012), p. 051302.

[97] G Bellini et al. ‘Measurement of the solar B 8 neutrino rate with a liquid scintillator target and 3 MeV energy threshold in the Borexino detector’. In: *Physical Review D* 82.3 (2010), p. 033006.

[98] Andre De Gouvea, Alexander Friedland and Hitoshi Murayama. ‘Earth matter effect in 7Be solar neutrino experiments’. In: *Journal of High Energy Physics* 2001.03 (2001), p. 009.

[99] Gianpaolo Bellini et al. ‘Absence of a day–night asymmetry in the 7 Be solar neutrino rate in Borexino’. In: *Physics Letters B* 707.1 (2012), pp. 22–26.

[100] A Renshaw et al. ‘First indication of terrestrial matter effects on solar neutrino oscillation’. In: *Physical review letters* 112.9 (2014), p. 091805.

[101] F Capozzi et al. ‘Status of three-neutrino oscillation parameters, circa 2013’. In: *Physical Review D* 89.9 (2014), p. 093018.

[102] MC Gonzalez-Garcia, Michele Maltoni and Thomas Schwetz. ‘Updated fit to three neutrino mixing: status of leptonic CP violation’. In: *Journal of High Energy Physics* 2014.11 (2014), pp. 1–28.

[103] André de Gouvêa et al. ‘Neutrinos’. In: *arXiv preprint arXiv:1310.4340* (2013).

[104] GL Fogli et al. ‘Hints of $\theta_{13} > 0$ from global neutrino data analysis’. In: *Physical review letters* 101.14 (2008), p. 141801.

[105] GL Fogli et al. ‘Evidence of $\theta_{13} > 0$ from global neutrino data analysis’. In: *Physical Review D* 84.5 (2011), p. 053007.

[106] M. Apollonio et al. ‘Limits on neutrino oscillations from the CHOOZ experiment’. In: *Phys.Lett.* B466 (1999), pp. 415–430. DOI: `10.1016/S0370-2693(99)01072-2`. arXiv: `hep-ex/9907037 [hep-ex]`.

[107] M Apollonio et al. ‘Search for neutrino oscillations on a long base-line at the CHOOZ nuclear power station’. In: *The European Physical Journal C-Particles and Fields* 27.3 (2003), pp. 331–374.

[108] Y. Abe et al. ‘Indication for the disappearance of reactor electron antineutrinos in the Double Chooz experiment’. In: *Phys.Rev.Lett.* 108 (2012), p. 131801. DOI: `10.1103/PhysRevLett.108.131801`. arXiv: `1112.6353 [hep-ex]`.

[109] F.P. An et al. ‘Observation of electron-antineutrino disappearance at Daya Bay’. In: *Phys.Rev.Lett.* 108 (2012), p. 171803. DOI: `10.1103/PhysRevLett.108.171803`. arXiv: `1203.1669 [hep-ex]`.

[110] J.K. Ahn et al. 'Observation of Reactor Electron Antineutrino Disappearance in the RENO Experiment'. In: *Phys.Rev.Lett.* 108 (2012), p. 191802. DOI: `10.1103/PhysRevLett.108.191802`. arXiv: `1204.0626 [hep-ex]`.

[111] F.P. An et al. 'Spectral measurement of electron antineutrino oscillation amplitude and frequency at Daya Bay'. In: *Phys.Rev.Lett.* 112 (2014), p. 061801. DOI: `10.1103/PhysRevLett.112.061801`. arXiv: `1310.6732 [hep-ex]`.

[112] K Abe et al. 'Indication of electron neutrino appearance from an accelerator-produced off-axis muon neutrino beam'. In: *Physical Review Letters* 107.4 (2011), p. 041801.

[113] K Abe et al. 'Observation of electron neutrino appearance in a muon neutrino beam'. In: *Physical review letters* 112.6 (2014), p. 061802.

[114] P Adamson et al. 'Electron neutrino and antineutrino appearance in the full MINOS data sample'. In: *Physical review letters* 110.17 (2013), p. 171801.

[115] Michael E Peskin and Daniel V Schroeder. *An introduction to quantum field theory*. Westview, 1995, pp. 713–715.

[116] Rabindra Nath Mohapatra and Palash B Pal. *Massive neutrinos in physics and astrophysics*. Vol. 72. World scientific, 2004.

[117] M Fukugita and T Yanagida. 'Sphaleron-induced baryon-number nonconservation and a constraint on Majorana neutrino masses'. In: *Physical Review D* 42.4 (1990), p. 1285.

[118] Gian Francesco Giudice et al. 'Towards a complete theory of thermal leptogenesis in the SM and MSSM'. In: *Nuclear Physics B* 685.1 (2004), pp. 89–149.

[119] Andrei D Sakharov. 'Pisma Zh. Eksp. Teor. Fiz. 5, 32 (1967)[JETP Lett. 5, 24 (1967)]'. In: *Sov. Phys. Usp* 34 (1991), p. 392.

[120] Stephen F King. 'Neutrino Mass Models: Impact of non-zero reactor angle'. In: *arXiv preprint arXiv:1106.4239* (2011).

[121] D Ayres, NOvA Collaboration et al. 'NOvA proposal to build a 30 kiloton off-axis detector to study neutrino oscillations in the Fermilab NuMI beamline'. In: *arXiv preprint hep-ex/0503053* (2005).

[122] Ryan Patterson. *First oscillation results from NOνA*. `http://nova-docdb.fnal.gov/cgi-bin/ShowDocument?docid=13883`. Accessed: 2015-08-30.

[123] Yu-Feng Li et al. ‘Unambiguous determination of the neutrino mass hierarchy using reactor neutrinos’. In: *Physical Review D* 88.1 (2013), p. 013008.

[124] Emilio Ciuffoli, Jarah Evslin and Xinmin Zhang. ‘Sensitivity to the Neutrino Mass Hierarchy’. In: *arXiv preprint arXiv:1305.5150* (2013).

[125] Mattias Blennow et al. ‘Quantifying the sensitivity of oscillation experiments to the neutrino mass ordering’. In: *Journal of High Energy Physics* 2014.3 (2014), pp. 1–41.

[126] Marc Kamionkowski, Arthur Kosowsky and Albert Stebbins. ‘Statistics of cosmic microwave background polarization’. In: *Physical Review D* 55.12 (1997), p. 7368.

[127] G Hinshaw et al. ‘Nine-year Wilkinson Microwave Anisotropy Probe (WMAP) observations: cosmological parameter results’. In: *The Astrophysical Journal Supplement Series* 208.2 (2013), p. 19.

[128] Planck Collaboration et al. ‘Planck 2015 results. XIII. Cosmological parameters’. In: *arXiv preprint arXiv:1502.01589* (2015).

[129] Richard A Battye and Adam Moss. ‘Evidence for massive neutrinos from cosmic microwave background and lensing observations’. In: *Physical review letters* 112.5 (2014), p. 051303.

[130] Ch Kraus et al. ‘Final results from phase II of the Mainz neutrino mass searchin tritium β decay’. In: *The European Physical Journal C-Particles and Fields* 40.4 (2005), pp. 447–468.

[131] VN Aseev et al. ‘Upper limit on the electron antineutrino mass from the Troitsk experiment’. In: *Physical Review D* 84.11 (2011), p. 112003.

[132] Joachim Wolf, Katrin Collaboration et al. ‘The KATRIN neutrino mass experiment’. In: *Nuclear Instruments and Methods in Physics Research Section A: Accelerators, Spectrometers, Detectors and Associated Equipment* 623.1 (2010), pp. 442–444.

[133] Ettore Majorana and Luciano Maiani. ‘A symmetric theory of electrons and positrons’. In: *Ettore Majorana Scientific Papers*. Springer, 2006, pp. 201–233.

[134] M Gell-Mann, P Ramond and R Slansky. ‘Supergravity, Proceedings of the Workshop, Stony Brook, New York, 1979’. In: (1979).

[135] J Schechter and José WF Valle. ‘Neutrinoless double-β decay in SU (2)$\times$ U (1) theories’. In: *Physical Review D* 25.11 (1982), p. 2951.

[136] DR Artusa et al. ‘Searching for neutrinoless double-beta decay of 130 Te with CUORE’. In: *Advances in High Energy Physics* 2015 (2015).

[137] M Agostini et al. ‘Results on $\beta\beta$ decay with emission of two neutrinos or Majorons in ^{76}Ge from GERDA Phase I’. In: *arXiv preprint arXiv:1501.02345* (2015).

[138] A Gando et al. ‘Limit on Neutrinoless β β Decay of Xe 136 from the First Phase of KamLAND-Zen and Comparison with the Positive Claim in Ge 76’. In: *Physical Review Letters* 110.6 (2013), p. 062502.

[139] R Arnold et al. ‘Probing new physics models of neutrinoless double beta decay with SuperNEMO’. In: *The European Physical Journal C* 70.4 (2010), pp. 927–943.

[140] J.J Gómez-Cadenas and Justo Martín-Albo. *Phenomenology of neutrinoless double beta decay*. arXiv: `0902.0885 [quant-ph]`.

[141] C Athanassopoulos et al. ‘Evidence for $\nu_\mu \rightarrow \nu_e$ oscillations from the LSND Experiment at the Los Alamos Meson Physics Facility’. In: *Physical Review Letters* 77.15 (1996), p. 3082.

[142] C Athanassopoulos et al. ‘Results on $\nu_\mu \rightarrow \nu_e$ neutrino oscillations from the LSND experiment’. In: *Physical Review Letters* 81.9 (1998), p. 1774.

[143] Michel Sorel, Janet M Conrad and MH Shaevitz. ‘Combined analysis of short-baseline neutrino experiments in the (3+1) and (3+2) sterile neutrino oscillation hypotheses’. In: *Physical Review D* 70.7 (2004), p. 073004.

[144] AA Aguilar-Arevalo et al. ‘A Combined $\nu_\mu \rightarrow \nu_e$ And $\bar{\nu}_\mu \rightarrow \bar{\nu}_e$ Oscillation Analysis of the MiniBooNE Excesses’. In: *arXiv preprint arXiv:1207.4809* (2012).

[145] AA Aguilar-Arevalo et al. ‘Improved Search for $\nu_\mu \rightarrow \nu_e$ Oscillations in the MiniBooNE Experiment’. In: *Physical review letters* 110.16 (2013), p. 161801.

[146] MicroBooNE Collaboration et al. ‘The MicroBooNE Technical Design Report’. In: *MicroBooNE docdb* 1565 (2012).

[147] McroBooNE collaboration. *MicroBooNE website*. 2015. URL: `http://www-microboone.fnal.gov/index.html`.

[148] C Adams et al. ‘LAr1-ND: testing neutrino anomalies with multiple LArTPC detectors at Fermilab’. In: *arXiv preprint arXiv:1309.7987* (2013).

[149] Th A Mueller et al. ‘Improved predictions of reactor antineutrino spectra’. In: *Physical Review C* 83.5 (2011), p. 054615.

[150] G Mention et al. ‘Reactor antineutrino anomaly’. In: *Physical Review D* 83.7 (2011), p. 073006.

[151] Patrick Huber. ‘Determination of antineutrino spectra from nuclear reactors’. In: *Physical Review C* 84.2 (2011), p. 024617.

[152] A Gando et al. ‘White paper: CeLAND-Investigation of the reactor antineutrino anomaly with an intense 144Ce-144Pr antineutrino source in KamLAND’. In: *arXiv preprint arXiv:1309.6805* (2013).

[153] JA Formaggio and J Barrett. ‘Resolving the reactor neutrino anomaly with the KATRIN neutrino experiment’. In: *Physics Letters B* 706.1 (2011), pp. 68–71.

[154] A. de Gouvea et al. ‘Working Group Report: Neutrinos’. In: *Community Summer Study 2013: Snowmass on the Mississippi (CSS2013) Minneapolis, MN, USA, July 29-August 6, 2013*. 2013. arXiv: `1310.4340 [hep-ex]`. URL: `http://inspirehep.net/record/1260555/files/arXiv:1310.4340.pdf`.

[155] E Baussan et al. ‘A very intense neutrino super beam experiment for leptonic CP violation discovery based on the European spallation source linac’. In: *Nuclear Physics B* 885 (2014), pp. 127–149.

[156] Corey Adams et al. ‘The long-baseline neutrino experiment: exploring fundamental symmetries of the universe’. In: *arXiv preprint arXiv:1307.7335* (2013).

[157] Y Abe et al. ‘Reactor ν^{-} e disappearance in the Double Chooz experiment’. In: *Physical Review D* 86.5 (2012), p. 052008.

[158] Y Abe et al. ‘First measurement of θ_{13} from delayed neutron capture on hydrogen in the Double Chooz experiment’. In: *Physics Letters B* 723.1 (2013), pp. 66–70.

[159] Y. Abe et al. ‘Background-independent measurement of θ_{13} in Double Chooz’. In: *Phys.Lett.* B735 (2014), pp. 51–56. DOI: `10.1016/j.physletb.2014.04.045`. arXiv: `1401.5981 [hep-ex]`.

[160] Y Abe et al. ‘Improved measurements of the neutrino mixing angle θ_{13} with the Double Chooz detector’. In: *Journal of High Energy Physics* 2014.10 (2014), pp. 1–44.

[161] F.P. An et al. ‘Improved Measurement of Electron Antineutrino Disappearance at Daya Bay’. In: *Chin.Phys.* C37 (2013), p. 011001. DOI: `10.1088/1674-1137/37/1/011001`. arXiv: `1210.6327 [hep-ex]`.

[162] FP An et al. ‘Independent measurement of the neutrino mixing angle θ 13 via neutron capture on hydrogen at Daya Bay’. In: *Physical Review D* 90.7 (2014), p. 071101.

[163] Soo-Bong Kim. ‘New results from RENO and prospects with RENO-50’. In: *arXiv preprint arXiv:1412.2199* (2014).

[164] P Adamson et al. ‘Improved search for muon-neutrino to electron-neutrino oscillations in MINOS’. In: *Physical Review Letters* 107.18 (2011), p. 181802.

[165] Joseph A Formaggio and GP Zeller. ‘From eV to EeV: Neutrino cross sections across energy scales’. In: *Reviews of Modern Physics* 84.3 (2012), p. 1307.

[166] Daniel Greiner et al. ‘Double Chooz detectors design’. In: *Nuclear Instruments and Methods in Physics Research Section A: Accelerators, Spectrometers, Detectors and Associated Equipment* 581.1 (2007), pp. 139–142.

[167] A Cabrera. ‘The Double Chooz detector’. In: *Nuclear Instruments and Methods in Physics Research Section A: Accelerators, Spectrometers, Detectors and Associated Equipment* 617.1 (2010), pp. 473–477.

[168] Christoph Aberle et al. ‘Light yield and energy transfer in a new Gd-loaded liquid scintillator’. In: *Chemical Physics Letters* 516.4 (2011), pp. 257–262.

[169] Christoph Aberle et al. ‘Large scale Gd-beta-diketonate based organic liquid scintillator production for antineutrino detection’. In: *Journal of Instrumentation* 7.06 (2012), P06008.

[170] T Matsubara et al. ‘Development and evaluation of 10-inch Photo-Multiplier Tubes for the Double Chooz experiment’. In: *arXiv preprint arXiv:1104.0786* (2011).

[171] T Matsubara et al. ‘Evaluation of 400 low background 10-in. photo-multiplier tubes for the Double Chooz experiment’. In: *Nuclear Instruments and Methods in Physics Research Section A: Accelerators, Spectrometers, Detectors and Associated Equipment* 661.1 (2012), pp. 16–25.

[172] C Bauer et al. ‘Qualification tests of 474 photomultiplier tubes for the inner detector of the Double Chooz experiment’. In: *Journal of Instrumentation* 6.06 (2011), P06008.

[173] D Dietrich et al. ‘Monte Carlo aided design of the inner muon veto detectors for the Double Chooz experiment’. In: *Journal of Instrumentation* 7.08 (2012), P08012.

[174] Junpei Maeda et al. ‘Online data acquisition and the control system for the Double Chooz experiment’. In: *Journal of Physics: Conference Series*. Vol. 331. 2. IOP Publishing. 2011, p. 022018.

[175] Y Abe et al. ‘The waveform digitiser of the Double Chooz experiment: performance and quantisation effects on photomultiplier tube signals’. In: *Journal of Instrumentation* 8.08 (2013), P08015.

[176] F Beissel et al. ‘The trigger and timing system of the Double Chooz experiment’. In: *Journal of Instrumentation* 8.01 (2013), T01003.

[177] Rene Brun and Fons Rademakers. ‘ROOT—an object oriented data analysis framework’. In: *Nuclear Instruments and Methods in Physics Research Section A: Accelerators, Spectrometers, Detectors and Associated Equipment* 389.1 (1997), pp. 81–86.

[178] Sea Agostinelli et al. ‘GEANT4—a simulation toolkit’. In: *Nuclear instruments and methods in physics research section A: Accelerators, Spectrometers, Detectors and Associated Equipment* 506.3 (2003), pp. 250–303.

[179] John Allison et al. ‘Geant4 developments and applications’. In: *Nuclear Science, IEEE Transactions on* 53.1 (2006), pp. 270–278.

[180] AB MySQL. *MySQL: the world’s most popular open source database*. MySQL AB, 1995.

[181] Y Abe et al. ‘Precision muon reconstruction in Double Chooz’. In: *Nuclear Instruments and Methods in Physics Research Section A: Accelerators, Spectrometers, Detectors and Associated Equipment* 764 (2014), pp. 330–339.

[182] Peter D Wilson. *The nuclear fuel cycle from ore to wastes*. 1996.

[183] Olivier Méplan et al. ‘MURE: MCNP Utility for Reactor Evolution-Description of the methods, first applications and results’. In: (2005).

[184] G Marleau, A Hébert and R Roy. ‘DRAGON: A Collision Probability Transport Code for Cell and Multicell Calculations’. In: *Report IGE-100*. École Polytechnique de Montréal, 1990.

[185] P Vogel and John F Beacom. ‘Angular distribution of neutron inverse beta decay, $\nu_e + p \rightarrow e^+ + n$’. In: *Physical Review D* 60.5 (1999), p. 053003.

[186] K Schreckenbach et al. ‘Determination of the antineutrino spectrum from 235 U thermal neutron fission products up to 9.5 MeV’. In: *Physics Letters B* 160.4 (1985), pp. 325–330.

[187] F Von Feilitzsch, AA Hahn and K Schreckenbach. ‘Experimental beta-spectra from 239 Pu and 235 U thermal neutron fission products and their correlated antineutrino spectra’. In: *Physics Letters B* 118.1 (1982), pp. 162–166.

[188] AA Hahn et al. ‘Antineutrino spectra from 241 Pu and 239 Pu thermal neutron fission products’. In: *Physics Letters B* 218.3 (1989), pp. 365–368.

[189] M Fallot et al. ‘New antineutrino energy spectra predictions from the summation of beta decay branches of the fission products’. In: *Physical review letters* 109.20 (2012), p. 202504.

[190] Y Declais et al. ‘Study of reactor antineutrino interaction with proton at bugey nuclear power plant’. In: *Physics Letters B* 338.2 (1994), pp. 383–389.

[191] G Horton-Smith. *An introduction to GLG4sim features*. 2005.

[192] Romain Roncin. ‘From the measurement of the θ_{13} mixing angle to the search for geo-neutrinos: studying ν_e with Double Chooz and Borexino’. PhD thesis. Université Paris Diderot (Paris 7) - Università degli Studi dell’Aquila, 2014.

[193] B Hamermesh, GR Ringo and S Wexler. ‘The thermal neutron capture cross section of hydrogen’. In: *Physical Review* 90.4 (1953), p. 603.

[194] Brookhaven National Laboratory. *Chart of Nuclides NNCD*.

[195] *Double Chooz internal document*.

[196] Rachel Carr. ‘Measurements of Electron Antineutrino Disappearance in the Double Chooz Experiment’. PhD thesis. Columbia University, 2015.

[197] John Betteley Birks. *The Theory and Practice of Scintillation Counting: International Series of Monographs in Electronics and Instrumentation*. Vol. 27. Elsevier, 2013.

[198] Marvin L Roush, MA Wilson and William F Hornyak. ‘Pulse shape discrimination’. In: *Nuclear Instruments and Methods* 31.1 (1964), pp. 112–124.

[199] RA Winyard, JE Lutkin and GW McBeth. ‘Pulse shape discrimination in inorganic and organic scintillators. I’. In: *Nuclear Instruments and Methods* 95.1 (1971), pp. 141–153.

[200] Gioacchino Ranucci, Augusto Goretti and Paolo Lombardi. ‘Pulse-shape discrimination of liquid scintillators’. In: *Nuclear Instruments and Methods in Physics Research Section A: Accelerators, Spectrometers, Detectors and Associated Equipment* 412.2 (1998), pp. 374–386.

[201] E Gatti and F De Martini. 'A new linear method of discrimination between elementary particles in scintillation counters'. In: *Nuclear Electronics II. Proceedings of the Conference on Nuclear Electronics. V. II*. 1962, pp. 265–276. DOI: `IAEAWien`.

[202] K. Nakamura et al. 'Review of particle physics'. In: *J.Phys.* G37 (2010), p. 075021. DOI: `10.1088/0954-3899/37/7A/075021`.

[203] D Franco, G Consolati and D Trezzi. 'Positronium signature in organic liquid scintillators for neutrino experiments'. In: *Physical Review C* 83.1 (2011), p. 015504.

[204] HJ Ache. *Advances in Chemistry Series, Positronium and Muonium Chemistry*. 1979.

[205] Alessandro Minotti and Stefano Perasso. 'Observation of ortho-Positronium formation in Double Chooz '. In: *37th International Conference on High Energy Physics (ICHEP 2014) Valencia, Spain, July 2-9, 2014*. 2014. URL: `http://indico.ific.uv.es/indico/contributionDisplay.py?contribId=661&sessionId=16&confId=2025`.

[206] G Bellini et al. 'First Evidence of p e p Solar Neutrinos by Direct Detection in Borexino'. In: *Physical Review Letters* 108.5 (2012), p. 051302.

[207] Yasushi Kino et al. 'Positron annihilation in liquid scintillator for electron antineutrino detection'. In: *Journal of Nuclear and Radiochemical Sciences* 1.2 (2000), pp. 63–68.

[208] G Consolati et al. 'Characterization of positronium properties in doped liquid scintillators'. In: *Physical Review C* 88.6 (2013), p. 065502.

[209] Y Abe et al. 'Ortho-positronium observation in the Double Chooz experiment'. In: *Journal of High Energy Physics* 2014.10 (2014), pp. 1–17.

[210] Rene Brun and Fons Rademakers. 'ROOT-an object oriented data analysis framework'. In: *Nuclear Instruments and Methods in Physics Research Section A: Accelerators, Spectrometers, Detectors and Associated Equipment* 389.1 (1997), pp. 81–86.

[211] Fred James and MINUIT Roos. 'Minuit-a system for function minimization and analysis of the parameter errors and correlations'. In: *Computer Physics Communications* 10.6 (1975), pp. 343–367.

[212] G Consolati et al. ‘A new anti-neutrino detection technique based on positronium tagging with plastic scintillators’. In: *arXiv preprint arXiv:1504.01884* (2015).

[213] Marshall Crouch. ‘An improved world survey expression for cosmic ray vertical intensity vs. depth in standard rock’. In: *International Cosmic Ray Conference*. Vol. 6. 1987, p. 165.

[214] Edgar V Bugaev et al. ‘Atmospheric muon flux at sea level, underground, and underwater’. In: *Physical Review D* 58.5 (1998), p. 054001.

[215] Isadore Berlman. *Handbook of florescence spectra of aromatic molecules*. Elsevier, 2012.

[216] Terry L Brewer. ‘Oxygen quenching of the aromatic excited singlet state’. In: *Journal of the American Chemical Society* 93.3 (1971), pp. 775–776.

[217] Yasushi Kino et al. ‘Positron annihilation in liquid scintillator for electron antineutrino detection’. In: *Journal of Nuclear and Radiochemical Sciences* 1.2 (2000), pp. 63–68.

[218] Gioacchino Ranucci, Augusto Goretti and Paolo Lombardi. ‘Pulse-shape discrimination of liquid scintillators’. In: *Nuclear Instruments and Methods in Physics Research Section A: Accelerators, Spectrometers, Detectors and Associated Equipment* 412.2 (1998), pp. 374–386.

[219] George Placzek. *The Rayleigh and Raman Scattering*. Vol. 526. Lawrence Radiation Laboratory, 1959.

[220] G Alimonti et al. ‘Light propagation in a large volume liquid scintillator’. In: *Nuclear Instruments and Methods in Physics Research Section A: Accelerators, Spectrometers, Detectors and Associated Equipment* 440.2 (2000), pp. 360–371.

[221] Andreas G Piepke, S Wayne Moser and Vladimir M Novikov. ‘Development of a Gd loaded liquid scintillator for electron anti-neutrino spectroscopy’. In: *Nuclear Instruments and Methods in Physics Research Section A: Accelerators, Spectrometers, Detectors and Associated Equipment* 432.2 (1999), pp. 392–398.

[222] Leonidas Kalousis. ‘Calibration of the Double Chooz detector and cosmic background studies’. PhD thesis. Strasbourg, 2012.

[223] M. Dracos, L. Kalousis and J. Wurtz. ‘The Inner Veto Light Injection System’. Double Chooz internal document (DocDB 1772-v3). 2010.

[224] Maury Goodman Thierry Lasserre. ‘Double chooz, a search for the neutrino mixing angle theta-13’. In: *arXiv preprint hep-ex/0606025* (2006).

[225] C. Buck. personal communication. 2nd Apr. 2015.